Development of Elastomeric Composites from Iron Sand and Natural Rubber for Vibration Damping

A thesis

submitted in fulfilment

of the requirements for the degree

of

Doctor of Philosophy in Engineering

at

The University of Waikato

by

RAA KHIMI

THE UNIVERSITY OF
WAIKATO
Te Whare Wānanga o Waikato

2015

Abstract

Material with high damping capability is used to reduce vibration in structures. Magnetorheological elastomers (MREs) are a new group of damping materials which consist of an elastomeric matrix containing a suspension of magnetically permeable particles. Damping occurs mainly by the viscous flow of the rubber matrix and inclusion of magnetic particles in the rubber enables additional damping through magnetic particle interaction and interfacial damping. The aim of this thesis was to produce MREs based on iron sand and natural rubber that have good damping performance for potential use in vibration damping.

Dynamic Mechanical Analysis (DMA) was carried out in an isothermal shear mode to measure the changes in material properties caused by vulcanization in order to assess the optimum cure time of rubber compounds to ensure the best damping performance. The results revealed that the shear storage modulus (G′), shear loss modulus (G″) and tan δ all reflect the vulcanization process, however, tan δ gave the best representation of the level of vulcanization. Indeed, tan δ was able to be used to derive the optimum cure time for rubber compounds and showed good agreement with the results using conventional methodology.

The Taguchi method was employed to investigate the effect of a number of factors, namely, iron sand content, iron sand particle size and applied magnetic field during curing on tan δ and energy dissipated during hysteresis tests. The data were then statistically analysed to predict the optimal combination of factors and experiments were then conducted for verification. It was found that the iron sand content had the greatest influence on tan δ when measured over a range of frequency

(0.01-130Hz at 0.5% strain amplitude and at room temperature) as well as on the energy dissipated during the hysteresis tests. The iron sand content and magnetic field were also found to influence the width of the peak in tan δ as a function of temperature (studied over the range -100 to 50ºC at 1Hz and 0.5% strain amplitude). However, none of the factors showed significant influence on tan δ for the plateau region from 1.0-4.5% strain amplitude at 100Hz and at room temperature, which is likely to be due to breakdown of weak interactions between iron sand and rubber at low strain amplitudes and therefore, damping being dominated by the viscous flow of the rubber matrix and friction of rubber chains and iron sand. Evidence from SEM micrographs of MRE sections showed that isotropic MREs had uniform particle distribution and that alignment of magnetic particles occurred for anisotropic MREs as a consequence of an applied magnetic field. However, obvious gaps between iron sand and rubber were evident, suggesting weak interaction between iron sand and rubber.

Bis-(3-triethoxysilylpropyl) tetrasulphane (TESPT) was employed for surface modification of iron sand. The amount of TESPT was varied at five levels (2, 4, 6, 8 and 10wt%) relative to iron sand content to assess the optimum amount of coupling agent for interfacial bonding and damping performance. Evidence that coupling had occurred between iron sand and TESPT was identified by Raman Spectroscopy and the grafting percentage was determined by thermogravimetric analysis. Crosslink density assessment by swelling testing provided evidence that the tetrasulphane group of TESPT formed crosslinks with the rubber chains. The results exhibited the advantages of TESPT as a coupling agent between iron sand particles and rubber and also revealed that 6% TESPT content produced the highest crosslink density. It was

found that the silane coupling agent improved the amount of energy dissipated during hysteresis tests as well as tan δ over the range of frequency and strain amplitude explored. The results also revealed that with silane treated iron sand, tan δ increased with increasing magnetic field up to a saturation point at 600 mT. However, the presence of coupling agent and formation of different lengths of aligned particles did not strongly affect the peak height and width of the tan δ versus temperature curves.

Tan δ and energy dissipated during hysteresis testing of isotropic and anisotropic MREs containing silane modified iron sand particles were compared with existing antivibration rubbers. The chosen antivibration rubbers for comparison contained different contents of carbon black filler (30, 50 and 70 phr) in a natural rubber matrix. Energy absorption for comparative samples was generally higher than isotropic and anisotropic MREs over the range of frequency and strain amplitude explored, as well as in hysteresis testing and this was believed to be largely due the presence of carbon black in the existing antivibration rubber formulations. Further assessment was carried out on materials that were the same as the anisotropic MREs except they had additions of carbon black. The energy absorption was generally found higher than comparative samples with the same carbon black contents, supporting the use of iron sand to improve damping. However, this trend was found to reverse at around T_g, which is considered to be due to the segmental motion of rubber chains being by far the most significant influence on energy absorption in the glass transition zone.

A model was developed to include viscous flow of the rubber matrix, interfacial damping and magnetism-induced damping to give the total damping capacity of MREs (ψ_{MRE}). The proposed model was assessed experimentally using a

series of isotropic and anisotropic MREs. Comparison between tan δ with ψ_{MRE} showed that ψ_{MRE} matched the experimental trends with average percentage difference of 8.1% and 21.8% for MREs with modified iron sand and unmodified iron sand, respectively.

Acknowledgements

I would like to express the deepest appreciation to my chief supervisor, Professor Kim Pickering who has tirelessly assisted me with every step of my research and who was never short of good advice and direction when it was needed most. I would like to thanks my co-supervisors, Professor Ilanko Sinniah and Professor Brian Mace for their support, guidance and helpful suggestions. Their guidance has served me well and I owe them my heartfelt appreciation.

I would like to acknowledge Emeritus Professor Cam Nelson and Honorary Fellow Roger Briggs for providing information, books and valuable advice on the iron sand. A special thanks to all technical officers who provided the technical assistance for my research especially Chris Wang, Brett Nichols, Yuanzi Zhang, Alan Smith, Helen Turner, Stewart Finlay, Ian Honey, Annette Rodgers, Stephen Hardy and Peter Jarman. I would like to thank Dr Woei Chet Lim of Department of Computing & Mathematical Sciences for assistance with solving mathematical equations. Thank you to Andrea Haines and Cheryl Ward for their help during the writing of this thesis. I would like to convey my sincere thanks to Mary Dalbeth and Janine Williams who were always ready to help me with a smile. Thank also to Professor Kim Pickering, Dr Johan Verbeek and Prof Janis Swan for the support and help during my trying times.

I would also like to thank the other composite group members for their constant encouragement and valuable suggestions. Thanks to all my friends and well-wishers for their encouragement which inspired me to complete this research.

A special thank to my lovely wife Ku Marsilla and my daughter Raaesya Zahra. They are my inspiration and my driving force. I owe them everything and wish I could show them just how much I love and appreciate them. I wish to thank my parents, my in-laws, brothers and sisters for their pray and unconditional support. I would never have been able to accomplish any of my goals without the support of my family members. I would like to acknowledge the Ministry of Education Malaysia and Universiti Sains Malaysia for the financial and academic supports on this research.

Publications

Journal publications

Title : A New Method to Predict Optimum Cure Time of Rubber Compound Using Dynamic Mechanical Analysis
Authors: S. Raa Khimi and K.L. Pickering
Parent Document: Wiley, Journal of Applied Polymer Science
Date Published: March 15, 2014

Title : Dynamic Properties of Magnetorheological Elastomers Based on Iron Sand and Natural Rubber
Authors: S. Raa Khimi, K.L. Pickering and B.R. Mace
Parent Document: Wiley, Journal of Applied Polymer Science
Date Published : October 7, 2014

Title : The Effect of Silane Coupling Agent on Iron Sand for Use in Magnetorheological Elastomers, Part 1: Surface Chemical Modification and Characterization
Authors: . K.L. Pickering, S. Raa Khimi and S. Ilanko
Parent Document: Elsevier, Composites Part A: Applied Science and Manufacturing
Date Published : October 12, 2014

Title : The Effect of Silane Coupling Agent on The Dynamic Mechanical Properties of Iron Sand/Natural Rubber Magnetorheological Elastomers.
Authors: S. Raa Khimi and K.L. Pickering
Parent Document: Elsevier, Composites Part B: Engineering
Status : Under revision for publication.

Title : Comparison of Dynamic Properties of Magnetorheological Elastomers with Existing Antivibration Rubbers
Authors: S. Raa Khimi and K.L. Pickering
Parent Document: Elsevier, Composites Part B: Engineering
Date Published : August 24, 2015

Title : Investigation and Modelling of Damping Mechanisms of Magnetorheological Elastomers
Authors: S. Raa Khimi and K.L. Pickering
Parent Document: Wiley, Journal of Applied Polymer Science
Status : Under revision for publication.

Book chapter

Title : Damping Materials: Magnetorheology, applications and challenges
Authors: S. Raa Khimi, K.L. Pickering, B.R. Mace and S, Ilanko
Parent Document: Diversity of Research for a Sustainable Challenging World: A Compilation of Research by Malaysian Postgraduates in New Zealand
Year Published: 2013
ISBN : 0475124030, 9780475124036

Conferences

Title : Damping Materials: Magnetorheology, applications and challenges
Authors: S. Raa Khimi, K.L. Pickering, B.R. Mace and S, Ilanko
Conference name, date and location: iMARCA 2012, 7th December 2013, Auckland

Title : Damping Properties and Microstructure of Magnetorheological Composites Based on Iron Sand and Natural Rubber
Authors: S. Raa Khimi and K.L. Pickering
Conference name, date and location: NZCCME 2013, 25th-26th November 2013,Auckland

Table of Contents

List of Figures

List of Tables

Symbols

$[X]$	Crosslink concentration
C	Correction factor
D	Average of observed data
d	Diameter of particle
E*	Complex modulus
E′	Storage modulus
E″	Loss modulus
f	Friction coefficient
G'	Shear storage modulus
G"	Shear loss modulus
G*	Complex shear modulus
H	Magnetic field strength
Hz	Hertz
i	Level in Taguchi's orthogonal array
I	Iron sand content
j	Factor in Taguchi's orthogonal array
J_s	Saturation magnetization
K	Normal stress concentration coefficient at the particle interface
M	Magnetic field
m	Magnetic moment
$\vec{m}$	Magnetic dipoles strength
m_{dry}	Dry MREs mass
m_{wet}	Swollen equilibrium mass
N	Total number of data points
ºC	Degree celcius
P	Particle size
Q^{-1}	Inverse amplification factor
r	Radius of particles
r_o	Initial centre distance between adjacent particles
S/N	Signal-to-noise ratio
SS	Sum of squares
T	Tesla
T_{90}	90% of the maximum achievable torque
t_{90}	Optimum cure time of rubber compound
tan δ	Loss tangent
T_c	Magnetic Curie temperature

T_g	Glass transition temperature
T_{max}	Maximum torque values
T_{min}	Minimum torque values
V_o	Molar volume of toluene
V_p	Volume fraction of the particle
V_r	Volume fraction of MREs
wt%	Weight percentage
X_a	Sum of observed data at factor *a*
Y_i	Observed data at level *i*
γ	Shear strain
δ	Phase angle
ϕ_{max}	Maximum tan δ values
ϕ_{min}	Minimum tan δ values
ϕ_{90}	90% of the minimum tan δ values
ε	Strain
η	Loss factor
ϑ	Poisson's ratio
μ_0	Permeability of the matrix
μ_1	Permeability of a vacuum
ξ	Log decrement
ρ_r	Density of natural rubber
ρs	Density of toluene
σ	Stress
σn	Normal stress
τ	Shear stress
φ	Proportion of weakly bonded interface in comparative relation to the total interfacial damping
χ	Interaction parameter between the rubber and toluene
ψ_I	Interfacial damping
ψ_I^s	Damping of strongly bonded interfaces
ψ_I^w	Damping of strongly bonded interfaces
ψ_M	Magnetism- induced damping
ψ_{MRE}	Total damping capacity of MREs
ψ_V	Viscous damping
ω	Frequency

Abbreviations

ANOVA	Analysis of variance
ASTM	American Society for Testing and Materials
ATVA	Adaptive tuned vibration absorber
BR	Butadiene rubber
CBS	N-Cyelohexy1-2-benzothiazole sulphonamide
CCD	Cooled charged coupled device detector
CTCS	2-4(-chlorosulfonylphenyl)-ethytrichlorosilane
DEHP	Di-ethylhexylphthalate
DMA	Dynamic mechanical analysis
DOP	Diisooctylphthalate
DPG	Diphenyl guanidine
HIDAMETS	High damping metals and alloys
ISO	International Standards Organisation
LVDT	Linear variable differential transformer
MBT	2-mercaptobenzthiazole
MDR	Moving die rheometer
MMCs	Metal matrix composites
MREs	Magnetorheological elastomers
MRFs	Magnetorheological fluids
MWD	Molecular weight distribution
NR	Natural rubber
OA	Orthogonal array
ODR	Oscillating disk rheometer
PA-66	Poly amide
PBA	Poly buthyl acrylate
PEG	Poly ethylene glycol
PMMA	Poly methyl methacrylate
PTFE	Poly tetra fluoro ethylene
S/N	Signal-to- noise ratio
SBR	Styrene butadiene rubber
SEM	Scanning electron microscopy
SMAs	Shape memory alloys
TESPT	Bis-(3-triethoxysilylpropyl) tetrasulphane
TGA	Thermogravimetric analysis
TMTD	Tetramethylthiuram disulphide
TSR	Technically Specified Rubbers
ZDBC	Zinc Dibutyldithiocarbamate

Chapter 1

Introduction

1.1 Background to the study

Material with high damping capability is desired for vibration suppression in structures. Damping relates to the energy dissipated in a material during vibration and assists in stabilizing a structure when it vibrates. In the last decade there has been development in high damping materials for structures and engineering applications. A major goal has been to develop material that combines excellent mechanical properties and good damping for structural purposes. Metallic, ceramic and polymeric alternatives have all been investigated and are overviewed in the following paragraphs.

High damping metals and alloys (HIDAMETS) such as ferromagnetic metals [1], metal matrix composites [2] and shape memory alloys [3, 4] are the most commonly used metal based materials in practical applications where high damping capacity and good mechanical properties are required. However, their associated costs are often prohibitively high and their manufacturing is very complex. Generally, they are initially cast, resulting in inhomogeneous materials. Homogenization heat treatment is carried out subsequently, which increases grain size, changes transition temperatures and phase compositions, resulting in improved mechanical properties and damping performance. However, over-ageing can lead to severe reduction of damping during service [5-8].

Cement-matrix composites including concrete are the most widely used ceramic based materials for civil structures. These materials have high stiffnesses, but low damping capability. The addition of silica fume to cement can enhance damping, but not enough to stabilize vibration in structures [9].

Elastomers in the form of rubber are another class of materials which offers several distinct advantages when compared to metals and cement-based materials. The term elastomer refers to a macromolecular material that returns rapidly to approximately its initial dimensions after substantial elastic deformation, on release of stress. Rubber usually refers to a material consisting of a compounded elastomer [10]. Rubber is cheaper than other high damping materials and its associated processing techniques are not complex. Natural rubber has the highest failure strain of any rubber and is unbeatable in terms of damping performance, resistance to wear, creep and cyclic deformation. For example, when an aircraft weighing 150 tonnes comes in to land at several hundred kilometres per hour, it is the natural rubber in the tyres that must withstand the enormous gravitational force and friction as well as absorb vibration. Natural rubber has elasticity similar to a metallic spring as well as energy absorbing properties like those of a viscous liquid. The combination of viscous and elastic behaviour of elastomers and many other polymers results in the definition of viscoelasticity. Rubber sustains elastic strains from 300% to over 900% at room temperature. It can be processed into a variety of shapes and can adhere to metal inserts or mounting plates. It can be compounded with different additives to produce widely varying properties. Furthermore, rubber does not corrode and normally requires no lubrication. This leads to rubber being effective and relatively maintenance free in applications such as vibration isolators [10-12]. However, rubber

generally does not exhibit correspondingly high mechanical properties. Figure 1.1 show a stiffness versus tan δ plot of common materials [13].

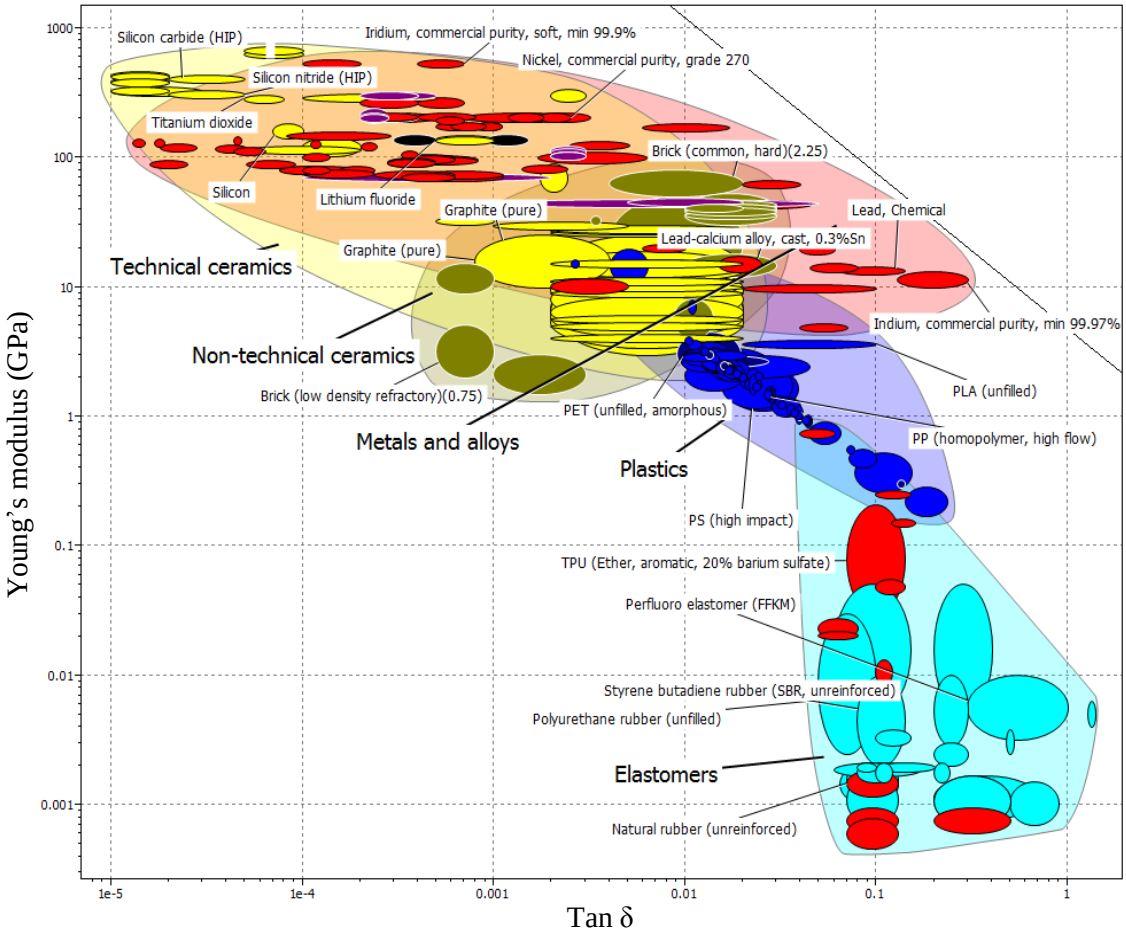

Figure 1.1 Stiffness-tan δ map of observed behaviour of some common materials

Rubber materials appear in the lower right corner with materials having high damping values but low stiffnesses. Metals and ceramics tend to occupy positions to the upper left hand side of the map, a region of low damping and high stiffnesses. Materials that combine high damping and high stiffness are not common and there is an obvious gap in the upper-right corner of Figure 1.1. Although rubber has proved useful in vibration damping, its low stiffness, low strength, low toughness and relatively low glass transition and melting temperatures limit its usefulness in practical applications. Incorporation of metallic or ceramic particles in a rubber

provides potential for improving mechanical properties of the material without sacrificing high damping performance [14-16]. More recently, magnetically permeable metallic and ceramic particles (such as iron and ferrite) have been included in rubber to create elastomeric magnetic composites, resulting in improvement of damping performance as well as structural properties. Generally, combinations of rubber with magnetic particles are termed magnetorheological elastomers (MREs) or magnetoelastic rubber or elastomer-ferromagnetic composites [17].

MREs offer several distinct advantages when compared with basic rubbers. MREs promote damping mainly by the viscous flow of the rubber matrix as do basic rubber, but inclusion of magnetic particles in rubber enables additional damping through magnetic particle interaction and interfacial damping as well as increased stiffness. Furthermore, damping and stiffness can be varied by application of an applied magnetic field during fabrication or in service. MREs are often referred to as the solid analogue of previously developed magnetorheological fluids (MRFs) used for example in damping of automotive suspensions. In MRFs, magnetic particles are contained within an oil. The main advantage of MREs over MRFs is that particle sedimentation is overcome. Moreover, MREs do not need containers or seals to hold the fluid or prevent leakage [18]. MREs can be utilised for damping, either alone or within a composite structure such as those including steel plates.

MREs can be fabricated to contain a uniform suspension of magnetic particles (isotropic MREs). However, it has been found that when a magnetic field is applied during curing, chain-like structures of magnetic particles are formed within the rubber (anisotropic MREs) which provides much larger damping and stiffness [19]. Formation of such chain-like structures relies on the mechanism such that when

individual particles are exposed to an applied magnetic field, magnetic dipole moments pointing along the field direction are induced within them. A magnetic force will cause the north pole of one particle to attract the south pole of its neighbour, resulting in the formation of chains and columnar structures inside the matrix. Upon curing of the matrix, the particles are set in place [18].

The most common magnetic particles used in MREs are iron particles and suitable matrix materials include natural rubber, silicone rubber, polybutadiene, polyisobutylene, polyisoprene, and polyurethene rubber [19-25]. These materials are nonmagnetic viscoelastic materials into which the magnetic particles can be added and subsequently processed into a final solid form through conventional rubber or plastic processing [26-28]. Recent work has focused on carbonyl iron and natural rubber MRE because of their associated ease of processing and good damping performance [29-31]. However, one of the biggest challenges in developing MREs is cost. Carbonyl iron particles, the most commonly used particles, are expensive at \$13-15/kg in bulk. More cheaply produced iron particles, iron oxide (Fe_3O_4) and barium ferrite ($BaFe_{12}O_{19}$) tend to be irregular in shape, have wider size distributions, and simply do not perform as well [16, 32]. Some iron alloy particles actually perform better than carbonyl iron, but are significantly more expensive [33]. It is apparent that more applications would quickly become commercially viable if the material cost could be reduced.

1.2 Context and rationale

In this study, iron sand was used as the magnetic particles in natural rubber based MREs. Iron sand was chosen because it has high permeability and saturation magnetisation, low cost, and is readily available in New Zealand. It is derived from erosion of andesitic and rhyolitic volcanic rocks which are the main types of iron ore deposits in New Zealand. Iron sand is a dark, high-density sand that occurs along the west coast of the North Island from Wanganui to Kaipara Harbour near Auckland, over a distance of 480 km. It contains titanomagnetite, a mineral itself containing iron and titanium, which is highly magnetic [34, 35].

Development of MREs based on iron sand and natural rubber in this work is a novel direction. Indeed, at present, general research in MREs is still in its infancy. Optimal selection of MRE components, the technology of their manufacture, characterization and analysis, as well as development of mathematical models describing their mechanical and dynamic properties are unresolved scientific issues [36]. The volume fraction, size, shape as well as adhesion between the particles and matrix have been identified as the main factors that influence the energy absorption capability of MREs. The volume fraction of magnetic particles in the MREs can be increased up to 50%, but the optimum volume fraction for achieving good damping performance has been reported to be around 30% [37]. The preferred particle shape is considered to be spherical with size ranging between 3μm - 60μm [27, 29]. However, the incompatibility of inorganic magnetic fillers and the matrix can lead to poor wettability and adhesion between the filler and matrix as well as non-uniformity of filler dispersion leading to low energy absorption [38-40]. Therefore, it is sensible to

modify the surface of the iron sand in order to improve ease of adhesion with and dispersion within the rubber matrix in order to realise the full potential of MREs.

At present, numerous models have been developed to investigate the dynamic mechanical properties of MREs [17, 24, 41-45]. However, little work has been carried out to model the actual damping mechanisms and previous works have not comprehensively considered individual components (viscous flow of rubber matrix, interfacial damping and magnetism-induced damping) in MREs and their contributions to damping [37, 46-49]. Therefore, a substantial study on the damping mechanisms of the individual components in MREs is essential in order to develop a model to understand the relative importance of damping mechanisms in MREs.

1.3 Research objectives

The objective of this research was to produce new MREs with the motivation to reduce their cost by using natural resource materials. The goal was to fabricate isotropic and anisotropic MREs based on iron sand and natural rubber that have good damping performance for potential use in vibration damping. The specific research objectives are as follows:

- To identify methods to fabricate and characterise MREs using readily available and conventional equipment.
- To study the effect of iron sand content, particle size, microstructure (isotropic and anisotropic) and magnetic field on the material damping performance.
- To assess the effect of surface modification of iron sand for improving the adhesion between iron sand and rubber matrix and to evaluate its influence on

dynamic mechanical properties of isotropic and anisotropic MREs containing modified iron sand.

- To compare the dynamic mechanical properties of MREs based on iron sand and natural rubber with existing antivibration rubbers in order to assess the potential of MREs to be use as isolation materials.
- To understand the actual damping mechanisms in MREs and predict the damping performance of the materials by means of theoretical modeling.

Chapter 2

Literature review

2.1 Overview of damping materials

Efficient control of vibration is of universal concern for product designers due to its occurrence in most machines and structures. Vibration often leads to undesirable consequences such as unpleasant motion, noise and dynamic stresses that lead to fatigue and failure of structures. In many practical situations, it is possible to reduce but not eliminate the dynamic forces that cause vibration.

Damping of structures can be attained by passive or active methods. Passive damping control refers to a structure's ability to absorb vibrational energy as a result of its structural design, material properties or the incorporation of a device to dissipate energy to make the system less responsive to its vibrating environment [50]. Active damping involves the addition of elements that sense the amount of vibration and trigger some remedial action to dampen the movement. The most common system of this type can be achieved by embedding sensors to detect vibrations and actuator devices which extend and retract in response to the sensor signals in such a way as to counteract the vibration; the sensors and actuators are normally piezo-electric devices [51].

Damping materials are used for energy absorption to reduce vibration in mechanical and structural systems. Viscoelastic character can contribute greatly to damping. The damping performance achieved by particular viscoelastic materials is the product of the fraction of vibration energy that gets into the damping materials

and the ability of the material to dissipate the energy within it. The loss tangent, commonly called tan δ, is considered as the fundamental parameter to assess energy dissipation capability in a viscoelastic material. Tan δ, is obtained by dividing the loss modulus (E″) by the storage modulus (E′) [13].

Materials used for vibration damping mainly consist of metals and polymers due to their viscoelastic behaviour. Table 2.1 shows a general comparison of the damping performance for a range of materials including polymers, metals, cement-based materials, metal-matrix and polymer-matrix composites [52, 53]. Damping capacity depends not only on the materials, but also on the loading frequency, part geometry and temperature. Unfortunately, these details were not available to be added to Table 2.1. However, it can be seen that among these classes of materials, polymers provide the highest damping performance (tan δ), followed by metals and cement-based materials. Rubber exhibits an outstandingly high value of tan δ and is extensively applied for damping [54].

Table 2.1 Materials damping performance

Material	Tan δ
Cement paste (plain)	0.016
Mortar with silica fume (treated) (15% by wt. of cement)	0.021
Al/AIN (58%) alloy	0.025
Zn-Al alloy	0.021
Zn-Al/SiC (27%) alloy	0.032
Poly tetra fluoro ethylene (PTFE)	0.19
Poly methyl methacrylate (PMMA)	0.09
Poly amide (PA-66)	0.04
Acetal	0.03
Epoxy	0.03
Natural rubber	0.10-0.25
Silicone rubber	0.10-0.25
Nitrile rubber	0.20-0.30

2.1.1 Metals for vibration damping

Metals and alloys that have high damping capacity are termed as High Damping Metals (HIDAMETS) [1]. The application of high damping metal for structural applications may eliminate the need for vibration absorbers or dampers to stabilize structures and attenuate mechanical vibration. Unfortunately, an increase in damping is often associated with a corresponding decrease in mechanical properties, notably stiffness and strength. An intuitive approach to utilize the inherent damping capacity of high damping metals while maintaining good mechanical properties is through the use of metal matrix composites (MMCs) where reinforcement is used for mechanical performance enhancement [55, 56].

Aluminium and magnesium based MMCs are well known and used extensively because of having low density with high damping capacities. Addition of reinforcements to increase damping such as SiC particulates, Al_2O_3 particulates, graphite or piezoelectric materials increases damping and mechanical performance. The main means of energy dissipation is through movement of weakly pinned basal plane dislocations, viscous sliding at the metal reinforcement interface and the intrinsic damping of the reinforcement [2].

Ferromagnetic damping alloys attract considerable attention due to their unique damping mechanism they demonstrate. As they can be used in active damping, they are categorized as a group of smart materials. Ferromagnetic alloys provide damping by movement of the magnetic domain boundaries during vibration, a process known as magneto-mechanical damping [1]. Ferromagnetic alloys useful for vibration damping include those based on iron, nickel,cobalt, chromium, aluminium and manganese (e.g. Fe-Ni, Fe-Cr, Fe-Al and Fe-Mn-Co) [53]. Although

they exhibit good damping capacity, their associated high costs, complex processing and poor damping performance at high temperature, limits competition with other damping materials. For example, Fe-Cr base damping alloys have good damping capacity as well as mechanical properties, and corrosion resistance. Unfortunately, their manufacture is difficult and expensive because the process requires vacuum induction melting with high-purity alloying elements. Mn-Cu based damping alloys have high damping capacity and good mechanical properties at room temperature but the performance significantly decrease when the Mn-Cu based alloy is heated to 100^{o}C [57].

Shape memory alloys (SMAs) are another group of damping materials which provide excellent damping capacity and good mechanical performance. The shape of the materials, stiffness, damping coefficient and other mechanical characteristics can be changed in response to a change in temperature and stress. A damping mechanism specific to SMAs arises from the reversible phase transformation between different crystallographic structures of the materials known as twinned martensite and austenite. The phase transformation caused by the micromechanical motion of structural imperfections in the material is called pseudoelasticity. The pseudoelastic behaviour results in a large hysteresis loop with energy dissipated as heat [2, 3, 58].

2.1.2 Ceramics for vibration damping

Ceramics are not good for vibration damping, but they have high stiffness which makes them useful for structures. The use of the structural materials themselves for damping reduces the need for non structural damping materials, which tend to be limited in durability and temperature resistance, in addition to being low in

stiffness. Therefore, improvement of damping of structural ceramics would be valuable.

The most widely used type of structural ceramic is cement-matrix composites. A lot of research has been carried out in an attempt to enhance the damping ability and mechanical properties of cement-matrix composites using additives. Addition of silica fume (a very fine non-crystalline silica) in cement results in the formation of a large interfacial area between the matrix and reinforcement phase. The interface dissipates energy through slippage of silica fume particles and the cement matrix and hence results in a significant increase in the damping capacity [9].

2.1.3 Polymers for vibration damping

Polymers have been applied widely for achieving acoustic and vibration damping as well as isolation due to their viscoelastic behaviour [59, 60]. However, homopolymers exhibit good damping only in a narrow temperature range of 20–30^{o}C around their glass transition temperature (T_g), which is not broad enough for many practical applications. Secondly, damping materials derived from polymers often exhibit a strong dependence on temperature and frequency, such that damping is variable even over a narrow range of conditions. Traditional methods of modification and broadening the T_g involve use of copolymers, modified crosslinking agents, plasticizers and fillers, blending of various polymers, grafting and formation of interpenetrating polymer networks [61-64].

Recently, polymeric matrix composites have been of interest in the development of damping materials due to their relatively high strength and excellent damping characteristics [65, 66]. A polymeric matrix composite containing

piezoelectric ceramic powder and electrical conductive particles has been developed [67, 68]. The damping mechanism of such a composite is obtained by transformation of mechanical vibration energy by the piezoelectric ceramic grains into electrical energy which is further converted to heat in the polymeric matrix [68]. Although the piezo-damping effect exists in such conductive piezoelectric polymer composites, the values of tan δ in the room temperature region may be not high enough for practical applications [60].

Rubber is well-known for its damping ability compared with other polymeric materials due to its particularly extreme viscoelastic behaviour. Its viscous component, enables conversion of kinetic energy into heat by internal friction of the disentangling long chain molecules and the elastic components can return the product quickly to its original state and ready for the next cycle of deformation [10].The ability of rubber to convert energy of motion to heat, allows it to absorb vibrational energy. However, strong damping cannot be maintained under a large variation of temperature and frequency. Therefore, filler reinforcement, blending, copolymerization and interpenetrated networks have been used to enhance the damping of rubber over a wide range of temperature and frequencies [42, 59].

2.2 Parameters characterizing damping

The methods for assessing damping of a material can be classified into free vibration methods and forced vibration methods. For free vibration methods, the material is allowed to vibrate at its natural frequency and the rate of amplitude and frequency to decay is measured. For forced vibration methods, a sinusoidal force at different frequencies and strain amplitudes is applied and displacement of the

material is measured. Measuring sinusoidal response under forced vibration is the most commonly used technique by far due to this type of excitation being the easiest to instrument and the frequency and amplitude at which the test is performed can be selected to simulate the type of service anticipated [69].

For viscoelastic materials, when a sinusoidal oscillating stress (σ) at an angular frequency (ω) is applied, the cyclic strain (ε) always lags behind the applied stress by a phase angle δ as represented in Figure 2.1. The material deforms and returns back to its original form in one cycle.

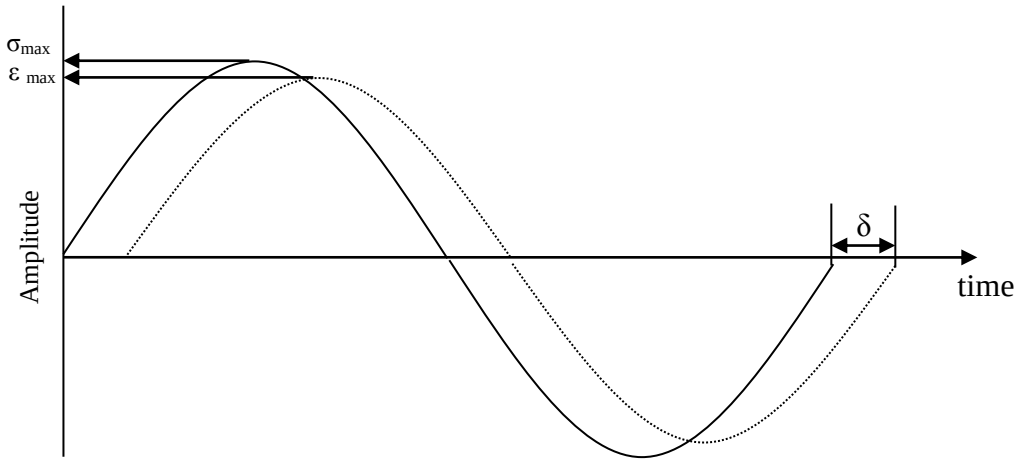

Figure 2.1 Stress and strain amplitude versus time of a viscoelastic material sinusoidal response

The amplitude of the stress and strain in sinusoidal form can be expressed as follows:

$$\sigma = \sigma_{max} e^{i(\omega t+\delta)} \quad (2.1)$$

$$\varepsilon = \varepsilon_{max} e^{i\omega t} \quad (2.2)$$

where σ_{max} is the maximum amplitude of stress, ε_{max} is the maximum amplitude of strain, ω is angular frequency, t is time and δ is the phase angle (phase lag between stress and strain). The complex modulus (E*) can be derived by dividing the stress by the strain as follows:

$$E^* = \frac{\sigma_{max}}{\varepsilon_{max}} e^{i\delta} \tag{2.3}$$

Equation 2.3 can be further expressed as

$$E^* = \frac{\sigma_{max}}{\varepsilon_{max}} (\cos\delta + i \sin\delta) \tag{2.4}$$

$$E^* = E' \cos\delta + i\, E'' \sin\delta \tag{2.5}$$

where E' as a real part of the complex modulus and E" as an imaginary part of the complex modulus. The E' (known as storage modulus) represents the ability of the viscoelastic material to store deformation energy. The E" (known as loss modulus) represents the ability of the material to dissipate deformation energy. Equation 2.5 can be represented graphically using a trigonometry vector diagram as shown in Figure 2.2

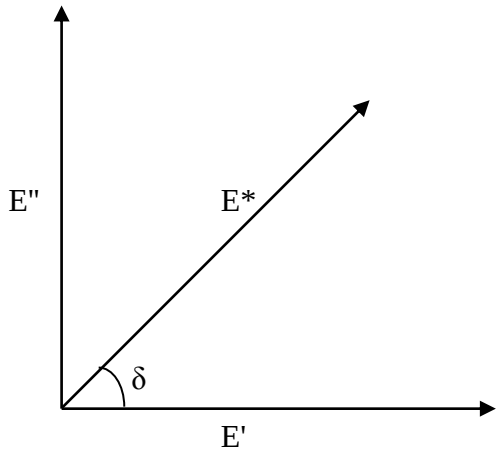

Figure 2.2 Vector diagram of complex modulus

As can be seen in the vector diagram, the tangent of the phase angle δ (tan δ) can be calculated as :

$$\tan\delta = \frac{E''}{E'} \tag{2.6}$$

When a material is tested under shear load, equation 2.6 appears in a modified form as follows:

$$\tan\delta = \frac{G''}{G'} \tag{2.7}$$

where G' is shear storage modulus and G" is shear loss modulus. Considering small values of tan δ (tan δ<1) the following approximation of tan δ with other common damping measures can be assumed [70]:

$$\tan\delta \approx \eta \approx Q^{-1} \approx \frac{\xi}{\pi} \tag{2.8}$$

where η is loss factor, defined as the specific damping capacity per radian of damping cycle, Q^{-1} is inverse amplification factor which can be measured from the resonance response peak of amplitude versus frequency plot using the Power-Bandwidth method and ξ is log decrement; this measures the rate of vibration amplitude decay as a function of time when a material is allowed to vibrate freely after an initial exciting force is removed.

Yet, another estimate of damping can be assessed by the amount of hysteresis energy loss. Hysteresis energy loss is defined as the amount of energy dissipated during cyclic deformation when the samples are completely stretched and then allowed to retract at the same rate to the unstretched state. Figure 2.3 shows typical stress-strain curve of a rubber material. Hysteresis loss can be calculated as follows:

Hysteresis loss = area under the loading curve - area under the recovery curve (2.9)

so the shaded area shown.

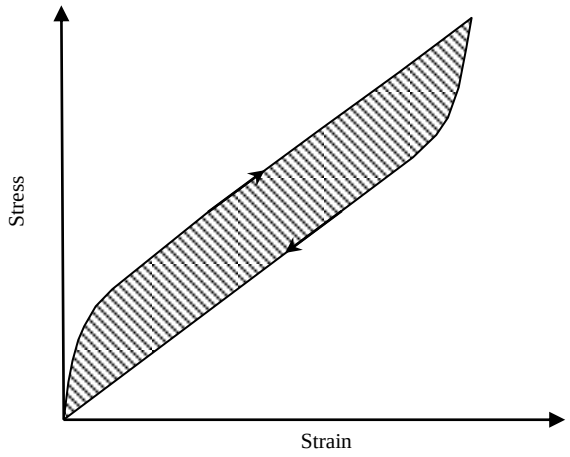

Figure 2.3 Hysteresis loop of a rubber material

2.3 Magnetorheological materials

Increasing numbers of new materials are being developed with the aim of overcoming the limitations of rubber as a commonly used material for damping; in this area enhancement of damping through rubber modification or rubber selection to increase viscous flow, not surprisingly, generally results in reduction in stiffness and strength [13]. A new class of damping materials, magnetorheological (MR) materials, offers several distinct advantages when compared to rubbers on their own. MR materials consist of a non-magnetic medium (normally an oil or elastomer) containing a suspension of magnetically permeable particles. These materials promote damping mainly by the viscous flow of the non-magnetic medium, but inclusion of magnetic particles enables additional damping through magnetic particle interaction and interfacial damping. These materials also have rheological properties that can be changed by variation of the magnetic field during fabrication or in service. Since the MR effect was discovered by Rainbow in 1948 [71], MR materials have

expanded to become a large family which includes MR fluids (MRFs) and MR elastomers (MREs) [28].

2.3.1 Magnetorheological fluids (MRFs)

MRFs are the most common MR materials. They are composed of oils with micrometer sized ferromagnetic particles. They exhibit Newtonian like behaviour in the absence of a magnetic field, but become viscoelastic solids with a certain yield stress when a magnetic field is applied. When an MRF is exposed to a magnetic field, the ferromagnetic particles are magnetized and attracted to each other to form chains in the direction of the external magnetic field which restricts the flow of the fluid and results in a change in rheological behaviour to that more of a solid [28, 45]. Figure 2.4 shows MRF structure in the absence of a magnetic field and under a magnetic field.

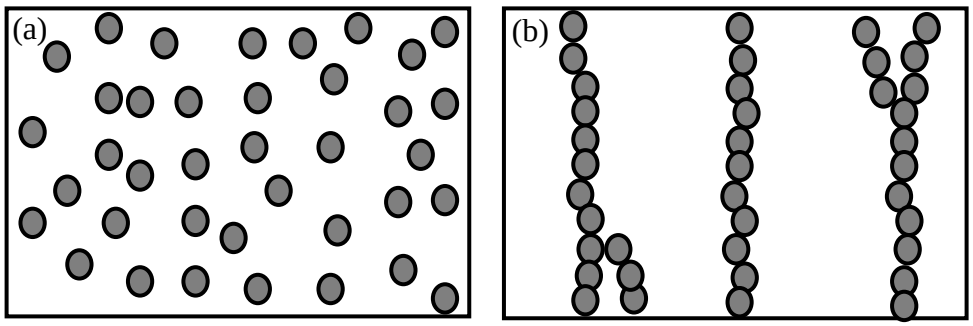

Figure 2.4 MRF structure; (a) in the absence of magnetic field and (b) under a magnetic field.

The mechanical energy needed to yield these structures increases as the applied magnetic field increases, resulting in a field dependent yield stress. In order to deform the MRFs under an applied magnetic field, extra force must be exerted to break the cluster of chains and columns [28, 45].

MRFs have been proven to be commercially viable and well suited for many applications, such as automotive suspensions, clutches, brakes, actuators and artificial joints [72]. However, a number of limiting problems still exist with MRFs. MRFs are prone to particle settling with time due to the density mismatch of particles and the carrier fluid, which may degrade the MR response. In addition, the wear of the magnetic particles can also lead to a reduction in the fluid's performance and eventual failure of the MRF device.

2.3.2 Magnetorheological elastomers (MREs)

MREs can be thought of as a new generation of MR materials following on from MRFs where the matrix is a solid elastic polymer rather than carrier oil. The obvious advantage from using elastic polymer as a matrix material is that the particle sedimentation problem in MRFs is overcome. Moreover, MREs do not need containers or seals to hold or prevent leakage. MREs can be utilized for damping, either separately incorporated or within a composite structure such as with steel plates.

Suitable matrix materials for MREs include natural rubber, silicone rubber, polybutadiene, polyisobutylene, polyisoprene, and polyurethene rubber [19-25]. These materials are usually nonmagnetic viscoelastic materials that can be uniformly mixed with the magnetizable particles and subsequently processed into final solid form through conventional rubber or plastic processing equipment. The particle material of choice for MREs is iron. This is because of its high permeability, low remanent magnetisation and high saturation magnetisation. High permeability and

saturation magnetisation provide high inter-particle attraction, and thereby produce strong chains and columnar structures [26-28].

MRFs and MREs have another difference in the way they behave; MREs are generally used in their pre-yield state while MRFs typically work in their post-yield state. In the pre-yield state, a material behaves like a linear viscoelastic material, while in the post-yield state flow occurs. Figure 2.5 indicates typical pre-yield and post yield states in MR materials. MREs have recently gained attention because pre yield behavior gives higher stiffness and damping performance compared to MRFs.

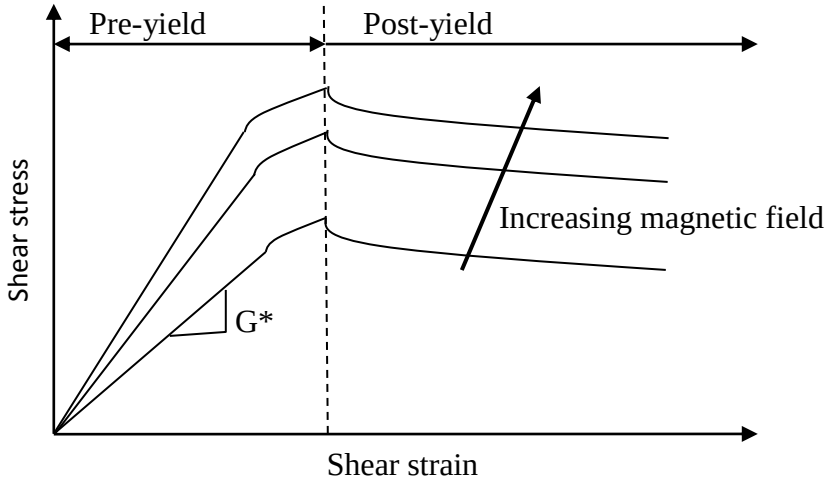

Figure 2.5 Typical pre-yield and post-yield states in MR materials.

MREs can be fabricated either with or without a magnetic field. The former results in isotropic MREs, while the latter results in anisotropic MREs. Isotropic MREs can be characterized by a uniform magnetic particle distribution in the matrix. Anisotropic MREs have a special chain like structure of magnetic particles in a matrix as a result of curing the matrix under a strong magnetic field. When individual

particles are exposed to an applied magnetic field during curing, magnetic dipole moments pointing along the field direction are induced in them. A magnetic force will cause the north pole of one particle to attract the south pole of its neighbour resulting in formation of chains and columnar structures inside the matrix. Upon curing the matrix, the particle is locked into place [18]. Anisotropic MREs are found to produce material with much larger stiffness and damping compared to those cured in the absence of a magnetic field. Furthermore, during service, a magnetic field can be used to affect Young's modulus of isotropic and anisotropic MREs and hence provide benefits in vibration control [19].

2.3.3 MRE applications and challenges

MREs have many potential engineering applications for vibration control in damping and vibration isolation systems. MRE devices have begun to see successful commercial applications, with most of them in automotive and industrial engine mounts. The Ford Motor Company has patented a tunable automotive bushing based on MREs [73]. The stiffness of the bushing is adjusted by a variable magnetic field generated from a suspension control module. The dynamic stiffness control reduces suspension deflection and improves passenger comfort. Deng and Gong have also developed a shear mode adaptive tuned vibration absorber (ATVA) based on MREs [74]. Results have shown that the natural frequency of the ATVA can be tuned from 27.5 Hz to 40 Hz which provides better performance compared to conventional passive absorbers in terms of frequency-shift property and vibration absorption capacity. Ginder *et al.* have constructed MRE tunable automotive engine mounts that have excellent damping to reduce engine vibration and fatigue [22].

With the rapid growth of commercial applications over the last few years, many people consider they are just witnessing the beginning of an explosion of MRE devices and applications. Indeed, numerous applications are currently at the research and development stage. Dyke *et al.* have developed a semi-active MRE damper which can be utilized to suppress vibration caused by earthquakes in civil structures such as building and bridges [75]. Furthermore, some work has been carried out to explore the use of MRE in sensors, microwave absorption, electronic writing pads and touch-sensitive screens [76, 77].

It is known that one of the most significant issues for commercializing any MRE device is cost. The material cost could be reduced by reducing the amount of iron employed. However the desire to obtain sufficient influence with low particle concentration is a big challenge. Furthermore, the particles used have a magnetic saturation point. Once this is reached, no matter how much the field is increased, no additional change in rheological properties is observed. This obviously limits the size of change in rheological properties obtainable [78]. Overcoming limitations will lead to improvement in materials performance and, as well as foster the development of new applications.

2.4 Rubber matrix

The matrix materials for MREs are usually non magnetic rubbers that can be uniformly mixed with the magnetic particles and subsequently processed into a solid. Appropriate selection of matrix material is crucial, particularly in anisotropic MREs, because the degree of freedom of movement for magnetic particles to organise into chain like columnar structures is mainly influence by the viscosity of the matrix

material. In addition, the magnetic permeability of matrix materials must be as low as possible to prevent interaction between matrix and particles which could reduce the interaction between neighbouring particles. Table 2.2 describes the advantages and disadvantages of some of the most commonly used matrix materials for MREs.

Table 2.2 Matrix materials used in MREs

Matrix type	Advantages	Disadvantages	References
Natural rubber	• natural resource • low cost • high tensile and tear strength • high fatigue life • medium damping	• poor heat resistance • poor fluid and aging resistance	[16, 20, 26, 30, 31, 42, 79-85]
Silicone rubber	• broadest useful temperature range • low temperature flexibility • medium to high damping • good heat aging resistance	• synthetic rubber • medium cost • low mechanical properties • poor fuel and oil resistance	[14, 45, 86-96]
Polybutadiene rubber	• medium to high damping • good resistance to ozone and aging	• synthetic rubber • medium cost • poor fuel and oil resistance	[21, 24, 97, 98]
Nitrile rubber	• Excellent oil resistance • good resistance to ozone and aging • medium damping	• synthetic rubber • medium cost • poor ozone resistance • medium cost • poor low temperature performance	[27, 40]
Polyurethane rubber	• high damping • high tensile and tear strength • excellent oil resistance • excellent resistance to ozone and aging	• synthetic rubber • medium to high cost • poor solvent resistance	[19, 99]

As shown in Table 2.2, the matrix materials in most studies have been silicone rubber and natural rubber. Silicone rubber is supplied as a liquid precursor and

therefore is the preferred matrix for fabrication of complicated geometries products. In addition, curing can be carried out at room temperature. However, its low mechanical properties and low fatigue life limit its usefulness for practical applications.

Recent work has focused on natural rubber because of its associated ease of processing, high durability and compatibility with other components. MREs based on natural rubber generally perform better in terms of mechanical properties and damping performance than MREs based on silicone rubber or other type of rubbers. For instance, the tensile and the tear strengths of MREs based on natural rubber are almost ten times higher [30] and the tan δ is approximately 20% higher [29] when compared to those of MREs based on silicone rubber. Therefore, MREs based on natural rubber could provide for a wide range of applications especially in mechanical systems such as tuneable vibration absorbers, stiffness variable bushings, and mountings. In this study, natural rubber was chosen as the matrix and the properties, processing and advantages of natural rubber are further discussed in the following section.

2.4.1 Natural rubber

Natural rubber is an elastic polymer produced using sap obtained from a tree named *Haveabraziliensis* which is originally indigenous to the Amazon Valley Forest, but has been cultivated principally in Southeast Asia, Sri Lanka, India and Nigeria. It is a linear polymer and built up from repeated units of cis-polyisoprene (Figure 2.6). *Haveabraziliensis* sap contains more than 90% cis-polyisoprene, water and small quantities of other ingredients such as protein and dirt [10]. The typical content of sap from *Haveabraziliensis* is shown in Table 2.3 [100]. The sap is

generally processed into either sap concentrate (latex) for manufacture of dipped goods such as glove or it can be coagulated into skim block rubber (gum rubber) for manufacture adhesives and bulk rubber products.

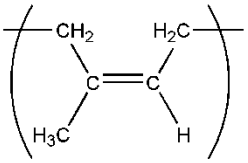

(a)

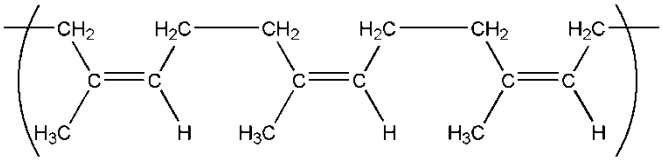

(b)

Figure 2.6 (a) cis-polyisoprene, (b) linear chain structure of cis-polyisoprene

Table 2.3 Typical content of the sap

Component	**Percentage, %**
Water	0.6
Acetone extract	2.9
Protein	2.8
Dirt	0.4
Cis-polyisoprene	93.3

Gum rubber can be classified according to the Technically Specified Rubbers (TSR) scheme developed by the International Standards Organisation (ISO) in 1964. This standard indicates the maximum permissible content of dirt, ash, nitrogen and volatile substances. The nomenclature describing technically specified rubbers consists of a three letter code followed by a letter code or numeral indicating the

maximum permissible dirt content for that grade. The following table shows some TSR grades [101].

Table 2.4 TSR scheme for natural rubber

Property	TSR CV	TSR L	TSR S	TSR 10	TSR 20	TSR 50
Dirt content, max, wt%	0.05	0.05	0.05	0.1	0.2	0.5
Ash content, max, wt%	0.6	0.6	0.5	0.75	1	1.5
Nitrogen content, max, wt	0.6	0.6	0.5	0.6	0.6	0.6
Volatile matter, max, wt%	0.8	0.8	0.8	0.8	0.8	0.8
Initial Wallace Plasticity P0, min	N/A	30	30	30	30	30
Plasticity retention index, min	60	60	60	50	40	30

Gum rubber needs to be compounded with other chemicals and additives and then is vulcanized to produce natural rubber products. Natural rubber is a viscoelastic material that has highest elastic failure strain of any rubber, excellent vibration absorption and high resistance to wear and creep during cyclic deformation. It is also capable of sustaining a deformation of as much as 900% at room temperature. The glass transition temperature of natural rubber is about -70^{o}C and its average molecular weight ranges from 200,000 to 400,000. This broad molecular weight distribution (MWD) results in good processing capabilities. The maximum tensile strength for natural rubber is 25 MPa and Young's modulus ranges between 1-5 MPa. Furthermore, it can maintain high level of elasticity down to -60^{o}C and its maximum service temperature is approximately at 100^{o}C [102].

The major advantage of natural rubber, which makes it dominant in many engineering applications, is its dynamic performance. It has high damping capability over the range of 1 to 200Hz [10]. Its dynamic properties generally out-perform any synthetic rubbers or combinations of rubbers available to date. It also can be processed into a variety of shapes and can adhere to metal inserts or mounting plates.

Furthermore, rubber does not corrode and normally requires no lubrication. This leads to rubber being effective and relatively maintenance free in applications such as vibration isolators, tyres and bearings. Other products include hoses, conveyor belts, gasket, seals, rolls, elastic bands and pharmaceutical goods such as rubber plunger [10-12].

2.4.1.1 Rubber compounding

Rubber compounding is the process of introducing chemicals and additives into gum rubber to modify its properties to make it a more useful material. Generally, gum rubber has very limited use, although adhesives provide one example. Gum rubber is mechanically weak, subject to significant swelling in liquids and easily attacked by oxygen or ozone that consequently degrade the rubber. These disadvantages can be ameliorated by rubber compounding. The choice of chemicals and additives needs to consider many aspects such as environmental safety, processability, required service life, required mechanical and physical properties and optimum production cost [102].

Typical rubber compound formulations consist of ten or more ingredients that are added to enhance mechanical and physical properties, affect vulcanization and improve processability. These ingredients are added in amounts based on weight in parts per hundred of rubber (phr). Table 2.5 describes some of the most common additives used in rubber compounds.

Table 2.5 Typical additives for natural rubber compound

Material	Function	Example
Crosslinking agents	• crosslinking agents are necessary for conversion of rubber molecules into a network by formation of crosslinks.	• sulphur • peroxides • metallic oxides • tellurium • thiuram disulphides • quinone dioximes
Accelerator-activators	• accelerator-activator are the ingredients added to improve the processability, activate and accelerate the vulcanization process and helps the other accelerators to react effectively	• zinc oxide • stearic acid
Accelerators	• accelerators increase the rate of the cross linking reaction and lower the sulphur content necessary to achieve optimum vulcanizate properties.	• N-Cyelohexy1-2-benzothiazole sulphonamide (CBS) • Tetramethylthiuram disulphide (TMTD) • 2-mercaptobenzthiazole (MBT) • Zinc Dibutyldithiocarbamate (ZDBC) • Diphenyl guanidine (DPG)
Antidegradents	• antidegradent increase the resistance to attacks of ozone, UV light and oxygen and improve long-term stability of rubber	• p-phenylene diamines
Plastisizers	• plastisizers are additives used to enhance the dispersion of fillers, to reduce uncured compound viscosity and to improve deformability at low temperature.	• naphthenic and paraffinic oils

2.4.1.2 Vulcanization

Vulcanization is a chemical process in which the sticky uncured natural rubber compound is converted into a more durable material. In vulcanization, the overall elasticity of rubber increases by formation of chemical crosslinks between the chains. This process decreases the amount of slippage of chains and produces a three dimensionally bonded structure. Vulcanization involves reaction of crosslinking agent (commonly sulphur) at allylic hydrogen atoms of cis-polyisoprene molecular chains; allylic hydrogen atoms are hydrogen atoms that are bonded to the first saturated carbon atom adjacent to carbon-carbon double bonds. There are many allylic hydrogen atoms called cure sites along the cis-polyisoprene molecular chains where reaction can potentially occur. Figure 2.7 represents sulphur crosslinking of cis-polyisoprene to produce vulcanizate rubber. During vulcanization the eight-membered ring of sulphur breaks down into smaller parts with varying numbers of sulphur atoms. These parts are quite reactive. At each cure site on the rubber molecule, one or more sulphur atoms can attach and from there, a sulphur chain can grow until it eventually reaches a cure site on another rubber molecule. These sulphur bridges are typically between two and eight atoms long. The number of sulphur atoms in a sulphur crosslink has a strong effect on the physical properties of the final rubber products. Short sulphur crosslinks impart very good heat resistance while long sulphur crosslinks lead to very good dynamic performance which is useful for rubber products such as dampers, bearings and vibration absorbers. Without good dynamic performance, cyclic loading will lead to formation of cracks and product failure [103, 104].

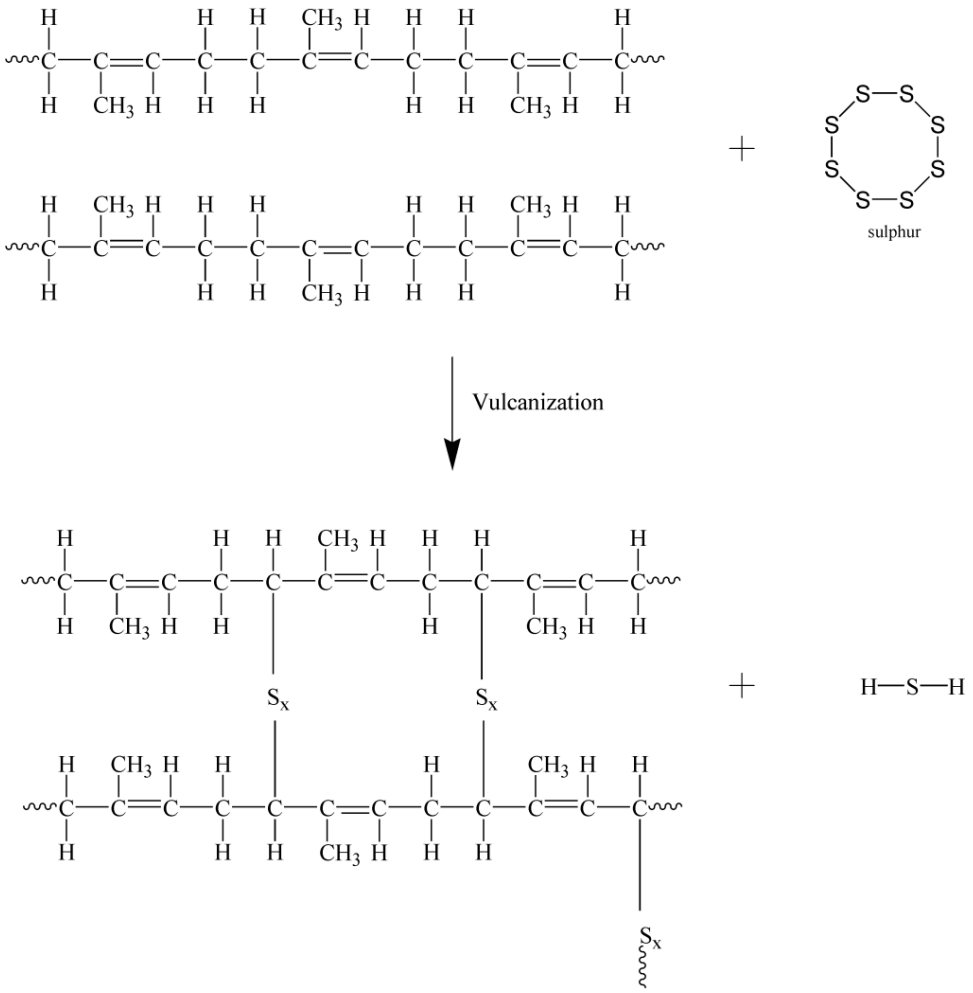

Figure 2.7 Sulphur vulcanization of cis-polyisoprene

2.5 Magnetic Particles

The most commonly used particle types for MREs are soft magnetic particles with high magnetic permeability and high saturation magnetization. High permeability and high saturation magnetization provides strong inter-particle interactions between neighbouring particles and thereby produces longer and bulkier chains and columnar structures. In addition, the particles should be large enough to support at least several magnetic dipoles in order to have a substantial magnetic

particle interaction between neighbouring particles. Table 2.6 lists particle types, shapes and sizes of some of the most commonly use particles for MREs.

Table 2.6 Particle type, shape and size of commonly used particles in MREs

Particle type	Shape	Size	References
Carbonyl iron	spherical	1-3 μm	[20, 91, 95]
Carbonyl iron	spherical	3.5 μm	[45, 79-81, 87, 89, 105-107]
Carbonyl iron	spherical	3-7 μm	[21, 25, 90, 96, 108, 109]
Carbonyl iron	spherical	6-9 μm	[94, 98, 99]
Pure iron	irregular	10-20 μm	[19]
Pure iron	irregular	< 60 μm	[18, 26, 82-84, 110]
Pure iron	irregular	< 200 μm	[27, 39]
Terfenol-D	irregular	< 300 μm	[33, 111, 112]
Iron oxide	spherical	10-50 nm	[32, 38, 42]
Barium ferrite	irregular	45-200 μm	[16]
Strontium ferrite	irregular	90 nm	[40]

As supported by the references in Table 2.6, the most common particles in MREs are spherical carbonyl iron particles which have been extensively used in MRFs. The preferred particle sizes range from 1 – 9 μm. Iron particles with irregular shape, porous surfaces with much larger size ranging from 10 -200 μm have also been used. Some iron alloy particles such as terfenol-D and strontium ferrite which have even larger saturation magnetization than carbonyl iron and pure iron have also been used but are significantly more expensive and used as much as carbonyl iron and pure iron.

Lokander *et al*. [26, 27] have shown experimentally that particle size and shape have an influence on dynamic shear modulus of MREs, however, tan δ was not reported. In their work, isotropic MREs based on nitrile rubber containing irregular shaped pure iron particles with size ranging from < 60μm to 200μm and spherical carbonyl iron particles with size ranging from 3μm to 5μm were produced. The dynamic shear modulus was measured over a range of frequency (0-25 Hz) and strain amplitude (0-12%). It was found that dynamic shear modulus for MREs containing larger irregularly shaped iron particles was higher when compared to those containing smaller spherical shaped carbonyl iron particles. The results also showed that the dynamic shear modulus of MREs decreased for MREs with particles larger than 60 μm. It has also been reported that the volume fraction of magnetic particles in MREs can been increased up to 50%, but the optimum volume fraction for achieving good damping performance has to be around 30%.

Yancheng *et al.* [97] studied the influence of filler particle size on anisotropic MREs based on cis-polybutadiene rubber containing different sizes of carbonyl iron particles (1.1μm and 9 μm). Tan δ was used as a parameter to assess damping. The results showed that the tan δ for MREs containing 60wt% and 80wt% of larger carbonyl iron particles were higher compared with those containing smaller carbonyl iron particles.

In current literature, carbonyl iron and pure iron are the most preferable magnetic particles use in MREs, however, these types of particle are quite expensive. Therefore, iron sand was chosen as a new type of magnetic particles in this study. Iron sand is a natural resourced material that is readily available in New Zealand. It

has high potential to be used in MREs due to its high magnetic permeability and saturation magnetisation. It is discussed further in the following section.

2.5.1 Iron sand

"Iron sand" or "black sand" are names given to dark, high density, titanomagnetite sand which occurs extensively on the west coast of New Zealand's North Island. About one and a half million years ago there was a series of volcanic eruptions between Raglan and Waikato Heads (including the volcano of Karioi). Volcanic activity continued until a quarter of a million years ago, spreading north to Auckland, south-east to the Taupo volcanic area and south to Mount Taranaki, dramatically altering the coastal geographic area. Volcanic deposits were slowly eroded by major rivers such as the Waikato, Wanganui and Whangaehu rivers which brought vast quantities of volcanic material to the coast. The darker andesitic rocks of Taranaki volcanoes and the lighter-coloured rhyolitic rocks of the Taupo volcanic area have provided the majority of the raw materials for the iron sand deposits. Ocean currents have moved the deposit along the coastline and the action of wind and waves has concentrated them on the sea floor, on beaches and in dunes [113, 114].

Iron sand was first noted by Captain James Cook who described a "black sandy sea bottom" during his first voyage to New Zealand in 1769. In 1839, Ernst Dieffenbach, hired by the New Zealand Company to describe New Zealand's natural resources, noted the iron sand on beaches along the Taranaki coast. In fact, the iron sand deposit occurs along 480 km of the west coast of the North Island from

Wanganui to Kaipara Harbour (Figure 2.8) [115]. The deposit includes the beach and dune sand, and older coastal sand deposits that have been preserved by tidal uplift.

Iron sand deposits on the west coast of the North Island of New Zealand contain a total identified resource of over 850 million tonnes. Table 2.7 shows estimated resources of iron sand deposits for different locations calculated by Kear in 1979 [113]. One of the largest deposits identified was at Waikato Heads, where the New Zealand Steel Investigation Co. Ltd carried out more detailed exploration including geological and magnetic surveys. Deposits at Waikato Heads and Taharoa are currently mined for New Zealand's iron ores, whereas a mine at Waipipi closed in 1987 [113, 116, 117].

The iron sand deposits are divided into those of the northern Auckland-Waikato region and southern Taranaki-Wanganui region. In the northern region, the iron sand deposit is categorised as Kaihu sand. Kaihu sand consists of beach sand and dune sand and has a maximum thickness of 180 metres, mostly loose, dark dune but it is weathered to brown sand in the upper part. It typically contains up to 29 wt% titanomagnetite but a few richer layers contain up to 60 wt% titanomagnetite. In the Taranaki-Wanganui region, iron sand is derived from the Taranaki andesites and categorized as Pouakai sand. Pouakai sand was formed by conglomeration of marine sand, peat, alluvial sediments, volcanic ash, volcanic lahar deposits and volcanic rock. The sediments overlaid and formed terraces at a height of up to 300 metres above sea level. In the southern region, there are 12 separate terraces ranging in age from 7,000 to 60,000 years old. The iron sand deposits are mainly concentrated within the youngest of the terrace formations. Weathered and ashy dune sand of low grade titanomagnetite which consists of less than 15wt% is present in some of the

older terraces, but high ash and clay contents make these deposits less attractive and of little value [113, 116].

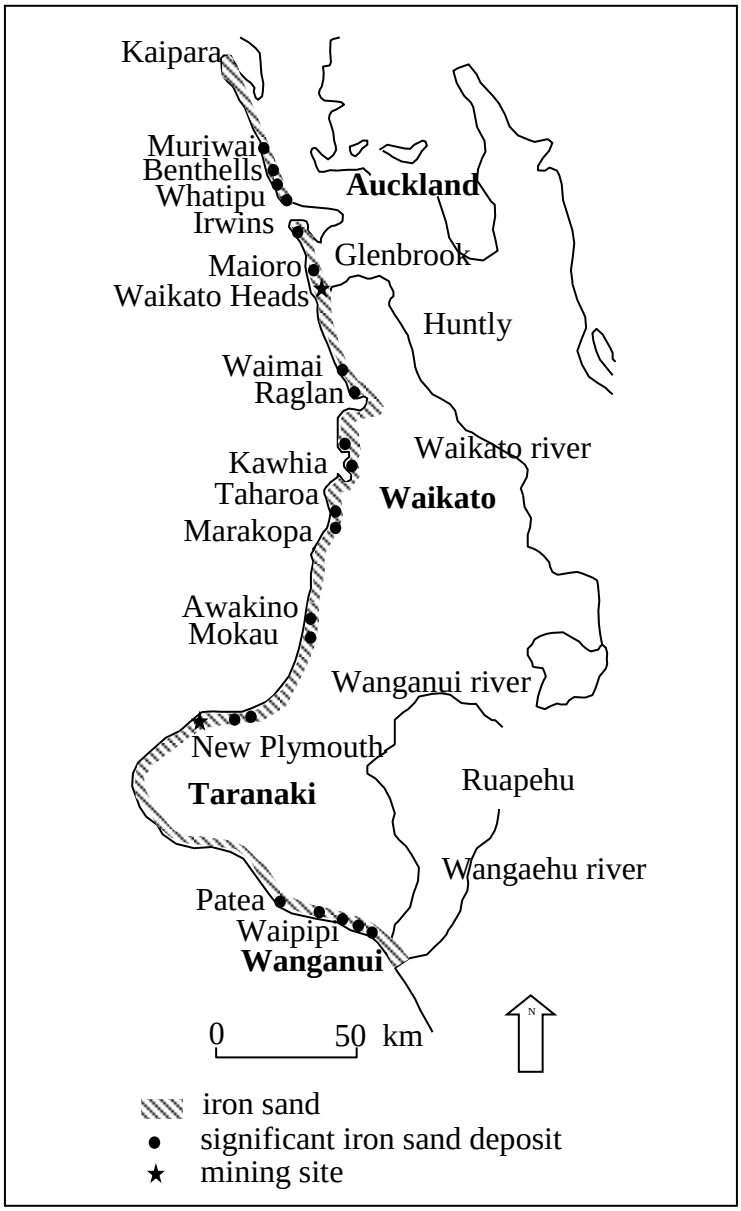

Figure 2.8 Location of iron sand deposits, west coast, North Island.

Table 2.7 Iron sand resources, west coast, North Island

Deposit	Quantity of iron sand (Mt)	Grade (% magnetics)
Muriwai	13	15
Bethells	3	15
Whatipu	5.3	31
Irwins	5	18
Maioro	20	10
Waikato Heads	140	18
Waimai	43	44
Raglan	15.5	20.4
Kawhia	200	13
Taharoa	208	35
Marakopa	25	45
Awakino	5.8	63
Mokau	3.9	37
New Plymouth	8	24
Patea	23.5	33
Waipipi	40	26
Wanganui	37	16

2.5.1.1 Chemical composition of iron sand

Rich layers of iron sand are dominated by opaque minerals, mostly titanomagnetite with minor constituents of hornblende, augite, quartz, plagioclase, feldspar and volcanic rock fragments (Table 2.8) [118].

Table 2.8 Mineral compositions of iron sand

Mineral	Concentration (%)
Titanomagnetite	60.9
Hornblende	21.4
Augite	7.5
Quartz	1.3
Plagioclase	1.8
Feldspar	1
Volcanic rock fragments	6.1

Titanomagnetite is a solid solution of titanium, magnesium, manganese and vanadium in magnetite (Fe_3O_4). Its chemical composition is summarised in Table 2.9 It is distinctively blue-black in reflected light and strongly magnetic. The titanomagnetite is either a homogeneous or heterogeneous variety, the former being most abundant. The heterogeneous variety contains lamellae of ilmenite within titanomagnetite [35]. Typically, titanomagnetite is separated from impurities by using magnetic separation. New Zealand's iron sand deposits are the most extensive and the most concentrated in titanomagnetite in the world [34, 35].

Table 2.9 Chemical analyses of titanomagnetite

Mineral	Concentration (%)
Magnetite	83.10%
Titanium oxide	8%
Aluminium oxide	4%
Manganese oxide	3%
Vanadium oxide	0.50%
Silica	0.30%
Calcium oxide	0.30%
Others	0.80%

2.5.1.2 Physical properties of iron sand

There is a significant cross-shore variation in titanomagnetite concentration and grain size on New Zealand's beaches. The upper beach is dominated by a high concentration of titanomagnetite, however, titanomagnetite, hornblende and augite occur in about equal proportions in the mid beach and the lower beach to the low tide water line is made up almost entirely of plagioclase and volcanic rock fragments.

Their small size, higher dense and magnetic nature causes titanomagnetite grains to aggregate and settle more quickly at the higher tide water line [34, 35].

The shape of titanomagnetite is assumed to be spherical with size ranging between 0.15 – 0.20 mm in diameter. The titanomagnetite particles are more dense than the non-magnetic particles (titanomagnetite 4.74 g/cm^3, non-magnetic 2.99 g/cm^3). Their density is lower than pure iron (7.87 g/cm^3) and comparable with titanium (4.54 g/cm^3) [115, 119].

Titanomagnetite is a non-conductive mineral. The deficiency of electrical conduction through the particles can be related to a very high contact resistance between adjacent grains within the particle. The resistivity is 28.5 Ohm-m under DC-resistivity measurement and 29.6 Ohm-m under AC-resistivity measurement [115]. High resistivity of titanomagnetite indicates that this material is good for electrical insulation.

2.5.1.3 Magnetic properties of iron sand

Magnetism is the phenomenon by which materials exert attractive or repulsive forces on other materials in response to an applied magnetic field [120]. The source of magnetism is magnetic dipoles. Magnetic dipoles are found to exist in magnetic material and can be thought of as small bar magnets composed of north and south poles. A magnetic field exerts a torque that tends to orient the dipoles with the field. Orientation of magnetic dipoles contributes to the magnetic behaviour of materials. The strength of a magnetic dipole, called the magnetic moment, may be thought of as a measure of a dipole's ability to align itself with an applied magnetic field.

Generally, the macroscopic behaviour of magnetic materials can be classified using a few magnetic parameters. The most significant parameter is susceptibility. Susceptibility is a dimensionless proportionality between magnetic moment (m) and magnetic field strength (H) that indicates the degree of magnetization of a material in response to an applied magnetic field [121]. It varies with temperature. With increasing temperature, the increased thermal motion of atoms tends to randomize the directions of dipoles that may be aligned and gradually diminishes the susceptibility which abruptly drops to zero at what is called the Curie temperature (T_c) [121, 122]. Magnetic behaviour can be classified principally into diamagnetism, paramagnetism, ferromagnetism, antiferromagnetism and ferrimagnetism.

Diamagnetism: Diamagnetism is a very weak form of magnetism that is only present while a magnetic field is being applied; diamagnetic materials possess no magnetic dipoles in the atoms or molecules in the absence of an applied field. In an applied magnetic field, magnetic moments are induced and dipoles align in opposition to the field direction. A weak negative magnetisation is produced which causes repulsion instead of attraction. The susceptibility for diamagnetic materials is of the order of -10^{-5} [120]. The susceptibility is constant at constant temperature for relatively low values of magnetic field. Figure 2.9 illustrates the magnetic dipoles for a diamagnetic material with and without an applied field. Many materials exhibit diamagnetism, the most common materials being graphite, quartz and silica.

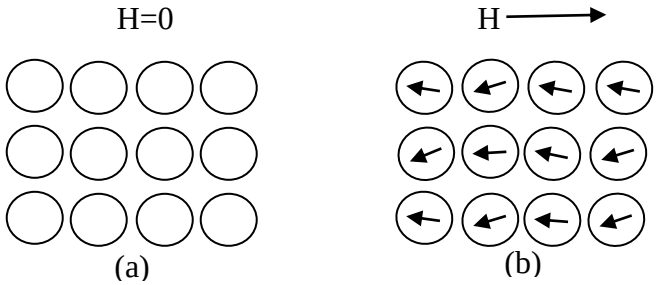

Figure 2.9 The magnetic dipoles for a diamagnetic material with and without a magnetic field. In the absence of an external field, no magnetic moments exist; in the presence of a field, magnetic moments are induced and dipoles are aligned opposite to the field direction.

Paramagnetism: In paramagnetic materials, each atom or molecule has a net magnetic moment in the absence of a magnetic field, but the orientations of dipoles are random leading to no net magnetization. In an applied magnetic field, these dipoles start to align parallel to the field, resulting in weak positive magnetization. However, a large magnetic field is required to align all of the dipoles because the dipoles behave individually with no interaction between adjacent dipoles. Susceptibility for paramagnetic materials ranges from about 10^{-5} to 10^{-2} and since thermal agitation randomizes the direction of the magnetic dipoles, an increase in temperature decreases the paramagnetic effect [120]. In addition, the magnetization is lost as soon as the magnetic field is removed. Figure 2.10 illustrates the magnetic dipoles for a paramagnetic material with and without an applied field. Examples of paramagnetic materials are aluminium, calcium, titanium and alloys of copper. Both diamagnetic and paramagnetic materials are considered as non-magnetic because they exhibit magnetization only in presence of an external field [123].

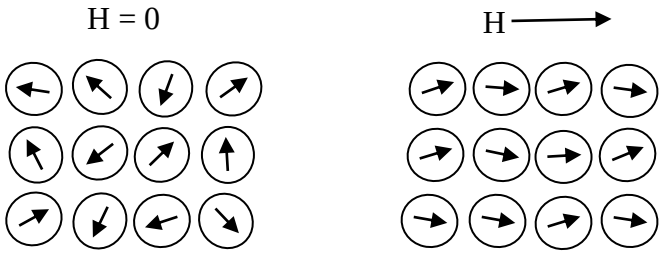

Figure 2.10 Magnetic dipole orientations with and without an applied magnetic field for a paramagnetic material.

Ferromagnetism: Ferromagnetism is explained by the concept that some magnetic materials possess atoms with permanent magnetic moments that align parallel to each other due to inter-atomic forces arising from the spin of electrons on their own axes. In ferromagnetic material, coupling interaction of adjacent magnetic moments create small regions in which there is alignment of all magnetic dipoles, as illustrated in Figure 2.11. Such a region is called a domain and each one has different dipole orientations. Adjacent domains are separated by domain walls, across which the direction of dipoles gradually changes (Figure 2.12). Normally, domains are microscopic in size and in polycrystalline materials a single grain may consist of more than a single domain. As a magnetic field is applied, the domains change shape and size by the movement of domain walls. The domains that are favorably aligned to the applied field grow at the expense of those that are unfavorably aligned. This process continues with increasing applied field until the favorably aligned domains diminish other domains and becomes a large domain at which the magnetization approaches a definite limit called saturation. The new domain alignment persists once the field is removed. Figure 2.13 illustrates the mutual alignment of atomic dipoles and domains in the absence of magnetic field, in an applied field and after the field is

removed for ferromagnetic materials. The magnetization remaining after a magnetic field is removed is called remanent magnetization. Susceptibility for ferromagnetic materials is greater than 1 and typically can have values as high as 10^6. The value of susceptibility varies with temperature; when temperature rises above the T_c, ferromagnetic materials lose their magnetization and behave as paramagnetic materials in the absence of a field [123-125]. Examples of ferromagnetic materials are nickel, cobalt and samarium.

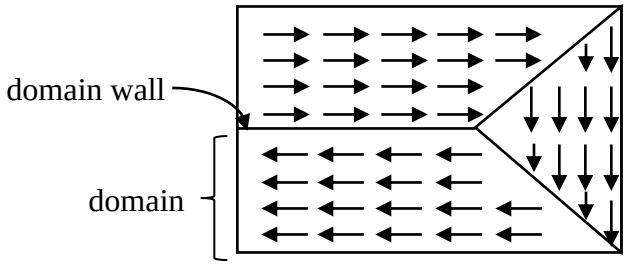

Figure 2.11 Schematic depiction of domains in a ferromagnetic material.

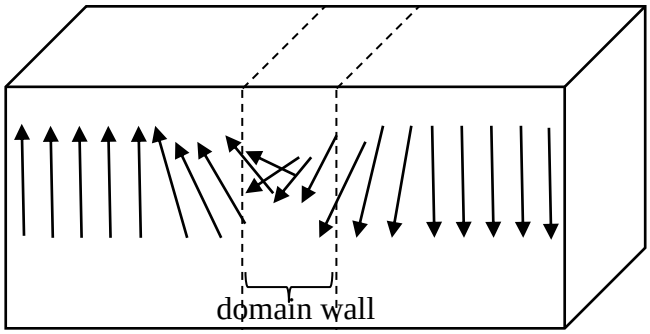

Figure 2.12 Schematic illustration of the gradual change in magnetic dipole orientation across a domain wall.

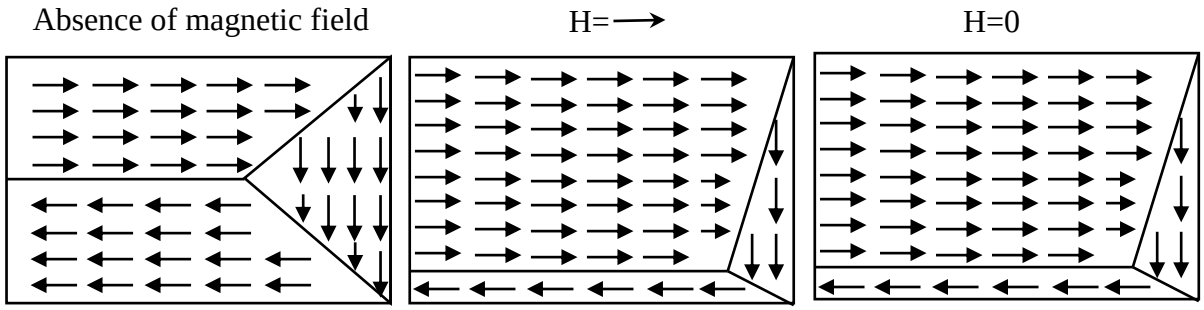

Figure 2.13 Schematic illustration of the mutual alignment of atomic dipoles and domains for a ferromagnetic material.

Antiferromagnetism: Antiferromagnetic materials can be regarded as anomalous paramagnets since they have a small positive susceptibility in an applied magnetic field, but, their magnetic dipole alignment after the magnetic field is removed is entirely different to paramagnets. When the magnetic field is removed, the coupling interaction of magnetic moments tends to align the dipoles anti-parallel to each other and magnetic moments cancel out. As a consequence, antiferromagnetic materials possess no net magnetization. Manganese oxide and hematite are the most common examples. Figure 2.14 shows schematic representation of antiparallel magnetic moments for antiferromagnetic materials [126].

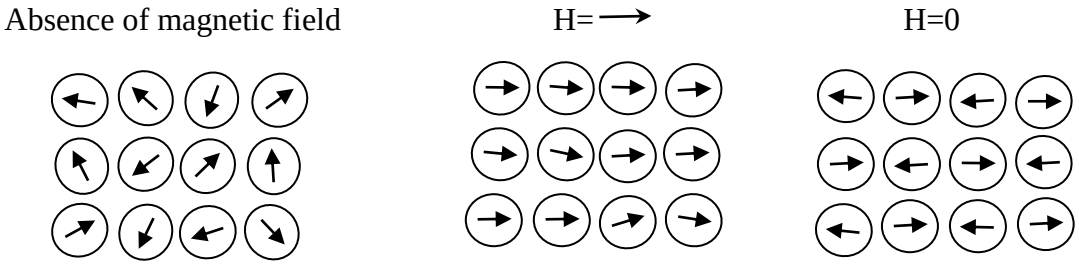

Figure 2.14 Schematic representations of antiparallel magnetic moments for antiferromagnetic materials.

Ferrimagnetism: The magnetic characteristics of ferromagnets and ferrimagnets are similar; the distinction lies in the source of the net magnetic moments [120, 121, 127]. Like ferromagnetic materials, ferrimagnetic materials consist of magnetically saturated domains separated by domain walls, and they exhibit the phenomena of magnetic saturation and remanent magnetization. Their magnetization also disappears above T_c when then they become paramagnetic. The most important ferromagnetic substances are called ferrites. Ferrites are ionic compounds and their magnetic properties are influenced by the magnetic ions they contain. One of most commonly known ferrites is magnetite. The formula can be written as $Fe^{2+}\ O^{2-}\ (Fe^{3+})_2\ (O^{2-})_3$ in which the Fe ions exist in both +2 and +3 valence states in the ratio of 1:2. A net spin magnetic moment exists for Fe^{2+} as well as Fe^{3+} but there are antiparallel spin coupling interactions between the Fe^{3+} indicating that the moments of the Fe^{3+} ions cancel out. The net magnetization is equal to the magnetic moments of the Fe^{2+} ions [121]. Thus, the net magnetization for ferrimagnetic materials is not as high as for ferromagnetic materials. Figure 2.15 illustrates the alignment of ionic dipoles and domains in the absence of a magnetic field, in an applied field and after field is removed for ferrimagnetic material. Examples of ferrimagnetic materials are magnetite and ilmenite.

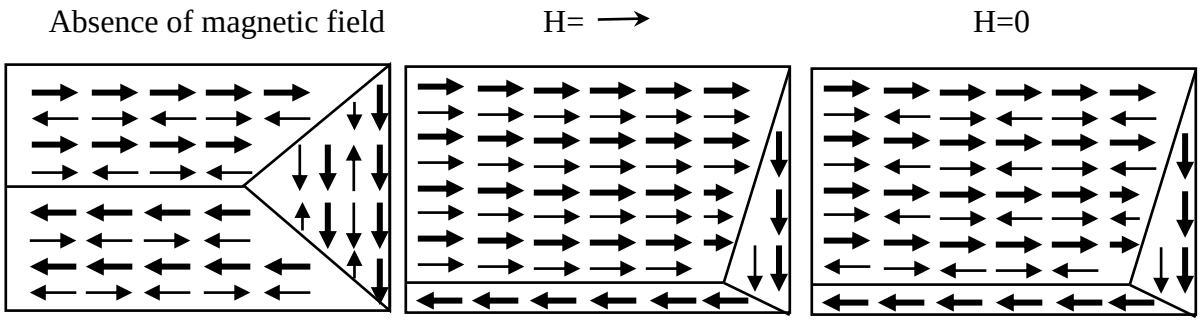

Figure 2.15 Schematic representations of magnetic moments for ferromagnetic materials.

Iron sand which is dominated by titanomagnetite is categorized as a ferrimagnetic material [123, 125]. The susceptibility of titanomagnetite is 2.27. Figure 2.16 compares the susceptibility of a range of materials including iron sand [128]. It has also been reported that the susceptibility of iron sand is not affected by variation of particle size [115]. In addition, titanomagnetite also possess a remanent magnetization. The value of remanence is about 6.23 Am^{-1}[115] and T_c ranges between 290^{o}C to 520^{o}C with no sharp Curie point, such that magnetization of titanomagnetite decreases gradually over a range of temperature rather than suddenly at a single clearly defined temperature [129].

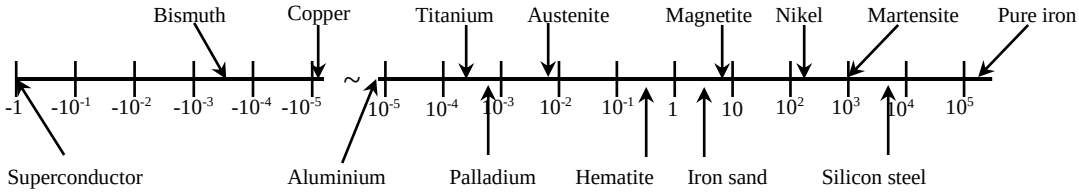

Figure 2.16 Susceptibility spectrum. The diagram uses a logarithmic scale to indicate the full range of magnetic susceptibility values: It extends from susceptibility = -1.0 for superconductors to susceptibility > 100,000 for pure iron.

2.6 Factors influencing damping performance of MREs

2.6.1 Magnetic field strength

The magnetic field strength applied during curing is one of the most important factors that affect the damping performance of MREs. In the presence of a magnetic field during curing, the magnetic dipoles start to align parallel to field direction, resulting in the north pole of one particle to attract the south pole of its neighbour.

The maximum possible increase in damping through magnetic particle interactions occurs when the aligned particles become magnetically saturated. Pure iron has the highest saturation magnetization (J_s) among commonly used particles of J_s=2.1 Tesla. However, alloys of iron and colbalt have higher saturation magnetization (up to J_s=2.4 Tesla) than pure iron and they have also been used in MRFs [28]. Chen *et al.* [30] reported that for MREs based on natural rubber containing 60 wt% carbonyl iron particles, saturation occurred around 400 mT and Qiao *et al.* [107] reported that for MREs based on thermoplastic elastomer matrix containing modified carbonyl iron, the saturation occurred at around 500 mT.

In addition, some researchers have studied the microstructure of MREs under different magnetic field strength during curing. It has been found that more particles aggregate with each other and the chain like columnar structures became longer and thicker as the magnetic field strength increased. Formation of such chain-like columnar structures was found to provide much larger damping and stiffness [80, 130].

2.6.2 Surface modification of magnetic particles

Damping of MREs depends not only on the type of rubber matrix and magnetic particles used, but also on the level of adhesion between the particles and the rubber matrix; the strength of interaction between the particles and matrix has to be sufficiently strong to obtain efficient interfacial damping. For MREs this sets a challenge. Here, as for other MRE components, the incompatibility of the inorganic magnetic fillers and the rubber matrix can lead to poor wettability and adhesion between the filler and matrix as well as non-uniformity of filler dispersion leading to

low energy absorption [38-40]. Therefore, a lot of work has focused on surface modification of the magnetic particles in order to improve ease of adhesion with and dispersion within the rubber matrix in order to realise the full potential of MREs.

Surface modification of inorganic magnetic particles can be achieved using a number of approaches; most commonly, the filler surface is chemically modified to become more compatible with the matrix using methods such as grafting of coupling agents, particle coating, reactions with species to enhance surface chemistry and surfactant absorption. Table 2.10 presents most commonly used methods for surface modification of MREs.

Table 2.10 Methods of surface modification for MREs

Method	Matrix	Particle	Reference
Coupling agent (silane)	silicone rubber	carbonyl iron	[87]
Coupling agent (silane)	polyurathene rubber	carbonyl iron	[108]
Coupling agent (silane)	nitrile rubber	strontium ferrite	[40]
Coupling agent (titanate)	thermoplastic elastomer	carbonyl iron	[107]
Particle coating (PEG)	natural rubber	iron oxide	[32, 42]
Particle coating (CTCS)	silicone rubber	carbonyl iron	[90]
Particle coating (PMMA)	silicone rubber	carbonyl iron	[131]
Reaction with maleic anhydride	polybutadiene rubber	carbonyl iron	[132]
Anionic and non-ionic surfactant absorption	natural rubber	carbonyl iron	[79]

Among the various modification approaches, treatment using silane based coupling agents has been seen to be the most successful and cost effective treatment for improving the adhesion between magnetic particles and the rubber matrix. These chemicals are silicon-based chemicals that contain hydrolysable groups (such as

methoxy, ethoxy or acetoxy) at one end that will interact with inorganic materials and organofunctional groups (such as amino, vinyl or sulphide) at the other end that can react with the rubber matrix. Therefore, inorganic and organic materials can be coupled together with the silane coupling agent acting as a bridge between them. This type of surface modification is also well established for enabling different types of fillers such as silica [133, 134], aluminium powder [135], halloysite nanotubes [136], wood flour [137] and natural fibre [138, 139] to be used as reinforcement in rubber compounds. It has been also reported that surface modification of magnetic particles using coupling agents such as silane and titanate coupling agents increases the mechanical and damping performance of MREs due to decreased interfacial tension resulting in improved dispersion of magnetic particles in isotropic MREs and improved degree of freedom of movement for magnetic particles to organise into chain like columnar structures in anisotropic MREs [40, 87, 107, 108].

Particle coating is usually carried out by surface polymerization of magnetic particles using functionalised polymers such as polyethylene glycol (PEG), polymethyl methacrylate (PMMA) and polybutyl acrylate. This typically uses complex polymerization processes such as emulsion polymerisation or atom transfer radical polymerisation to graft the polymer on the magnetic particles before they are subsequently mixed with the matrix. MREs with surface coated particles have shown improved dynamic shear storage modulus and superior mechanical properties [32, 42, 90, 131].

It has also been reported that when magnetic particles are modified by anionic, non-ionic and compound surfactants, longer and bulkier magnetic chains in ansotropic MREs have been obtained and the damping performance during

application can be increased up to 188% due to the good compatibility between the particles and matrix [79].

In this study, Bis-(3-triethoxysilylpropyl) tetrasulphane (known as TESPT or Si 69) which is the most popular and effective silane coupling agent for hydrocarbon rubber was used for surface modification of iron sand particles [140]. TESPT possesses ethoxy hydrolysable groups at both ends and the tetrasulphane group at its centre. The ethoxy hydrolysable groups can react with the hydroxyl groups on the surface of iron sand during surface treatment and should lead to the formation of stable iron sand and TESPT bond. Tetrasulfane groups are rubber reactive and can react in the presence of accelerators at elevated temperatures with or without elemental sulphur being present, to form crosslinks with rubbers [141]. Therefore, the iron sand and rubber could likely be coupled together with the silane coupling agent acting as a bridge between them.

2.6.3 Miscellaneous

A number of other factors that influence the damping performance of MREs have also been reported by several authors. For instance, plasticiser has been used to soften the matrix in order to improve the degree of freedom of movement for magnetic particles during curing for anisotropic MREs and to improve the dynamic mechanical properties of isotropic and anisotropic MREs. Lokander *et al.* [26] added the plasticiser di-ethylhexylphthalate (DEHP) in isotropic MREs based on nitrile rubber and iron particles and obtained a slight improvement of the dynamic shear modulus, however, tan δ was not reported. Chen *et al.* [30] investigated the influence of plasticiser content on dynamic shear modulus and tan δ of anisotropic MREs based

on natural rubber and carbonyl iron. The results showed that the dynamic shear modulus decreased and the tan δ increased with increasing plasticiser content from 10 to 20 wt%. Wu *et al.* [142] incorporated the plasticiser diisooctylphthalate (DOP) into MREs based on polyurethane rubber and carbonyl iron. It was found that the viscosity of the matrix decreased resulting in longer magnetic particle alignment in anisotropic MREs. However, the tan δ slightly decreased as well as thermal stability and compressive strength.

It has also been reported that addition of nanosized reinforcement such as carbon black into MRE formulations can improve the damping. Nayak *et al.* [93] fabricated MREs based on silicone rubber and carbonyl iron with addition of 7 wt% of carbon black. It was observed that the Young's modulus increased about 56.8%, the dynamic shear modulus increased about 13% and tan δ increased about 40%. Addition of carbon black in anisotropic MREs based on natural rubber and iron particles has also provided good improvement of mechanical and damping performance [20, 31].

2.7 Processing of MREs

The flow diagram of MREs fabrication process for MREs is shown in Figure 2.17.

2.7.1 Raw materials

As previously discussed, the main materials comprising MREs are rubber matrix and magnetic particles. The magnetic particles used can be unmodified or surface modified prior to mixing and compounding. In addition, additives like crosslinking agents, antioxidants and mixing aids may be used.

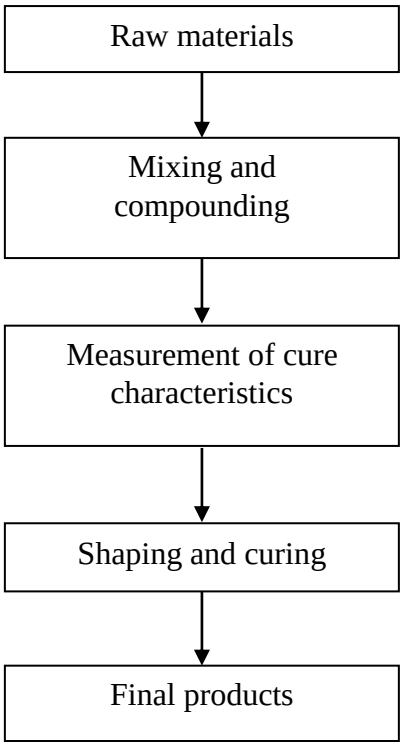

Figure 2.17 Flow diagram of MREs fabrication process

2.7.2 Mixing and compounding

The mixing and compounding methods for MREs can be carried out using conventional rubber-mixing/compounding equipment (two roll mill). The conceptual view of a two roll mill is shown in Figure 2.18.

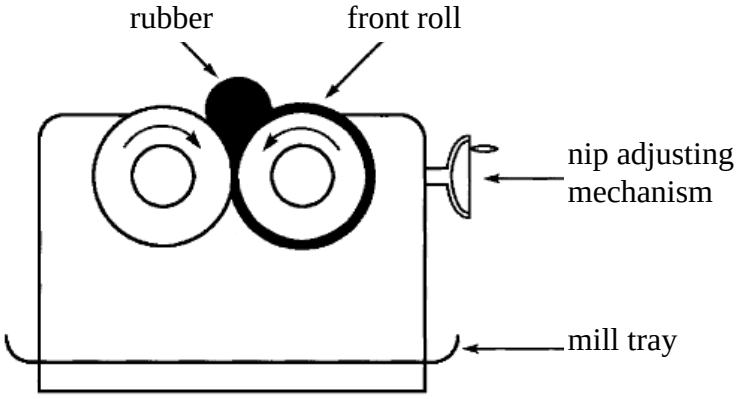

Figure 2.18 Conceptual view of two roll mill

The front roller temperature is set typically at between around 40-80^{o}C and the mixing and compounding time is approximately around 30-40 minutes. The first stage of the compounding involves softening the rubber on its own in the two roll mill (mastication). Mastication reduces the viscosity and increase the plasticity of rubber which are brought about by heat generated in a two roll mill through conduction from the heated roller and shearing of rubber during milling. After mastication, most of the additives (other than accelerators and sulphur) and magnetic particles are then added and homogenously dispersed in the rubber. Addition of accelerators and the crosslinking agent needs to be delayed to the last part of the process to prevent premature vulcanization during compounding. The art and skill of the operator plays a significant part in compounding. A good compound should have uniform distribution, high level of dispersion and consistent rheological properties.

2.7.3 Measurement of cure characteristics

The degree of vulcanization of MRE compound has a big influence on the properties of the final product. Therefore, precisely defining curing characteristics including optimum cure time is important to ensure the production of final products having high performance. However, at present, there is little work that has assessed the influence of cure time of MRE compounds. A single study [143] has thoroughly studied the cure time of anisotropic MREs containing silicone rubber and carbonyl iron particles. In this work, MREs were prepared with different cure times and the microstructures and dynamic shear modulus were observed to determine the optimum cure time that produced the highest damping performance. However, this optimum cure time is only suitable to use for the same types of MRE.

The conventional rubber curemeters such as oscillating disk rheometer (ODR) and moving die rheometer (MDR) are the most commonly used equipment to measure cure time [10, 144, 145]. In a curemeter, a piece of rubber compound is contained in a sealed test cavity with a rotor that oscillated at a constant angular displacement. As vulcanization proceeds at a specific temperature, the torque required to shear the compound is monitored and a curve of torque versus time can be generated [10, 102]. The optimum cure time of rubber compound (t_{90}), is defined as the time required for the torque to reach 90% of the maximum achievable torque and relates to the time necessary for the rubber to crosslink to produce optimal mechanical performance [146]. The working principal of the curemeter is based on the fact that the stiffness of the rubber compound increases with the formation of the crosslinks during vulcanization. The use of a curemeter to determine the vulcanization characteristics is specified in ASTM D 2084 [147]. A new method to predict optimum cure time of MREs using dynamic mechanical analysis (DMA) was assessed in this study.

2.7.4 Shaping and curing

After compounding and measurement of cure time, a predetermined amount of MRE compound is weighted and inserted into a mould for shaping and curing. For isotropic MREs, the compound is typically cured in a compression moulder at around 150-170^{o}C under a pressure of approximately 10-12 MPa [26, 29]. A schematic of a compression moulder is shown in Figure 2.19. The curing temperature and pressure is important to ensure that the compound flow and take shape according to the mould. The pressure also helps to contain the expansion of volatiles within the rubber

compound until dimensional stability is achieved. For anisotropic MREs, the mould containing MRE compound is subjected to an applied magnetic field prior to compression moulding. The magnetic field is commonly generated by an electromagnetic devices [21, 24, 30, 42, 80, 81, 97, 132, 142] or permanent magnets [18, 85]. The mould is placed within the magnetic field at elevated temperature to soften the rubber matrix and allows the magnetic particles to organize into chain like columnar structures [30, 81]. Subsequently, the MRE compound is cured in a compression moulder at around 150-170^{o}C under a pressure of approximately 10-12 MPa [98]. Upon curing the matrix, the particles are set in place.

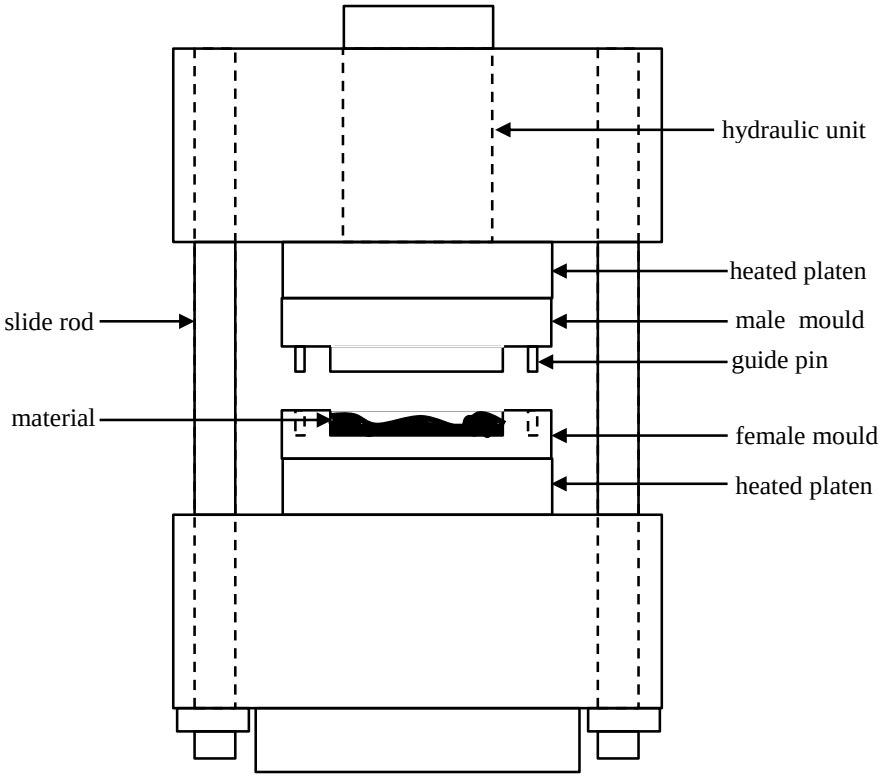

Figure 2.19 Conceptual view of compression moulder

2.8 Damping mechanisms of MREs

Damping of material originates from the energy loss associated with a few different energy dissipation mechanisms such as viscous damping which is associated with molecular chain motion in polymers, dislocation damping, point defect damping and grain boundary damping due to microstructural defects in metal, thermoelastic damping which is caused by local temperature gradients resulting from non-uniform stresses acting on the material, interfacial damping arising from different types of interfaces between reinforcement and matrix as well as magnetism-induced damping due to eddy current loss, residual magnetic loss or magnetomechanical effects. The damping capacity in a material is generally due to the sum of several energy dissipative mechanisms. The purpose of this section is to briefly review some of the important mechanisms that lead to vibration damping in MREs based on natural rubber and iron sand.

2.8.1 Viscous damping

Rubber is a viscoelastic material which exhibits both viscous and elastic behaviour. Under cyclic deformation, its elastic component allows rubber to return quickly to its original shape and does not contribute to damping; the viscous flow of the rubber molecular chains during deformation converts kinetic energy into heat by internal friction of the disentangling long chain molecules and is responsible for damping [148, 149]. Viscous damping is mainly influenced by temperature and frequency [149]. The effect of temperature is illustrated in Figure 2.20 which highlights four distinct regions. In the glassy region, the chains are rigidly ordered and crystalline in nature, with glass-like behaviour; the storage modulus is at its

maximum value whilst loss modulus is at a minimum. As temperature increases into the transition region, the storage modulus decreases while the loss modulus increase to a peak value and then starts to drop off. In this region, the long molecular chains are in a semi-rigid and semi-flowing state, and able to rub against adjacent chains. These frictional effects result in viscous damping in the material. In the rubbery region, the storage modulus and loss modulus only varies slightly with changes in temperature. Rubber materials for vibration damping and isolation are always in practice used in the rubbery region. As temperature increases into the flow region, storage modulus and loss modulus start to decrease [150, 151].

Frequency change may have the same effect on material damping as a temperature change. At low frequency, an applied stress deforms the long chains rotation and bending. This is a slow process for which low frequency allows time for the chains to readjust back to the equilibrium state, resulting in low energy dissipation. As the frequency increases, chains undergo coiling and uncoiling motion and break crosslinks. In this region, high damping occurs by internal friction between molecular chains during deformation. At high frequencies, molecular chains are not permitted to relax and energy dissipates as heat; stress and strain are out of phase [152].

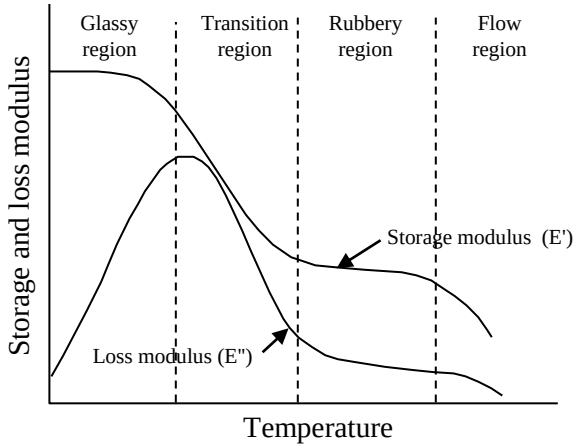

Figure 2.20 Variation of viscoelastic properties with temperature

2.8.2 Interfacial damping

The interface between reinforcement and the matrix is also important in determining the damping of MREs. Little work has been carried out to study the interfacial damping of MREs and previous work has not comprehensively considered the condition of the interfacial bonding [97, 153]. Interfacial bonding can be classified into three categories [154, 155]: ideal interfaces, strongly bonded interfaces and weakly bonded interfaces. An ideal interface between a particle and matrix enables efficient stress and strain transfer between the components and therefore does not contribute to overall damping. For strongly bonded interfaces, damping is mainly due to energy absorbed during viscous flow which is more constrained due to the formation of interfacial bonding between particles and the matrix and energy loss due to stress released after debonding of particles from the matrix. For weakly bonded interfaces, damping is mainly due to interfacial friction between the surfaces of the two materials where the relative motion takes place. In addition, an increased of strain amplitude could possibly results in breakdown of strongly bonded interfaces into weakly bonded interfaces.

The main factors that influence interfacial properties include particle size, particle loading, dispersion and formation of agglomerates. It is known that for smaller particles, there is a larger overall surface area for the same particle volume fraction and therefore, the total interfacial surface area available for interfacial damping increases and energy dissipation increases. However, the tendency of smaller particles to form agglomerates is higher as the particle loading increases and poor dispersion occurs. When the particles agglomerate, some rubber segments will be trapped within the particles, as shown in Figure 2.21 [97]. The rubber which is

located outside the agglomerate is defined as free rubber, while the rubber inside the agglomerate is defined as trapped rubber. The trapped rubber reduces the effective interfacial damping area between the free rubber and the particles and behaves as a hard filler, leading to a decrease in energy dissipation. The agglomeration is strongly amplitude and temperature dependent. At high amplitude, the agglomerates are broadly destroyed and release the trapped rubber to take part in energy absorption. On the other hand, increasing the temperature would increase the flowability of the trapped rubber molecules, overcoming inter-particles interaction in the agglomerates and leads to breakdown of agglomerates.

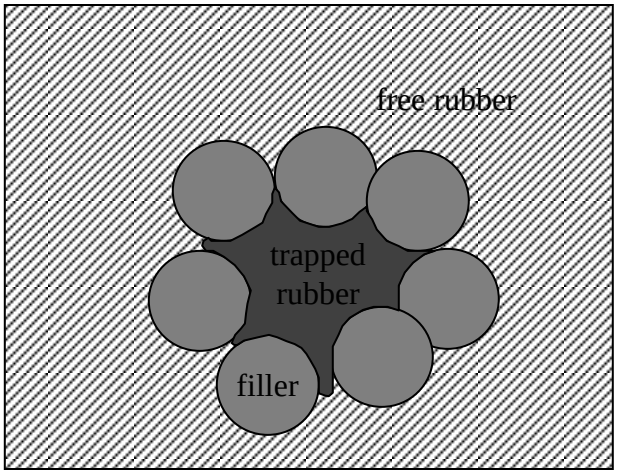

Figure 2.21 The restrained rubber and free rubber in agglomerate.

2.8.3 Magnetism-induced damping

As previously discussed in Section 2.5.1.3, magnetic particles can be divided into regions of uniform magnetic polarization, known as domains and each one has different dipole orientations. Upon application of an applied magnetic field during curing, the particles align and form continuous columnar structures in the magnetic

field direction. The magnetic domains, nominally in random orientation, are oriented, resulting in anisotropic MREs.

Possible magnetism-induced damping in MREs is due to energy absorbed to overcome magnetic interaction between neighbouring particles; this process transforms elastic energy into magnetic energy and subsequently dissipates by magnetic hysteresis [21]. Other mechanisms include eddy current loss, residual magnetic loss and magnetomechanical damping. Eddy current loss is due to electrical resistance losses inside the materials when it is subjected to an alternating magnetic field. The circulation of the currents in a material generates a magnetic field which will interact with the applied field, resulting in a force that opposes the change in flux and due to the electrical resistance of the material, the induced currents will be dissipated into heat [156]. However, iron sand used in this study is a non-conductive mineral with high electrical resistivity at 28.5 Ohm-m under DC-resistivity measurement and 29.6 Ohm-m under AC-resistivity measurement [115] and therefore, damping resulting from eddy current loss can be disregarded and will not be further discussed. The residual magnetic loss is associated with deviation of atomic magnetic spin waves from the equilibrium position and resonance phenomena of magnetic moment orientation within the magnetic domain walls in permanent magnets such as nickel, cobalt, and some alloys of rare earth metals [157]. Therefore, damping due to residual magnetic loss can be assumed negligible as iron sand is a soft magnetic material.

The process for energy absorption by the magnetomechanical damping is due to change of magnetic domain structure induced by application of stress [111, 112, 158]. The effect of domain interaction before and after applied tensile, compressive

and shear stresses are shown in Figure 2.22. Tensile stress tends to align domains parallel to the tensile load whilst the compressive stress also orientates domains parallel to the compressive load. Shear loading can be resolved into a biaxial stress state such that the two stresses perpendicular to each other with one directed towards the natural and the other away from the natural (see Figure 2.22 c). The effect of shear stress on domain orientation can be represented by coalescence of tension and compression stresses such that the tensile stress tends to align domains parallel to the tensile load and the compressive stress further encourages alignment of domain in the tensile direction.

When the material is subjected to a cyclic load, the matrix phase transfers load to the damping phase and the domains align correspondingly to the loading direction. At a critical stress level, the domains switch from one stable orientation to another. Each domain reorientation absorbs a quantifiable amount of energy under an applied cyclical load. After the domains have orientated, they behave elastically until an opposite critical stress is applied, causing them to reorient back to a new state, absorbing more energy. Furthermore, the mechanical energy required for domain motion increases when an external magnetic field is applied during services.

Kallio [159] reported that the effect of magnetomechanical damping for MREs based on silicon rubber and iron particles was much less than that through inter-particle magnetic interactions. Furthermore, the energy losses due to change of the magnetic domain structure is very difficult to directly measured.

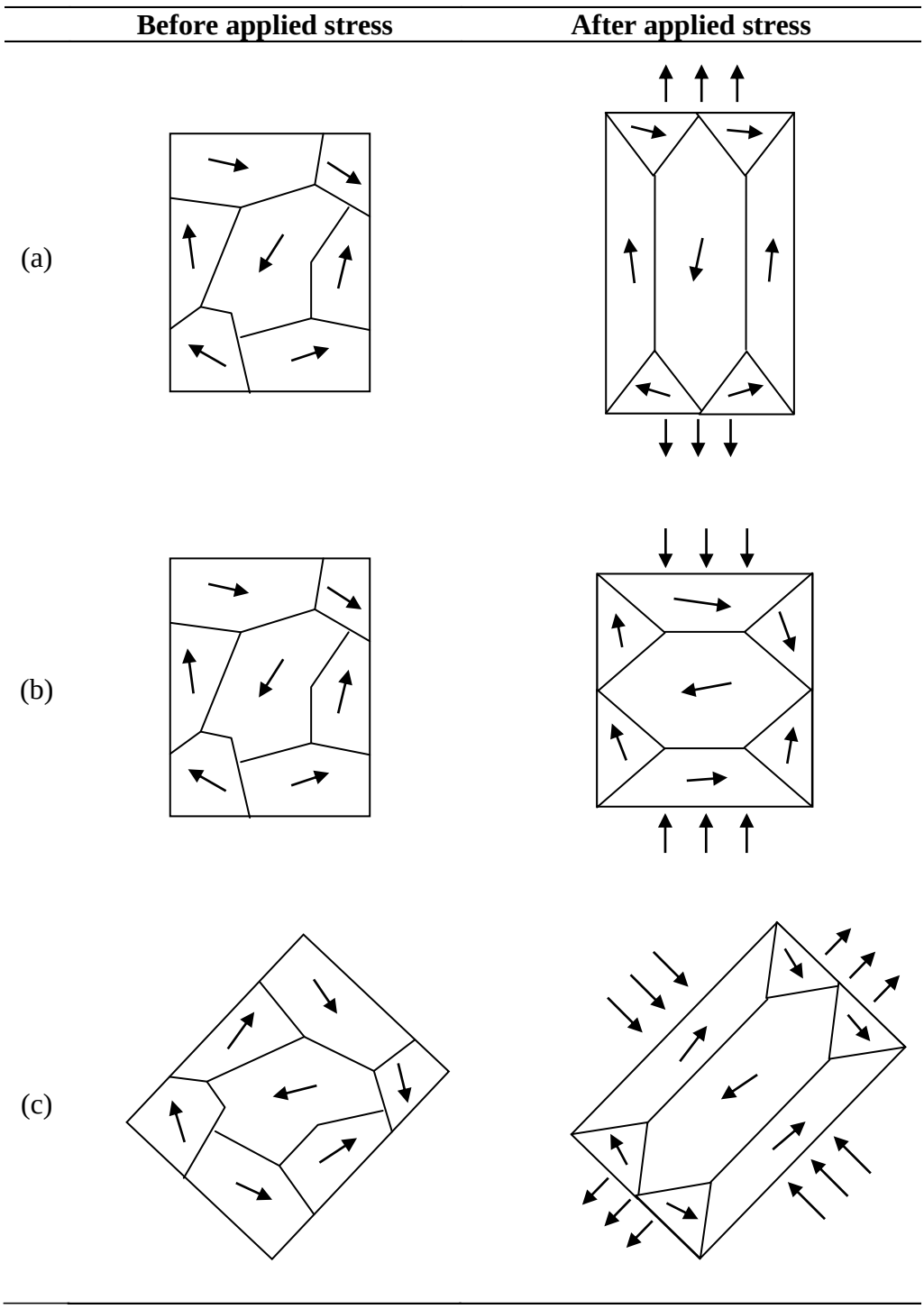

Figure 2.22 Results of domain interaction before and after applied tensile, compressive and shear stresses

2.8.4 Modelling of MRE damping mechanisms

Literature on the modelling of MRE damping mechanisms is limited. Early models were developed by Davis [37] and Jolly *et al.* [46] describing the effect of inter-particle magnetic interactions on the elastic properties of MREs, particularly on the shear modulus. Their work was based on prior theoretical and finite element analyses of MRFs. The developed models use assumptions that the particles are spherical and aligned in perfect chains where the quasi-static shear strains and associated stresses are uniformly distributed over the length of each particle chain. These models have the ability to predict shear modulus well. However, prediction of damping was neglected and mechanisms other than inter-particle magnetic interactions were not included. Lin [153] and Yancheng *et al.* [97] proposed interfacial slip models to describe contributions of the interface between magnetic particles and the rubber matrix to damping but not damping mechanisms associated with the matrix and magnetic particle interactions and so these models would be expected to be limited with respect to describing total damping. Furthermore, these models were not verified experimentally.

Chen and Jerrams [49] were the first to try to take account of all damping mechanisms. They proposed a model to predict overall shear modulus of MREs under cyclic deformation from separate shear moduli representing the different mechanisms, taking into account the viscoelasticity of the rubber matrix, interfacial slippage between magnetic particles and the matrix and inter-particle magnetic interactions. Tan δ was then obtained from the combined shear modulus. The model is suggested to be potentially reliable for prediction of the overall damping for MREs with weakly bonded interfaces between magnetic particles and the matrix, but less

accurate for MREs containing surface modified particles with strongly bonded interfaces due to additional energy absorbed during viscous flow which is more constrained due to the formation of interfacial bonding between particles and the matrix and energy loss due to stress released after debonding of particles from the matrix. The effectiveness of the model was tested by numerical simulations, however, the results were not verified experimentally.

More recently, Jie *et al.* [48] developed a model that also aimed to take account of all possible damping mechanisms to predict overall damping of MREs. This took account of intrinsic damping of component materials, interfacial damping and inter-particle magnetic damping. In their model, the rule of mixtures (commonly used to model the strength of unidirectional, continuous fibre composites) [160] was used to describe the intrinsic damping, assuming MREs as particle reinforced composites with magnetic particle chains of infinite length. The contribution to damping for strongly bonded interfaces was proposed based on Eshelby inclusion theory [161] and the contribution for weakly bonded interfaces was proposed based on Coulomb's law of friction [162]. The contribution for inter-particle magnetic damping was described using the inter-particle magnetic interactions model developed by Jolly *et al.* [46]. The model has the ability to explain the experimental trends but the differences between predicted damping values and experimental values were more than 40% which is most likely due to over-simplication in prediction of intrinsic damping by using the ROM. Furthermore, the dependence of frequency on material damping was neglected.

The aim of the current work was to accurately predict total damping capacity of MREs taking account the separate mechanisms that would contribute to damping, namely:

i) viscous flow of the rubber matrix,

ii) interfacial damping through strongly bonded interfaces and weakly bonded interfaces,

iii) magnetism-induced damping.

The contribution of viscous flow of the rubber matrix on the overall damping was characterised using the Kelvin Voight model [163]. The contribution to damping for strongly bonded interfaces was described using Schoeck theory [164] which is originally based on Eshelby inclusion theory [161] and the contribution for weakly bonded interfaces was proposed based on Lavernia analysis [165] which is based on Coulomb's law of friction [162]. The inter-particle magnetic interactions model developed by Jolly *et al.* [46] was adopted to evaluate the magnetism-induced damping.

Chapter 3

Curing of Rubber Compound Using Dynamic Mechanical Analysis

3.1 Introduction

In this chapter, a new method to predict optimum cure (t_{90}) time of rubber compounds was proposed. Dynamic Mechanical Analysis (DMA) was carried out in an isothermal shear mode to measure the changes in material properties caused by vulcanization. Storage modulus (G′), loss modulus (G″) and tan δ were recorded as a function of time and correlation between G', G" and tan δ with t_{90} were investigated. To assess that DMA is reliable for assessment of t_{90}, the t_{90} of 21 different rubber compounds with various filler loading and particle size were analysed and results were compared with cure time obtained using a conventional rubber curemeter, moving die rheometer (MDR).

3.2 Experimental

3.2.1 Material and specimen preparation

In order to check the applicability of DMA to predict the optimum cure time and to evaluate the consistency of the measurements, 21 formulations of rubber compound were investigated. The formulations used in this study are shown in Table 3.1. Natural rubber (SMR L) and other chemicals such as zinc oxide, stearic acid, n-cyclohexyl-2-benzothiazole sulfenamide (CBS), tetra methyl thiuram disulphide

(TMTD), paraffin oil, naphthenic oil were all purchased from Field Rubber Limited, Auckland. Both unfilled and filled rubbers were involved in this study. Iron sand was used as filler, which was milled to various sizes using planetary mono mill (Pulverisette 6) produced by Fristech GmbH.

The mixing and compounding was carried out using a conventional laboratory two roll mill (model XK150). The front roller speed was 24 rpm, the rear roller speed was 33 rpm, the roller diameters were 150 mm, friction ratio of two rollers was 1:1.4 and the roller temperature was set to 80^{o}C. The nip gap (distance between front and back roller) was maintained at 2 mm during compounding. The compounding began with softening the rubber on its own in the two roll mill (mastication). Mastication reduces the viscosity and increase the plasticity of natural rubber which is brought about by heat generated in two roll mill through conduction from the heated roller and shearing of rubber during milling. After 2-3 minutes the rubber became invested on the hot roll and additives (other than accelerators and sulphur) were then added followed by filler; addition of accelerators and sulphur were delayed to the last part of the process to prevent premature vulcanization during compounding. The mixing time was approximately 40 minutes. Samples were punched from the uncured compound in the form of circular discs with 10 mm diameter and thickness of 3 mm for DMA shear mode testing.

3.2.2 Equipment and procedure

Moving Die Rheometer (MDR)

The MDR 2000 is a rotor less curemeter designed to measure vulcanization of rubber compounds under isothermal test conditions with constant strain and frequency. It has gained much acceptance by the rubber industry and offers several

substantial advantages over previous ODR techniques as described in ASTM D 2084. The design of the MDR 2000 allows the lower half of the die to perform an oscillating rotation of 0.5^{o} with torque measured at the upper die by a torque transducer. The curing characteristics of the compound were determined at $150^{o}C$ under a constant frequency of 1.66 Hz and the t_{90} values were derived from the vulcanization curve. The results of the cure time measurements with the MDR are listed in Table 3.2

Dynamic mechanical analysis (DMA)

The DMA instrument used to perform these experiments was a Perkin Elmer DMA 8000. It is made up of six major components (Figure 3.1): a force motor, a drive shaft, a high sensitivity displacement detector (LVDT), a sample fixture, a furnace and a temperature controller. DMA measurements were conducted on circular disc specimens in shear mode. The specimen loading is shown in Figure 3.2 The driveshaft motion was kept in a horizontal direction during the test and the temperature controller was placed at a minimum distance from the sample. The furnace was first preheated to $150^{o}C$ and then an isothermal test was carried out under a fixed frequency of 1.66 Hz and constant displacement amplitude of 0.1 mm. The temperature was held at $150^{o}C$ for 15 minutes to allow full vulcanization to occur. Data were collected approximately every 5 second in the isotherm period. Shear storage modulus (G′), shear loss modulus (G″) and tan δ were recorded as a function of time in order to deduce a direct connection between the dynamic time sweep test and optimum curing time.

Table 3.1 Formulation of rubber compounds

Material	Natural Rubber	ZnO	Stearic Acid	CBS	TMTD	Paraffin oil	Naphthenic oil	Sulphur	Iron sand loading	Iron sand particle size
Sample/Unit	**phr**	**phr**	**phr**	**phr**	**phr**	**phr**	**phr**	**phr**	**phr**	**µm**
1	100	5	1	2	1	2	3	1.5	0	0
2	100	5	1	2	1	2	3	1.5	30	0 - 32
3	100	5	1	2	1	2	3	1.5	30	32 - 45
4	100	5	1	2	1	2	3	1.5	30	45 - 56
5	100	5	1	2	1	2	3	1.5	30	56 - 75
6	100	5	1	2	1	2	3	1.5	30	75 - 106
7	100	5	1	2	1	2	3	1.5	50	0 - 32
8	100	5	1	2	1	2	3	1.5	50	32 - 45
9	100	5	1	2	1	2	3	1.5	50	45 - 56
10	100	5	1	2	1	2	3	1.5	50	56 - 75
11	100	5	1	2	1	2	3	1.5	50	75 - 106
12	100	5	1	2	1	2	3	1.5	70	0 - 32
13	100	5	1	2	1	2	3	1.5	70	32 - 45
14	100	5	1	2	1	2	3	1.5	70	45 - 56
15	100	5	1	2	1	2	3	1.5	70	56 - 75
16	100	5	1	2	1	2	3	1.5	70	75 - 106
17	100	5	1	2	1	2	3	1.5	100	0 - 32
18	100	5	1	2	1	2	3	1.5	100	32 - 45
19	100	5	1	2	1	2	3	1.5	100	45 - 56
20	100	5	1	2	1	2	3	1.5	100	56 - 75
21	100	5	1	2	1	2	3	1.5	100	75-106

*phr= per hundred rubber

Table 3.2 Optimum cure time (t_{90}) of the formulations as evaluated by MDR

Sample	1	2	3	4	5	6	7	8	9	10	11
t_{90} MDR (min)	5.10	4.65	5.19	4.85	5.25	4.71	4.41	4.82	4.64	4.51	4.92

Sample	12	13	14	15	16	17	18	19	20	21
t_{90} MDR (min)	4.46	4.42	4.58	4.31	4.47	4.47	4.70	4.55	4.54	4.20

.

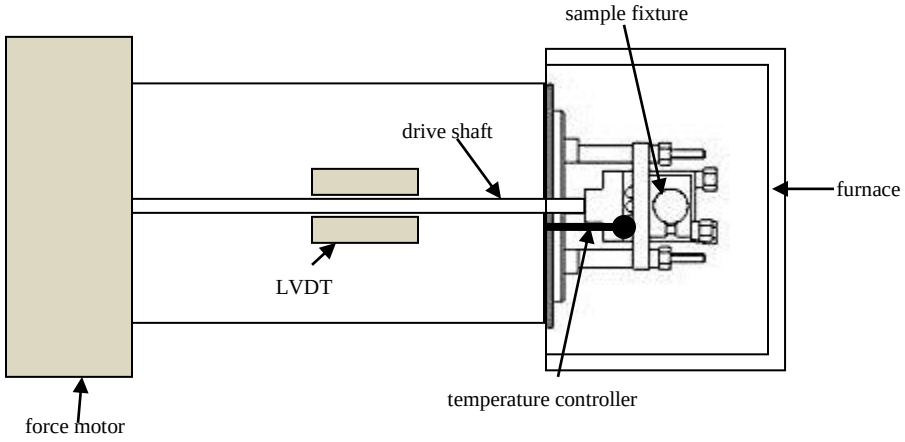

Figure 3.1 Scheme of the DMA 8000

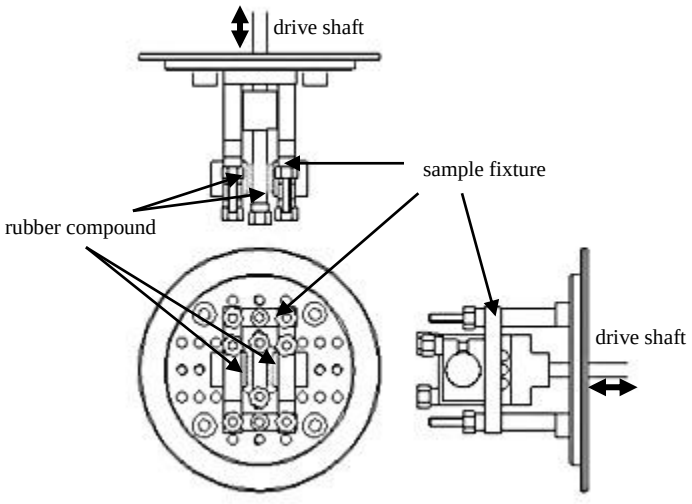

Figure 3.2 Scheme of the shear mode specimen loading in DMA

3.3 Results and discussion

A typical time sweep plot of the unfilled natural rubber compound (NR) measured by DMA is shown in Figure 3.3, including G′ and G″. As can be seen, G″ increases representing when the curing process started and reached a peak after 5 minutes. This is thought to be due to softening of the material as the material is exposed to the curing temperature. After the maximum point, G″ was found to decrease rapidly for 3 minutes, followed by a gradual decrease for approximately 15 minutes. This is believed to occur due to the reduction of viscous flow in the material and therefore low energy being absorbed. In contrast, it is apparent that G′ does not change at the beginning of the curing stage. This indicates that the stiffness of the rubber remains low at the early stage of vulcanization. After 5 minutes, a rapid increase of G′ was observed, followed by a continuous increment up to 15 minutes. This represents the increase of stiffness as a result of crosslink formation. The results obtained agreed with previous work carried out by Gatos *et al.* [166] using a plate-plate rheometer.

Altogether, it can be seen that neither parameter shows a plateau value that indicates an equilibrium degree of vulcanization. A gelation point can be detected at 6.1 minutes; the gelation point is taken to be the crossover of G″ and G′ where tan δ equals 1. In monitoring cure of thermosetting resins by DMA, the gelation point can be defined as a point where the crosslinks have progressed to form a network across the specimen and the material changes from a viscous liquid to a viscoelastic solid [167]. However, the values obtained show a significant difference with the value from a conventional curemeter with an average percentage error of 20% (Table 3.3).

It can be concluded that there is not a direct correlation between t_{90} and G″ or G′ graphs.

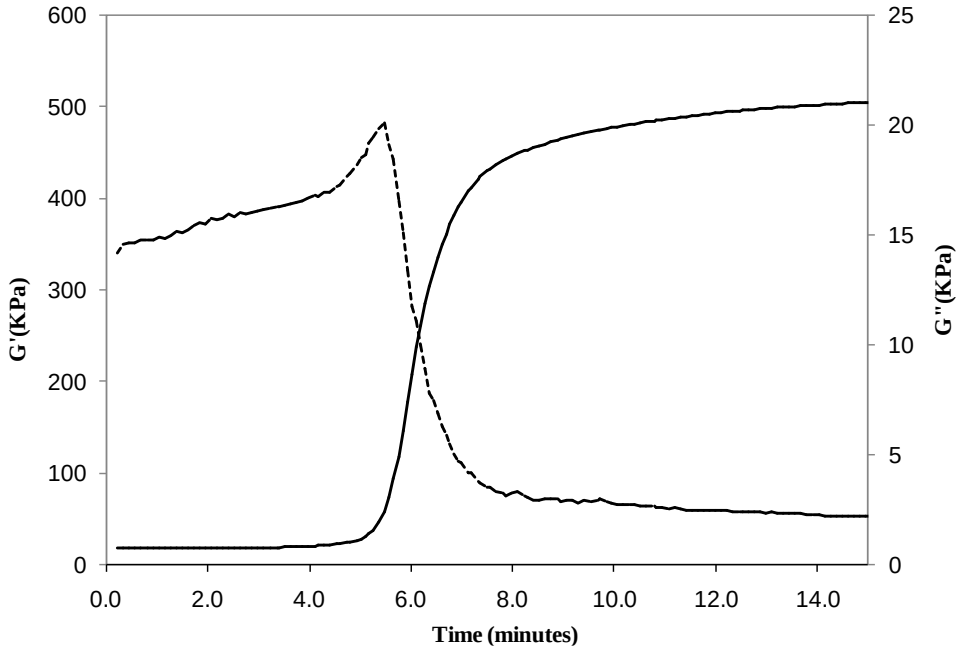

Figure 3.3 Time sweep plot, including G″ and G′ for NR compound

Table 3.3 Differences of t_{90} value measured by MDR and calculated from the gelation point of G″ or G′ graphs for unfilled natural rubber compound (NR)

		Time
Method	t_{90} MDR	5.1 minutes
	t_{90} Gelation Point	6.1 minutes
Error (%)		20%

Another important parameter obtained in dynamic time sweep test is tan δ. Tan δ is calculated as the quotient of the loss and the storage moduli. Therefore, it reveals the ratio of the viscous and the elastic portions of the materials [168]. The results for tan δ as a function of time for NR are depicted in Figure 3.4. As can be seen, three stages of curing process can be observed for the tan δ curve suggests that,

this parameter and its changes with time apparently reflect the development of crosslinking reaction inside the rubber. In induction period, tan δ increased to a maximum which indicates the softening of the material and slow chemical reaction between vulcanizing agent, rubber and other compound constituents. The peak could relate to where optimum flow of the rubber compound through the mould cavity can occur giving the compound its final shape for curing. In the curing stage, tan δ was found to decrease rapidly which can again be explained by development of crosslinks between the rubber molecular chains that increase the elasticity of the material. As previously discussed, the end of this stage corresponds to the optimum vulcanization time (t_{90}). In most cases of torque versus time graphs (vulcanization curves) generated by the MDR, the final stage of vulcanization is characterized by a plateau at a maximum value [166]. A potentially equivalent plateau is well resolvable in the tan δ curve, but tan δ stabilizes at a minimum value as a function of time.

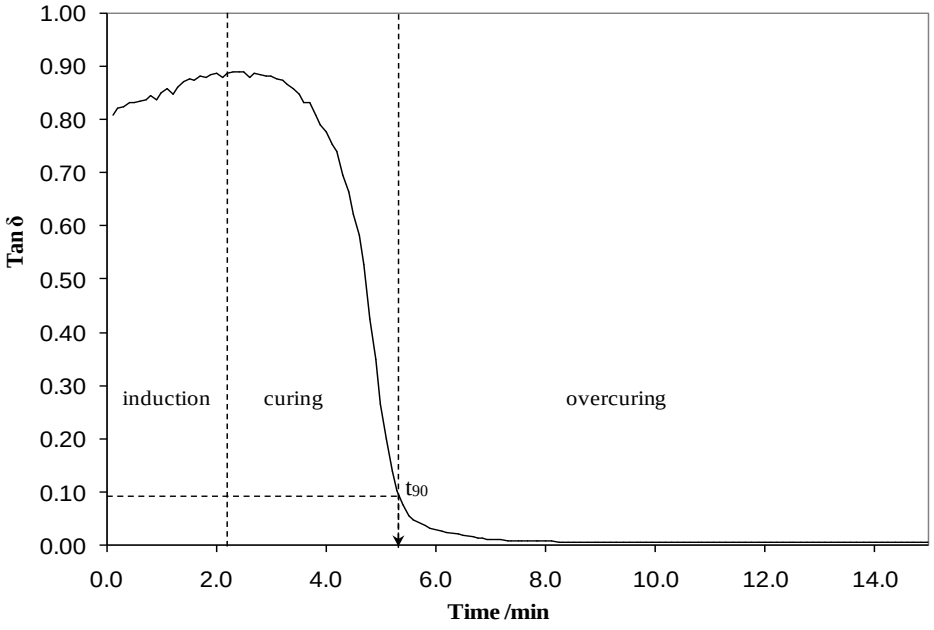

Figure 3.4 Tan δ curve as a function of time for NR compound

In a typical MDR vulcanization curve, the time to achieve the optimum network density, at a given temperature is the time required for the torque to reach 90% of the maximum achievable torque [147]. The T_{90} can be calculated as follows:

$$T_{90} = T_{min} + 0.9(T_{max}-T_{min}) \quad (3.1)$$

where T_{max} and T_{min} are the maximum and minimum torque values. The value of t_{90} can now be found from the graph of torque versus time. Considering the capability of the DMA to monitor the formation of the crosslinking network by the tan δ curve, an equivalent t_{90} could be obtained similiarly from ϕ_{90} according to Equation 3.2 :

$$\phi_{90} = \phi_{max} - 0.9(\phi_{max} - \phi_{min}) \quad (3.2)$$

where now ϕ_{max} and ϕ_{min} are the maximum and minimum tan δ values. It is assumed that t_{90} could now be obtained from tan δ versus time graphs at ϕ_{90}. From the tan δ curve of NR in Figure 3.4, the t_{90} value obtained using Equation 3.2 is 5.3 minutes. There was little difference between MDR and DMA values with percentage error of 3.9%. It should be mentioned at this point that even different types of conventional curemeters present variation of optimum curing time for the same sample [166]. Therefore, as both techniques use a shear excitation and measure a quantity that is related to the shear modulus, the similarity is reasonable.

In addition, it is possible that cure rate could also be determined from the tan δ versus time curve, as a decrease in tan δ value with time such that it could be obtained by the slope in the curing stage. However, further work would be needed to assess that. The sensitivity of the DMA is also sufficient to record the overcuring of rubber (after t_{90}).

In order to assess that DMA is reliable for assessment of t_{90}, further rubber compounds were analysed. In this step, t_{90} of 20 further rubber compounds with various filler loading and particle size as mentioned in Table 3.1 were measured using MDR and DMA. A percentage error criterion was used for comparison of these two techniques. The percentage errors for t_{90} measurements using DMA are given in Table 3.4. In view of the results obtained, the percentage errors for all compounds were lower than +/- 5 % with average percentage error of 0.58 %. The results for all compounds at different particle sizes and loading were satisfactory and reliable with acceptable proximity. This indicates that the DMA is capable to measure different types of curing behaviours which is more apparent in the compounds with fillers as discussed ealier.

Table 3.4 Percentage error of optimum cure time (t_{90}) measured by DMA

Sample	t_{90} MDR (min)	t_{90} DMA (min)	DMA (%)
1	5.10	5.30	3.92
2	4.65	4.70	1.08
3	5.19	5.10	-1.73
4	4.85	4.80	-1.03
5	5.25	5.40	2.86
6	4.71	4.50	-4.46
7	4.41	4.30	-2.49
8	4.82	4.70	-2.49
9	4.64	4.50	-3.02
10	4.51	4.60	2.00
11	4.92	4.80	-2.44
12	4.46	4.50	0.90
13	4.42	4.20	-4.98
14	4.58	4.50	-1.75
15	4.31	4.20	-2.55
16	4.47	4.50	0.67
17	4.47	4.60	2.91
18	4.70	4.90	4.26
19	4.55	4.60	1.10
20	4.54	4.60	1.32
21	4.20	4.40	4.76
Average error (%)			**0.58**

3.4 Chapter conclusion

This work was devoted to assess the capability of DMA to predict the optimum curing time (t_{90}) of rubber compounds. This was performed by investigating natural rubber compounds with a conventional sulphur crosslinking system. It is known that the oscillating disk rheometer (ODR) and moving die rheometer (MDR) are by far the most commonly used equipment to characterize the curing behaviour of rubbers. The results of isothermal curing test of the DMA indicate that several parameters such as shear storage modulus (G′), shear loss modulus (G″) and tan δ reflect the vulcanization process. However, only the tan δ curve shows a strong correlation with crosslink development. This means that the three stages of curing can be clearly observed, with the final stage of vulcanization characterised by a plateau. Contradictory to the typical MDR vulcanization curve where the torque reaches maximum, tan δ stabilizes at a minimum value and the t_{90} can be calculated as the time when tan δ reduces to 90 % of its maximum value. The measured values were generally in agreement with results obtained by a MDR with range of errors lower than +/- 5% and average percentage error of 0.58 %. Overall, the presented results show for the first time that DMA can be used to predict the optimum curing time of rubber.

Chapter 4

Dynamic Properties of Magnetorheological Elastomers Based on Iron sand and Natural rubber

4.1 Introduction

In this study, magnetorheological elastomers (MREs) based on iron sand and natural rubber were prepared. The Taguchi method was employed to investigate the effect of a number of factors, namely, iron sand content, iron sand particle size and applied magnetic field during curing on tan δ and energy dissipated during hysteresis tests. Tan δ was measured through dynamic mechanical analysis (DMA) over a range of frequency (0.01–130Hz), strain amplitude (0.1–4.5%), and temperature (-100–50 °C). Energy dissipated was measured using a universal tester under cyclic tensile loading. The data were then statistically analysed to predict the optimal combination of factors and finally experiments were conducted for verification. The morphological characteristics of the MREs were also examined using scanning electron microscopy (SEM). In the next section the Taguchi method is briefly reviewed. Then, the experimental methods used to fabricate the MREs, the factors investigated and the characterisation methods are described. This is followed by a presentation of the results and discussion. Finally, the conclusions are summarised and some finding remarks made.

4.2 Experimental

4.2.1 Taguchi method

The Taguchi method, pioneered by Genichi Taguchi, provides a simple, efficient, and systematic approach to study the effects of multiple variables by identifying the performance trend for each factor and determining the combination that yields optimum conditions.

The Taguchi method generally includes the following steps: (1) identification of the factors and their levels; (2) selection of an appropriate orthogonal array (OA) and assignment of the factors and levels to the OA; (3) conducting of the experiment; (4) analysis of experimental data and determination of the optimal levels; (5) verification of the optimum design factors through experiment.

The key component in designing the experiment is the identification of factors and their levels. With the finalised factors and levels, the Taguchi method makes use of an OA for experimental design. The Taguchi method allows for 18 different standards of OAs and the details of OA selection are published in references [169, 170]. After OA selection, experiments are carried out and results can then be analysed using signal-to-noise (S/N) ratio to determine the effect of each factor and the level that maximizes the performance. The S/N ratio can be divided into three categories depending on the desired output performance: nominal (used where a target value is desired), smaller-the-better and larger-the-better, for which Equations 4.1, 4.2 and 4.3 are used respectively to determine S/N:

$$\frac{S}{N} = -10\, log \frac{\sum_{i=0}^{n} (Y_i\text{-D})^2}{n} \tag{4.1}$$

$$\frac{S}{N} = -10\, log \frac{\sum_{i=0}^{n} Y_i{}^2}{n} \tag{4.2}$$

$$\frac{S}{N} = -10\, log \frac{\sum_{i=0}^{n} \left(\frac{1}{Y_i{}^2}\right)}{n} \tag{4.3}$$

where D is the average of observed data, *n* is the number of observation, *i* is the level and Y_i is the observed data at level *i*. Another function of S/N is that it is able to determine the ranking of factors by calculating the average effect of a factor at a level. This is given by simple statistical calculation as follows [171]

$$Aj = \frac{\sum_{i=0}^{n} \left(\frac{S}{N}\right) i}{n} \tag{4.4}$$

where A_j is the average for factor j , $(S/N)_i$ represents the S/N observation of a factor at level *i*, and *n* represents the total number of observations for that factor. By plotting the average factor effect against the corresponding factor level, a main effect plot is obtained and the trend of the influence of each factor on the results is extracted. The relative effects of factors affecting the response can be calculated by analysis of variance (ANOVA). ANOVA is a powerful statistical analysis tool that can be used in the Taguchi method to determine statistically significant factors and to explore the relative contribution of each factor and level to the total variation. ANOVA provides information on sum of squares, degrees of freedom, percentage confidence level and percentage contribution. The sum of squares is a measure of the total variability of observed data. The sum of squares is defined as

$$SS = \frac{\sum_{i=0}^{n} X_j{}^2}{n} - \frac{T^2}{N} \tag{4.5}$$

where SS is the sum of squares, n is the number of observations, j is the factor, X_j is the sum of observed data at factor j, $T = \Sigma X_j$ is the sum of all data and N is the total number of data points. The degree of freedom represents the number of levels for each factor that may vary independently and equals the number of levels of each factor minus one. The percentage confidence level represents the probability of the occurrence and the reliability of the data. The percentage contribution can is given by

$$\text{Percentage contribution} = \frac{SS_j}{SS_T} \times 100\% \tag{4.6}$$

where SS_j is the sum of squares of factor j and SS_T is the total sum of squares. With S/N ratio and ANOVA analyses, the optimal combination of the factors can be predicted and finally, an experiment can be conducted to verify the optimal factors.

4.2.2 Materials

A fixed masterbatch formulation for rubber was used in this study (Table 4.1). Natural rubber (SMR L grade) and other chemicals including zinc oxide, stearic acid, n-cyclohexyl-2-benzothiazole sulfenamide (CBS), tetramethylthiuram disulphide (TMTD), paraffin oil, and naphthenic oil were all purchased from Field Rubber Limited, Auckland. Iron sand was collected from Ngarunui Beach, Raglan. The iron sand was then milled using a planetary mono mill (Pulverisette 6) produced by Fristech GmbH and subsequently sieved to obtain a wide range of particle size fractions.

Table 4.1 Masterbatch formulation

Materials	Function	phr*
Natural Rubber	raw material/matrix	100
ZnO	accelerator/activator	5
Stearic Acid	accelerator/activator	1
CBS	accelerator	2
TMTD	accelerator	1
Paraffin Oil	plasticiser	2
Naphthenic Oil	plasticiser	3
Sulphur	crosslinking agent	1.5

*parts per hundred rubber

4.2.3 Experimental Design

Selection of factors and levels

In this study, three factors were considered: iron sand content, particle size and applied magnetic field during curing. These factors were varied at five levels as shown in Table 4.2, based on the existing literature [18, 19, 24, 29, 31].

Table 4.2 Experimental control factors and their respective levels

Factors	Symbol	Unit	Level 1	Level 2	Level 3	Level 4	Level 5
Iron sand content	I	phr	0	30	50	70	100
Particle size	P	µm	0–32	32–45	45–56	56–75	75–106
Magnetic field	M	mT	0	300	500	700	1000

*phr=part per hudred rubber, *µm = micrometer,*mT=miliTesla

Selection of orthogonal array and analysis of data

Given the three factors and five levels considered in this study, an L25 orthogonal array (OA) was selected for the Taguchi method. The L25 OA is shown in Table 4.3 and consists of 25 experiments corresponding to 25 rows and three design factors assigned to the respective columns along with their levels. Analysis of the S/N ratio was subsequently used to evaluate the experimental results. In the present study, since the tan δ and amount of energy dissipated (hysteresis tests) were intended to be

maximized, the larger-the-better target for S/N ratio was chosen. Analysis of variance (ANOVA) was used to statistically assess the percentage contribution between each factor. ANOVA was performed by using STATISTICA software. In addition, it is possible to study the interaction effects of the factors and their levels by using ANOVA, however, the use of L25 OA does not allows for the determination of interactions and further work would be needed to assess that.

Table 4.3 Experimental layout of an L25 orthogonal array according to the Taguchi method

Sample type	Factors and their levels		
	I	**P**	**M**
1	1	1	1
2	1	2	2
3	1	3	3
4	1	4	4
5	1	5	5
6	2	1	2
7	2	2	3
8	2	3	4
9	2	4	5
10	2	5	1
11	3	1	3
12	3	2	4
13	3	3	5
14	3	4	1
15	3	5	2
16	4	1	4
17	4	2	5
18	4	3	1
19	4	4	2
20	4	5	3
21	5	1	5
22	5	2	1
23	5	3	2
24	5	4	3
25	5	5	4

4.2.4 Preparation of isotropic and anisotropic MREs

Formulations were determined according to the OA and were compounded using a conventional laboratory two roll mill (model XK150) according to ASTM designation D3184-80. The front roller speed was 24 rpm and the rear roller speed was 33 rpm, the roller diameters were 150 mm, friction ratio of two rollers was 1:1.4 and the roller temperature was set to 80^{o}C. The nip gap (distance between front and back roller) was maintained at 2 mm during compounding. The compounding began with softening the rubber on its own in the two roll mill (mastication). Mastication reduces the viscosity and increase the plasticity of natural rubber which is brought about by heat generated in two roll mill through conduction from the heated roller and shearing of rubber during milling. After 2-3 minutes the rubber became invested on the hot roll and additives (other than accelerators and sulphur) were then added followed by iron sand; addition of accelerators and sulphur were delayed to the last part of the process to prevent premature vulcanization during compounding. The mixing time was approximately 40 minutes. The cure time at 150°C was then determined according to the procedure as described in Chapter 3 and the results are attached in the Appendix I. Compounded rubber samples weighing 13g were placed in a mould 60 x 50 x 3 mm. The isotropic MREs were cured in a compression moulder at 150°C under a pressure of approximately 12 MPa. The anisotropic MREs were subjected to an external magnetic field in a specially developed electromagnetic-thermal coupled device (as shown in Figure 4.1) at 80°C for 30 minutes and subsequently were cured in a compression moulder at 150°C under a pressure of approximately 12 MPa. Finally, post-cure treatment was performed by cooling the anisotropic MREs at room temperature for 30 minutes under an external

magnetic field of the same strength as that used during pre-curing. The post-cure treatment was considered necessary to reorientate the magnetic dipoles after compression moulding.

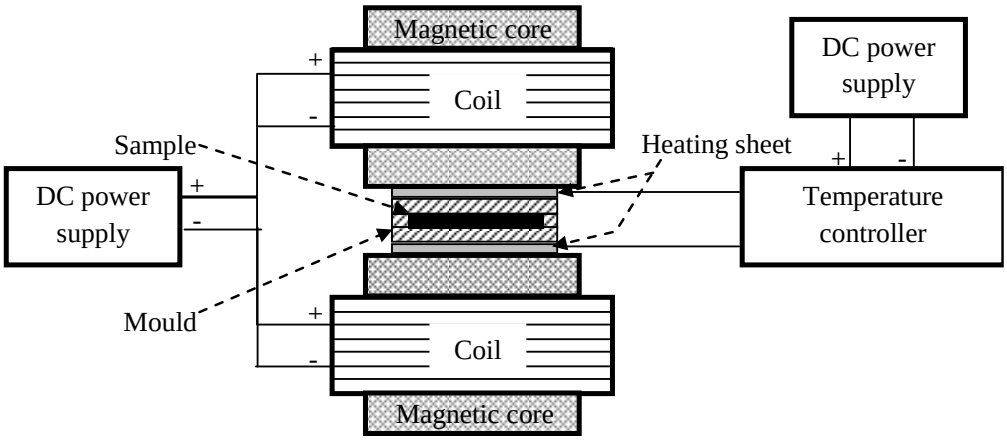

Figure 4.1 Sketch of specially developed electromagnetic-heat coupled device.

4.2.5 Characterisation

Dynamic mechanical analysis

Dynamic mechanical analysis was carried out using a Perkin Elmer Dynamic Mechanical Analyser (DMA 8000). Tan δ was measured over a wide range of frequency, strain amplitude and temperature. The influence of frequency and strain amplitude on tan δ was assessed using two circular disc specimens with a diameter of 10 mm and a thickness of 3 mm in shear mode at room temperature. Tan δ was measured over the frequency range of 0.01–130 Hz at a fixed strain amplitude of 0.5% and over a strain amplitude range of 0.1–4.5% at a fixed frequency of 100Hz. For the influence of temperature on tan δ, the samples were analysed in dual cantilever mode at a frequency of 1 Hz, with a strain amplitude of 0.5% and over a temperature range from -100 – 50 °C. The samples were rectangular with dimensions 30 mm ×6 mm ×3 mm.

Hysteresis

Hysteresis loss is defined as the amount of energy dissipated during cyclic deformation when the samples are stretched and then allowed to retract at the same rate to the unstretched state. In this study, the hysteresis loss was determined on tensile dumbbells using an Instron 4204 at a crosshead speed of 500 mm/min according to ASTM D412-80. The stress-strain curve was recorded and hysteresis loss was calculated as

Hysteresis loss = Area under the loading curve - Area under the recovery curve (4.7)

Morphology

The microstructures of isotropic and anisotropic MREs were observed using a Hitachi S-4700 scanning electron microscope (SEM). The samples were cut into pieces with a surface area of 5 mm × 3 mm and coated with a thin layer of platinum prior to observation at an accelerating voltage of 20 kV.

4.3 Results and discussion

Typical trends obtained in this work for the influence of frequency [29, 99, 110], strain amplitude [31, 172] and temperature [173, 174] on tan δ as well as the hysteresis loop obtained after a complete reversed stress cycle [175, 176] are shown in Figure 4.2. In order to calculate the optimum levels for the different factors using S/N ratio and ANOVA, reference points for tan δ were selected. For optimising tan δ over a range of frequency of 0.01-130 Hz, the maximum value of tan δ was taken as the reference point, which was consistently observed at 130 Hz (the maximum frequency applied). For optimising tan δ over a range of strain amplitude (0.1–4.5%), the reference point was chosen to be within the plateau region at 3% strain amplitude.

With respect to choosing a reference point over a range of temperature, attention was given to the peak of the curve of tan δ versus temperature which represents the glass transition temperature (T_g) where the material undergoes drastic changes in the mechanical energy of the molecular vibrational motion (see Figure 4.2 (c)). Addition of particulate fillers into rubber is generally not expected to change the temperature at which tan δ reaches a peak. What is commonly apparent, however, is broadening of the transition region after T_g to the plateau region [173, 177]. In this study, T_g of natural rubber is -47 °C and the transition region after T_g to the plateau region was observed at -47– 0 °C. To reflect the broadening of the peak, a reference point for tan δ was selected at -35 °C. In hysteresis testing, the amount of energy dissipated was calculated from the area of the hysteresis loop (see Figure 4.2 (d)). Table 4.4 shows the values of tan δ and hysteresis loss obtained for these reference points that were subsequently used to calculate S/N ratios and ANOVA, each value representing an average from 3 samples. The highest values for each test type are shown in bold.

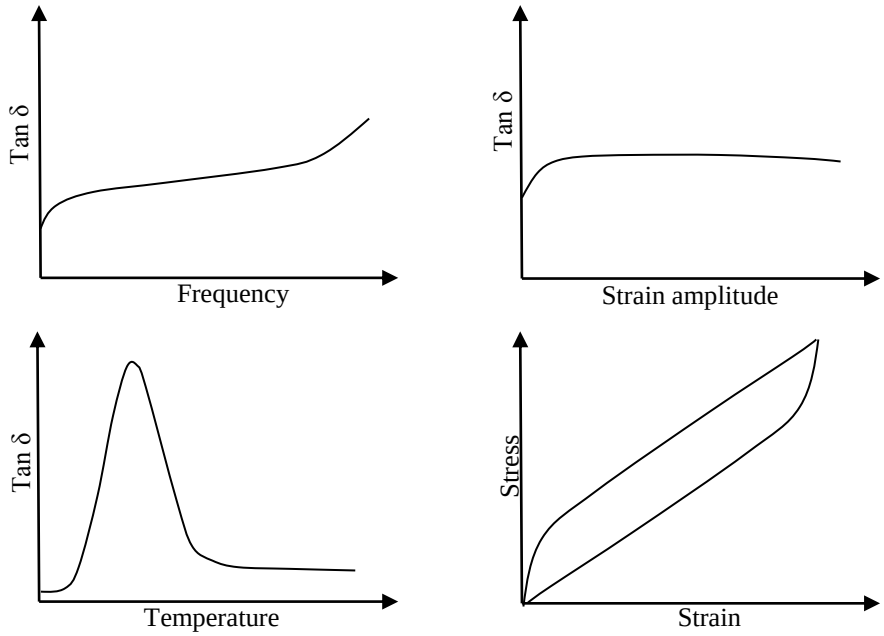

Figure 4.2 Typical trends for influence of (a) frequency, (b) strain amplitude, (c) temperature on tan δ and (d) typical hysteresis for a complete reversible stress cycle.

Table 4.4 Tan δ and hysteresis loss used to calculate S/N ratios and ANOVA, highest value shown in bold

Sample type	Maximum tan δ over 0.01-130 Hz (130 Hz) *[a]	Tan δ at plateau over 0.1–4.5% strain amplitude (3%)*[b]	Tan δ in transition region of -47– 0 °C (-35 °C) *[c]	Hysteresis loss (kJ/m^3)
1	0.093	0.098	0.758	31.59
2	0.093	0.098	0.749	31.96
3	0.097	0.099	0.720	31.71
4	0.096	0.098	0.758	31.72
5	0.095	0.098	0.744	32.44
6	0.111	0.103	1.082	39.04
7	0.078	0.129	0.870	52.46
8	0.131	0.112	0.946	69.98
9	0.095	0.137	1.142	55.11
10	0.112	0.113	0.958	49.46
11	0.118	0.099	0.881	45.55
12	0.114	0.107	1.025	94.15
13	0.125	0.110	1.128	110.92
14	0.103	0.090	0.676	96.41
15	**0.171**	**0.155**	0.670	57.10
16	0.133	0.104	0.913	57.58
17	0.112	0.098	**1.216**	119.48
18	0.158	0.118	0.843	95.26
19	0.161	0.134	0.952	70.09
20	0.169	0.130	0.842	75.51
21	0.114	0.095	1.061	100.05
22	0.113	0.098	0.920	99.29
23	0.103	0.090	0.851	**154.61**
24	0.151	0.148	0.851	104.10
25	0.078	0.071	0.946	133.34

*[a] Strain amplitude = 0.5%

*[b] Frequency = 100 Hz

*[c] Strain amplitude = 0.5% and frequency = 1 Hz

4.3.1 Morphology

Figure 4.3 shows SEM images of the isotopic and anisotropic MREs. From the SEM micrographs, it can be seen that isotropic MREs have a homogeneous iron sand particle distribution in the rubber matrix without obvious aggregation (Figure 4.3 a). Figure 4.3 b-e show anisotropic MREs cured at different magnetic field. Clearly, as expected, applying a magnetic field at elevated temperature allowed the iron sand particles to organise into chain-like columnar structures. It can also be noted that the chains became longer and more aligned as the magnetic field strength increased. A higher magnification micrograph (Figure 4.3 f) highlights that there are obvious gaps between iron sand particle and rubber, which suggests weak interaction between iron sand and rubber.

4.3.2 Effect of frequency on tan δ

The trends for influence of frequency on tan δ when the factors were varied over their different levels are shown on the main effect plots in Figure 4.4. As discussed earlier, the higher the value of the S/N ratio, the better the signal, which implied that the highest value in the main effect plots can be used to attain optimised tan δ for variable frequency loading. The S/N ratio increases with increasing iron sand content until it reaches a maximum value at 70 phr and thereafter decreases at the highest iron sand content (100 phr). The increase of S/N ratio with increasing iron sand content can be explained by the increase in energy absorbed due to interfacial friction caused by the increase in interfacial area with increase in iron sand content. The decrease in S/N ratio at the highest iron sand content can be explained by poor dispersion of iron sand particles due to the insufficient amounts of rubber matrix to

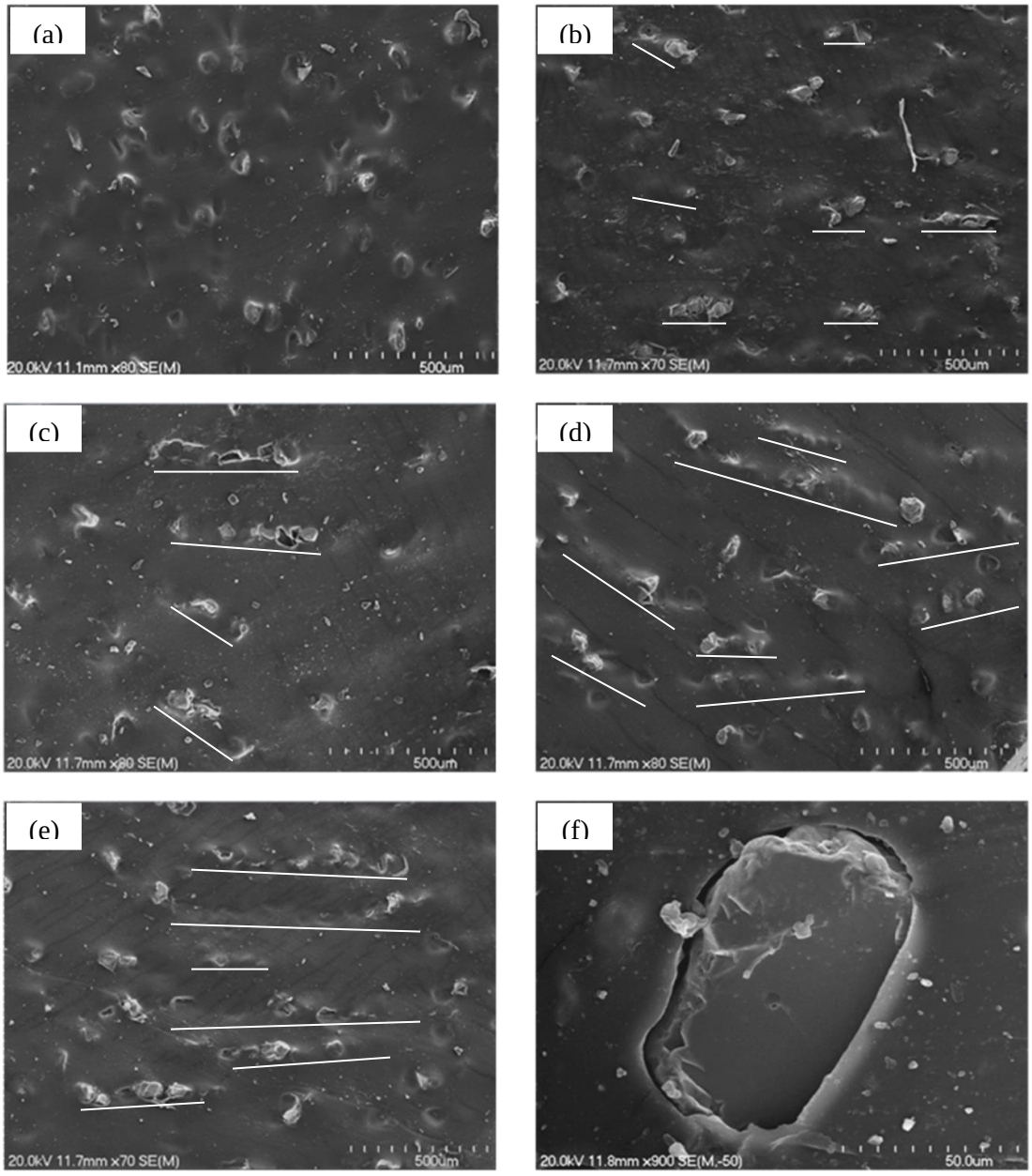

Figure 4.3 SEM images of iron sand-natural rubber MREs: (a) isotropic MRE – 0 mT; (b) anisotropic MRE – 300 mT; (c) anisotropic MRE – 500 mT; (d) anisotropic MRE – 700 mT; (e) anisotropic MRE – 1000mT; and (f) interphase of iron sand-natural rubber matrix.

wet the iron sand thoroughly. Similar findings have been observed in other studies [30, 97]. From Figures 4.4 (b) and (c), it can be seen that the particle size and magnetic field had a minimal influences on S/N ratio but the S/N ratios at 45-56μm and 300 mT are the highest. The minimal influence of magnetic field on S/N ratios would appear to be due to minimal increase of particle separation as the test was performed at a low fixed strain amplitude (0.5%) in shear mode such that particle chains would generally rotate rather than extend. The results suggest that the highest value for tan δ might be obtained by using 70 phr iron sand, a 45–56 μm particle size and a 300 mT magnetic field during curing.

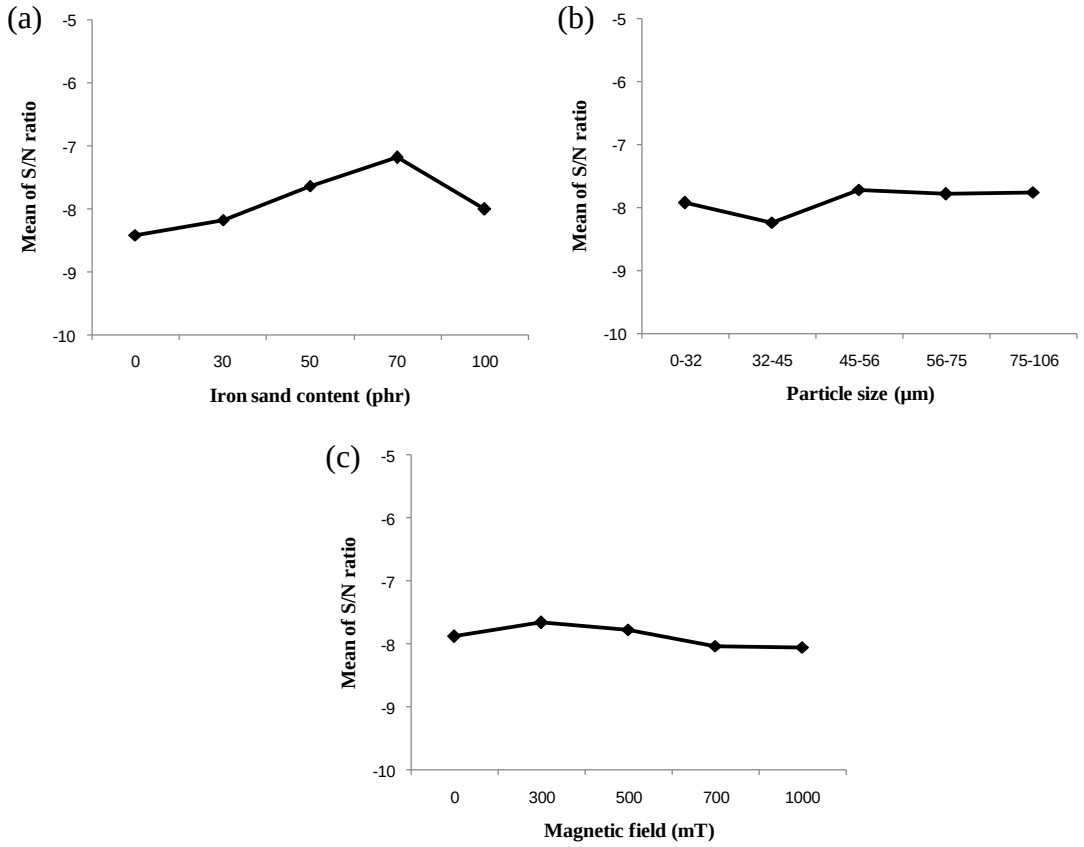

Figure 4.4 Main effect plots for S/N ratio of tan δ at 130Hz (a) effect of iron sand content, (b) effect of iron sand particle size and (c) effect of magnetic field during curing.

Table 4.5 shows ANOVA results for the effect of frequency on tan δ. It can be seen from the level of contribution that iron sand content has the greatest influence on tan δ with a 99.9% confidence level. The particle size and magnetic field show much less influence (lower % contribution) with confidence levels of 99% and 97%, respectively.

Table 4.5 ANOVA results for the effect of frequency on tan δ

Factor	Sum of squares	Degrees of freedom	% confidence level	% contribution
Iron sand content (phr)	0.024	4	99.9	72.73
Particle size (μm)	0.005	4	99	15.15
Magnetic field (mT)	0.004	4	97	12.12

The final and essential step to complete the Taguchi analysis, namely conducting an experiment to verify the suggested optimum conditions, was carried out using optimised conditions (70 phr iron sand, 45-56 μm particle size and 300 mT) and the value of tan δ found (0.22) was indeed higher than the highest value achieved previously (0.171 for sample type 15). This supports the optimum conditions suggested by S/N ratio and ANOVA. The variation of tan δ with frequency is shown in Figure 4.5a. Tan δ is higher for the optimised sample over the whole frequency range explored. G′ and G″ are also plotted in Figure 4.5 (b and c) to help highlight the mechanisms involved. G′ and G″, similar to tan δ are frequency dependent and it can be seen that the increase of tan δ as the frequency increases is mainly due to increasing in G″ as opposed to G′. The increase in G″ can again be explained by the increased energy loss due to the increase of interfacial friction between the iron sand and rubber with increasing frequency.

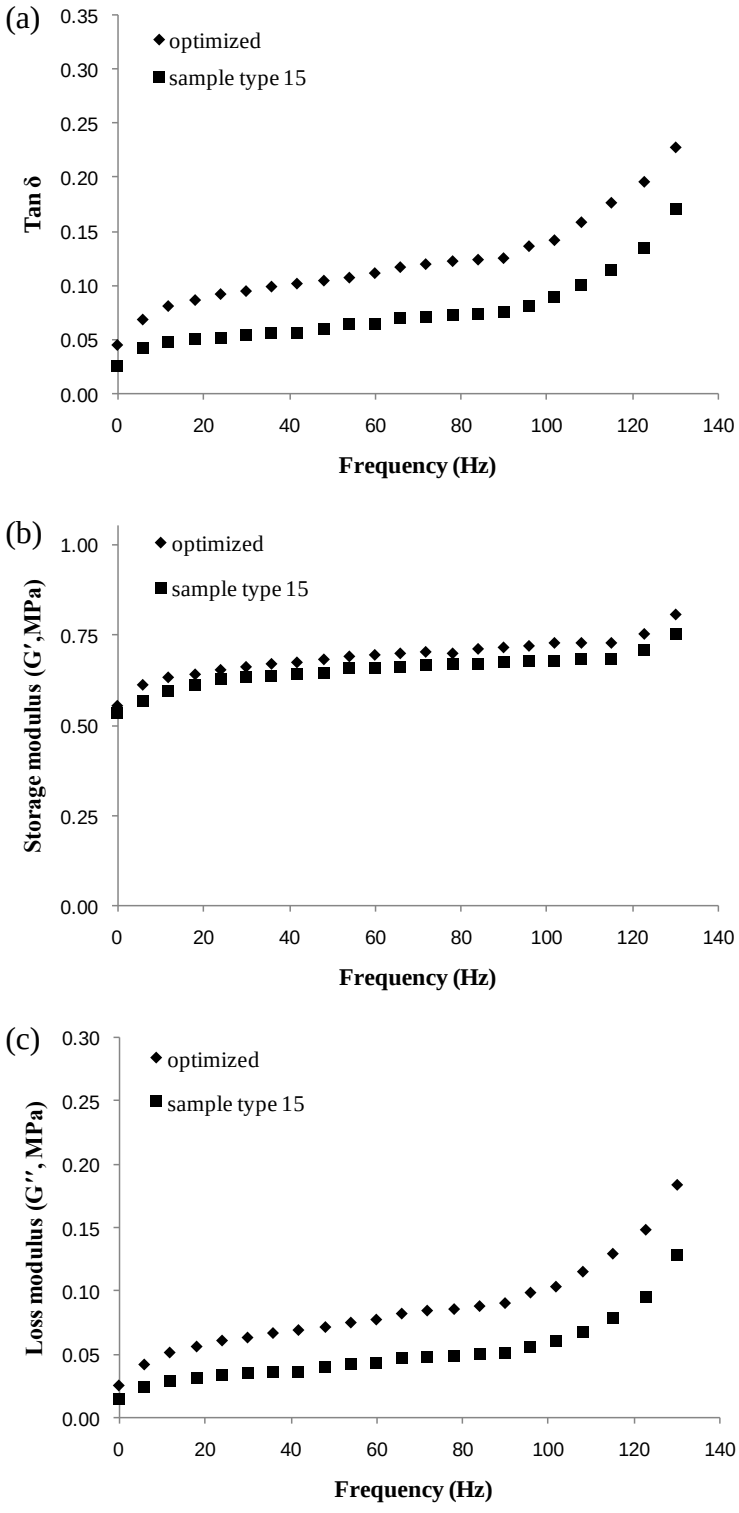

Figure 4.5 (a) Tan δ, (b) storage modulus (G′) and (c) loss modulus (G″) versus frequency for the optimised sample and sample type 15.

4.3.3 Effect of strain amplitude on tan δ

Figure 4.6 shows the main effect plots of the S/N ratios for the influence of strain amplitude on tan δ. The highest S/N ratios are observed at 30 phr iron sand content, 56-75 μm particle size and 500 mT magnetic field during curing. However, no obvious trend of the S/N ratios is seen for any factor as the level changes. This could be attributed to the poor bonding between iron sand and rubber as supported by morphology. This is in agreement with the results reported by other researchers [97]. The weak interaction between the iron sand and natural rubber is fully disrupted at low strain amplitude and therefore, at high strain amplitude, the damping is dominated by the viscous flow of the rubber matrix and friction between rubber chains and iron sand. For the selected reference point (3% strain amplitude) here, it should also be noted that the suggested optimum conditions for variable strain amplitude loading are different compared with the optimum conditions for the effect of frequency on tan δ (70 phr, 45-56 μm, 300 mT). A lower optimum iron sand content (30 phr) here supports that at the reference point for this experiment on effect of strain amplitude on tan δ, energy absorbed is more dominated by the viscous flow in rubber matrix. However, the suggested optimum magnetic field is higher, which indicates that formation of longer particle chains opposed the higher shearing force with increasing strain amplitudes such that the particle chain orientation changes and transforms elastic energy into magnetic energy, which then dissipates by magnetic hysteresis [21, 178]; the increased energy could also be absorbed through the magnetomechanical effect (change of magnetic domain structure induced by application of stress).

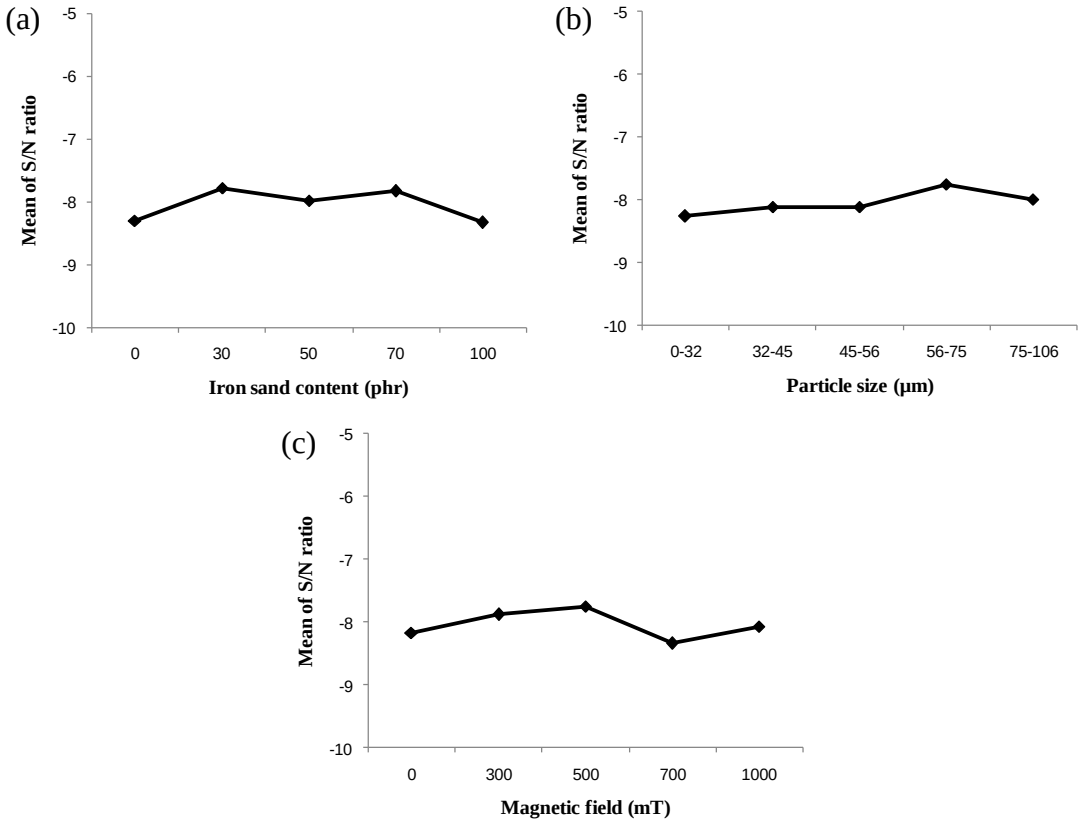

Figure 4.6 Main effect plots for S/N ratio of tan δ at 3% strain amplitude (a) effect of iron sand content, (b) effect of iron sand particle size and (c) effect of magnetic field during curing.

Table 4.6 shows ANOVA results for the effect of strain amplitude on tan δ. Also seen that the variability for each factor was tested at 99.9% confidence level. None of the factors have a significant influence on tan δ and hence the percentage contribution is approximately the same for each factor.

Table 4.6 ANOVA results for the effect of tan δ on strain amplitude

Factor	Sum of squares	Degrees of freedom	% confidence level	% contribution
Iron sand content (phr)	0.005	4	99.9	35.71
Particle size (μm)	0.004	4	99.9	28.57
Magnetic field (mT)	0.005	4	99.9	35.71

As expected, an experiment using optimised conditions (30 phr iron sand content, 56-75 μm particle size and 500 mT) results in slightly higher value of tan δ (0.160) compared with the highest achieved previously (0.155 for sample type 15). Figure 4.7 shows tan δ, the storage modulus (G′) and the loss modulus (G″) of the optimised sample and sample type 15 over a range of strain amplitude (0.1–4.5%). It was found that tan δ and G′ were amplitude dependent at low strain amplitudes reaching a plateau at about 1% strain amplitude. The amplitude dependence at low strain is typically attributed to the Payne effect [179]. This effect is frequently explained by the breakdown of filler aggregates to release trapped rubber to allow more viscous flow, separation of dipole-dipole interaction between neighbouring particle and filler rubber detachment and reformation that increases with increasing strain amplitude. Once the strain amplitude is high enough, all the interactions are destroyed to such an extent that it cannot be reconstructed and the Payne effect diminishes. Consequently, the energy loss is largely reliant on the rubber matrix and friction of rubber chains and iron sand.

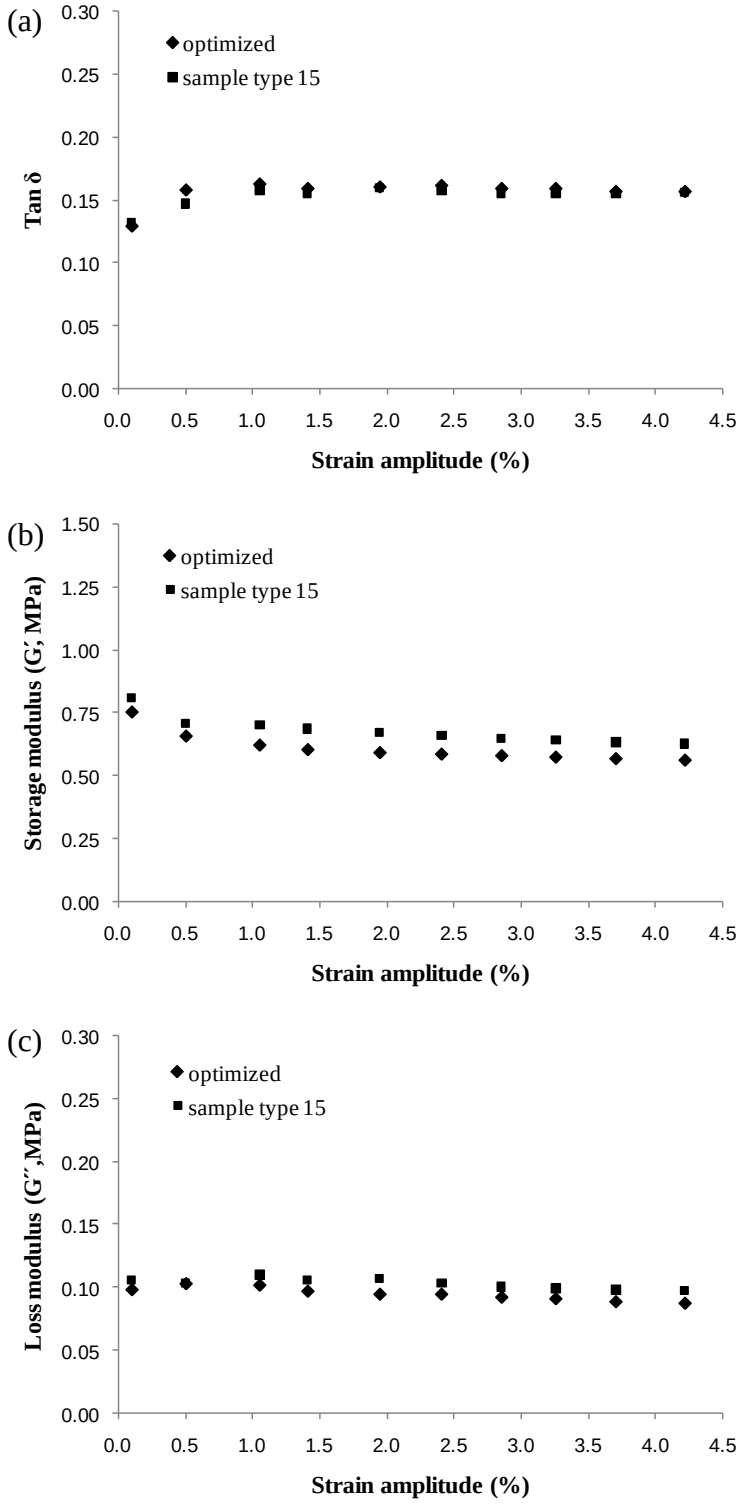

Figure 4.7 (a) Tan δ, (b) storage modulus (G′) and (c) loss modulus (G″) versus strain amplitude for the optimised sample and sample type 15.

4.3.4 Effect of temperature on tan δ

The main effect plots of the S/N ratios for influence of temperature on tan δ are depicted in Figure 4.8. The Taguchi method suggests that the optimised tan δ for variable temperatures loading could be obtained by using 30 phr of iron sand content, a 32-45 μm of particle size and a 1000 mT magnetic field during curing. As can be seen from Figure 4.8 (a), S/N ratios of the filled compounds are higher compared to those of the unfilled compound. Addition of iron sand has constrained rubber chains and therefore increased the temperature required for their mobility, thus increasing relaxation at the reference temperature [177]. From Figure 4.8 (b), it can be seen that the S/N ratios decrease with increasing particle size, which is likely to be due to the decrease of surface area of iron sand adhered to rubber. In Figure 4.8 (c), the S/N ratio increases with increasing magnetic field until it reaches a maximum at 1000 mT. This indicates that the formation of magnetic particle chains and columnar structures provides additional damping by further restriction of the intermolecular conformational changes during relaxation, as supported by morphology. As can also be noted, the suggested optimum conditions are different compared with those observed previously for the effect of frequency and strain amplitude on tan δ. As this test was performed in dual cantilever mode at a fixed low frequency (1Hz) and strain amplitude (0.5%) over the temperature range, the deformation of material would be much lower compared with that tested in shear loading. Therefore, at selected reference point used for this experiment, the additional damping through interfacial friction and magnetic interactions (inter-particle interaction and magnetomechanical damping) would be expected to be much lower. A lower optimum iron sand content (30 phr) supports that the damping is largely reliant on the intermolecular relaxation

of the rubber matrix. However, the suggested optimum magnetic field at 1000 mT suggests that the energy absorbed by formation of longer particles chains would not be due to separation of dipole-dipole interaction or magnetomechanical damping, perhaps the longer particle chains provide additional damping by further restriction of the intermolecular conformational changes during relaxation.

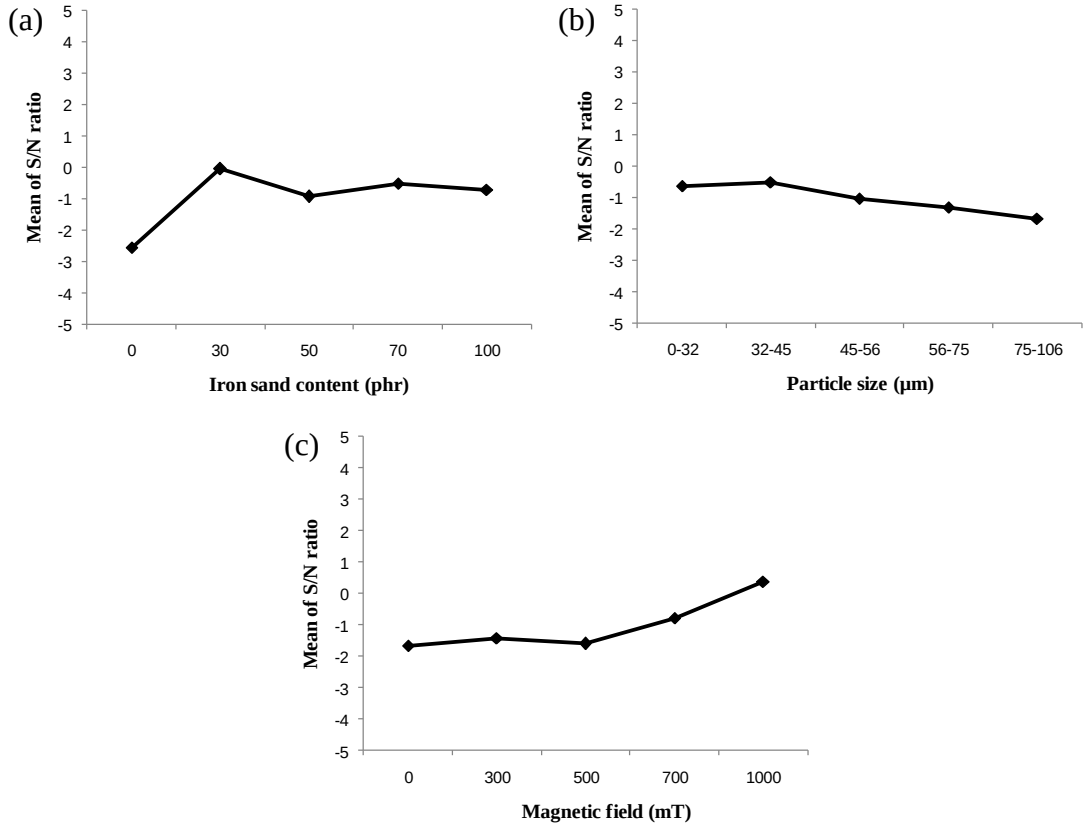

Figure 4.8 Main effect plots for S/N ratio of tan δ at -35 °C (a) effect of iron sand content, (b) effect of iron sand particle size and (c) effect of magnetic field during curing.

Table 4.7 shows ANOVA results for the effect of temperature on tan δ. Iron sand content and magnetic field both show a significant influence on tan δ with

confidence levels of 99%. It is also apparent that the particle size has much less influence with less than 10% contribution.

Table 4.7 ANOVA results for effect of temperature on tan δ

Factor	Sum of squares	Degrees of freedom	% confidence level	% contribution
Iron sand content (phr)	0.185	4	99	48.15
Particle size (μm)	0.035	4	70	9.22
Magnetic field (mT)	0.164	4	99	42.62

Finally, an experiment was carried out to compare the value of tan δ for the optimised sample (30 phr of iron sand content, 32-45 μm particle size and 1000 mT) with those achieved previously for the sample with the highest value of tan δ in the transition zone (sample type 17). In addition, unfilled natural rubber was included for comparison (see Figure 4.9). The values of tan δ for the optimised sample, sample type 17 and unfilled natural rubber are 1.280, 1.216 and 0.803, respectively. As can also be seen, the tan δ peak of natural rubber is higher compared to the optimised sample and sample type 17. It should be noted, however, that the width of the tan δ peaks for the optimised sample and sample type 17 are wider and tan δ for the optimised sample at -35ºC is the highest. This can again be explained as being due to confinement of molecular chain movement. Since rubber materials are always in practice used in the rubbery phase, the performance and behaviour of the materials in the temperature range after the transition region is more crucial. In the rubbery phase (occurring in the plateau after the peak), it can also be seen that the optimised sample has the largest value of tan δ, followed by sample type 17 and unfilled natural rubber.

This is because at higher temperature the thermal energy is comparable to the potential energy barriers for the viscous flow, therefore, interfacial friction, breakdown and reformation of the filler-filler interaction and filler-rubber detachment would be the main causes of damping.

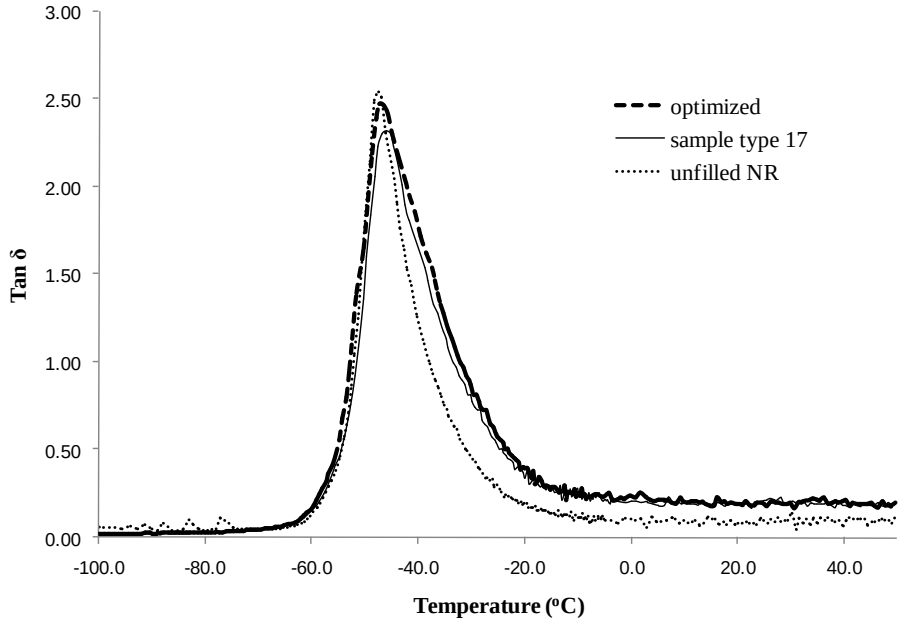

Figure 4.9 Tan δ versus temperature for natural rubber, the optimised sample and sample 17.

4.3.5 Hysteresis

The main effect plots of the S/N ratios for hysteresis loss are presented in Figure 4.10. The relationship between iron sand content and the S/N ratio is approximately linear, with the amount of energy dissipated increasing with iron sand content up to 100 phr. The increase in energy dissipated could be attributed to interfacial friction, breakdown of filler aggregates to release trapped rubber to allow more viscous flow and filler rubber detachment and reformation. From Figure 4.10

(b) and (c), it can be seen that the particle size and magnetic field have minimal influence on hysteresis loss but the S/N ratios at 45-56 μm and 1000 mT are the highest. It is also noted that the suggested optimum conditions to obtain highest hysteresis loss are similar to those for the optimum conditions when assessing influence of frequency on tan δ; the Taguchi method suggests that highest hysteresis loss and tan δ could be obtained by using high iron sand content (100 phr and 70 phr, respectively) with particle size not being greatly influential (although 45-56 μm gave the highest for both hysteresis and tan δ). However, the suggested magnetic field during curing gives a contrary conclusion (1000 mT and 300 mT, respectively for hysteresis and tan δ) which could be due to the different mode of loading during testing (tensile versus shear). This suggests that energy absorption due to interaction between magnetic particles alignment is less efficient in a tensile mode compare with a shear mode using the DMA, which is not surprising, given that in tension, it is largely only the spacing increasing between chains, whereas in shear, the spacing within chain between the particles increases (see Figure 4.11).

Table 4.8 shows ANOVA results for hysteresis loss. Confidence levels for all factors are 98% and higher. From the levels of contribution, it can be seen that the most influential factor by far is iron sand content followed by particle size (80.71% and 14.38%, respectively). The influence of magnetic field was much less at 4.91%.

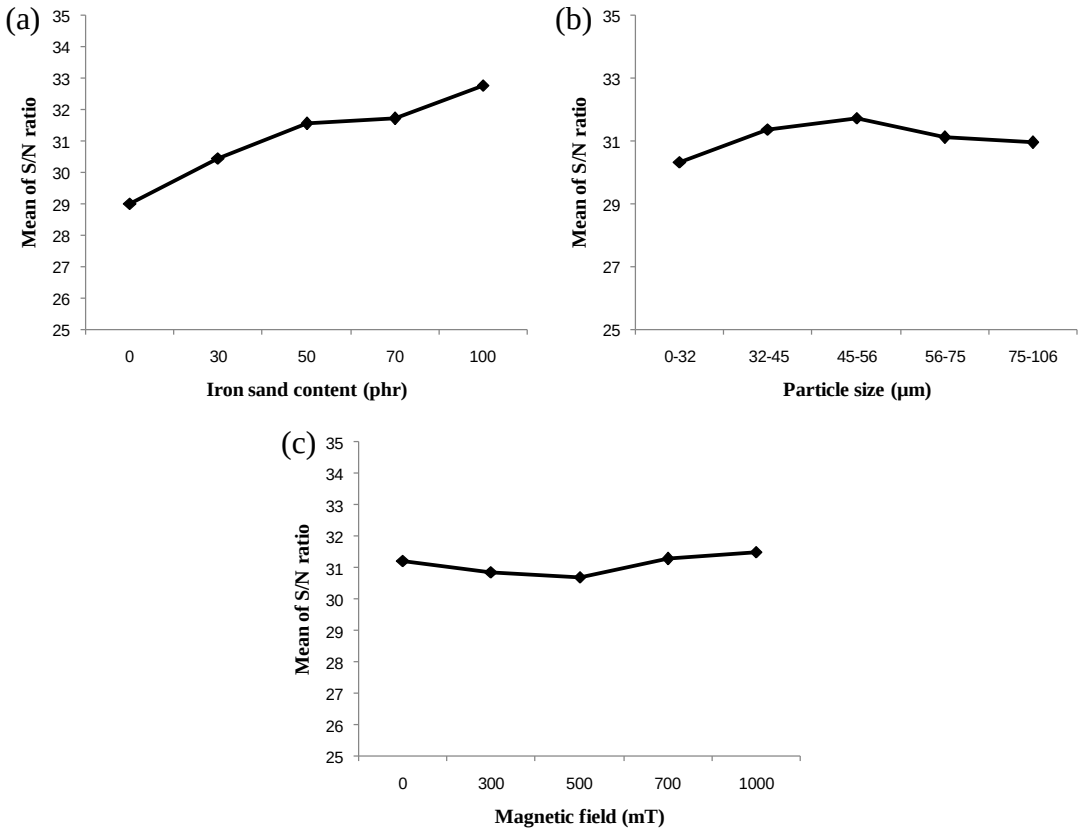

Figure 4.10 Main effect plots for S/N ratio of hysteresis loss (a) effect of iron sand content, (b) effect of iron sand particle size and (c) effect of magnetic field during curing.

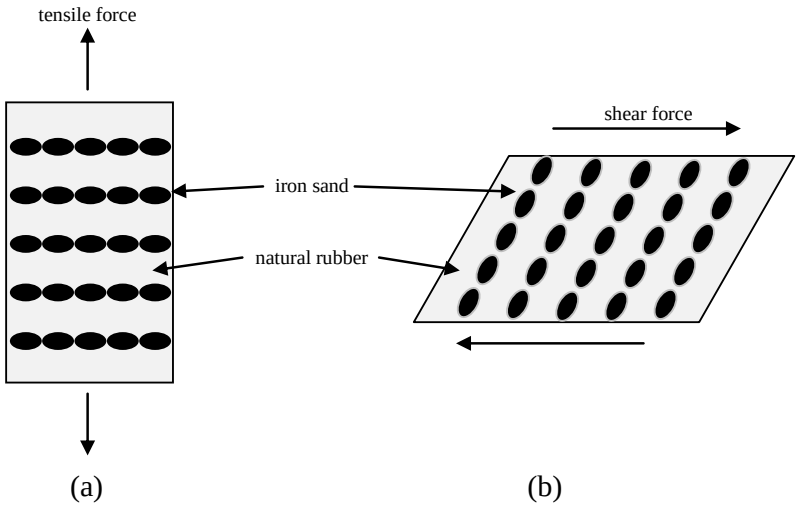

Figure 4.11 Comparison of influence of loading types on particle separation, (a) tensile mode and (b) shear mode.

Table 4.8 ANOVA results for hysteresis loss

Factor	Sum of squares	Degrees of freedom	% confidence level	% contribution
Iron sand content (phr)	43038.6	4	99.9	80.71
Particle size (μm)	7669.1	4	99.9	14.38
Magnetic field (mT)	2616.7	4	98	4.91

Figure 4.12 shows stress-strain loops of the sample at the suggested optimum conditions (100 phr iron sand, 45-56 μm particle size and 1000 mT) and those for the highest hysteresis loss achieved previously (sample type 23) after a complete reversed stress cycle. As can be seen, the area of the hysteresis loop for the optimised sample is larger than sample type 23. The amount of energy loss for the optimised sample and sample type 23 are 160.96 kJ/m^3 and 154.61 kJ/m^3, respectively. This supports the optimum conditions suggested by the S/N ratio and ANOVA. As the strain increases, the curvilinear part at the beginning of stretching is attributed to interfacial friction, breakdown of filler aggregates and filler rubber detachment and reformation and as the strain increases, the amount of energy dissipated increases, which is believed to be mainly dominated by the viscous flow in the rubber phase as reported in the literature [176]. As the strain increases, the cross sectional area of the tested samples reduces and the rubber molecular chains come closer to each other. Under further strain, the chains constrain each other, therefore they slide with respect to each other, resulting in further increased of dissipated energy. Upon removing the load, the rubber molecular chains do not completely regain their original configuration and the energy dissipated would be expected to have been converted into heat [176, 180].

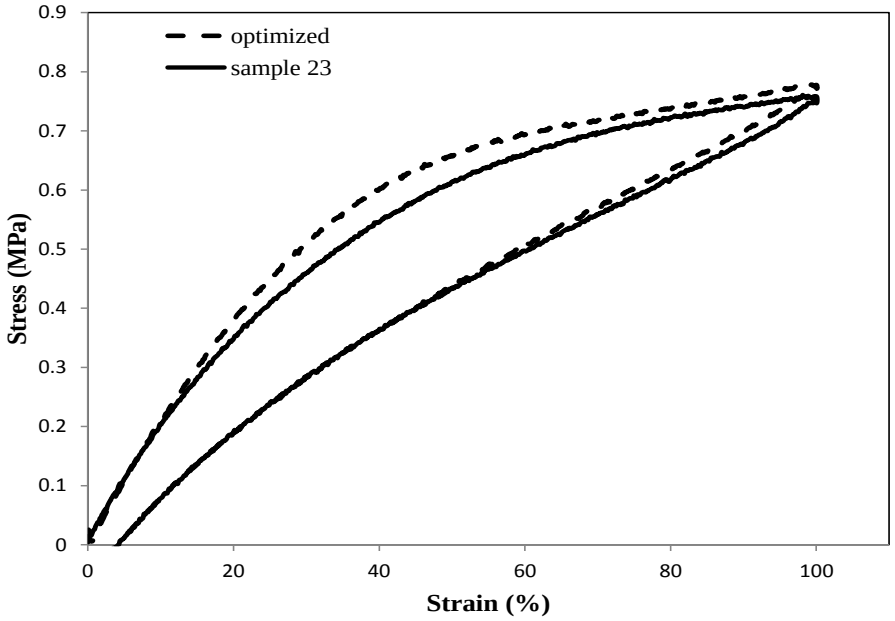

Figure 4.12 Hysteresis loops of optimised sample and sample 23.

4.4 Chapter conclusion

In this work, iron sand and natural rubber MREs were manufactured and experiments were designed using the Taguchi method in order to assess the effect of iron sand content, iron sand particle size, and applied magnetic field during curing on the tan δ (over a wide range of frequency, strain amplitude and temperature) and energy dissipated during cyclic loading. SEM micrographs revealed that isotropic MREs had homogeneous iron sand particle distribution and curing the materials under an applied magnetic field at elevated temperature resulted in the iron sand particles organising into chain-like columnar structures. For the effect of frequency on tan δ, the Taguchi method suggested that the optimum conditions can be obtained by using 70 phr iron sand, a 45–56 μm particle size and a 300 mT magnetic field which was supported by experiment. It was found that iron sand had the greatest influence on tan δ followed by particle size and magnetic field. The suggested

optimum conditions to obtain highest hysteresis loss were similar to that for the optimum conditions when assessing influence of frequency on tan δ; the Taguchi method suggests that highest hysteresis loss could be obtained by using 100 phr iron sand (slightly different to the 70 phr iron sand for frequency) with particle size not being greatly influential (although 45-56 μm gave the highest for both hysteresis and tan δ). However, the optimum magnetic field during curing is different for maximizing tan δ and hysteresis loss (300 mT and 1000 mT, respectively) which could be due to the different mode of loading during testing (tensile versus shear). For the effect of strain amplitude on tan δ, none of the factors showed significant influence on tan δ for the plateau region from 1.0-4.5% strain amplitude, which could be attributed to the poor bonding between iron sand and rubber such that the weak interaction between the iron sand and natural rubber is fully disrupted at low strain amplitude and therefore, at high strain amplitude, the damping is dominated by the viscous flow of the rubber matrix and friction of rubber chains and iron sand. For the effect of temperature on tan δ, the optimum conditions suggested by the Taguchi method are 30 phr iron sand, a 32–45 μm particle size and a 1000 mT. It was found that addition of iron sand and formation of magnetic particle chains constrained conformational changes of rubber molecular chains from taking part in relaxation process and therefore, increased the temperature at which the molecular chains start to mobilize, such that the width of the peak of tan δ is increased. The different optimum conditions for different tests carried out herein would appear to be due to the relatively different amounts of energy absorbed by different degree that different mechanisms are involved with different loading conditions and at different frequencies and strain amplitudes.

Chapter 5

The Effect of Silane Coupling Agent on Iron Sand for Use in Magnetorheological Elastomers Part 1: Surface Chemical Modification and Characterisation

5.1 Introduction

Bis-(3-triethoxysilylpropyl) tetrasulphane (TESPT) was employed for surface modification of iron sand for use in MREs. The amount of TESPT was varied at five levels (2, 4, 6, 8 and 10 wt%) relative to iron sand content to assess the optimum amount of coupling agent for interfacial bonding and damping performance. Evidence that coupling had occurred between iron sand and TESPT was identified by Raman Spectroscopy and the grafting percentage was determined by thermogravimetric analysis. Subsequently, isotropic MREs containing unmodified and modified iron sand particles and natural rubber were prepared. Formation of crosslinks between tetrasulphane group of TESPT with the rubber chains was identified by crosslink density assessment by swelling testing. The effects of the amount of TESPT on dynamic mechanical properties the morphological characteristics of the MREs were also investigated.

5.2 Experimental

5.2.1 Materials

Natural rubber (SMR L grade) and other chemicals including zinc oxide, stearic acid, n-cyclohexyl-2-benzothiazole sulfenamide (CBS), tetramethylthiuram disulphide (TMTD), paraffin oil, and naphthenic oil were all purchased from Field Rubber Limited, Auckland. Bis-(3-triethoxysilylpropyl) tetrasulphane (TESPT) was purchased from Leap Lab Chem Co. Limited, China. Iron sand was collected from Ngarunui Beach, Raglan. The iron sand was milled using a planetary mono mill (Pulverisette 6) produced by Fristech GmbH and subsequently sieved to obtain a 45-56 μm particle size range.

5.2.2 Surface modification of iron sand

The surface modification of iron sand was carried out by an aqueous alcohol solution method. The iron sand particles were subjected to surface treatment with TESPT at 2, 4, 6, 8, 10% by weight (wt%) of the particles. An aqueous alcohol solution of 95% ethanol was used and the pH of the solution was adjusted with acetic acid to 4.0 – 4.5. The TESPT of predetermined quantity was dispersed in the ethanol solution at a ratio of 1:100 and the mixed solution was stirred for 5 minutes to assure the hydrolization of the silane coupling agent. The iron sand particles were then added and stirred for an additional 30 minutes at room temperature to ensure a uniform distribution of the coupling agent on the surface of iron sand particles. The mixture was filtered and washed three times with ethanol to remove unreacted coupling agent. The treated iron sand particles were then dried at 80^{o}C in an oven until a constant weight was achieved.

5.2.3 Preparation of isotropic MREs

The compound formulation used in this study is given in Table 5.1. Formulations of isotropic MREs were compounded using a conventional laboratory two roll mill (model XK150). The front roller speed was 24 rpm and the rear roller speed was 33 rpm, the roller diameters were 150 mm, friction ratio of two rollers was 1:1.4 and the roller temperature was set to 80^{o}C. The nip gap (distance between front and back roller) was maintained at 2 mm during compounding. The compounding began with softening the rubber on its own in the two roll mill (mastication). Mastication reduces the viscosity and increase the plasticity of natural rubber which is brought about by heat generated in two roll mill through conduction from the heated roller and shearing of rubber during milling. After 2-3 minutes the rubber became invested on the hot roll and additives (other than accelerators and sulphur) were then added followed by iron sand; addition of accelerators and sulphur were delayed to the last part of the process to prevent premature vulcanization during compounding. The mixing time was approximately 40 minutes. The cure time at 150°C was then determined according to the procedure as described in Chapter 3 and the results are attached in the Appendix II. Compounded rubber samples weighing 13g were placed in a mould 60 x 50 x 3 mm and were cured in a compression moulder at 150°C under a pressure of approximately 12 MPa.

Table 5.1 Formulation of rubber compounds

Materials	**Function**	**loading (phr*)**					
Natural rubber	raw material/matrix	100	100	100	100	100	100
ZnO	accelerator/activator	5	5	5	5	5	5
Stearic acid	accelerator/activator	1	1	1	1	1	1
Paraffin oil	plasticiser	2	2	2	2	2	2
Naphthenic oil	plasticiser	3	3	3	3	3	3
Iron sand	filler	70	70	70	70	70	70
CBS	accelerator	2	2	2	2	2	2
TMTD	accelerator	1	1	1	1	1	1
Sulphur	crosslinking agent	1.5	1.5	1.5	1.5	1.5	1.5
Silane coupling agent level (wt %)							
TESPT	coupling agent	0	2	4	6	8	10

* phr = per hundred rubber

5.2.4 Characterisation

Raman spectroscopy

Raman spectra were acquired with a Ramanstation 400R (PerkinElmer) spectrometer equipped with an air cooled charged coupled device (CCD) detector and data points were recorded at 1 cm^{-1} intervals. The excitation source was a 785 nm near infrared laser focused on surface of samples with a spot approximately 200 μm in diameter. Calibration was validated against a polystyrene standard disk (PerkinElmer) prior to measurement. Samples were analysed while placed on aluminium foil. The Raman instrument was visually focused onto the surface of each location to be analysed on the modified iron sand samples. Laser power was set to approximately 40 mW (40% of maximum, estimated to be 6 $\times$105 W/m^2 on the 200 μm diameter spot) to acquire spectra from all samples (after initial trials) for consistency across the range of materials analysed. Spectra were collected over the range 200 – 3200 cm^{-1} and each spectrum was acquired as the sum of five repeats of

60s exposures on the sample. Five separate spectra were acquired at different locations on each sample analysed.

Thermogravimetric analysis

The grafting percentage of silane coupling agent with iron sand particles was determined by thermogravimetric analysis (TGA) using an TA Instrument SDT 2910 thermal analyser operated in dynamic mode, heating from ambient temperature to 300^{o}C at 5^{o}C/min in air purged at 150 ml/min with an empty pan used as a reference. Thermal gravimetric curves were obtained. The grafting percentage was calculated as the fraction of the mass of grafted silane coupling agent divided by the mass of iron sand particles at 280^{o}C [181, 182] as follows:

$$\text{Silane grafting (\%)} = \frac{\text{Grafted silane coupling agent/g}}{\text{iron sand particles/g}} \tag{5.1}$$

The amount of grafted silane coupling agent was calculated from the weight loss of treated iron sand at 280^{o}C minus weight loss of iron sand particles at 280^{o}C.

Crosslink Density

Determination of crosslink density in MREs was obtained using a swelling test. MREs samples with dimensions of 30 mm × 5 mm × 3 mm were weighed, and then immersed in toluene for 72 hours at room temperature in a dark environment. The toluene was replaced at 24 hours intervals over this time to minimise interference from toluene soluble fractions remaining in the samples. After 72 hours, samples were drained and dried and the swollen mass was recorded. Samples were then dried at 80^{o}C in an oven until a constant weight was achieved. For each experimental point, 3 samples were produced and the average values were calculated. The crosslink density was calculated by applying the Flory-Rehner equations as follows [183]

$$V_r = \frac{V_p}{V_p + V_s} = \frac{\frac{m_{dry}}{\rho_r}}{(\frac{m_{dry}}{\rho_r} + \frac{m_{wet} - m_{dry}}{\rho_s})} \quad (5.2)$$

$$[X] = \frac{-[\ln(1 - V_r) + V_r + \chi V_r^2]}{V_o(V_r^{\frac{1}{3}} - \frac{V_r}{2})} \quad (5.3)$$

where V_r is the volume fraction of MREs, m_{wet} is the swollen equilibrium mass, m_{dry} is the dry MREs mass, ρ_r is the density of natural rubber (910 kg/m^3), ρ_s is the density of toluene (866 kg/m^3), $[X]$ represents the crosslink concentration in mol/cm^3, χ is the interaction parameter between the rubber and toluene (0.393) and V_o is the molar volume of toluene (106.4 cm^3/mol).

Morphology

The microstructures of isotropic MREs were observed using a Hitachi S-4700 scanning electron microscope (SEM). The samples were frozen and snapped into pieces to expose their interior and coated with a thin layer of platinum prior to observation at an accelerating voltage of 20kV.

Dynamic mechanical analysis

Dynamic mechanical analysis was carried out using the method described in Section 4.2.5

Hysteresis

Hysteresis loss was carried out using the method described in Section 4.2.5

5.3 Results and discussion

5.3.1 Characterisation of surface modified iron sand particles

Figure 5.1 shows a schematic of the potential reaction mechanisms of TESPT with iron sand particles. In the presence of water in an ethanol solution and under acid catalysed conditions the ethoxy reactive groups of the silane are hydrolysed thereby forming silanol groups (-Si-O-OH) and liberating ethanol [184, 185]. The silanol groups are highly reactive intermediates which are presumed responsible for bond formation with the iron sand. When iron sand was added into the solution, the hydroxyl groups on the surface of the iron sand is believed to react with the silanol groups and subsequent drying condenses silanol groups to form siloxane linkages. Evidence for this was provided by Raman Spectroscopy analysis of unmodified and modified iron sand particles as shown in Figure 5.2. For iron sand, a number of peaks can be seen including a broad peak between 1100 and 1900 cm^{-1}, similar to observation elsewhere [186]. The growth of peaks at around 300 cm^{-1} for all modified iron sand particles is indicative of the formation of Si-O-iron sand and/or Si-O-Si bonds that would occur during reaction of iron sand with TESPT, although, the latter could also occur due to polymerisation of TESPT to produce siloxane; however, production of siloxane would not be expected to improve interfacial bonding. The increased height of the peaks around 1400 cm^{-1} (representing CH_2 bending in TESPT) from 0 to 6 wt% TESPT followed by no further increase from 6 wt% onwards suggests that coverage of iron sand particles by TESPT increases to 6 wt% when it reaches a saturation coverage [187].

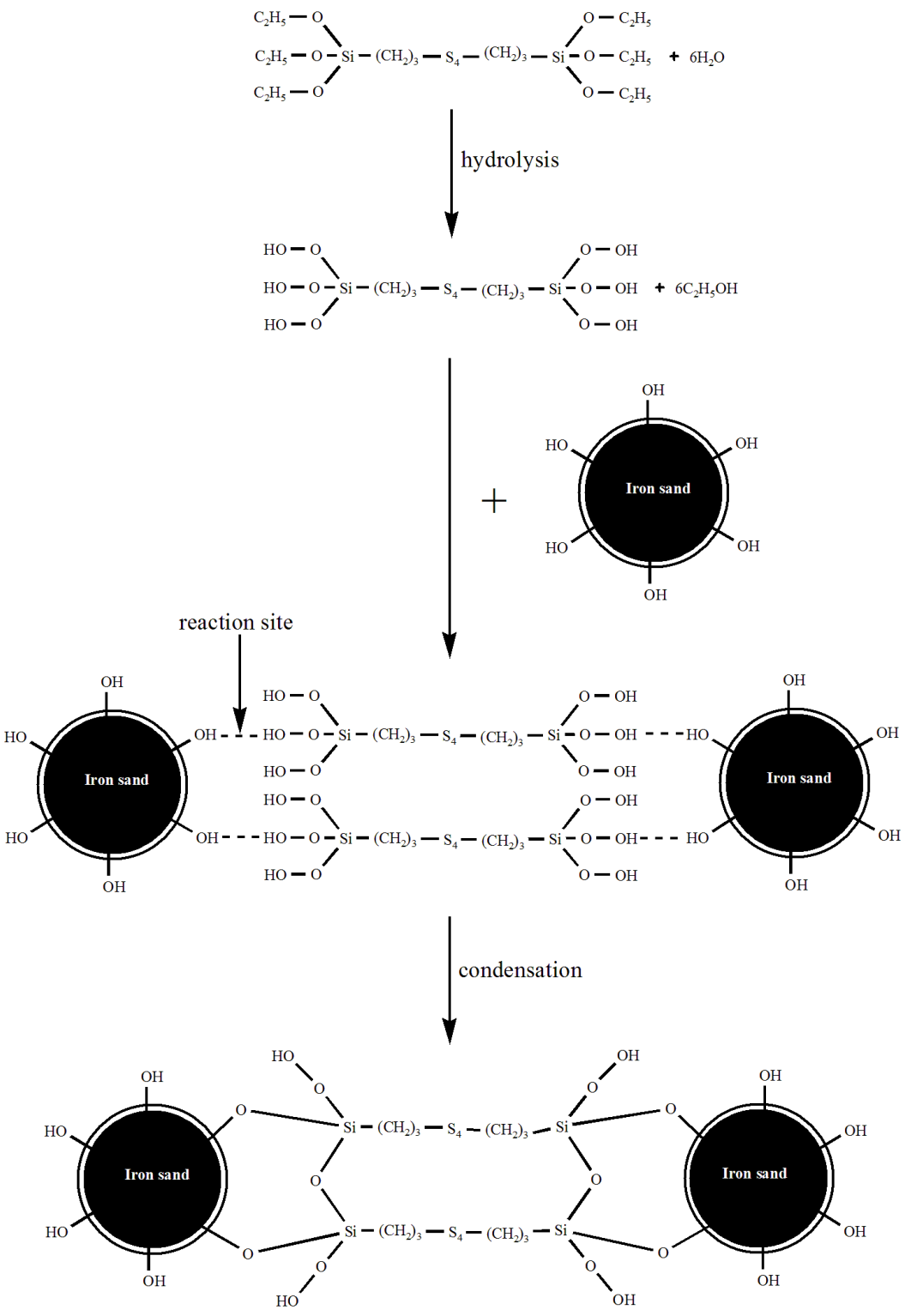

Figure 5.1 Illustration of the reactions of TESPT with iron sand particle surface.

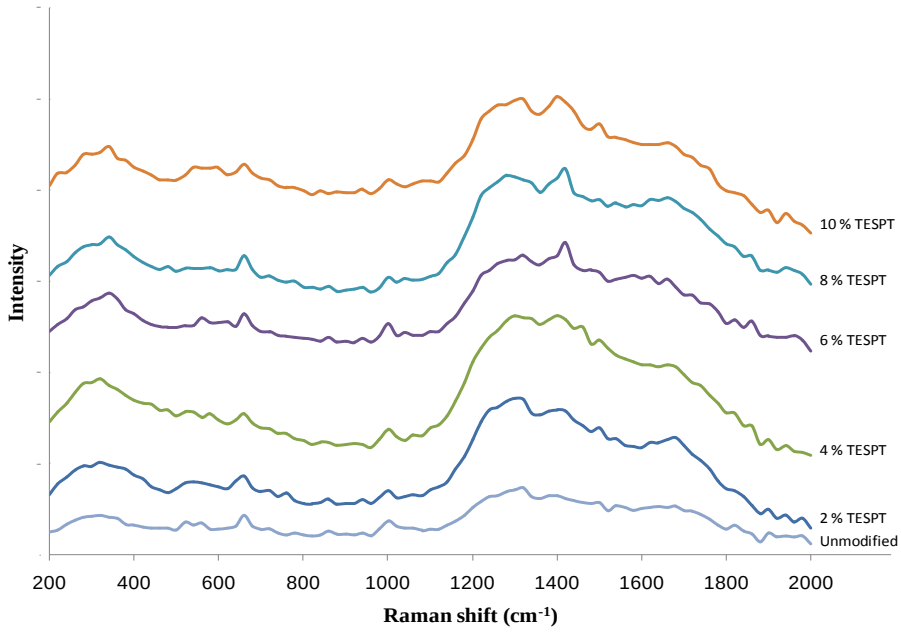

Figure 5.2 Raman spectra of iron sand particles at different TESPT contents

Figure 5.3 shows TGA curves for unmodified and modified iron sand particles at different TESPT contents. All samples showed weight loss over the temperature range of 50^{o}C to 280^{o}C with weight increase above 280^{o}C which is believed to have resulted from the oxidation of iron sand particles [188]. Similar trends have been observed in TGA curves for other magnetite particles [189]. As can also be seen, the unmodified iron sand particles were relatively stable in the air and only slightly weight loss between 100^{o}C to 280^{o}C which was probably due to vaporization of physically absorbed water at the surface of iron sand particles. The weight losses for modified particles increased with increasing TESPT content until 6% and then reduced for 8% and 10% TESPT. The weight loss for modified particles could be attributed to the decomposition and evaporation of silane coupling agent on the surface of iron sand particles such that suggests the silane coupling agent is strongly bound to particle surfaces by what is expected to be covalent bonds [190]. The

amount of TESPT attached to the surfaces of iron sand particles was quantitatively determined by TGA (taking the loss due to physically absorbed water into account) over the temperature range of 50^{o}C to 280^{o}C (each value representing an average from 3 samples) and is presented in Figure 5.4. It was not possible to conduct TGA analysis of TESPT on its own, however, a separate experiment was conducted where TESPT was heated at 280^{o}C in a furnace for which a residual weight of only 0.6% was obtained. Thus, residual TESPT is not considered to have a significant effect on the obtained data. It can be seen that the percentage of grafted silane appears to increase with increasing TESPT content until it reached a maximum value at 6% TESPT and thereafter decreased for higher TESPT contents (8% and 10%). At high TESPT content, the potential for hydrolysed TESPT to react with itself to produce polymeric siloxane increases as an alternative to reacting with iron sand. This polymeric siloxane could act as a barrier between TESPT and iron sand preventing reaction, particularly given that the siloxane polymer can react with multiple OH groups on the iron sand particles and screen other OH groups between those bonded with polymeric siloxane as described in the literature [191]. Polymeric siloxane that has not reacted with OH groups on iron sand would easily have been removed by washing the modified iron sand with ethanol and evaporation by drying during the preparation of the modified particles. This was checked by an extra wash with dichloromethane (DCM) following three times washing with ethanol for which the TGA weight loss and silane grafting percentage was found to be no significant different with those washed using just ethanol. Any remaining unreacted polymeric siloxane may also form e.g. oligomers by hydrogen bonding to the grafted TESPT

such that may weaken the composites properties since the silane molecules may not link the filler to the matrix [191].

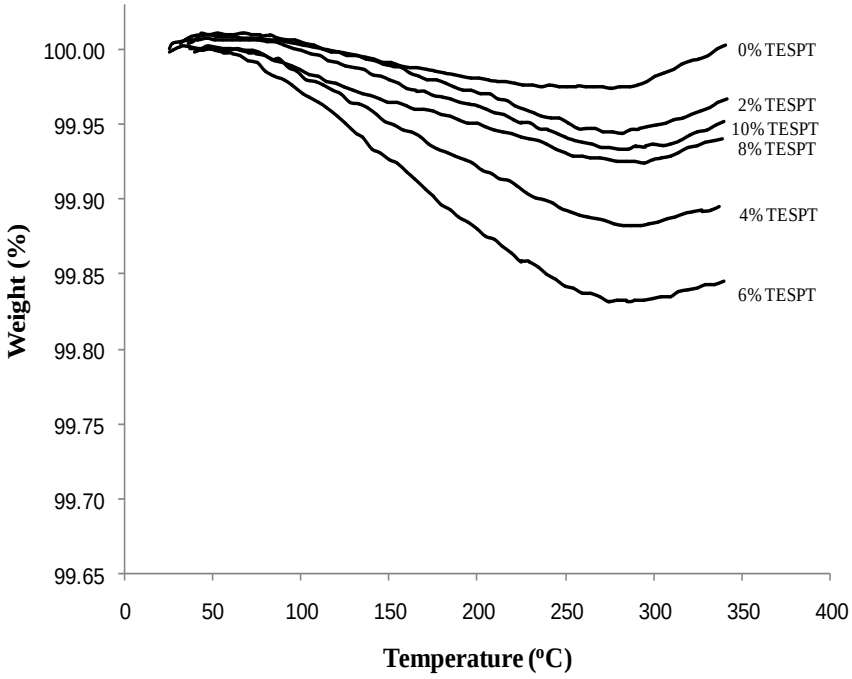

Figure 5.3 TGA curves for iron sand particles at different TESPT contents

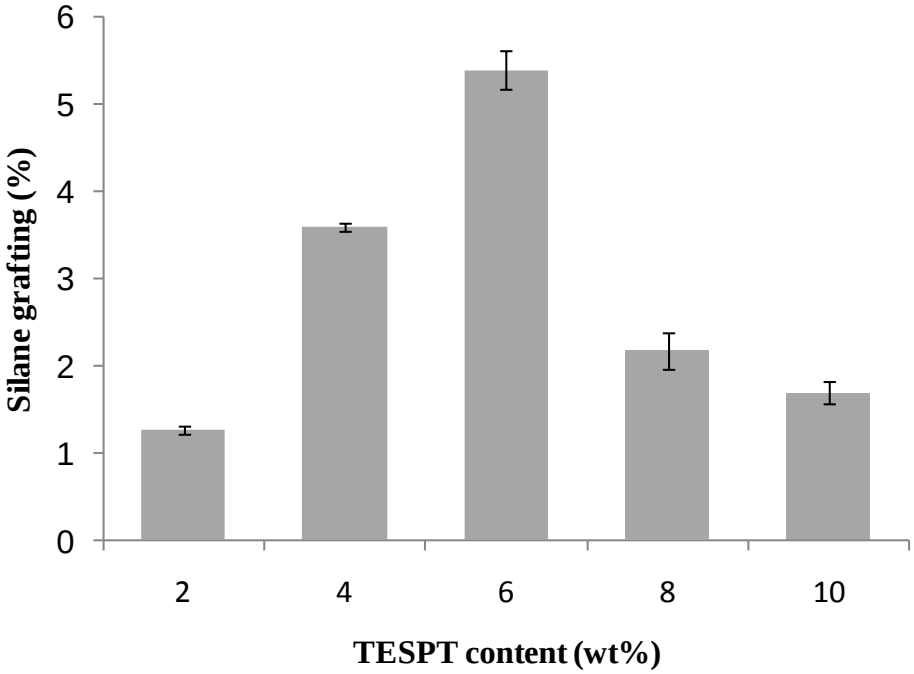

Figure 5.4 Silane grafting percentage for iron sand particles at different TESPT contents

Figure 5.5 shows a schematic of possible reaction mechanisms for the tetrasulphane group of TESPT with natural rubber. The tetrasulphane group of the TESPT could have been first dissociated during the compounding process to produce sulfidic radicals that subsequently react either directly or through sulphur crosslinking agent (S_x) with the rubber molecules in the presence of accelerators at elevated temperature during vulcanization to form crosslinks with the rubber molecules [141, 192, 193]. Evidence for this would be provided by crosslink density measurements of MREs filled with unmodified and modified iron sand particles at different TESPT contents as shown in Figure 5.6. It can be seen that the crosslink density gradually increased as the TESPT content increased from 2% to 6%; this highlights the potential formation of new crosslinks in the rubber network due to interaction between tetrasulphane group of TESPT with the rubber molecules. In order to assess the time required for the tetrasulphane group of TESPT to react with rubber and form crosslinks, another compound was prepared, the same as that containing 6 wt% silane coupling agent except that the sulphur crosslinking agent was excluded. It was found that the compound cured in 5.63 minutes which is not too different from time used here supporting substantial TESPT rubber crosslinking could have occurred. At higher TESPT contents (8% and 10%) the crosslink density decreased which is not surprising given the evidence from TGA results that at such TESPT contents less silane is coupled to the iron sand, which would be expected to lead to less crosslinking between iron sand and rubber. The obtained results support the use of TESPT as a coupling agent for iron sand particles and natural rubber and also a content of 6% TESPT is more suitable than 8% and 10% TESPT.

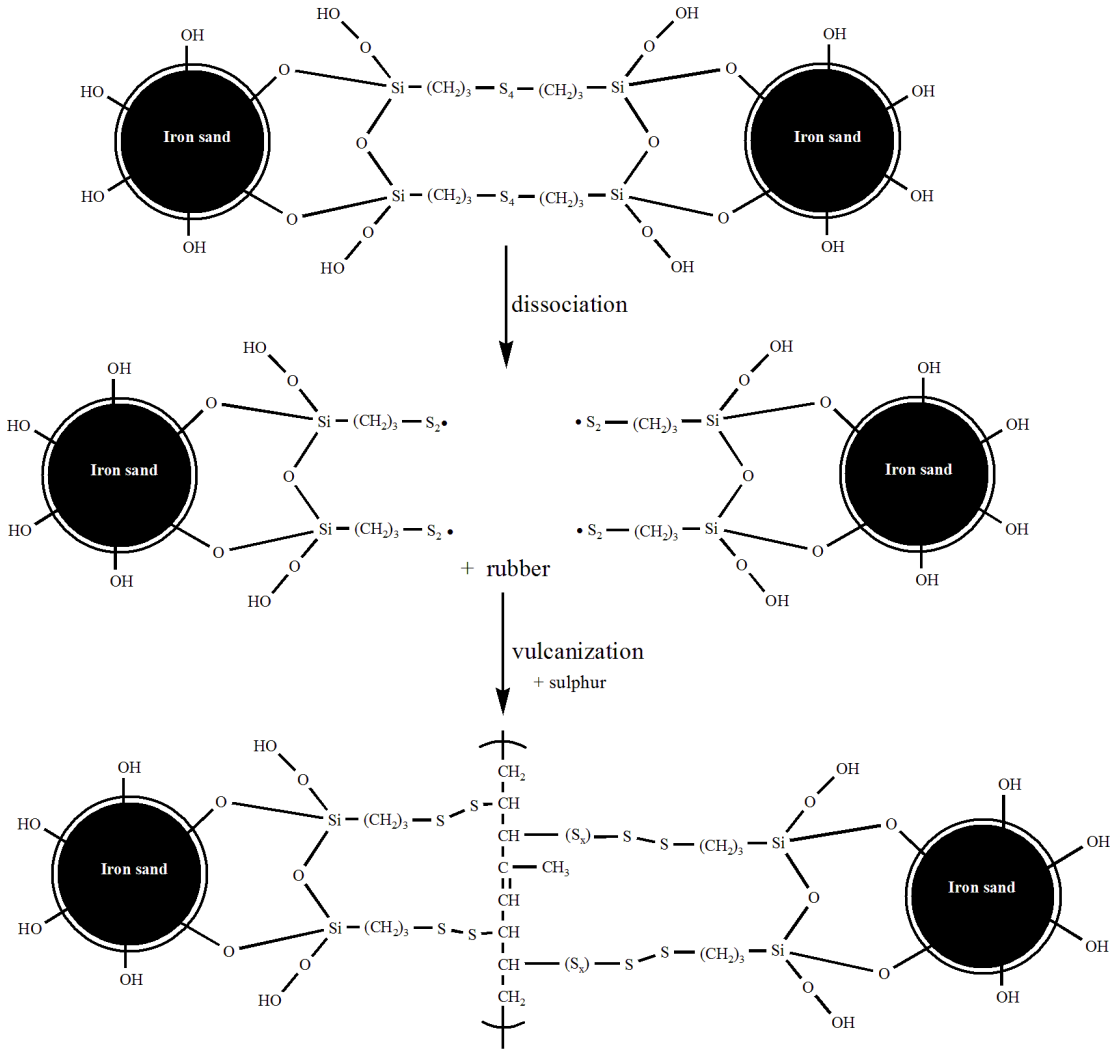

Figure 5.5 Schematic illustration of the reaction mechanisms of tetrasulphane group of TESPT with the natural rubber (S_2• represents sulfidic radicals of tetrasulphane group of TESPT)

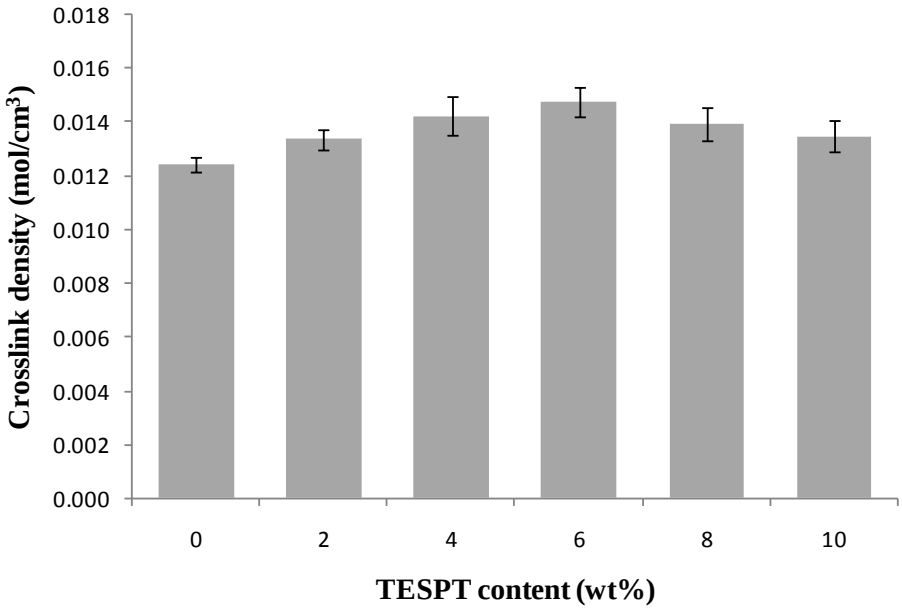

Figure 5.6 Crosslink density of MREs with different TESPT contents.

5.3.2 Morphology

Figure 5.7 shows SEM images of fracture surface of isotropic MREs with unmodified and modified iron sand particles. It can be seen for unmodified particle MREs, the surface is smooth with less matrix tearing and uneven distribution of iron sand particles in the rubber matrix. Clearly, there are a lot of cavities remaining due to the particle pull out from the rubber matrix and obvious gaps between iron sand particle and rubber, suggesting weak interaction between iron sand and rubber (Figure 5.7 a). In Figure 5.7 b, the surface of isotropic MREs with modified iron sand particles is rougher due to matrix tearing than for MREs with unmodified particles. It is also evident that iron sand particles are more evenly dispersed in the rubber with much less aggregates in the matrix. Clearly, much less particle pullout can be seen supporting improved interfacial adhesion between iron sand and natural

rubber suggesting stronger interaction between iron sand and rubber was obtained by using modified iron sand particles supporting Si-O-iron sand bonding.

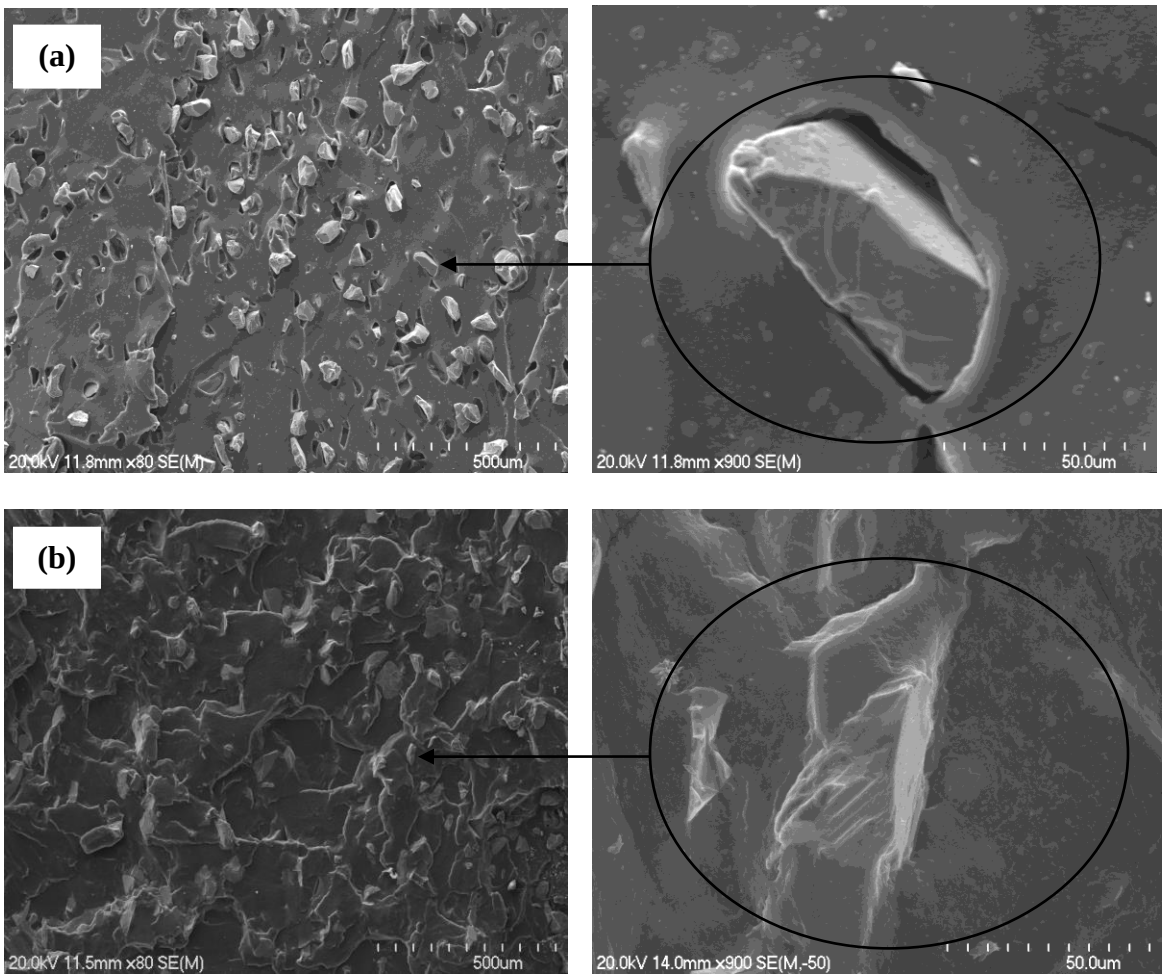

Figure 5.7 SEM images of fracture surface of isotropic MREs with; (a) unmodified and (b) modified iron sand particles (treated with 6% TESPT)

5.3.3 Dynamic mechanical analysis

The variation of tan δ with frequency for MREs with different TESPT contents is shown in Figure 5.8a. Tan δ is the highest for the MREs with modified iron sand treated with 6% TESPT and the increases in tan δ compared to MREs with unmodified iron sand is on average 40% over the whole frequency range explored. G'

and G" are also plotted in Figure 5.8 (b and c) to help highlight the mechanisms involved. G' and G", similar to tan δ are frequency dependent. It can be seen that the increase of tan δ as the frequency increased, is mainly due to increasing G" as opposed to changes in G'. The increased energy loss is assumed to be due to covalent bonding bringing about more intimate contact between the particles and rubber such that during deformation, increasing energy is expended overcoming friction, physical bonding as well as covalent bonding. At high TESPT content (8% and 10%), the lower tan δ values could again be explained by less silane grafting due to the formation of siloxane oligomer attached to the first layer of reacted TESPT on particle surfaces which could further reduce the energy absorption capability of the MREs. Energy loss in the materials could also be attributed to interfacial friction of weakly or partially bonded iron sand particles and rubber with increasing frequency. It is also apparent that the G' for MREs with modified iron sand are higher compared to MREs with unmodified iron sand. Explanation for general increment of G' for MREs with modified iron sand could be related to efficient stress transfer between particles and matrix which can improve stiffness, strength and failure strain of the materials [194]. Furthermore, improved interfacial bonding and degree of iron sand particle dispersion in the matrix might increase the effective particle-matrix interfacial area such that increased constraint of polymer chains occurs during deformation and improved the ability of the material to store elastic energy associated with recoverable elastic deformation [195].

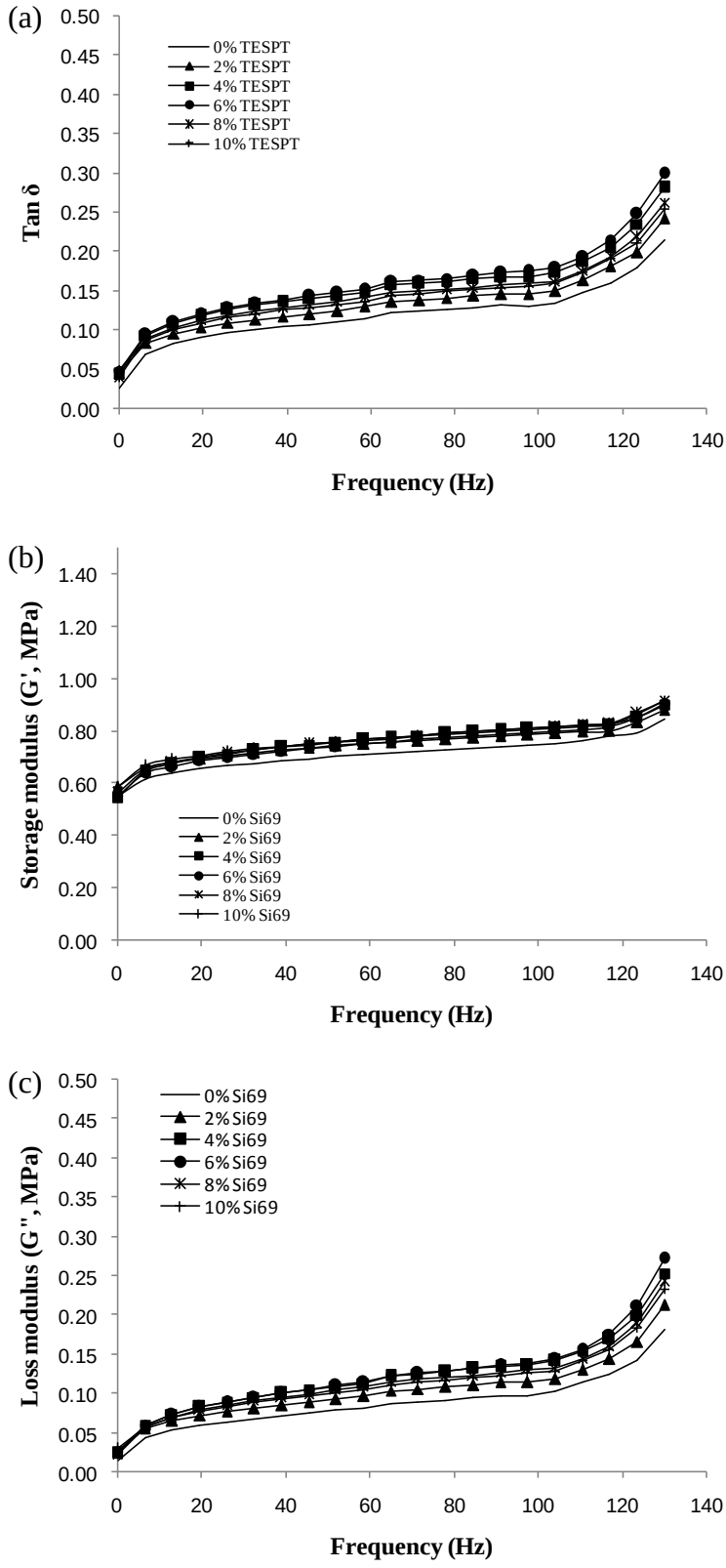

Figure 5.8 (a) Tan δ, (b) storage modulus (G') and (c) loss modulus (G'') versus frequency for MREs with different TESPT contents.

The variation of tan δ with strain amplitude for MREs with different TESPT contents is shown in Figure 5.9a; G' and G" are also plotted in Figure 5.9 (b and c). As expected, MREs with modified iron sand treated with 6% TESPT had the highest tan δ over the whole strain amplitude range explored with a 20% increase in tan δ compared to MREs with unmodified iron sand. As can be observed in Figure 5.9 (a and b), the tan δ and G' were amplitude dependent at low strain amplitudes before reaching a plateau, with the tan δ for MREs with modified iron sand reaching a plateau at around 2.5% strain amplitude, whereas the tan δ of the MREs with unmodified iron sand reached a plateau at 2% strain amplitude. It was evident that strong interfacial bonding between the iron sand and rubber as well as better dispersion increased the dependency of tan δ on the amplitude of the applied strain and the change of tan δ values over the strain amplitude range for all tested samples is mainly due to a decrease in G' as the strain amplitude increased. The decrease in G' as the strain amplitude increased for MREs with modified iron sand could be explained by the increase of particle detachment from the matrix with increasing strain amplitude. As can also be seen, G" for MREs with modified iron sand are higher compared to MREs with unmodified iron sand. The higher loss modulus could be attributed to the energy loss due to stress released after debonding and increase of energy absorbed during viscous flow which is more constrained due to formation of chemical linkages between iron sand and rubber. Once the strain amplitude is high enough, all the interactions are destroyed to such an extent it cannot be reconstructed and consequently, the energy loss is largely reliant on the viscous flow of the rubber matrix and friction between rubber chains and iron sand.

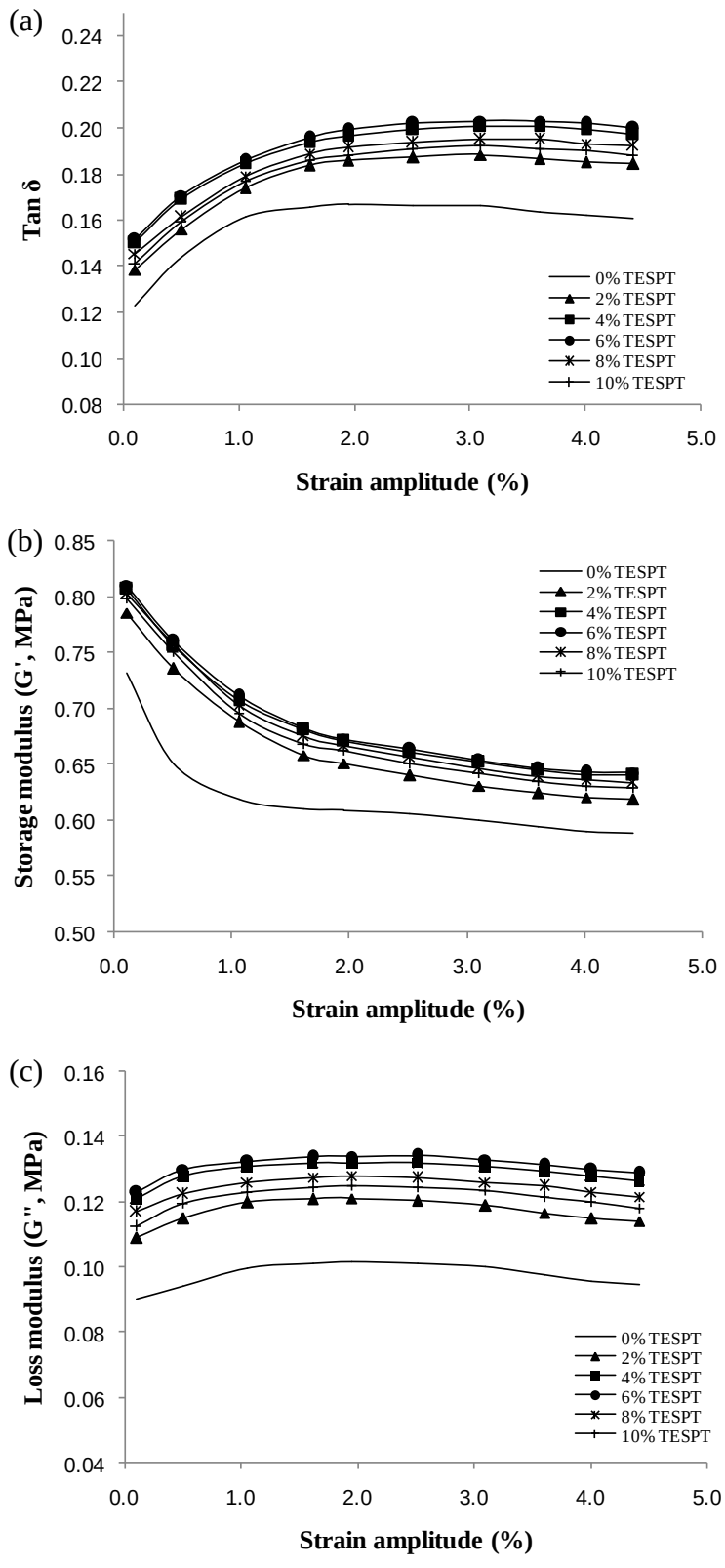

Figure 5.9 (a) Tan δ, (b) storage modulus (G') and (c) loss modulus (G'') versus strain amplitude for MREs with different TESPT contents.

Figure 5.10 presents the tan δ versus temperature curves for MREs with different TESPT contents. The tan δ peak is associated with glass transition temperature (T_g) of the materials. In the glass transition zone, the energy dissipation is mainly from the segmental motion of macromolecular chain of rubber matrix in spite of breakdown of filler-filler or filler rubber interaction [196]. It can be seen that the presence of coupling agent does not strongly affect the peak height and width of the curves. This is in agreement with similar finding reported by other researchers [138, 196, 197]. However, an enlarged graph of the tan δ versus temperature around the peaks showed a slight decrease of the height of the tan δ peak and the T_g values shifted to a slightly higher temperature for MREs with modified iron sand compared with MREs with unmodified iron sand. In addition, the decreased height of the tan δ peak was in an order similar to the silane grafting percentage as previously discussed. The decrease height of the damping peak and a shift of T_g to higher temperature could be attributed to strong filler rubber interaction which resulted in restriction in mobility and flexibility of rubber chains in the materials.

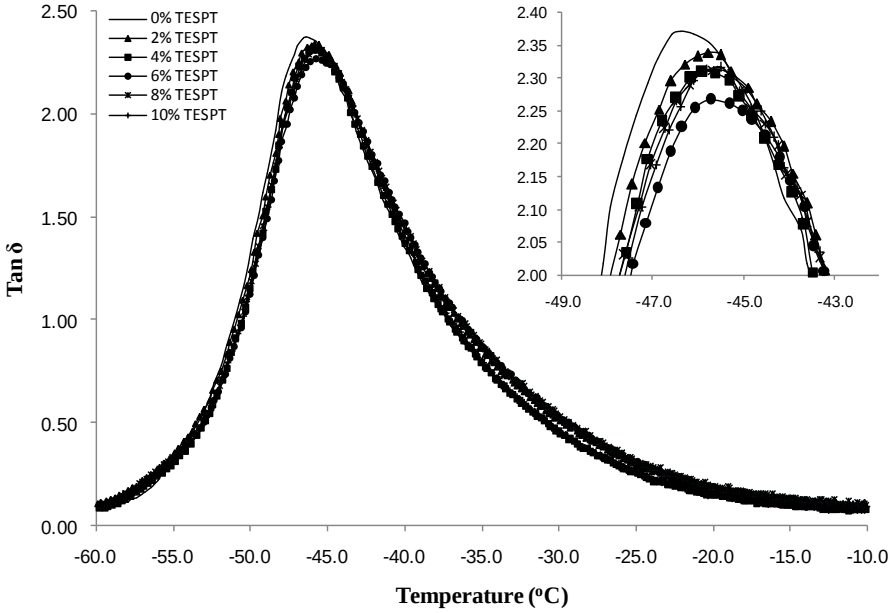

Figure 5.10 Tan δ versus temperature curves for MREs with different TESPT contents.

5.3.4 Hysteresis

Figure 5.11 shows hysteresis loss for MREs with different TESPT contents. As can be seen, hysteresis loss increased with increasing TESPT content until it reached a maximum value at 6% TESPT and thereafter decreased at higher TESPT content (8% and 10%). The results are in agreement with the silane grafting percentage as previously discussed. The effect of coupling agent on the hysteresis loss of MREs could again be explained by the energy loss due to stress released after debonding and increase of energy absorbed during viscous flow which is more constrained due to formation of chemical linkages between iron sand and rubber. Some authors have considered constraint in liaise of a rubber shell mechanisms [140]. The molecular chain mobility would be reduced by the formation of silane linkages between iron sand and rubber, resulting in a rubber shell on the filler surface in which the polymer viscosity and Young modulus would be increased. The higher Young's modulus of rubber near the surface of iron sand in the rubber shell would gradually decrease with increased distance from the filler surface and finally reach the same level as that of the rubber matrix at a certain distance. When the MREs were subjected to dynamic strain, the rubber shell around the particles would begin to break down and increase the amount of energy loss. In addition, hysteresis loss could also be attributed to interfacial friction at the filler matrix interface and breakdown of filler aggregates. The decrease of hysteresis loss at higher TESPT content could again be explained by the lower silane grafting and formation of weak siloxane oligomer that may begin to break down at a relatively lower level of strain.

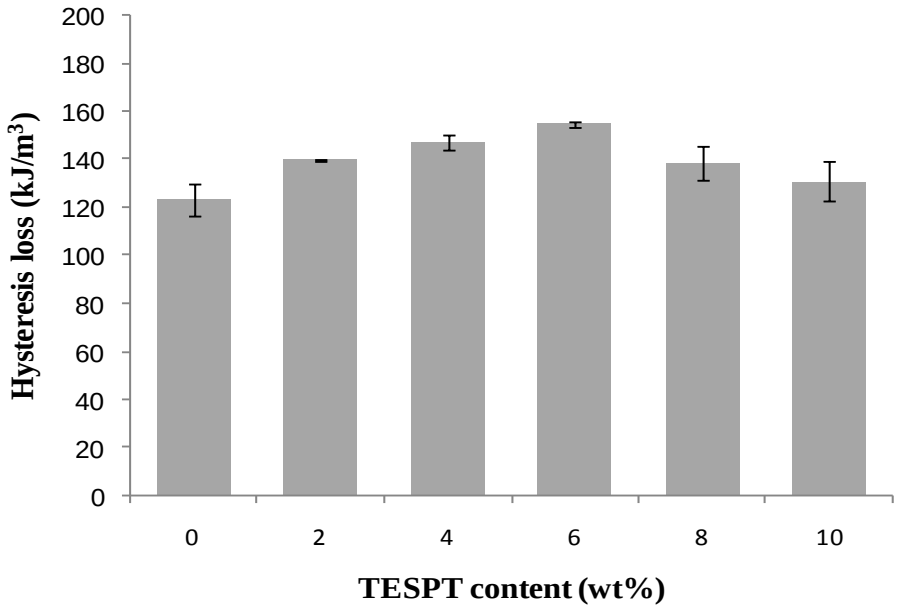

Figure 5.11 Hysteresis loss for MREs with different TESPT contents.

5.4 Chapter conclusion

In this work, iron sand particles were modified at five different TESPT contents (2, 4, 6, 8 and 10 wt%) relative to the iron sand content to assess the optimum amount of TESPT for use in MREs. TESPT contains ethoxy hydrolysable groups that enable bonding with iron sand particles and a tetrasulphane group capable of bonding with the rubber matrix. Raman spectroscopy showed evidence that siloxane linkages were formed between TESPT and iron sand. Weight loss measured using TGA supports that silane coupling agent is strongly bound to particle surfaces and the silane grafting percentage was found to be the highest at 6% TESPT. Crosslink density measurement of MREs made using TESPT treated iron sand highlight that the tetrasulphane group of TESPT formed crosslinks with the rubber molecular chains. Treated iron sand was found to be more evenly dispersed in the rubber with much less particle pullout on fracture surface supporting improved

interfacial adhesion with natural rubber. Tan δ was found to be highest for the MREs with modified iron sand treated with 6% TESPT and 40% larger than that unmodified iron sand over the whole frequency range explored and 20% higher over the whole strain amplitude explored. However, the presence of coupling agent did not strongly affect the peak temperature of tan δ versus temperature curves. An increase in hysteresis loss was also obtained for MREs with modified iron sand treated with 6% TESPT content compared with MREs with unmodified iron sand.

Chapter 6

The Effect of Silane Coupling Agent on Iron Sand for Use in Magnetorheological Elastomers Part 2: Dynamic Properties of Isotropic and Anisotropic Magnetorheological Elastomers

6.1 Introduction

In this chapter, isotropic and anisotropic MREs containing unmodified and silane modified iron sand (as optimised in Chapter 5) in a natural rubber matrix were prepared. For isotropic MREs, curing was carried out in the absence of a magnetic field. For anisotropic MREs, curing was carried out in the presence of five different magnetic fields (200, 400, 600, 800 and 1000 mT). The morphological characteristics of isotropic and anisotropic MREs were examined using SEM. Tan δ was measured through dynamic mechanical analysis (DMA) over a range of frequency (0.01–130Hz), strain amplitude (0.1–4.5%), and temperature (-100–50°C). Energy dissipated was measured using a universal tester under cyclic tensile loading.

6.2 Experimental

6.2.1 Materials

Natural rubber (SMR L grade) and other chemicals used in this study were the same as previously mentioned in Section 5.2.1. Iron sand was collected from Ngarunui Beach, Raglan. The iron sand was then milled using a planetary mono mill (Pulverisette 6) produced by Fristech GmbH and subsequently sieved to obtain a 45-56 μm particle size range.

6.2.2 Surface modification of iron sand

The surface modification of iron sand was carried out by using aqueous alcohol solution method as previously described in Section 5.2.2. The particles were subjected to surface treatment with TESPT at 6 (wt%) by weight of the particles.

6.2.3 Preparation of isotropic and anisotropic MREs

The compound formulation used in this study is given in Table 6.1. Isotropic and anisotropic MREs were fabricated according to the methods as previously described in Section 4.2.4. The cure time at 150ºC was 4.23 minutes as previously determined in Part 1, Section 5.2.3.

Table 6.1 Formulation of rubber compound

Materials	Function	phr*
Natural rubber	raw material/matrix	100
ZnO	accelerator/activator	5
Stearic Acid	accelerator/activator	1
Paraffin Oil	plasticiser	2
Naphthenic Oil	plasticiser	3
Iron sand	filler	70
CBS	accelerator	2
TMTD	accelerator	1
Sulphur	crosslinking agent	1.5

*parts per hundred rubber

6.2.4 Characterisation

Morphology

The microstructures of isotropic and anisotropic MREs were observed using the method described in Section 4.2.5

Dynamic mechanical analysis

Dynamic mechanical analysis was carried out using the method described in Section 4.2.5

Hysteresis

Hysteresis loss was carried out using the method described in Section 4.2.5

6.3 Results and discussion

6.3.1 Morphology

Figure 6.1 shows SEM images of isotopic and anisotropic MREs with modified iron sand. From the SEM micrographs, it can be seen that isotropic MREs have a homogeneous dispersion of iron sand particle in the rubber matrix without

obvious aggregation (Figure 6.1a). Figure 6.1 b-f show anisotropic MREs cured at different magnetic fields. It can be seen that the alignment of modified magnetic particles has occurred similarly to that obtained in Section 4.3.1 with unmodified iron sand. It can also be noted that the chains became longer and more aligned as the magnetic field strength increased.

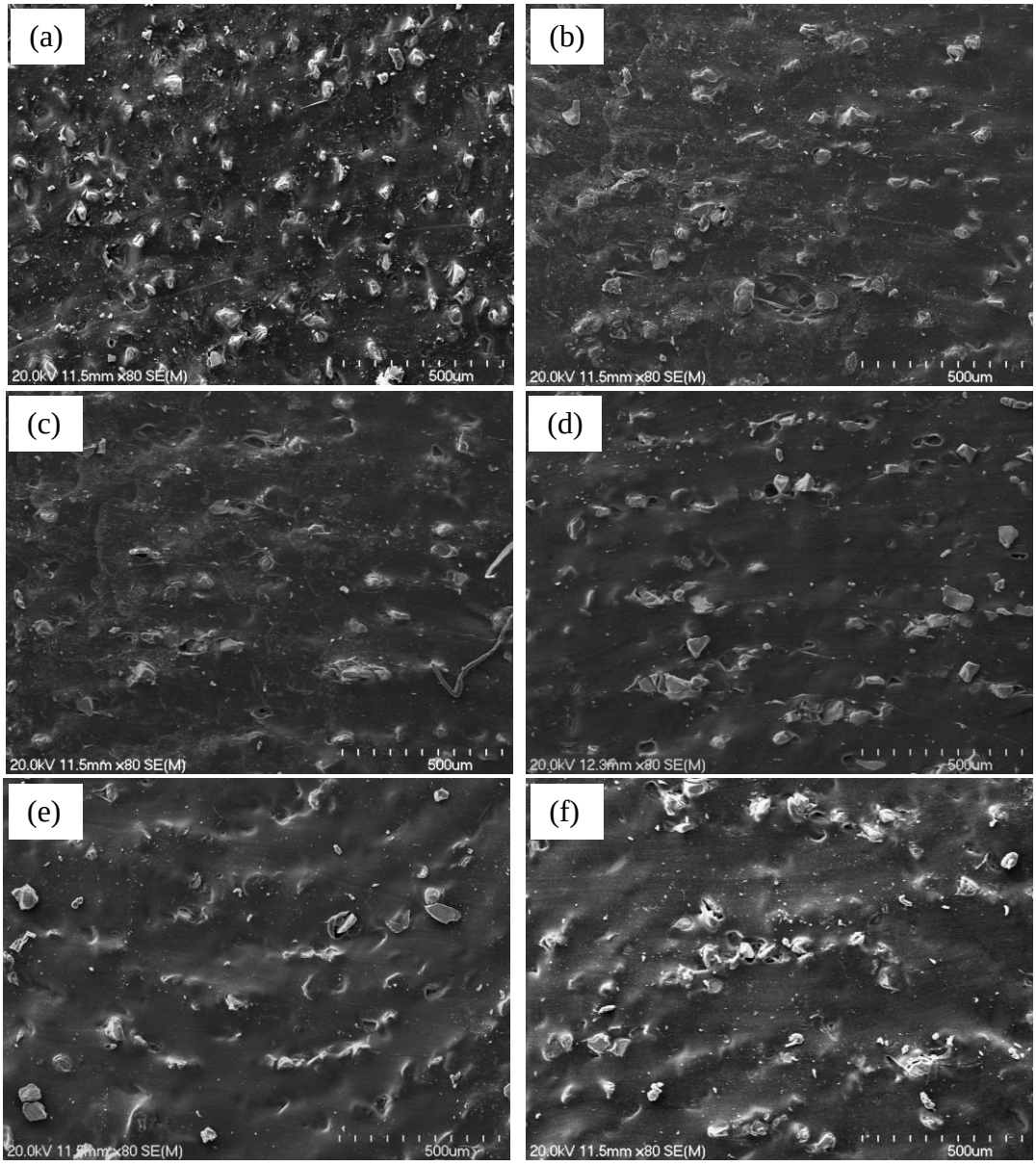

Figure 6.1 SEM images of iron sand-natural rubber MREs: (a) isotropic MRE – 0 mT; (b) anisotropic MRE – 200 mT; (c) anisotropic MRE – 400 mT; (d) anisotropic MRE – 600 mT; (e) anisotropic MRE – 800mT and anisotropic MRE – 1000mT.

6.3.2 Dynamic Mechanical Analysis

The variation of tan δ with frequency for isotropic and anisotropic MREs at different magnetic fields is shown in Figure 6.2. Generally, it was seen that tan δ increased with increasing frequency, rapidly at low frequencies, more slowly at intermediate frequencies, increasing again more rapidly at high frequencies. It can be also seen that tan δ is higher for MREs (isotropic and anisotropic) with modified iron sand compared to those with unmodified iron sand (it was reported in Part 1, Section 5.3.3 that silane treatment of iron sand improved tan δ for isotropic MREs by approximately 40% over the whole frequency range explored as shown in Figure 6.2a). The improvements for anisotropic MREs cured at 200, 400, 600, 800 and 1000 mT was approximately 30%, 27%, 18%, 24% and 20%, respectively (Figure 3b-f). Storage modulus (G') and loss modulus (G") are also plotted in Figure 6.3 and 6.4 to help highlight the mechanisms involved with change of tan δ. It can be seen that the increase of tan δ as the frequency increases, is mainly due to increasing G" as opposed to changes in G'. Considering the factors influencing G" (energy loss), modification with silane has brought about chemical bonding between the iron sand and the rubber, such that the rubber would be more constrained. Therefore, during cyclic deformation, more energy could be absorbed in breaking bonds and in bringing about viscous flow of more constrained material. At the low strain amplitude for this particular experiment, it is considered that few bonds would be broken and the major cause of the increase in energy absorption is that required to bring about viscous flow of the constrained rubber. In the literature, this constrained rubber is commonly regarded as a rubber shell with higher stiffness than the surrounding rubber [140]. For anisotropic MREs with modified iron sand, the aligned particles lead to the formation

of joint rubber shells between neighbouring particles (see Figure 6.5) in which the mobility of the rubber molecules would be further reduced and further increase the amount of energy absorbed [140]. The aligned structures in anisotropic MREs would also reduce particle aggregation and therefore reduce the amount of trapped rubber and allow a greater amount of rubber to take part in the energy dissipation process. Furthermore, better interfacial bonding with silane treatment will increase stress transfer to the iron sand and lead to increased energy loss through the magnetomechanical effect (change of magnetic domain structure induced by application of stress) and also prevent rotation of particles and avoid loss of dipole alignment which will enhance magnetic interaction between neighbouring particles, resulting in an increase of energy required to overcome the magnetic inter-particle interactions [107, 198]. G' for MREs with modified iron sand is higher than those with unmodified iron sand (isotropic and anisotropic), supporting increased stress transfer between matrix and particles. Overall, an increase of tan δ is seen for modified iron sand with the application of different magnetic fields which can be explained by the multiple mechanisms described above which can be summarized as constraint of joint rubber shells, release of trapped rubber and increased interfacial bonding leading to higher losses through magnetic interactions (magnetomechanical and inter-particle interaction). To demonstrate the increase in tan δ, G' and G" with increased magnetic field (and so degree of anisotropy) that can be seen in Figures 6.2, 6.3 and 6.4 better, tan δ, G' and G" have been plotted against magnetic field in Figure 6.6. As can be seen, there is generally a slight increase in tan δ, G' and G" with increase in magnetic field which levels off at about 600 mT. This supports saturation magnetisation to be occurring at around 600 mT and indicates that the influence of

magnetic interactions during cyclic stress outweighs the energy dissipation due to increase of joint rubber shells and trapped rubber released with increased degree of anisotropy. The limited influence of magnetic field on tan δ, G' and G" observed here would appear to be due to low strain amplitude (0.5%) as well as the stress being in shear.

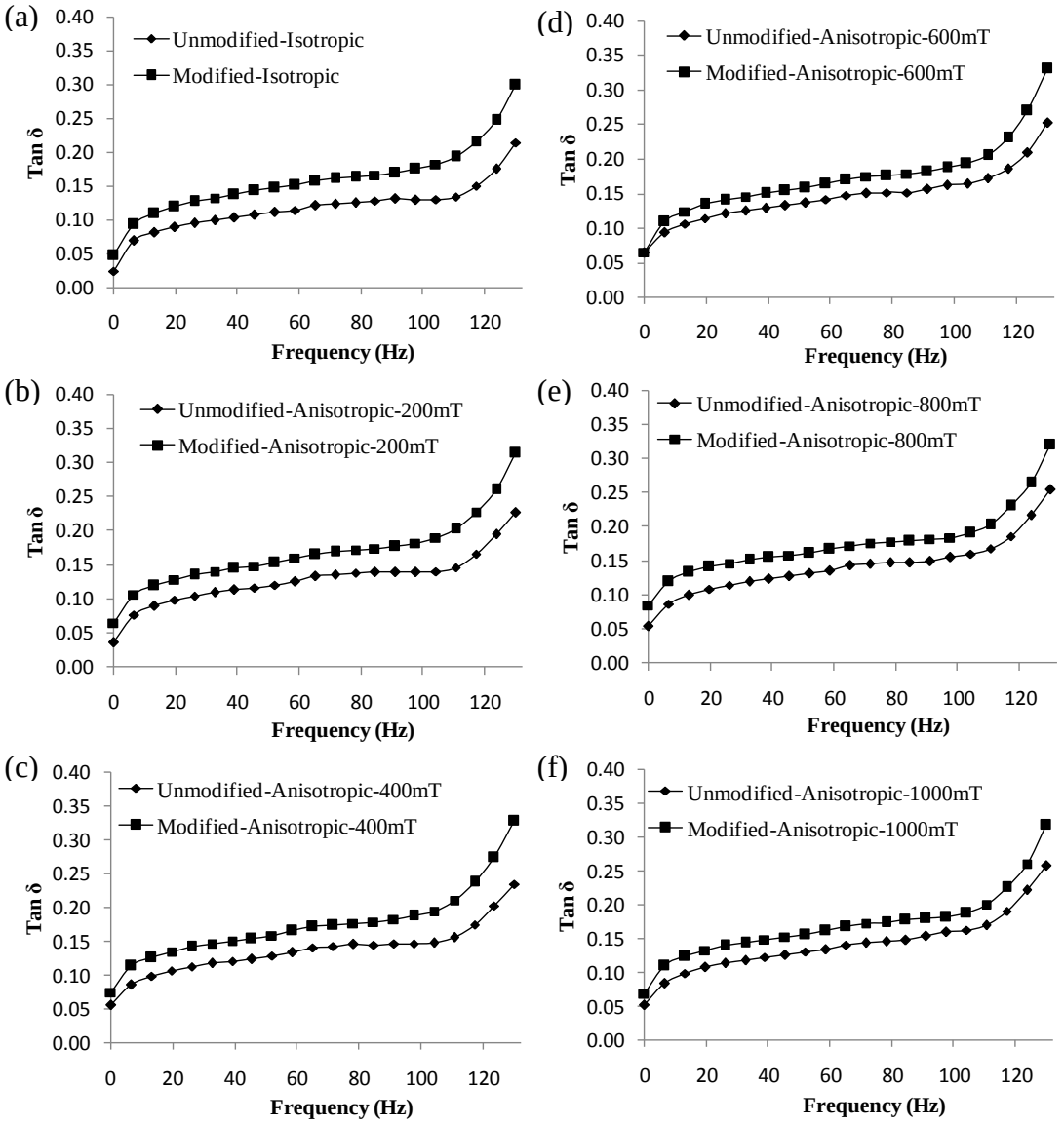

Figure 6.2 Tan δ versus frequency: (a) isotropic MRE – 0 mT; (b) anisotropic MRE – 200 mT; (c) anisotropic MRE – 400 mT; (d) anisotropic MRE – 600 mT; (e) anisotropic MRE – 800 mT and (f) anisotropic MRE – 1000 mT.

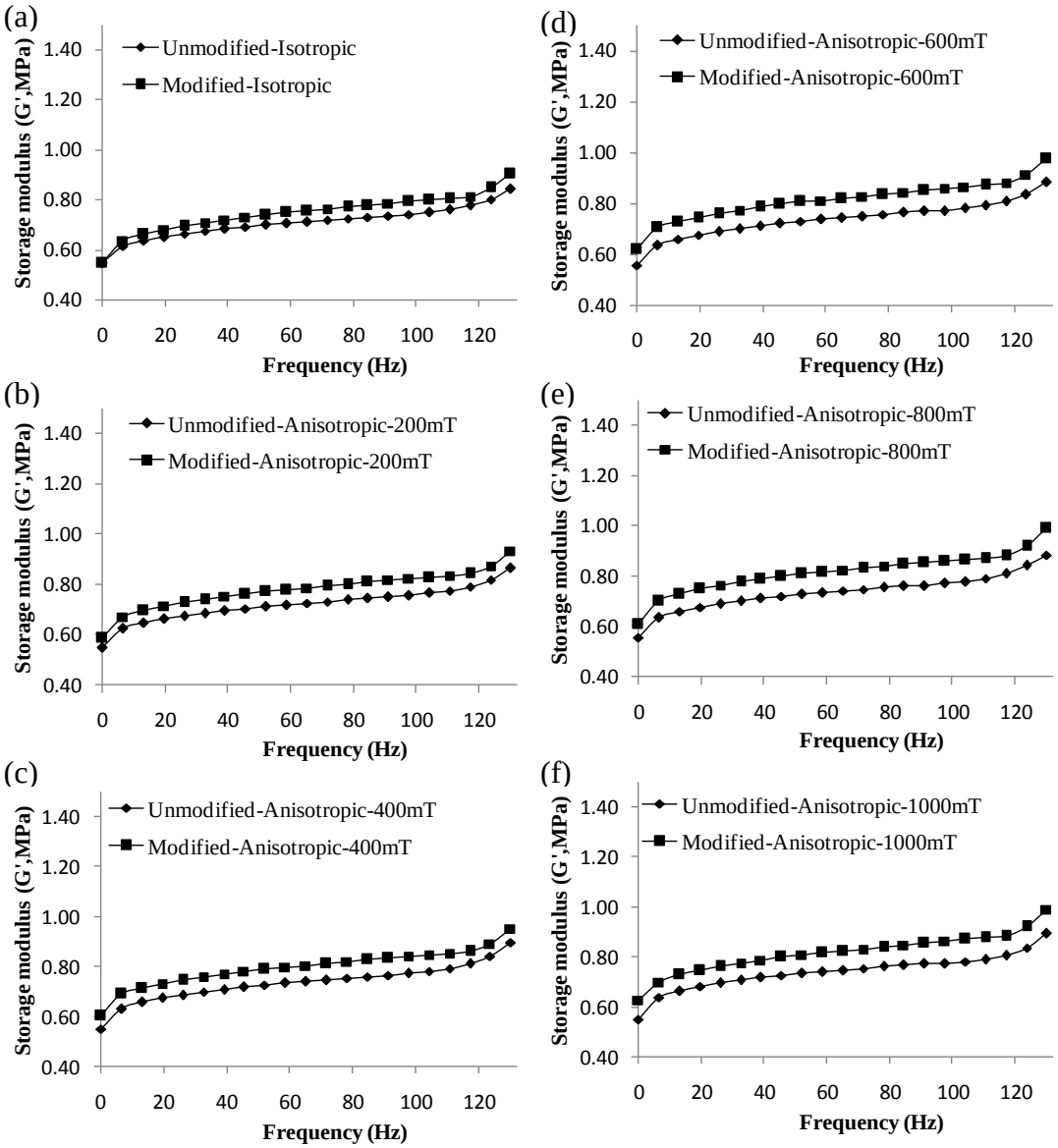

Figure 6.3 Storage modulus versus frequency: (a) isotropic MRE – 0 mT; (b) anisotropic MRE – 200 mT; (c) anisotropic MRE – 400 mT; (d) anisotropic MRE – 600 mT; (e) anisotropic MRE – 800 mT and (f) anisotropic MRE – 1000 mT.

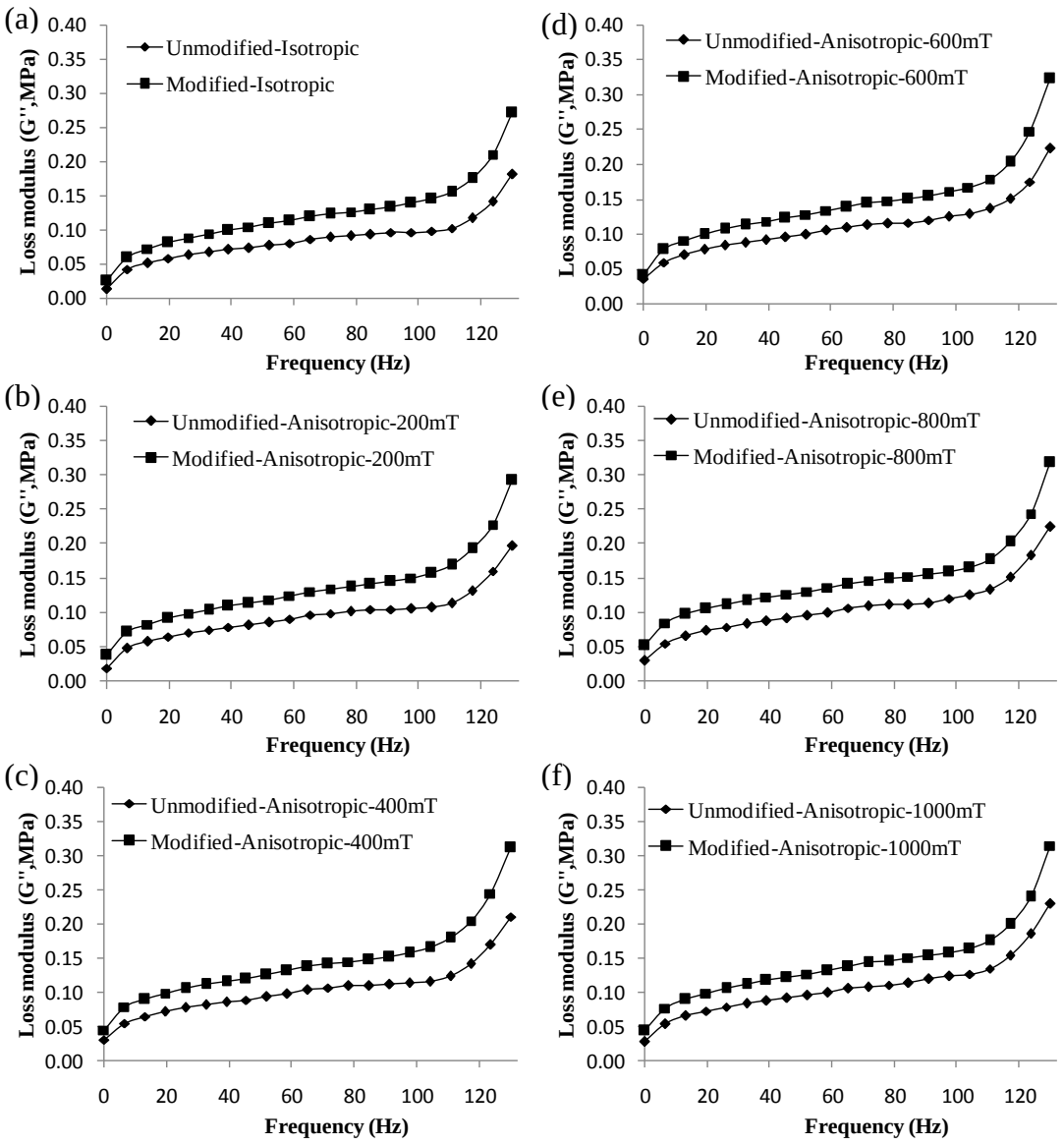

Figure 6.4 Loss modulus versus frequency: (a) isotropic MRE – 0 mT; (b) anisotropic MRE – 200 mT; (c) anisotropic MRE – 400 mT; (d) anisotropic MRE – 600 mT; (e) anisotropic MRE – 800 mT and (f) anisotropic MRE – 1000 mT.

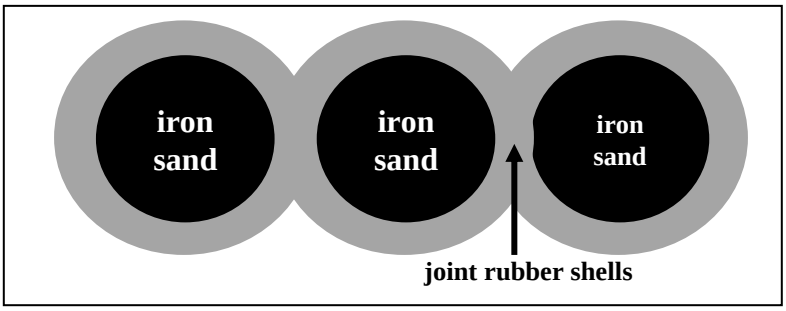

Figure 6.5 Joint rubber shells between adjacent particles in anisotropic MREs.

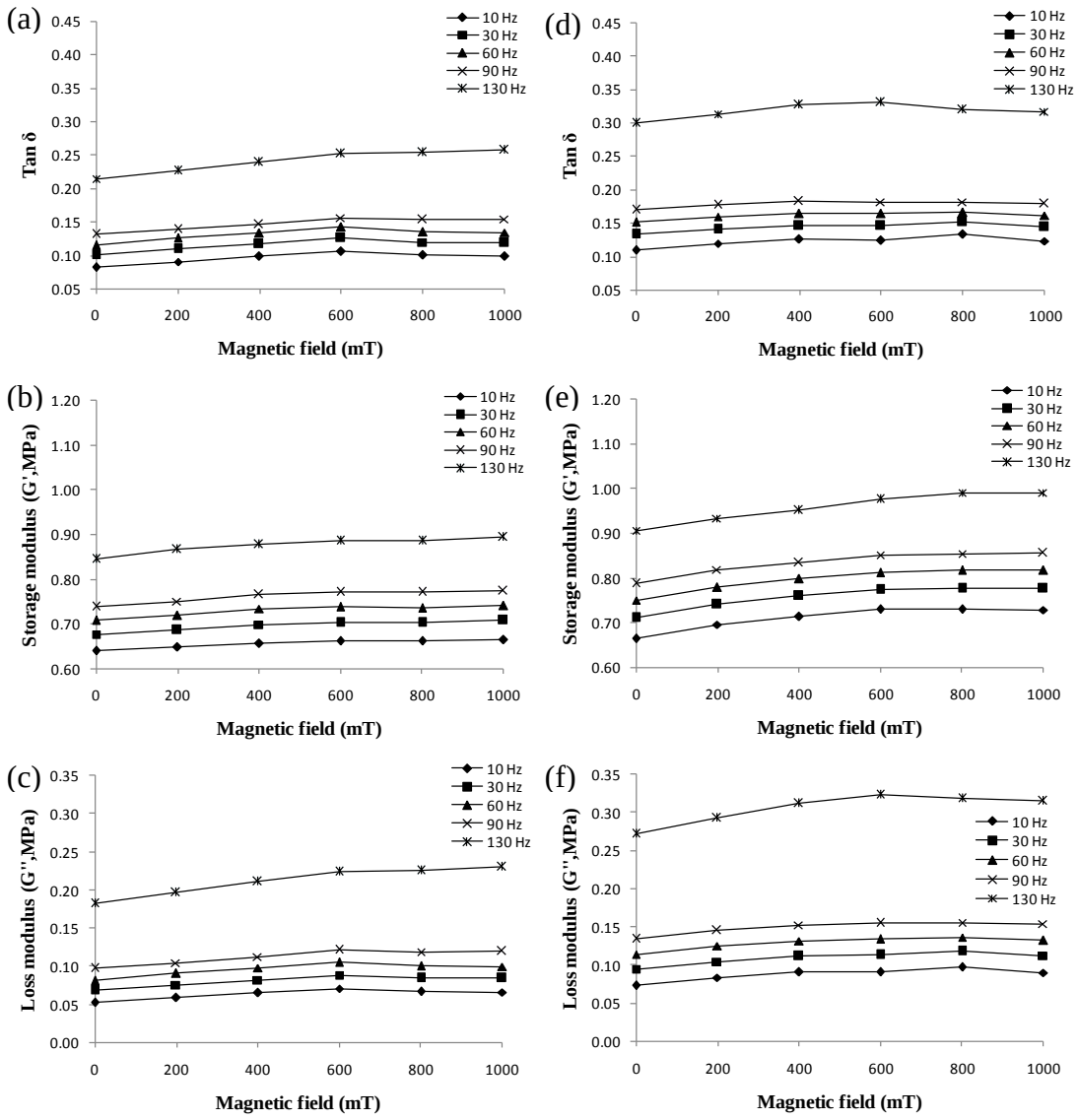

Figure 6.6 (a) Tan δ, (b) storage modulus (G') and (c) loss modulus (G") versus magnetic field (mT) for MREs with unmodified iron sand and (d) tan δ, (e) G' and (f) G" versus magnetic field (mT) for MREs with modified iron sand at different frequencies.

The variation of tan δ with strain amplitude for isotropic and anisotropic MREs at different magnetic fields is shown in Figure 6.7. Generally, tan δ increased with increase in strain amplitude at low strain amplitudes and plateaued at higher strain amplitudes. It can also be seen that tan δ for MREs with modified iron sand are higher compared to those with unmodified iron sand (isotropic and anisotropic) over the whole strain amplitude range explored. The improvement in tan δ with silane treatment for isotropic as well as anisotropic MREs cured at 200, 400, 600, 800 and 1000 mT were approximately 20%, 19%, 18%, 14%, 11% and 12%, respectively. The plateaux of tan δ for unmodified iron sand and those with modified iron sand occurred at different strain amplitudes (approximately 2% and 2.5%, respectively). Storage modulus (G') and loss modulus (G") are also plotted in Figures 6.8 and 6.9 to help highlight the mechanisms involved with change of tan δ. It is apparent that the change in tan δ with increased strain amplitude is mainly due to the decrease in G' which occurred at a faster rate for unmodified iron sand. The larger reduction of elasticity with increase in strain amplitude for MREs containing unmodified iron sand could be due to the relatively easier breakdown of physical bonding/mechanical interlocking between iron sand and rubber compared to breakage of stronger silane linkages with modified particles. Indeed, better interfacial bonding with silane treatment increased the dependency of G' on the strain amplitude such that plateau occurred at higher strain amplitude, supporting that stronger interfacial bonding between iron sand and rubber increased the amplitude of applied strain required to break bonds. At the plateau region G' and G" are largely reliant on the rubber matrix due to its detachment from particles and friction between rubber chains and iron sand. As can also be seen, G" for MREs with modified iron sand is higher compared to

those for MREs with unmodified iron sand. The higher energy loss for isotropic MREs with modified iron sand could be attributed to more energy absorbed at low strain amplitudes for the viscous flow of rubber better bonded to iron sand and at high strain amplitudes, to bring about bond failure and viscous flow of rubber chains that are more bulky due to the presence of coupling agent. For anisotropic MREs with modified iron sand, similar mechanisms would be involved as well as further energy loss attributed to breakdown of joint rubber shells, more trapped rubber released, as well as increased interfacial bonding leading to higher losses through magnetic interactions (magnetomechanical and inter particle interaction). G' for MREs with modified iron sand is higher than those with unmodified iron sand which can again be explained due to increased stress transfer between the matrix and iron sand. The increases of tan δ, G' and G" with increased magnetic field (as can be seen from Figures 6.7, 6.8 and 6.9) has been plotted in Figure 6.10. It can be seen that tan δ, G' and G" increased dramatically and then leveled off at 600 mT due to saturation magnetization, indicating increased energy dissipation is mainly dominated by the magnetic interactions with increased degree of anisotropy. The process for energy absorption by the magnetic interactions again can be explained due to magnetomechanical damping and increased energy absorbed to overcome inter-particle magnetic interaction; these processes transform elastic energy into magnetic energy which subsequently dissipates by magnetic hysteresis [21].

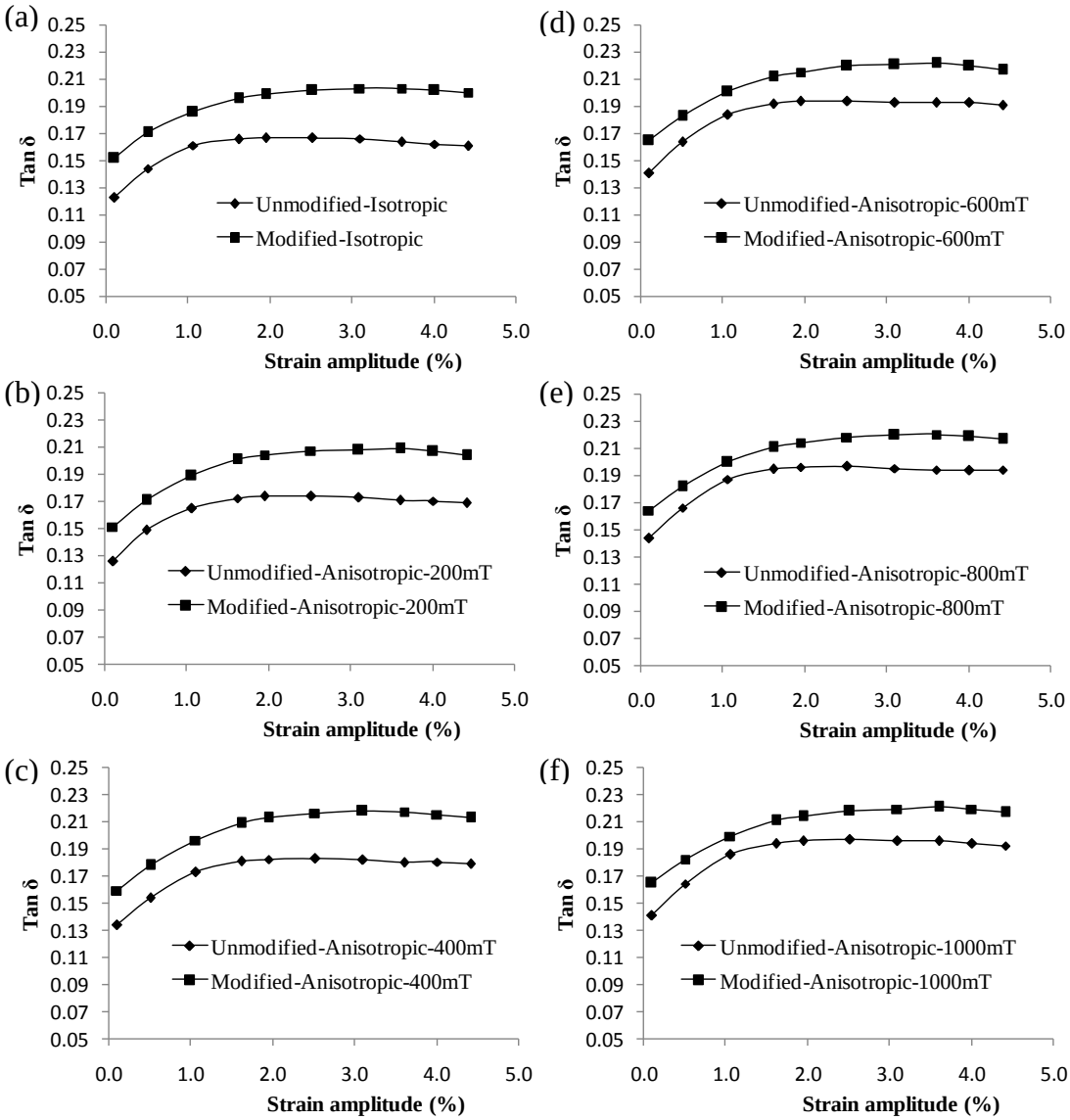

Figure 6.7 Tan δ versus strain amplitude: (a) isotropic MRE – 0 mT; (b) anisotropic MRE – 200 mT; (c) anisotropic MRE – 400 mT; (d) anisotropic MRE – 600 mT; (e) anisotropic MRE – 800 mT and (f) anisotropic MRE – 1000 mT.

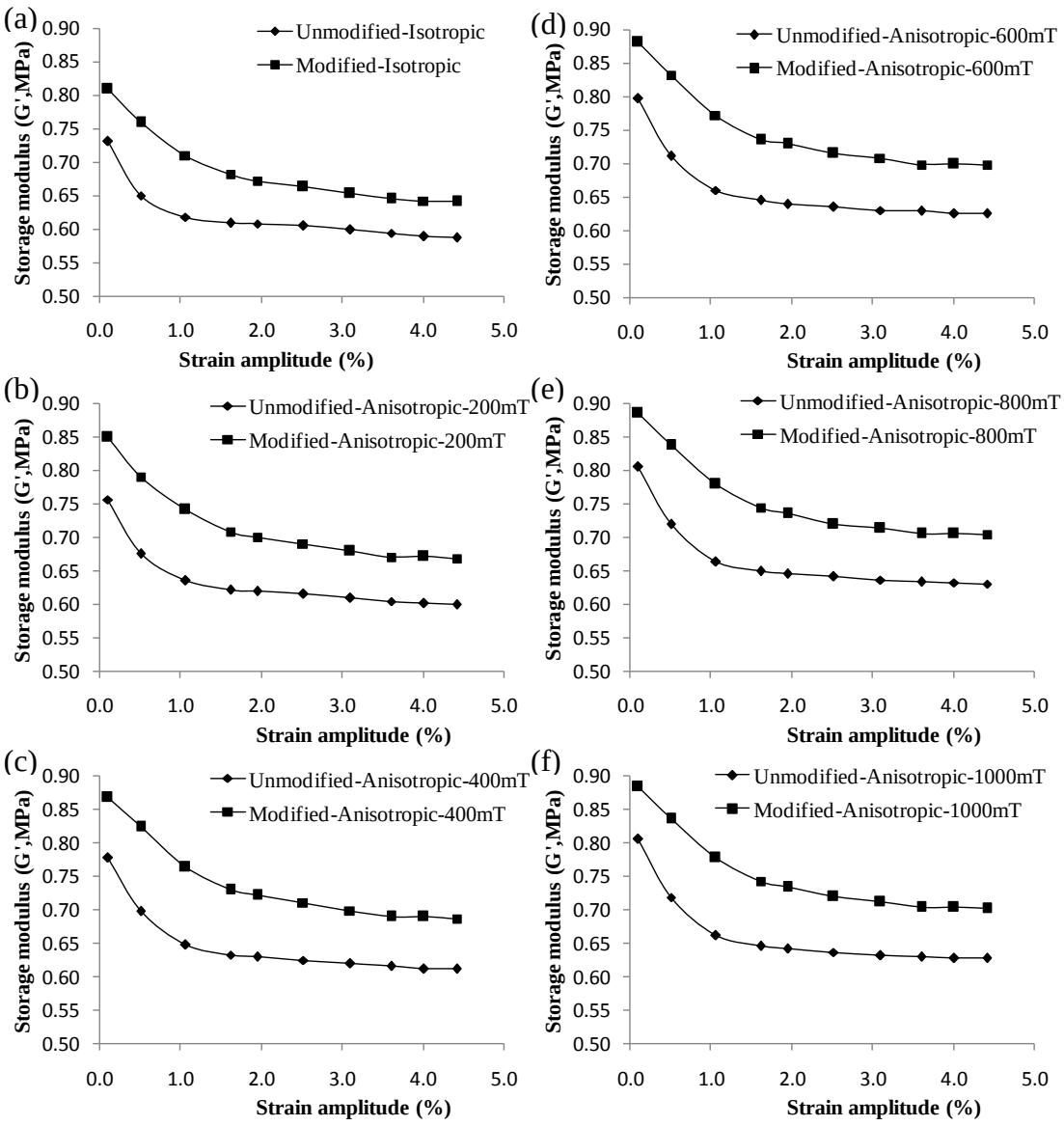

Figure 6.8 Storage modulus versus strain amplitude: (a) isotropic MRE – 0 mT; (b) anisotropic MRE – 200 mT; (c) anisotropic MRE – 400 mT; (d) anisotropic MRE – 600 mT; (e) anisotropic MRE – 800 mT and (f) anisotropic MRE – 1000 mT.

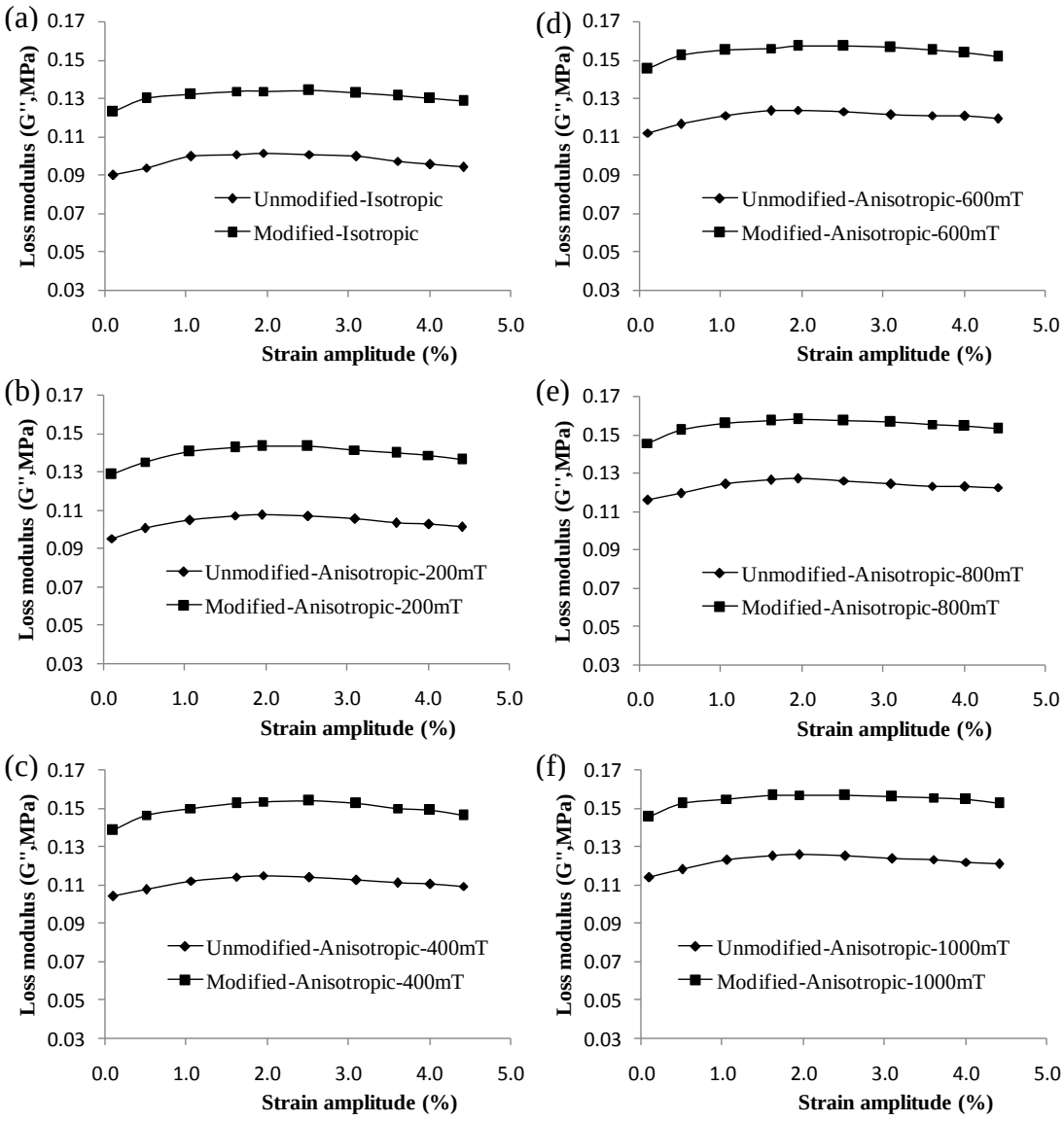

Figure 6.9 Loss modulus versus strain amplitude: (a) isotropic MRE – 0 mT; (b) anisotropic MRE – 200 mT; (c) anisotropic MRE – 400 mT; (d) anisotropic MRE – 600 mT; (e) anisotropic MRE – 800 mT and (f) anisotropic MRE – 1000 mT.

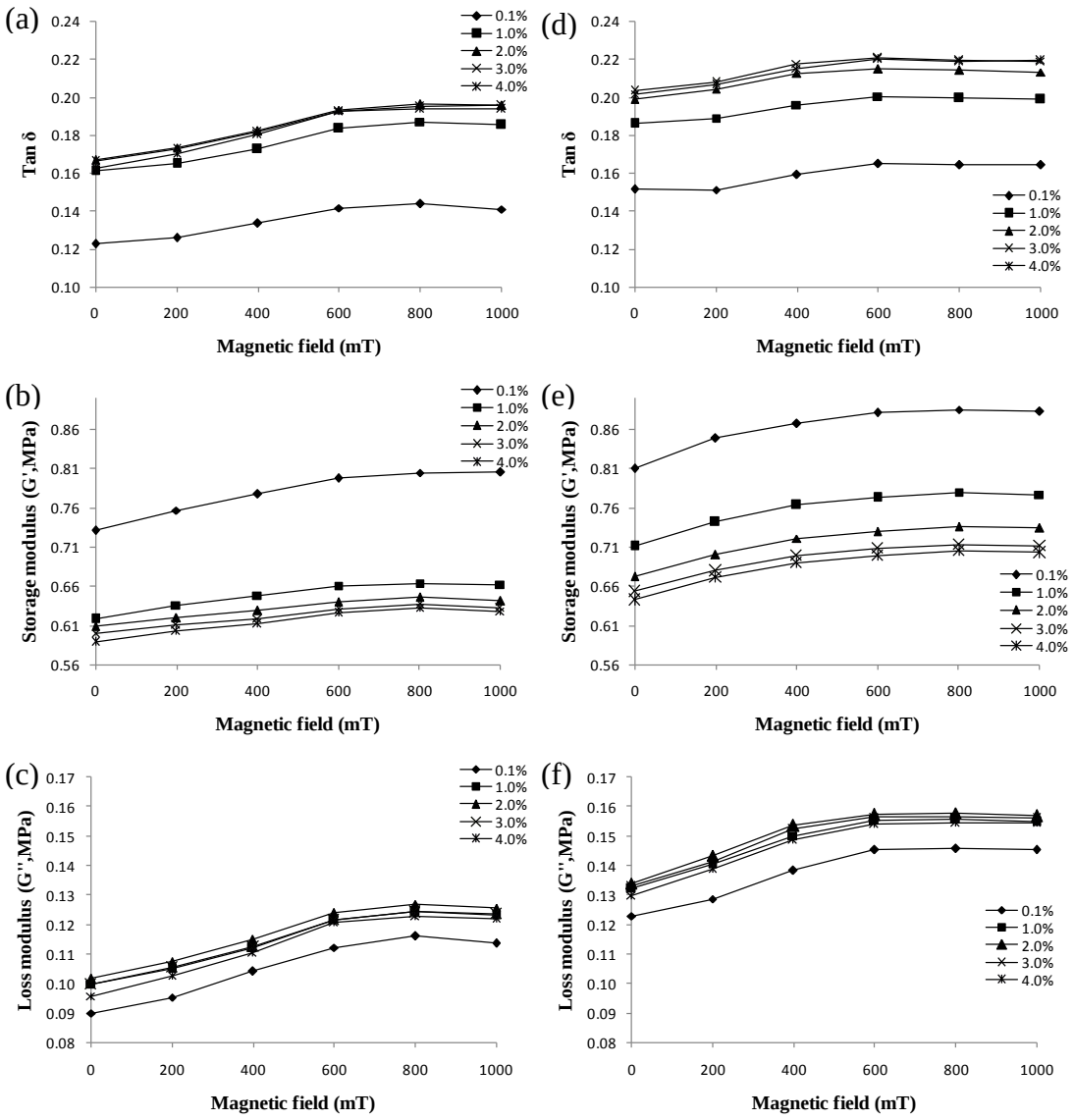

Figure 6.10 (a) Tan δ, (b) storage modulus (G') and (c) loss modulus (G") versus magnetic field (mT) for MREs with unmodified iron sand and (d) tan δ, (e) G' and (f) G" versus magnetic field (mT) for MREs with modified iron sand at different strain amplitudes

Table 6.2 presents the glass transition temperatures (T_g) and maximum values of tan δ (associated with the T_g of the materials) of isotropic and anisotropic MREs with unmodified and modified iron sand. It was shown in Part 1, Section 5.3.3 that the presence of coupling agent did not strongly affect the T_g and the height of the tan δ peak (maximum tan δ) of isotropic MREs; the T_g values shifted to a slightly higher temperature and the height of the tan δ peak slightly decreased with addition of coupling agent. The shift of T_g to higher temperature and a decrease height of the tan δ peak has been explained due to stronger interfacial bonding bringing more restriction in mobility of rubber chains in the materials. From Table 6.2, it can be seen that, the effect of silane treatment for anisotropic MREs similarly resulted in a slight increase of T_g value as well as a slight decrease of maximum tan δ. It is known for materials containing non-magnetic particles, that in the glass transition zone, the energy dissipation due to the segmental motion of macromolecular chains of the rubber matrix far overweighs that through breakdown of filler-rubber interactions [196]; furthermore for anisotropic MREs, the damping through magnetic interactions around T_g is thought to be insignificant with the height of the tan δ peak for anisotropic MREs having been observed to be lower than those of unfilled natural rubber, as previously obtained in Section 4.3.4. It is also noted that increasing magnetic field (and so degree of anisotropy) resulted in a slight increase in maximum tan δ but no change of T_g. The increase of maximum tan δ value with increased degree of anisotropy could be explained due to more trapped rubber released allowing a greater free volume of rubber to participate in large scale motions at T_g and consequently increased damping [159].

Table 6.2 Maximum tan δ at T_g and T_g values of isotropic and anisotropic MREs with unmodified and modified iron sand.

Iron sand modification	MRE type	Magnetic field (mT)	T_g (C°)	Maximum tan δ at T_g
Unmodified	isotropic	0	-46.4	2.372
	anisotropic	200	-46.3	2.386
	anisotropic	400	-46.3	2.395
	anisotropic	600	-46.3	2.421
	anisotropic	800	-46.3	2.413
	anisotropic	1000	-46.3	2.421
Modified	isotropic	0	-45.7	2.267
	anisotropic	200	-45.7	2.323
	anisotropic	400	-45.3	2.351
	anisotropic	600	-45.2	2.369
	anisotropic	800	-45.1	2.371
	anisotropic	1000	-45.2	2.374

6.3.3 Hysteresis

Figure 6.11 shows the hysteresis loss for isotropic and anisotropic MREs with unmodified and modified iron sand. As can be seen, hysteresis loss for isotropic and anisotropic MREs with modified iron sand is higher compared to those with unmodified iron sand. This improvement for isotropic, as well as anisotropic MREs cured at 200, 400, 600, 800 and 1000 mT was approximately 25%, 32%, 41%, 23%, 31% and 22%, respectively. The effect of coupling agent on the hysteresis loss of isotropic MREs could again be explained by increased energy absorbed during viscous flow which is more constrained due to formation of chemical linkages between iron sand and rubber and increased energy loss due to more stress released in breaking bonds (higher strain amplitude than the previous experiment assessing the effect of temperature on tan δ). For anisotropic MREs with modified iron sand, similar mechanisms would be involved as well as further energy loss due to

breakdown of joint rubber shells with more trapped rubber released. However, hysteresis loss for anisotropic MREs with unmodified and modified iron sand demonstrated no obvious trend with magnetic field. This suggests that formation of different lengths of magnetic particle chains in anisotropic MREs and magnetization of particles by curing the materials under different magnetic fields have minimal influence on hysteresis loss. This seems to contradict the previous results for the effect of magnetic field on tan δ at different frequencies and strain amplitudes. However, the differences observed could be due to the different mode of loading during testing, tensile versus shear (as shown in Figure 4.11); the energy absorbed due to magnetic particle interaction would be less in a tensile loading mode used in this experiment compared with shear loading using the DMA, given that in tension, it is largely only the spacing increasing between chains that is changing, whereas in shear loading, the spacing within chains and so between the particles increases.

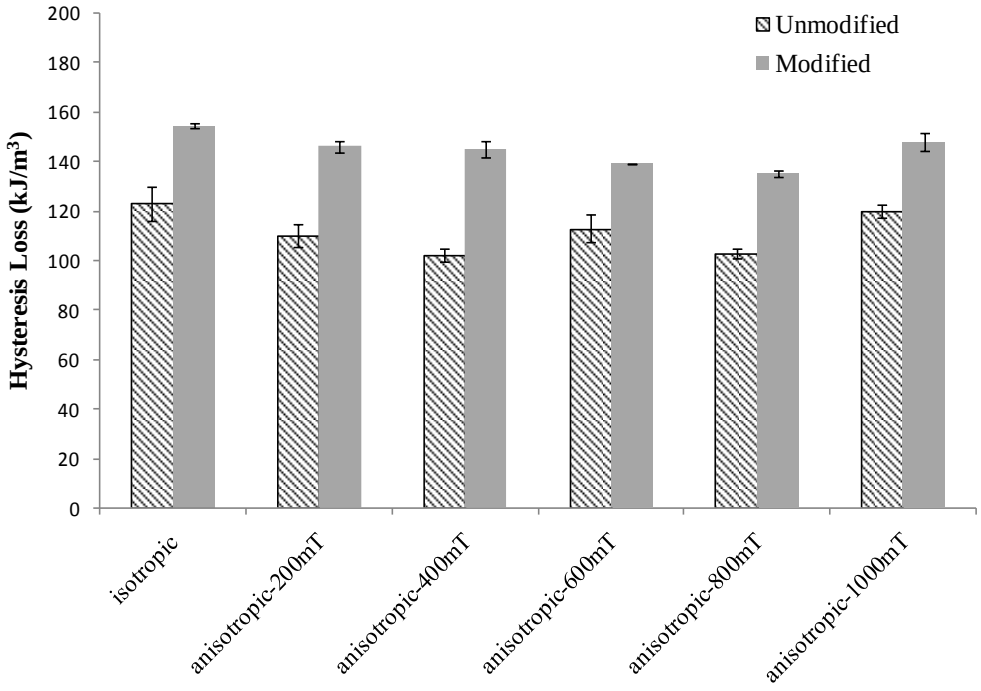

Figure 6.11 Hysteresis loss for isotropic and anisotropic MREs

6.4 Chapter conclusion

It was found that alignment of magnetic particles occurred as a consequence of an applied magnetic field for modified iron sand particles, similar to that obtained in Section 4.3.1 with unmodified iron sand and the chains became longer and more aligned as the magnetic field strength increased. Tan δ was found to be higher for isotropic and anisotropic MREs with modified iron sand compared to MREs with untreated iron sand, with 20-40% improvement over the whole frequency range explored and 11-20% improvement over the strain amplitude range explored. Tan δ increased with increasing magnetic field up to a saturation point at 600 mT. However, the presence of coupling agent and formation of different lengths of aligned particles did not strongly affect the value of T_g and maximum tan δ at T_g which can be explained by the segmental motion of rubber chains being by far the most significant influence on energy absorption at this temperature as supported by the literature. An increase in hysteresis loss was obtained for isotropic and anisotropic MREs through modification of iron sand, although no obvious trend was seen at different magnetic fields; this is in contrast to the results for the effect of magnetic field on tan δ at different frequencies and strain amplitudes which could be due to the different mode of loading used when studying hysteresis loss.

Chapter 7

Comparison of Dynamic Properties of Developed Magnetorheological Elastomers with Existing Antivibration Rubbers

7.1 Introduction

In this chapter, tan δ and energy dissipated during hysteresis testing of isotropic and anisotropic MREs developed during this thesis work were compared with existing antivibration rubbers. MREs containing 70 phr silane modified iron sand particles in a natural rubber matrix were prepared and curing was carried out in the absence or presence of a magnetic field. The antivibration rubbers for comparison were prepared according to existing formulations from published patents (see details in Table 7.1). Those chosen, contained different contents of carbon black filler (30, 50 and 70 phr) in a natural rubber matrix. In addition, anisotropic MREs containing 70 phr silane modified iron sand and a predetermined amount of carbon black were also prepared in order to investigate the influence of carbon black on the damping performance of the MREs. Tan δ was measured using dynamic mechanical analysis (DMA) over a range of frequency (0.01–130 Hz), strain amplitude (0.1–4.5%), and temperature (-100–50°C). Energy dissipated was measured using a universal tester under cyclic tensile loading. The morphological characteristics were examined using scanning electron microscopy (SEM).

Table 7.1 Comparative samples' patent specifications

Comparative sample	Patent number	Applicant	Title	Description
1	US 2011/0166276 A1 [199]	Tokai Rubber Industries Ltd	Antivibration rubber composition	The invention relates to a vibration damping rubber composition to be used for an engine mount or the like adapted to support an engine in an automobile or the like and suppress transmission of vibrations.
2	EP 0 481 810 B1 [200]	Sumitomo Rubber Industries Ltd	Rubber composition for laminated vibration proofing structure	The present invention relates to a rubber composition for use in the seismic isolation of a bridge, a building or a house.
3	US6180711 B1 [201]	Yokohama Rubber Co. Ltd	Rubber composition for seismic isolation laminates	This invention relates to a rubber composition for seismic isolation laminate for buildings.

7.2 Experimental

7.2.1 Materials

Natural rubber (SMR L grade) and other chemicals including zinc oxide, stearic acid, n-cyclohexyl-2-benzothiazole sulfenamide (CBS), tetramethylthiuram disulphide (TMTD), paraffin oil, and naphthenic oil were all purchased from Field Rubber Limited, Auckland. Bis-(3-triethoxysilylpropyl) tetrasulphane (TESPT) was purchased from Leap Lab Chem Co. Ltd. Carbon black was purchased from Shijiazhuang Changhang Co. Ltd. Iron sand was collected from Ngarunui Beach, Raglan. The iron sand was then milled using a planetary mono mill (Pulverisette 6) produced by Fristech GmbH and subsequently sieved to obtain a 45-56 μm particle size range.

7.2.2 Surface Modification of Iron Sand

The surface modification of iron sand was carried out by using aqueous alcohol solution method as previously described in Section 5.2.2. The particles were subjected to surface treatment with TESPT at 6 (wt%) by weight of the particles.

7.2.3 Preparation of MREs and comparative samples

The compound formulation used in this study is given in Table 7.2. The formulations of comparative samples based on published patents comprised of natural rubber and carbon black as the major components with processing aids and crosslinking agent. Additives such as anti-oxidant, anti-thermal aging agent and petroleum resin were excluded from the formulations. Isotropic and anisotropic MREs were fabricated according to the methods as previously described in Section

Table 7.2 Formulation of rubber compounds

Materials	**MRE/ISO**	**MRE/AN**	**MRE/AN/30CB**	**MRE/AN/50CB**	**Comparative sample 1 (CS/30CB)**	**Comparative sample 2 (CS/50CB)**	**Comparative sample 3 (CS/70CB)**
Natural Rubber	100	100	100	100	100	100	100
ZnO	5	5	5	5	5	5	5
Stearic Acid	1	1	1	1	1	1	1
Paraffin Oil	2	2	2	2	2	-	-
Naphthenic Oil	3	3	3	3	3	10	5
Iron sand	70	70	70	70	-	-	-
Carbon black	-	-	30	50	30	50	70
CBS	2	2	2	2	2	1.9	1
TMTD	1	1	1	1	1	0.8	-
Sulphur	1.5	1.5	1.5	1.5	1	0.8	1.5
Curing condition							
Temperature (ºC)	150	150	150	150	150	150	150
Pressure (MPa)	12	12	12	12	12	12	12
Magnetic field during curing (mT)	0	600	600	600	-	-	-

4.2.4. The comparatives samples were fabricate similar to methods used to fabricate isotropic MREs. The cure time at 150°C was then determined according to the procedure as described in Chapter 3 and the results are attached in the Appendix III.

7.2.4 Characterisation

Morphology

The microstructures of isotropic and anisotropic MREs were observed using the method described in Section 4.2.5

Dynamic mechanical analysis

Dynamic mechanical analysis was carried out using the method described in Section 4.2.5

Hysteresis

Hysteresis loss was carried out using the method described in Section 4.2.5

7.3 Results and discussion

7.3.1 Morphology

Figure 7.1 shows SEM images of MREs and comparative samples. It can be seen that MRE/ISO had uniform iron sand particle distribution in the rubber matrix without obvious aggregation (Figure 7.1a). Figure 7.1b shows an MRE/AN sample cured under an applied magnetic field of 600 mT at elevated temperature; as expected, the iron sand organized into chain-like columnar structures. For comparative samples, the carbon black particles were generally evenly distributed in the rubber matrix but with some aggregates ranged probably from below the resolution of the SEM up to 20 μm as seen in Figure 7.1c. For MRE/AN/50CB

sample (Figure 7.1d), it can be seen that the presence of carbon black has constrained the movement of iron sand particles and the chain-like columnar structures are shorter and less aligned than MRE/AN sample.

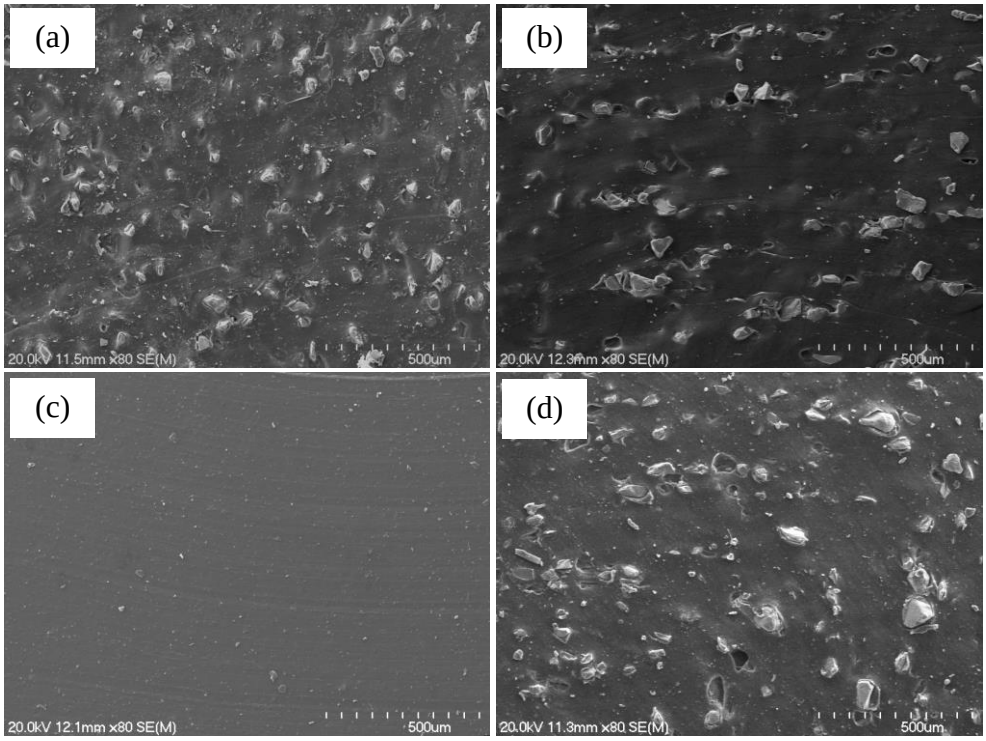

Figure 7.1 SEM images of surface of; (a) MRE/ISO (ISO), (b) MRE/AN, (c) CS/50CB and (d) MRE/AN/50CB

7.3.2 Dynamic Mechanical Analysis

The variation of tan δ with frequency for MREs and comparative samples is depicted in Figure 7.2a. Generally, tan δ increased with increasing frequency, with tan δ values for both MRE/ISO and MRE/AN found to be lower than for the others at most frequencies, although relatively larger increases in tan δ above 100Hz compared to other samples occurred, such that at the highest frequencies explored, tan δ values for MRE/ISO and MRE/AN were at the upper end of those obtained. The increase of tan δ as the frequency increased for isotropic MREs and comparative samples could

be due to increased energy absorbed through viscous flow of the rubber matrix and interfacial damping between the particle and the rubber matrix; for anisotropic MREs, similar mechanisms would be involved as well as potentially, energy absorbed through magnetic interactions; for samples containing carbon black, increased energy could be absorbed due to overcoming inter-particle interactions (Van der Waals) [140]. The difference in trends observed for MREs and comparative samples are likely to be due to the relatively different amounts of energy absorbed by different mechanisms involved with different reinforcement particles at different frequencies. It can also be seen that tan δ of MRE/AN is about 8% higher than MRE/ISO over the whole frequency range explored; the higher tan δ of MRE/AN can be attributed to multiple mechanisms described previously in Chapter 6 which can be summarized as constraint of joint rubber shells between neighbouring iron sand particles, less trapped rubber and damping through magnetic interactions (magnetomechanical damping and inter-particle magnetic interactions). For the comparative samples, tan δ increased in the following order: CS/30CB < CS/50CB < CS70/CB, correlating with the increased content of carbon black. A significant improvement of tan δ was observed for comparative samples when compared to MRE/ISO and MRE/AN; it was suspected that this could be due to the presence of carbon black in the formulation. In order to assess the influence of carbon black on damping performance of MREs, two compounds were prepared that were the same as MRE/AN except they had additions of 30 and 50 phr carbon black (MRE/AN/30CB and MRE/AN/50CB). It was found that such additions of carbon black gave good improvement of tan δ, the tan δ values for MRE/AN/30CB and MRE/AN/50CB were 21% and 43% higher than MRE/AN, indeed, the tan δ were 10% and 7% higher compared to CS/30CB and CS/50CB over

the whole frequency range explored, supporting the use of iron sand to improve damping. The effect of carbon black on tan δ can be analysed further using storage modulus (G') and loss modulus (G") plots as shown in Figure 7.2 (b and c). It is apparent that G' and G" for samples containing carbon black are much higher than those for MRE/ISO and MRE/AN. The G' increases with increasing carbon black content up to the highest values at 70 phr carbon black. The increase in G' can be explained by the increased carbon black particle-rubber interactions and carbon black particle-particle interactions, as reported by number of researchers [140, 202]. The particle-rubber interactions include physical adsorption of rubber chains on carbon black filler surfaces and chemical bonding between functional groups on the surface of carbon black (mostly quinonic groups) with rubber molecular chains which will restrain the mobility of rubber on the filler surface. The particle-particle interactions relate to the tendency of carbon black particles to form aggregates at different levels. Carbon black aggregates agglomerate together to form what are known as primary aggregates, held together by Van der Waals bonds. Further agglomeration occurs between primary aggregates to produce secondary aggregates, again held together by Van der Waals bonds, although the secondary aggregates are less rigidly held together. The particle-rubber interactions and particle-particle interactions lead to the formation of a carbon black filler networks in the rubber matrix as shown in Figure 7.3. These contain rubber with different degrees of constraint (bound rubber, occluded rubber and trapped rubber), higher than that for rubber away from carbon black particles. These constrained rubber regions improve the ability to store elastic energy, resulting in increased G'. The increase of G" with increasing carbon black

content during deformation can be explained by the increased energy loss that occurs due to the breakdown and reformation of the carbon black filler networks.

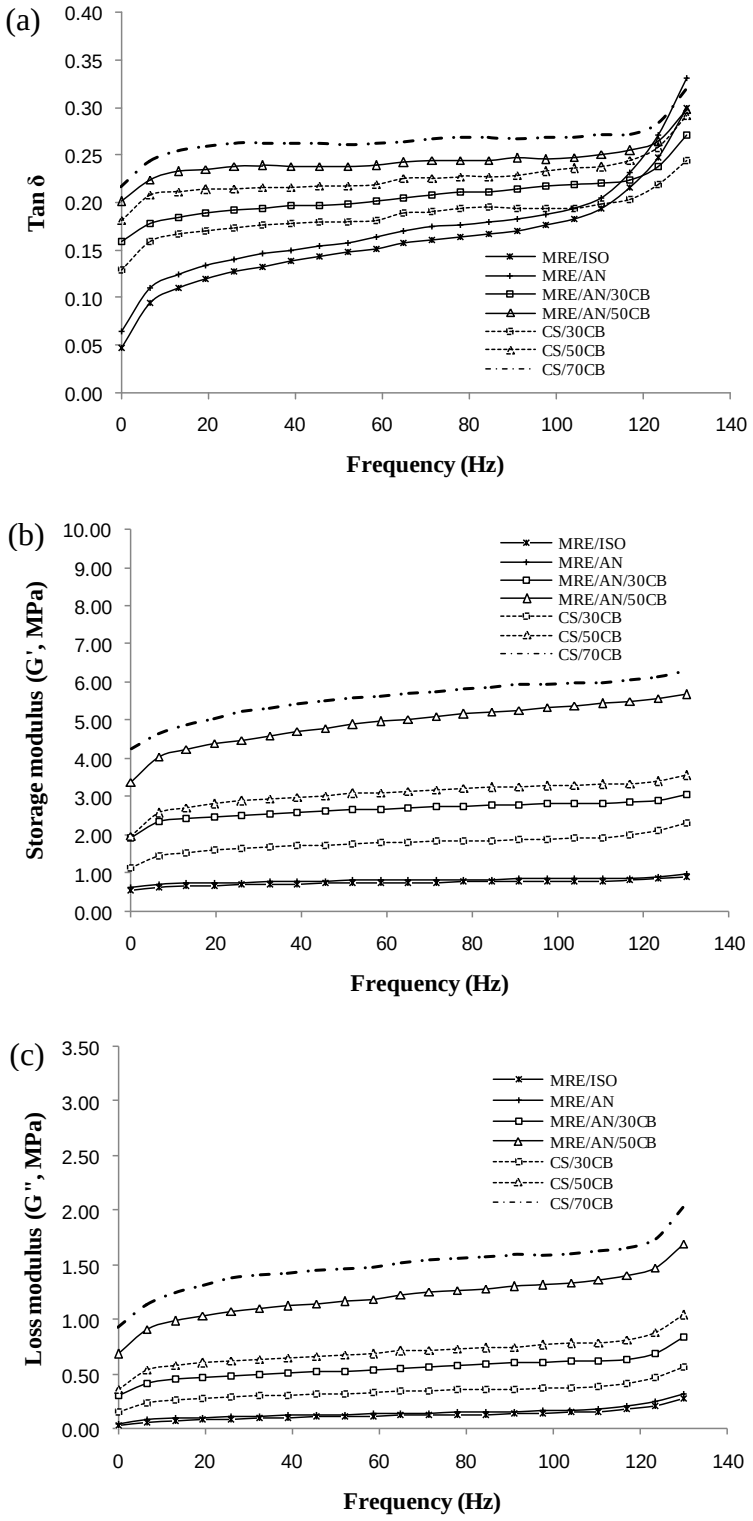

Figure 7.2 (a) Tan δ, (b) storage modulus (G') and (c) loss modulus (G'') versus frequency for MREs and comparative samples.

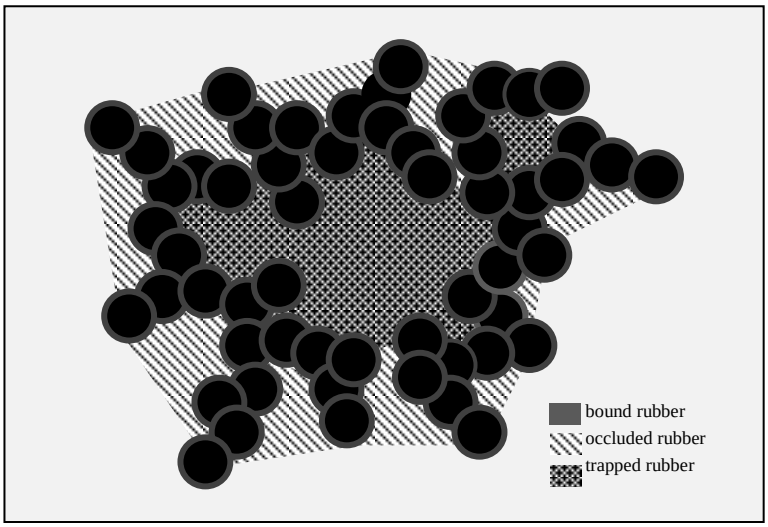

Figure 7.3 Schematic presentation of carbon black filler network

The variation of tan δ with strain amplitude for MREs and comparative samples is depicted in Figure 7.4a. Tan δ was amplitude dependent at low strain amplitude before reaching a plateau, with increasing tan δ for MRE/AN and MRE/ISO at around 2.5% strain amplitude, whereas for the other samples containing carbon black the tan δ reached a plateau at around 1.5% strain amplitude. The increased amplitude dependence for MRE/AN and MRE/ISO compared to comparative samples indicates that the amplitude of applied strain required to break stronger interfacial bonding between iron sand and rubber was relatively large compared to easier that required for breaking down carbon black filler networks. At the plateau region, it would appear that most of the filler-rubber interactions diminish (Van der Waals for carbon black and Van der Waals and covalent for iron sand) and tan δ is largely reliant on the rubber matrix which is at its largest due to greatest amount of rubber free to flow and friction between rubber chains and iron sand. Tan δ of MRE/AN was found to be 8.5% higher than that of MRE/ISO over the whole

strain amplitude range explored; the higher tan δ for MRE/AN can again be explained due to additional damping through breakdown of joint rubber shells, more trapped rubber released and magnetic interactions (magnetomechanical and inter particle interaction). Indeed, it can also be seen that although the tan δ for MRE/AN is lower at low strain amplitudes, it is slightly higher than for CS/30CB above a strain amplitude of 2%. For the comparative samples, tan δ increased in the following order: CS/30CB < CS/50CB < CS70/CB, along with the increased content of carbon black. Similarly, tan δ values for MRE/AN/30CB and MRE/AN/50CB were higher than MRE/AN (6% and 15%, respectively) and the tan δ approximately 4% and 5% higher compared to CS/30CB and CS/50CB over the strain amplitude range explored as was seen for range of frequency discussed in the previous paragraph. Again, the effect of carbon black on improved tan δ can be analysed further using G' and G" plots as shown in Figure 7.4 (b and c). It is apparent that G' and G" for samples containing carbon black are much higher than MRE/ISO and MRE/AN, which is not surprising given similar trends with influence of frequency on G' and G". As previously discussed, the increase of G' with increase in carbon black content can be explained by increased amount of constrained rubber in filler networks and the increased energy loss is likely due to breakdown and reformation of filler networks during cyclic deformation along with more constrained rubber flow.

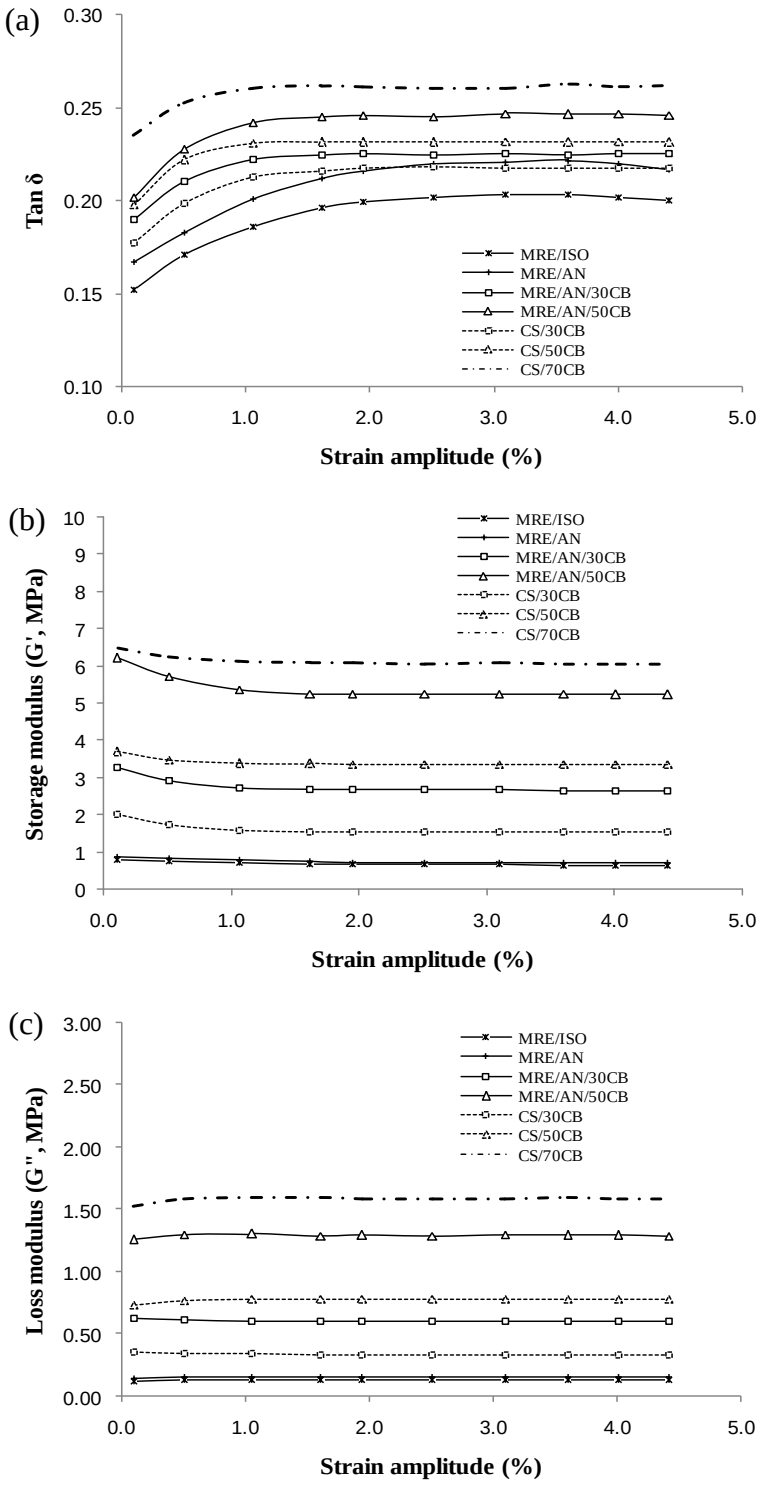

Figure 7.4 (a) Tan δ, (b) storage modulus (G') and (c) loss modulus (G") versus strain amplitude for MREs and comparative samples.

Figure 7.5 presents the tan δ versus temperature curves for MREs and comparative samples. The tan δ peak is associated with the glass transition temperature (T_g) of the materials. In general, the trend for the height of the tan δ peak is different compared to trends observed previously for the effect of frequency and strain amplitude on tan δ; the tan δ peaks for MRE/ISO and MRE/AN are higher than for the others and the height of the tan δ peak decreased with increasing carbon black content in the following order: CS/30CB > CS/50CB > CS70/CB. To explain the trend seen here, it is necessary to consider the relative change of contributions by different energy dissipation mechanisms in the glass transition zone. It is known for materials containing non-magnetic particles, that in the glass transition zone, contribution from segmental motion of rubber chains generally far outweighs the energy absorption through breakdown of filler-filler and filler-rubber interactions [196]. Furthermore for anisotropic MREs, the damping through magnetic interactions around T_g is thought to be insignificant compared with that due to segmental motion of rubber chains with the height of the tan δ peak for anisotropic MREs having been observed to be lower than unfilled natural rubber, as previously obtained in Section 4.3.4. Based on such importance of rubber chain motion, the higher tan δ peak for MRE/ISO and MRE/AN can be explained due to a greater volume of free rubber chains participating in large scale motions at T_g which is likely to be due to less constrained rubber with iron sand particles in the MRE/ISO and MRE/AN than with carbon black particles in the comparatives samples due to the difference in interfacial area, being much smaller in the case of the much larger iron sand particles. For samples containing carbon black, further regions of constrained rubber would also form within carbon black filler networks; this constrained rubber is shielded from

deformation and loses its ability to participate in the energy dissipation process. There also appears to be a slightly higher tan δ peak for MRE/AN compared with MRE/ISO which is likely to be due to formation of aligned structures in anisotropic MREs reducing the amount of trapped rubber. The decrease in height of the tan δ peak with increased carbon black content could be explained by the increased amount of constrained rubber on carbon black surfaces and within filler networks. The height of the tan δ peaks for MRE/AN/30CB and MRE/AN/50CB were found to be lower than the tan δ peaks for CS/30CB and CS/50CB, supporting iron sand contributing to rubber constraint. It is also apparent that T_g values for MREs (MRE/ISO, MRE/AN, MRE/AN/30CB and MRE/AN/50CB) are slightly higher compared to comparative samples (CS/30CB, CS/50CB and CS/70CB). This observation suggests that strong interfacial bonding between iron sand and rubber increased the temperature required for the rubber molecular chains to attain maximum segmental motion.

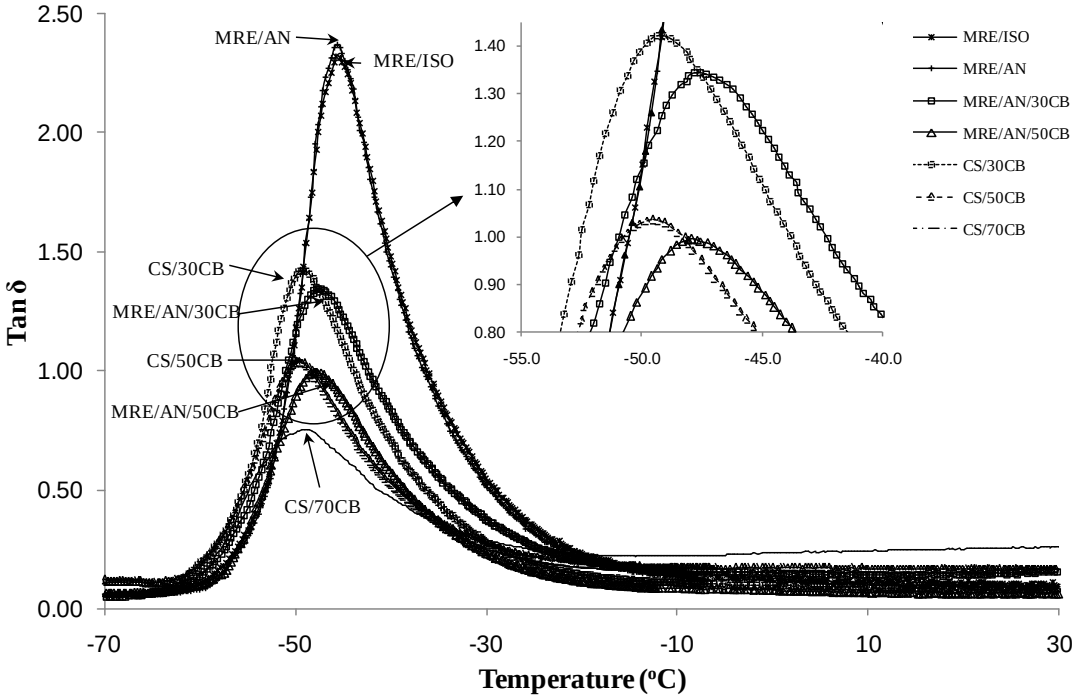

Figure 7.5 Tan δ versus temperature curves for MREs and comparative samples.

7.3.3 Hysteresis

Figure 7.6 shows hysteresis loss for MREs and comparative samples. Hysteresis loss for both MRE/ISO and MRE/AN was found to be lower than for the other samples. Hysteresis loss in isotropic MREs could be associated with the energy absorbed during viscous flow which is constrained due to strong interfacial bonding between iron sand and rubber and energy loss due to stress released in breaking the interfacial bonding and given higher hysteresis loss than for unfilled rubber (31 kJ/m^3, obtained in Section 4.3) ; for anisotropic MREs, similar mechanisms would be involved as well as further energy loss due to breakdown of joint rubber shells with more trapped rubber released, however, the damping through magnetic interactions would appear to be insignificant given that the hysteresis loss for MRE/AN was lower than MRE/ISO. This seems to contradict the results for the effect of frequency and strain amplitude on tan δ, which could be explained as being due to a different mode of loading during testing as previously discussed in Section 4.3.5 (tensile versus shear). In tension as in the case here, it is largely the spacing increasing between chains that is changing, whereas in shear loading, the spacing within chains and so between the particle increases. It is possible that in the direction of tensile loading, the particles are separated to such an extent in anisotropic MREs that inter-particle attraction is less effective than for the isotropic MREs. For the comparative samples, hysteresis loss increased in the following order: CS/30CB < CS/50CB < CS70/CB, along with the increased content of carbon black. This could be explained due to increased energy absorbed caused by breakdown and reformation of carbon black filler networks with increase in carbon black content which becomes more significant than the reduction of segmental motion of rubber chains (away from T_g).

Furthermore, when the applied strain increases to such an extent the filler network can be broken down, the constrained rubber would be released and therefore allow more viscous flow during deformation, resulting in an increase of dissipated energy. As can also be seen, hysteresis loss for MRE/AN/30CB and MRE/AN/50CB significantly increased compared to MRE/AN (21% and 71%, respectively), supporting the data obtained for assessment of the effect of frequency and strain amplitude on tan δ, that addition of carbon black results in higher energy dissipation in the materials (other than around T_g). Also hysteresis losses for MRE/AN/30CB and MRE/AN/50CB were approximately 5% and 8% higher compared to CS/30CB and CS/50CB, supporting the use of iron sand to improve hysteresis loss.

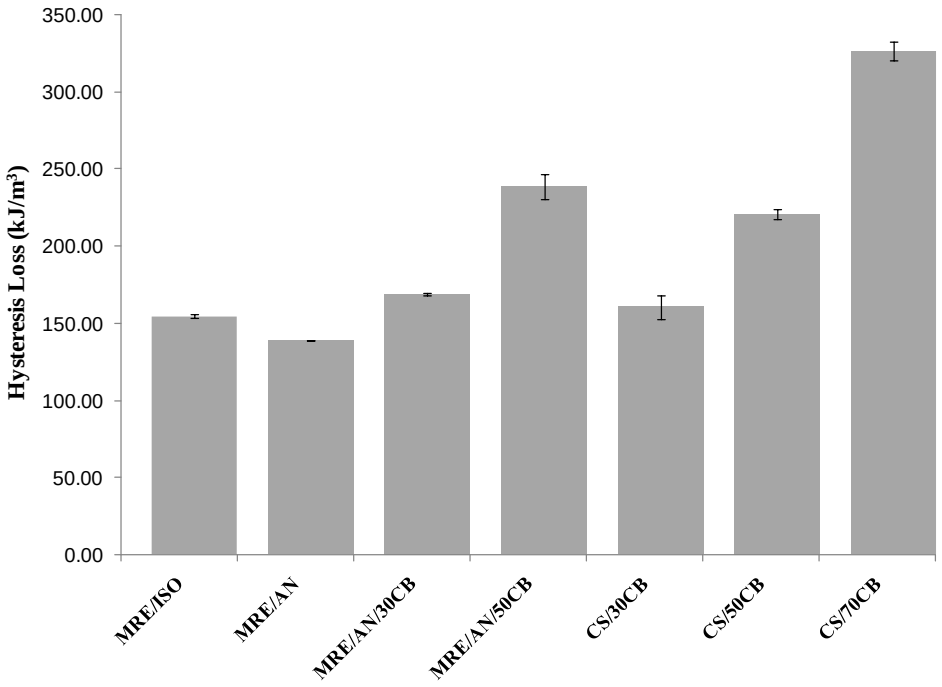

Figure 7.6 Hysteresis loss for MREs and comparative samples

7.4 Chapter conclusion

It was found that isotropic MREs had uniform iron sand particle distribution without obvious aggregation and curing the materials under an applied magnetic field at elevated temperature resulted in the iron sand organizing into chain-like columnar structures. For comparative samples, carbon black particles were generally evenly distributed in the rubber matrix but with some aggregates, but none larger than 20μm. SEM also revealed that addition of carbon black into anisotropic MREs constrained the movement of iron sand particles; chain-like columnar structures became shorter and less aligned. Energy absorption for comparative samples (CS/30CB, CS/50CB and CS/70CB) was generally found higher than MRE/ISO and MRE/AN over the range of frequency and strain amplitude explored, as well as in hysteresis testing and this was believed to be largely due the presence of carbon black in the formulation. Further assessment carried out on materials that were the same as MRE/AN except they had additions of 30 and 50 phr carbon black (MRE/AN/30CB and MRE/AN/50CB) gave generally higher energy absorption than comparative samples of the same carbon black contents (CS/30CB and CS/50CB), supporting the use of iron sand to improve damping. However, trends for energy absorption at around T_g were found to reverse which can be explained by the segmental motion of rubber chains being by far the most significant influence on energy absorption at this temperature as supported by literature and so care should be taken when using the materials at such temperature although this is likely to be away from the service temperature for these materials.

Chapter 8

Investigation and Modelling of Damping Mechanisms of Magnetorheological Elastomers

8.1 Introduction

Damping in MREs is considered to be ascribed to viscous flow of the rubber matrix, interfacial damping at the interface between the magnetic particles and the matrix and magnetism-induced damping. In this study, individual components in MREs that contribute to material damping were investigated. A corresponding model was developed to determine the total damping capacity (ψ_{MRE}) from all mechanisms as well as factors that influenced the damping capacity. Then, the proposed model was verified experimentally using a series of MRE samples. Isotropic and anisotropic MREs were prepared with different contents of silane modified iron sand particles and curing was carried out in the absence or presence of a magnetic field. Tan δ was used as the fundamental parameter to assess damping and was measured through dynamic mechanical analysis (DMA) under a series of frequency and strain amplitude ranging from 0.01Hz-130Hz and 0.1-4.5%, respectively.

8.2 Experimental

8.2.1 Damping mechanisms of MREs

MREs can be regarded as a type of particulate reinforced composite. In most particulate composites the reinforcement is much stiffer than the matrix and is practically non-dissipative material. Damping is essentially due to the viscous flow of the matrix and friction at the interface between the components. However, the damping in MREs also occurs due to magnetism-induced damping through magnetic particle interaction and magnetomechanical damping. Therefore, modelling damping capacity of MREs requires identification of the individual components in the material and a determination of their contributions to the total damping. Thus, the overall damping of MREs can be expressed as

$$\psi_{MRE} = \psi_V + \psi_I + \psi_M \tag{8.1}$$

where ψ_{MRE} is the overall material damping capacity, ψ_V is viscous damping, ψ_I is interface damping and ψ_M is magnetism-induced damping.

8.2.1.1 Viscous damping

Viscous damping of MREs is mainly provided by the rubber matrix. Rubber is a viscoelastic material which exhibits both viscous and elastic behaviour. The elastic stress follows Hooke's law where stress is directly proportional to strain while the viscous stress follows Newton's law of viscosity, which states that, viscous stress is proportional to strain rate. For a viscoelastic material, the stress-strain relationship is expressed by a linear differential equation with respect to time. A commonly

employed relationship is based on the Kelvin Voight model. This model can be represented by spring and dashpot elements (Figure 8.1) and can be expressed as:

$$\tau = G\gamma + G^* \frac{d\gamma}{dt} \tag{8.2}$$

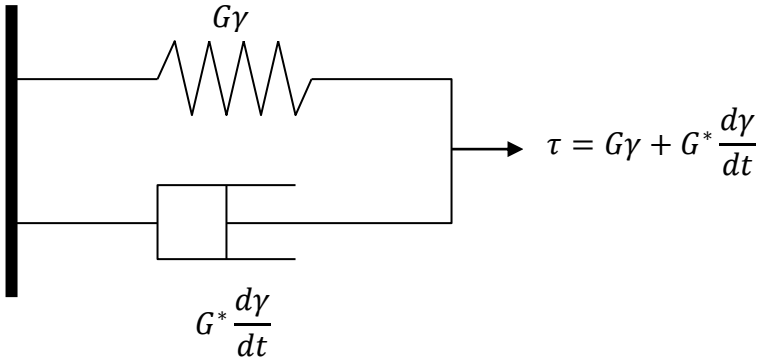

Figure 8.1 Representation of rubber elastic and viscous components according to the Kelvin Voight model

In equation 8.2, G is shear modulus and G* is a complex modulus. The term Gγ represents the elastic component which does not contribute to damping. The term G* dγ/dt is the viscous component and embodies for damping. From the Kelvin Voight model, the viscous damping per unit volume is

$$\psi_V = G^* \oint \frac{d\gamma}{dt}\, d\gamma \tag{8.3}$$

If the material is subjected to a harmonic (sinusoidal) excitation, at steady state, the strain can be expressed as follows

$$\gamma = \gamma_{max} \cos \omega t \tag{8.4}$$

By substituting Equation 8.4 into 8.3, the damping capacity per unit volume can be expressed as

$$\psi_V = \pi\omega G^* \gamma_{max}^2 \tag{8.5}$$

Now, $\gamma = \gamma_{max}$ when t = 0 in Equation 8.4, or when $d\gamma/dt = 0$. The corresponding stress according to Equation 8.2, is $\tau_{max} = G\gamma_{max}$. It follows that

$$\psi_V = \frac{\pi\omega G^* \tau_{max}^2}{G^2} \tag{8.6}$$

so it would be expected that ψ_V depends on the frequency, ω. At low levels of damping (tan δ < 1) for viscoelastic material, ψ_V can be equated with other common damping measures as estimated in references [70, 163] and can expressed as follows:

$$\psi_V = \eta = tan\ \delta \tag{8.7}$$

where η is the loss factor which is defined as the specific damping capacity per radian of damping cycle and tan δ is a comparison between energy lost to that stored as previously defined in Section 2.2.

8.2.1.2 Interfacial damping

The interface between magnetic particles and the matrix is also important in determining the damping of MREs. Interfacial damping can be attributed to damping through strongly bonded interfaces and weakly bonded interfaces. In the next section the model for damping through strongly bonded interfaces and weakly bonded interfaces are described.

Strongly bonded interfaces

For MREs containing particles with functionalized surfaces, polymer molecules can bond to the surface of the particles such that a third phase is formed

known as the interphase. The interphase possesses properties distinct from those of the matrix and the particles. The interphase mainly plays the role of transferring stress between the matrix to the reinforced particles. The energy absorption could be attributed to energy required to bring about viscous flow of constrained materials in the vicinity of the particle interfaces, as well as breakdown of interfacial bonding when the applied strain amplitude is high, resulting in transformation of elastic energy into kinetic energy, which then converts into heat. MREs with strongly bonded interfaces can be characterized by Schoeck theory [164]. Based on Schoeck theory, the contribution of interfacial damping of strongly bonded interfaces can be expressed as follows:

$$\psi_I^S = \frac{1}{\tau^2}\frac{1-\vartheta}{3\pi(2-\vartheta)}\frac{1}{V_p}\sum_{i=1}^{n} r_i^3\,(\tilde{\tau}^2)_i \tag{8.8}$$

where ψ_I^S denotes the strongly bonded interfacial damping, τ is the applied shear stress, ϑ is the Poisson's ratio of the matrix, V_p is volume fraction of the particle, r_i is the radius of the *i*th particle and $(\tilde{\tau})_i$ is the component of τ in the plane of the *i*th particle that has relative motion during viscous flow. The following assumption has been made to simplify the calculation; the particles all have the same diameter, the shear stress on each particle is identical and the stress concentration coefficient $\tilde{\tau}_i/\tau$ is taken as 1.5 as in the references [164, 165]. Then, the contribution of interfacial damping of strongly bonded interface in MREs can be simplified as

$$\psi_I^S = \frac{4.5\,(1-\vartheta)}{\pi^2(2-\vartheta)}V_p \tag{8.9}$$

Equation 8.9 indicates that the damping due to a strongly bonded interface is related to the particle content and the Poisson's ratio of the matrix materials.

Weakly bonded interfaces

Weakly bonded interfaces are formed due to weak interactions between particles and the matrix. For weakly bonded interfaces, the damping is mainly due to interfacial friction between the surfaces of particles and the matrix during deformation. The effect of weakly bonded interfaces on the overall damping of the composites can be characterised using Lavernia analysis [165]. In this analysis, the damping is determined by the friction coefficient between the two constituents and the normal stress at the interface where the relative moment is likely to occur as shown in Figure 8.2.

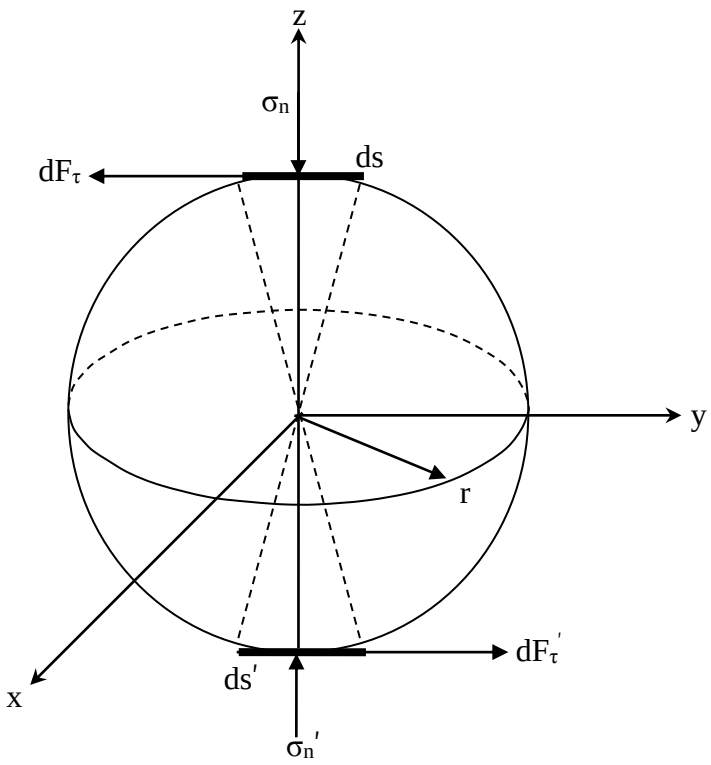

Figure 8.2 A schematic of the force at the interface where relative movement is likely to occur

As shown in Figure 8.2, the change of area that has relative movement is denoted as *ds* and the normal stress at *ds* is denoted as σ_n. When the applied stress is sufficient to overcome the resistance due to friction, relative displacement occurs, $r(\gamma_0-\gamma_{crt})$, where γ_0 is the corresponding strain amplitude and γ_{crt} is the critical strain of relative movement. The friction on the area *ds* is given as

$$dF_\tau = (f\sigma_n)ds \tag{8.10}$$

where f is the friction coefficient for the particle and matrix. Then, corresponding dissipated energy could be written as

$$dU_{dissipation} = r(\gamma_o - \gamma_{crt})(f\sigma_n)ds \tag{8.11}$$

The dissipation energy per unit volume in the materials over the whole particle surface can be expressed as

$$\begin{aligned} U_{dissipation} &= \frac{\sum_{i=0}^{n} \oint r(\gamma_o - \gamma_{crt})(f\sigma_n)ds}{V} \\ &= \frac{3\pi}{4} fV_p\sigma_n(\gamma_o - \gamma_{crt}) \end{aligned} \tag{8.12}$$

where V is volume of the MREs and V_p is the volume fraction of the particles. For simplification, equation $V_p = \frac{1}{V}\sum_{i=0}^{n} V_i$ is utilized where V_i is the volume of *i*th particle. The elastic energy stored in the material is determined as follows:

$$U_{elastic} = \frac{\frac{1}{2}\tau_o^2}{G} \tag{8.13}$$

where τ_o is applied stress, G is the shear modulus of the MREs. Subsequently, the damping can be expressed as

$$\psi_I^w = \frac{U_{dissipation}}{U_{elastic}} = \frac{3\pi}{2} \cdot \frac{fV_p\sigma_n(\gamma_o - \gamma_{crt})}{\tau_o^2/\mathrm{G}} \tag{8.14}$$

For a weakly bonded interface, it is assumed that γ_{crt} is much smaller than γ_o and therefore Equation 8.14 can be written as

$$\psi_I^w = \frac{3\pi}{2} \cdot \frac{fV_p\sigma_n}{\tau_0} \tag{8.15}$$

As stated in [203, 204], τ_0 can be equated as $\tau_0 = \sigma_{xy}$, where σ_{xy} is effective stress at the particle interfaces in the *xy* plane (see Figure 8.2). Then, Equation 8.15 can be simplified by introducing $K=\sigma_n/\sigma_{xy}$ which represents the normal stress concentration coefficient at the particle interface with relative moment. In addition, the non-uniform strain state throughout the material during deformation caused by relative movement at the interface, only occurs at part of the interface. Taking into account fraction of interface that has relative movement during deformation, a correction factor C can be introduced in Equation 8.15 as follows:

$$\psi_I^w = \frac{3\pi}{2} \cdot CfV_pK \tag{8.16}$$

Equation 8.16 indicates that the damping with weakly bonded interfaces is proportional to the particle content.

The interfacial damping of MREs can be thought as combination of both strongly bonded and weakly bonded interfaces. Therefore the total interfacial damping can be expressed as:

$$\psi_I = \psi_I^s + \psi_I^w = (1-\varphi)\frac{4.5\,(1-\vartheta)}{\pi^2(2-\vartheta)}V_p + \varphi\frac{3\pi}{2} \cdot CfV_pK \tag{8.17}$$

where φ is the proportion of weakly bonded interface in comparative relation to the total interfacial damping. According to Jie's analysis [48], φ is given by

$$\varphi = (1-V_p)^{1/3}(1-\gamma)^{1/3} \tag{8.18}$$

By substituting Equation 8.18 into Equation 8.17, the interfacial damping of MREs can be represented by:

$$\psi_I = \frac{4.5\ (1-\vartheta)}{\pi^2(2-\vartheta)}V_p + \left(\frac{3\pi}{2}\cdot CfK - \frac{4.5\ (1-\vartheta)}{\pi^2(2-\vartheta)}\right)\left((1-V_p)^{1/3}(1-\gamma)^{1/3}\right)V_p \quad (8.19)$$

Equation 8.19 indicates that the interfacial damping is related to the particle content and applied strain amplitude

8.2.1.3 Magnetism-induced damping

The processes for energy absorption through magnetism-induced damping are increased energy absorbed to overcome inter-particle magnetic interactions as well as magnetomechanical damping (change of magnetic domain structure induced by application of stress); these processes transform elastic energy into magnetic energy which subsequently dissipates by magnetic hysteresis [21]. The energy absorbed through inter-particle magnetic interactions is considered to far outweigh that through magnetomechanical damping as reported elsewhere [159]. Furthermore, the energy losses due to change of the magnetic domain structure is very difficult to directly measured. Therefore, the model is developed on the basis of inter-particle magnetic interactions.

Figure 8.3 shows schematic diagrams of two adjacent magnetic particles in a chain with the direction of applied magnetic field, $\vec{H}$ and deformation in response to the external shear strain, γ. Magnetic particles are assumed in the model to share the same spherical shape with diameter, d, and initial centre distance between adjacent particles is assumed to be, r_o. The length of the chain is assumed to be infinite. Upon loading with a shear strain perpendicular to $\vec{H}$, the particle chain deviates from the

direction of the magnetic field by θ degrees and the inter-particle distance is stretched to r.

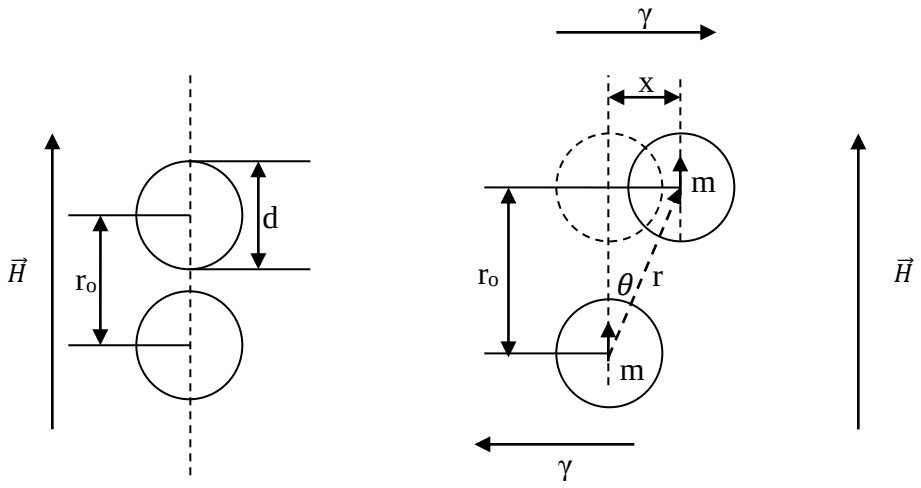

Figure 8.3 Schematic diagrams of two adjacent magnetic particles in a chain with the direction of applied magnetic field, $\vec{H}$ and deformation of the particle in response to the shear strain, γ.

The interaction energy of the two adjacent magnetic particles of equal dipole strength $\vec{m}$ [46] with north pole of one particle interacting with the south pole of its neighbour can be written as:

$$U_{interaction} = -\frac{\vec{m}^2(1-3cos^2\theta)}{4\pi\mu_1\mu_0|r|^3} \tag{8.20}$$

$$= -\frac{\vec{m}^2(1-3\frac{{r_0}^2}{{r_o}^2+x^2})}{4\pi\mu_1\mu_0({r_0}^2+x^2)^{\frac{3}{2}}}$$

where μ_1 is the permeability of the matrix and μ_0 is the permeability of a vacuum. By defining the scalar shear strain as $\gamma = x/r_o$, the dissipation energy due to separation of particles can be expressed as:

$$U_{dissipation} = -\frac{\vec{m}^2(\gamma^2 - 2)}{4\pi\mu_1\mu_0 {r_o}^3(\gamma^2 + 1)^{\frac{5}{2}}} \tag{8.21}$$

It is assumed that the particles are aligned in long chains and there are only magnetic interactions between adjacent particles within the chain. The total energy dissipation per unit volume associated with the one dimensional shear strain can be calculated by multiplying inter-particle dissipation energy by the volume fraction of the particles and dividing by the total particle volume as follows:

$$U_{dissipation} = \frac{3V_p\vec{m}^2(2 - \gamma^2)}{2\pi^2\mu_1\mu_0 d^3 {r_o}^3(\gamma^2 + 1)^{\frac{5}{2}}} \tag{8.22}$$

where V_p is the volume fraction of the particles in the MREs and d is is the particle diameter. The elastic energy stored in the material is determined as follows:

$$U_{elastic} = \frac{1}{2}G\gamma^2 \tag{8.23}$$

Subsequently, the magnetism-induced damping of MREs can be determined by

$$\psi_M = \frac{U_{dissipation}}{U_{elastic}} = \frac{3V_p\vec{m}^2(2 - \gamma^2)}{\pi^2\mu_1\mu_0 d^3 {r_o}^3 G\gamma^2(\gamma^2 + 1)^{\frac{5}{2}}} \tag{8.24}$$

As stated in the literature [46, 48], $\vec{m}$ can be defined as $\vec{m} = \frac{1}{6}\pi d^3 J_s$, where J_s is saturation magnetization and $r_o = 1.25d$. For iron sand, J_s is estimated to be 0.5 T [205]. Subsequently, the magnetism-induced damping of MREs can be rewritten as:

$$\psi_M = \frac{U_{dissipation}}{U_{elastic}} = \frac{0.083V_p{J_s}^2(2 - \gamma^2)}{1.95\mu_1\mu_0 G\gamma^2(\gamma^2 + 1)^{\frac{5}{2}}} \tag{8.25}$$

Equation 8.25 indicates that the magnetism-induced damping is related to the particle content, applied strain amplitude and the magnetism-induced damping is independent of the applied magnetic field over saturation magnetization.

8.2.1.4 Overall Damping

From the analysis, the overall damping capacity in MREs containing modified iron sand in natural rubber matrix is derived by substituting Equations 8.6, 8.19 and 8.25 into Equation 8.1, as follows:

$$\psi_{MRE} = \frac{\pi\omega G^{*}\tau_{max}^{2}}{G^{2}} + \frac{4.5\,(1-\vartheta)}{\pi^{2}(2-\vartheta)}V_p + \left(\frac{3\pi}{2}\cdot CfK - \frac{4.5\,(1-\vartheta)}{\pi^{2}(2-\vartheta)}\right)\left((1-V_p)^{1/3}(1-\gamma)^{1/3}\right)V_p + \frac{0.083V_p{J_s}^{2}(2-\gamma^{2})}{1.95\mu_1\mu_0 G\gamma^{2}(\gamma^{2}+1)^{\frac{5}{2}}} \tag{8.26}$$

For MREs containing unmodified iron sand in natural rubber matrix, the contribution of damping through strongly bonded interfaces can be neglected and the overall damping capacity can be derived by modifying Equation 8.26 and can be can be rewritten as:

$$\psi_{MRE} = \frac{\pi\omega G^{*}\tau_{max}^{2}}{G^{2}} + \frac{3\pi}{2}\cdot CfV_pK\left((1-V_p)^{1/3}(1-\gamma)^{1/3}\right) + \frac{0.083V_p{J_s}^{2}(2-\gamma^{2})}{1.95\mu_1\mu_0 G\gamma^{2}(\gamma^{2}+1)^{\frac{5}{2}}} \tag{8.27}$$

Equation 8.26 and 8.27 indicates that ψ_{MRE} depends on frequency, iron sand content, strain amplitude and $\psi_{MRE}$is independent of the applied magnetic field over saturation magnetization.

In this study, G*, τ_{max} and G were obtained from DMA. Poisson's ratio (ϑ) of rubber is 0.48. The correction factor C has been reported to be 0.5, which assumes 50% of the interface area subjected to the critical strain of relative movement during deformation [165]. The coefficient of friction between iron sand and natural rubber (*f*) was determined to be 0.21 (experimental methods to determine *f* is attached in Appendix IV). The stress concentration factor (K) at the interface between iron sand particle and matrix used was 1.2 [165]. The relative permeability of a rubber is 1 and the permeability of vacuum is $4\pi \times 10^{-7}$ NA^{-2}

8.2.2 Materials

Natural rubber (SMR L grade) and other chemicals used in this study were the same as previously mentioned in Section 5.2.1. Iron sand was collected from Ngarunui Beach, Raglan. The iron sand was then milled using a planetary mono mill (Pulverisette 6) produced by Fristech GmbH and subsequently sieved to obtain a 45-56 μm particle size range.

8.2.3 Surface Modification of Iron Sand

The surface modification of iron sand was carried out by using aqueous alcohol solution method as previously described in Section 5.2.2. The iron sand particles were subjected to surface treatment with TESPT at 6 (wt%) by weight of the particles.

8.2.4 Preparation of isotropic and anisotropic MREs

The compound formulation used in this study is given in Table 8.1. Isotropic and anisotropic MREs were fabricated according to the methods as previously described in Section 4.2.4. The cure time was then determined according to the procedure as described in Chapter 3 and the results are attached in the Appendix V.

Table 8.1 Formulation of rubber compounds

Materials	**Function**	**phr***
Natural Rubber	raw material/matrix	100
ZnO	accelerator/activator	5
Stearic Acid	accelerator/activator	1
Paraffin Oil	plasticiser	2
Naphthenic Oil	plasticiser	3
Iron sand	filler	0-70
Carbon black	filler	-
CBS	accelerator	2
TMTD	accelerator	1
Sulphur	crosslinking agent	1.5
Curing condition	**Unit**	
Temperature	^{o}C	150
Pressure	Mpa	12
Magnetic field during curing	mT	0-1000

8.2.5 Characterisation

Dynamic mechanical analysis

Dynamic mechanical analysis was carried out using a Perkin Elmer dynamic mechanical analyser (DMA 8000). Tan δ was measured over a series of frequency and strain amplitude ranging from 0.01Hz-130Hz and 0.1-4.5%, respectively. The influence of frequency and strain amplitude on tan δ was assessed using two circular disc specimens with a diameter of 10 mm and a thickness of 3 mm in shear mode at room temperature.

8.3 Results and discussion

8.3.1 Verification of MRE damping capacity, ψ_{MRE}

A preliminary assessment of the validity of the model was carried out by conducting an experiment using isotropic and anisotropic MREs. The dependency of frequency, strain amplitude, iron sand content and magnetic field on MRE damping capacity was investigated and the relationship between the theoretical model and experimental results assessed.

8.3.1.1 Viscous damping

As shown in Equation 8.6, viscous damping (ψ_V) is frequency dependent. For assessing the validity of the viscous damping, unfilled natural rubber sample was prepared and tan δ was measured through DMA over a range of frequency (0.01-130Hz) and strain amplitude (0.1-4.5%). The results are shown in Figure 8.4. Tan δ increased with increasing frequency and remained constant as the strain amplitude increased, supporting the proposed model for viscous damping. This trend was also in general agreement with other researchers [179].

8.3.1.2 Interfacial Damping

As represented in Equation 8.19, interfacial damping is related to the particle content and applied strain amplitude. For assessing the validity of this equation, a series of isotropic MREs containing different contents of silane modified iron sand (10, 30, 50 and 70 phr) was prepared giving covalent bonding at the interfaces (although it is accepted that weakly bound interfacial area is likely to also be present)

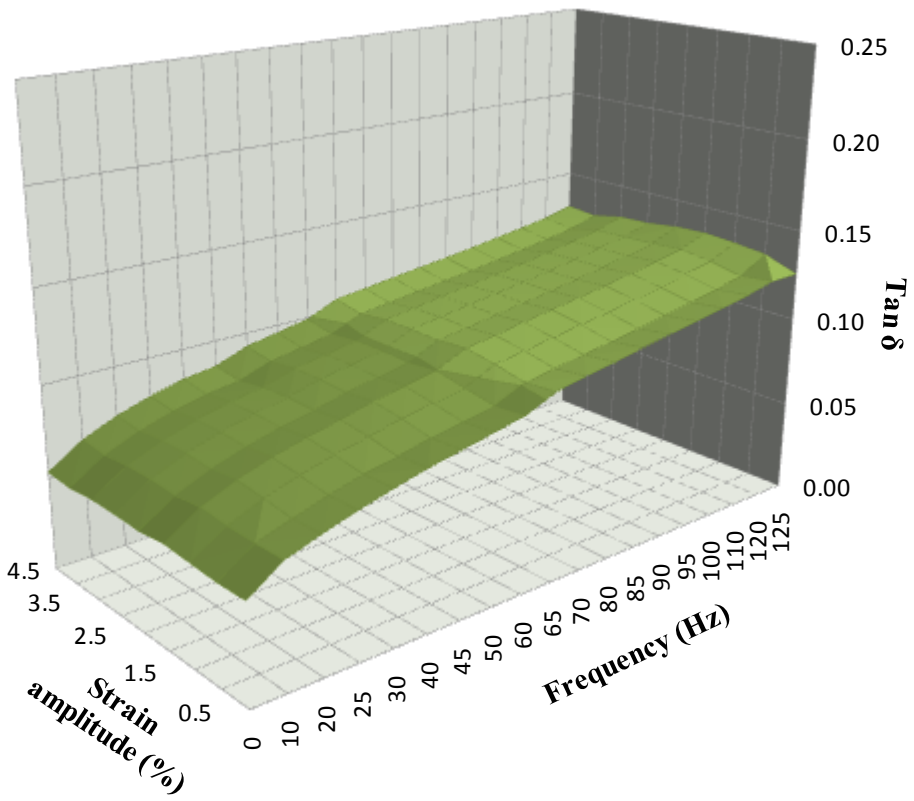

Figure 8.4 Influence of strain amplitude and frequency on tan δ

and curing was carried out in the absence of a magnetic field in order to rule out the influence of magnetism-induced damping. Tan δ was measured over a range of strain amplitude (0.1-4.5%) and the results are shown in Figure 8.5. Generally, tan δ increased with the increased content of iron sand as well as the strain amplitude. As can also be seen, at lower iron sand contents (10 and 30 phr), tan δ showed slight increases over the whole strain amplitude range explored, supporting that for low iron sand contents, energy absorption through viscous damping outweighs that through interfacial damping. At higher iron sand contents (50 and 70 phr), tan δ increased with increase in strain amplitude at low strain amplitudes and plateaued at higher strain amplitude. The amplitude dependence at low strain amplitudes for strongly bonded interfaces can be explained due to increased energy absorbed in bringing viscous flow of constrained materials at the particle interfaces and breakage of

interfacial bonding; for weakly bonded interfaces increased energy could be absorbed due to breakdown of physical bonding/mechanical interlocking between iron sand and rubber. At the plateau region (above approximately 2.5% strain amplitude), all interactions are destroyed to such an extent they cannot be reconstructed and damping is largely reliant on the rubber matrix which is at its largest due to greatest amount of rubber flow and the friction between rubber chains and iron sand. Overall, an increase of tan δ with increased iron sand content as well as strain amplitude showed good agreement with the proposed model for interfacial damping (ψ_I).

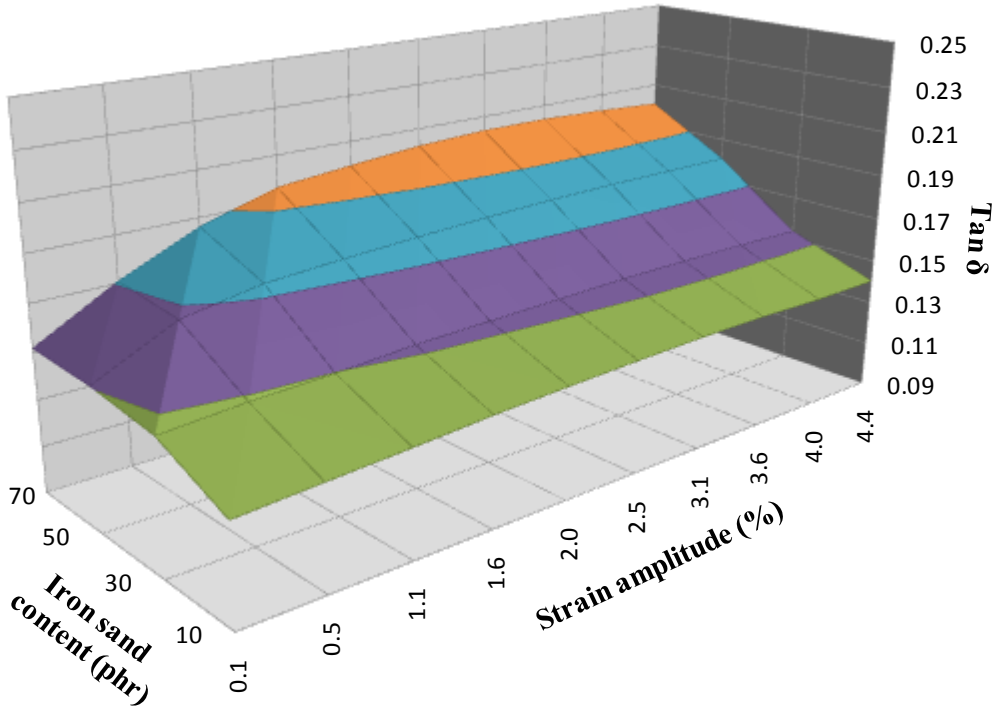

Figure 8.5 Influence of iron sand content and strain amplitude on tan δ

8.3.1.3 Magnetism-induced damping

As stated in Equation 8.25, magnetism-induced damping of MREs is related to iron sand content, strain amplitude and magnetic field up to saturation magnetisation. For assessing the validity of the magnetism-induced damping, a series

of MRE samples containing different contents of iron sand (10, 30, 50 and 70 phr) was prepared and curing was carried out in the absence and presence of different magnetic fields (100, 300, 500, 700 and 1000 mT).

Figure 8.6 shows the variation of tan δ with iron sand content and magnetic field which was measured at a fixed frequency (100Hz) and strain amplitude (0.5%). It can be seen that tan δ increased with increased content of iron sand as well as increasing magnetic field. The increase of tan δ with increasing iron sand content can be explained by the increase in energy losses caused by interfacial damping with increase in iron sand content; furthermore for anisotropic MREs, increased energy could be absorbed through magnetic interactions caused by the increased in inter-particle interaction and change of magnetic domain structures with increase in iron sand content. As can also be seen, there is generally a slight increase in tan δ with increased magnetic field which levels off at about 500 mT, supporting saturation magnetization to be occurring at around 500 mT.

The variation of tan δ with magnetic field and strain amplitude for MRE containing 70 phr silane modified iron sand is shown in Figure 8.7. It can be seen that tan δ increased with increasing magnetic field at most strain amplitudes and then leveled off at around 500 mT due to saturation magnetization. It is also apparent that tan δ increased with increase in strain amplitude at low strain amplitudes and plateaued at higher strain amplitude. The amplitude dependence at low strain amplitudes could again be explained due to increase energy absorbed through interfacial damping. For anisotropic MREs, similar mechanisms would be involved as well as further energy absorbed through inter-particle interactions and magnetomechanical damping. At the plateau region, tan δ is largely reliant on the

rubber matrix as previous explained in Section 8.3.1.2. Overall, the obtained data for the influence of iron sand content, strain amplitude and magnetic field on tan δ supports proposed model for magnetism-induced damping (ψ_M).

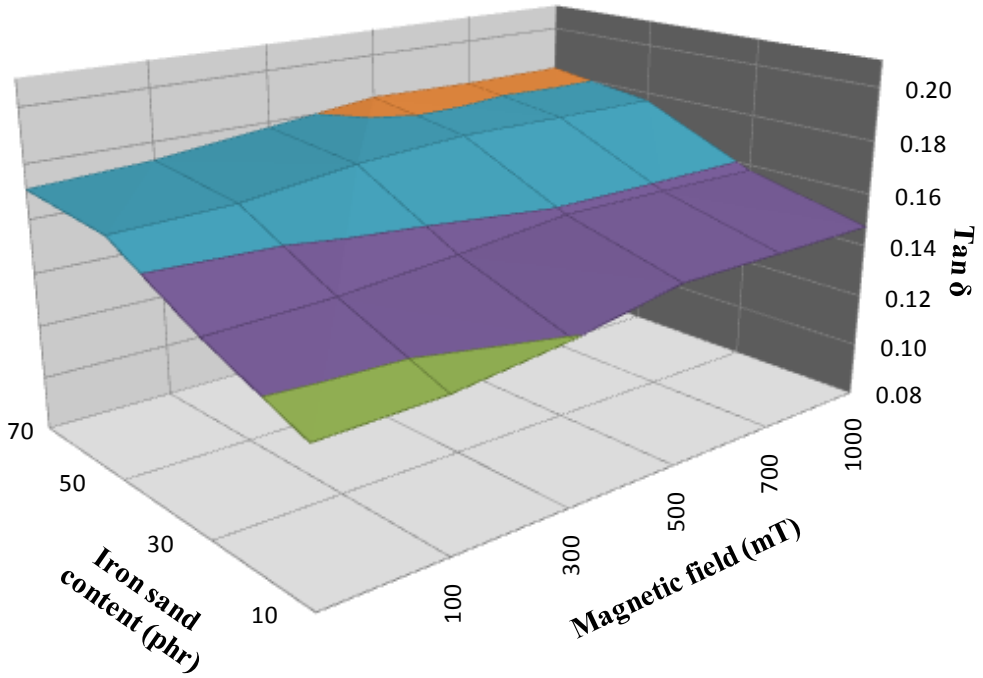

Figure 8.6 Influence of iron sand content and magnetic field on tan δ

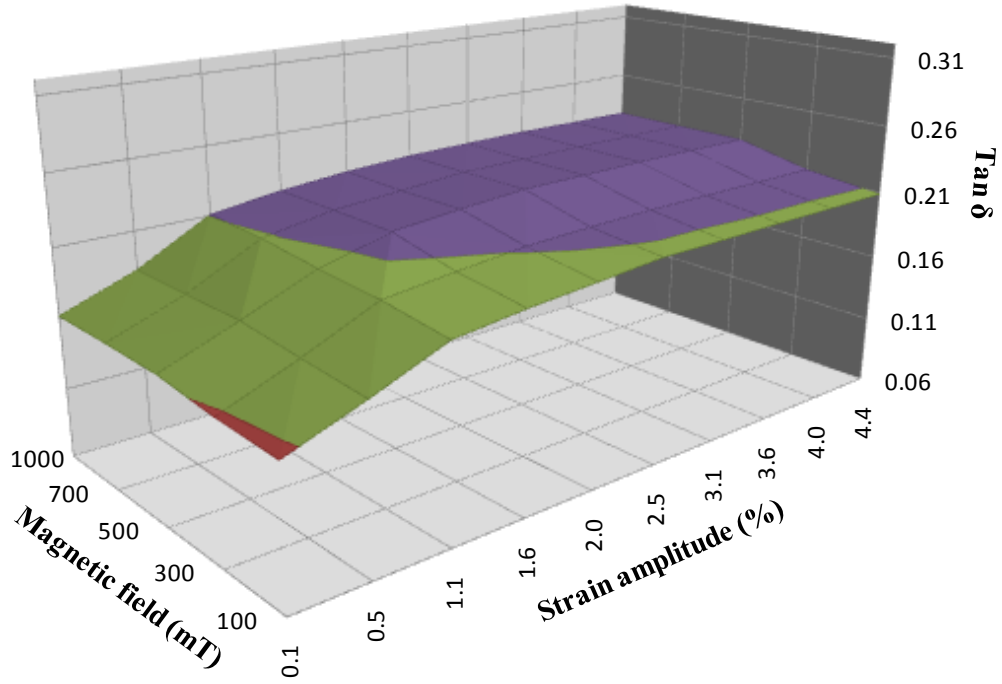

Figure 8.7 Influence of magnetic field and strain amplitude on tan δ

8.3.2 Comparison between tan δ with theoretical ψ_{MRE}

Comparison between tan δ with ψ_{MRE} was carried out on a series of isotropic and anisotropic MREs developed during this thesis work. ψ_{MRE} for MREs with modified and unmodified iron sand was calculated using Equation 8.26 and 8.27, respectively. The results are shown in Tables 8.2 and 8.3. Generally, ψ_{MRE} increases with increased in frequency, strain amplitude, iron sand content and magnetic field up to magnetic saturation and the trend matches the experimental trend; the values were generally higher than for tan δ with average percentage differences for modified and unmodified iron sand of 8.1% and 21.8%, respectively. This disparity is not surprising when all the assumptions of the model (previously described separately in the sections for different mechanisms) are considered which are summarized as follows:

- $\psi_{MRE} \approx \tan\delta$ (although $\psi_V \approx tan\,\delta$ is accepted for viscous damping, this has not been previously shown to cover all mechanisms in MREs).
- The viscous damping of MREs follows the linear Kelvin Voight model. In reality, however, nonlinearity could occur due to addition of iron sand particles in the rubber matrix.
- Iron sand particles were assumed to be spherical with the same diameter, however, the particles were not perfectly spherical or having the same diameter.
- In magnetism-induced damping, the energy absorbed through magnetomechanical damping was considered insignificant.
- The iron sand particles are assumed to be aligned in long chains, however, the particles were not perfectly aligned in long chains.

Table 8.2 Comparison of theoretical damping capacity (ψ_{MRE}) with tan δ obtained from experiments for MREs containing different contents of modified iron sand in a rubber matrix and tested at different frequencies, strain amplitudes and magnetic fields.

Factor				Damping capacity, ψ_{MRE} of MREs according to proposed model	Experimental tan δ of MREs	Difference (%)
Iron sand content (phr)	Frequency (Hz)	Strain amplitude (%)	Magnetic field (mT)			
0	100	0.5	0	0.1689	0.1202	40.5
10	100	0.5	500	0.1741	0.1472	18.3
30	100	0.5	500	0.1832	0.1584	15.6
50	100	0.5	500	0.1916	0.1772	8.1
70	100	0.5	500	0.1993	0.1828	9.0
70	50	0.5	500	0.1148	0.1493	-23.1
70	120	0.5	500	0.2330	0.2182	6.7
70	100	1.5	500	0.2043	0.2175	-6.1
70	100	4.0	500	0.2107	0.2265	-7.0
70	100	0.5	100	0.1988	0.1731	14.9
70	100	0.5	300	0.1990	0.1778	11.9
70	100	0.5	1000	0.1993	0.1822	9.3
Average difference (%)						**8.1**

Table 8.3 Comparison of theoretical damping capacity (ψ_{MRE}) with tan δ obtained from experiments for MREs containing different contents of unmodified iron sand in a rubber matrix and tested at different frequencies, strain amplitudes and magnetic fields.

Factor				Damping capacity, ψ_{MRE} of MREs according to proposed model	Experimental tan δ of MREs	Difference (%)
Iron sand content (phr)	Frequency (Hz)	Strain amplitude (%)	Magnetic field (mT)			
30	100	0.5	700	0.1745	0.1101	58.5
70	100	0.5	0	0.1804	0.1348	33.8
70	50	0.5	300	0.0961	0.1076	-10.6
70	100	0.5	300	0.1806	0.1421	27.1
70	120	0.5	300	0.2143	0.1965	9.0
70	100	1.5	300	0.1857	0.1615	15.0
70	100	4.0	300	0.1921	0.1605	19.7
Average difference (%)						**21.8**

However, given the limitations of other models that cover all mechanisms for MREs, this model can provide a guideline to manufacture MREs with desired damping performance. It also gives support that the following approximation can be used to determine damping of MREs at various variable factors:

$$\psi_{MRE} \approx \tan\delta \tag{8.28}$$

8.4 Chapter conclusion

A theoretical model was developed to determine the total damping capacity of MREs (ψ_{MRE}) from viscous flow of the rubber matrix, interfacial damping and magnetism-induced damping. ψ_{MRE} was found to be dependent on frequency, iron sand content, strain amplitude and magnetic field up to magnetic saturation. An experiment was carried out to assess the proposed model and comparison between tan δ with ψ_{MRE} on a series of isotropic and anisotropic MREs showed that ψ_{MRE} matched the experimental trends for tan δ with average percentage difference of 8.1% and 21.8% for MREs with modified and unmodified iron sand, respectively. It is considered that the model can provide a guideline to manufacture MREs with desired damping performance.

Chapter 9

Conclusions

The capability of DMA for use in predicting the optimum curing time (t_{90}) of rubber compounds was assessed for different rubber compounds with various filler contents and particle sizes. The curves of G′, G″ and tan δ as a function of time were found to reflect the vulcanization process. However, only the tan δ curve showed a strong correlation with crosslink development. Three stages of curing (induction, curing and overcuring) were observed on the tan δ versus time curve and t_{90} was calculated as the time when tan δ reduces to 90% of its maximum value. The measured values were compared with results obtained by conventional methodology. The percentage errors for all compounds were found to be lower than +/- 5% with an average percentage error of 0.58%. The results showed for the first time that DMA is capable of measuring the optimum cure time of rubber.

The effect of a number of factors (iron sand content, iron sand particle size and applied magnetic field during curing) on tan δ and energy dissipated during hysteresis tests was explored using a designed experiment (Taguchi) to minimise sample preparation and testing effort. Iron sand content had the greatest influence on tan δ when measured over a range of frequency (0.01-130Hz) as well as on the energy dissipated during the hysteresis tests, followed by particle size and magnetic field. Energy absorption for isotropic MREs can occur due to viscous flow of the rubber matrix and interfacial friction between the particle and the rubber matrix; for anisotropic MREs, similar mechanisms would be involved as well as potentially,

energy absorbed through magnetic interactions. However, a smaller contribution to energy absorption observed for tensile loading in hysteresis tests compared with shear loading in the DMA, is believed to be due to the fact that it is largely the spacing increasing between chains that is changing, whereas in shear loading, the spacing within chains is changing, such that closer particles are moving more relative to each other. It was also found that addition of iron sand and formation of magnetic particle chains constrained conformational changes of rubber molecules from relaxation and therefore increased the temperature at which the molecular chains started to mobilize, such that the width of the peak of tan δ was increased. It was observed that none of the factors investigated had significant influence on tan δ for the plateau region from 1.0-4.5% strain amplitude, which is likely to be due to disruption of weak interfacial bonding between iron sand and rubber at low strain amplitudes. SEM analysis of MRE sections showed that isotropic MREs had uniform particle distribution and curing the materials under an applied magnetic field at elevated temperature resulted in the iron sand organizing into chain-like columnar structures. Evidence from SEM also supported weak interfacial bonding between iron sand and rubber.

Surface modification of iron sand using TESPT was found to provide coupling between iron sand and natural rubber; Raman spectroscopy gave evidence that siloxane linkages were formed between TESPT and iron sand. The results were supported by grafting percentage determined using TGA. Crosslink density measurements showed evidence that the tetrasulphane group of TESPT formed crosslinks with the rubber chains. The optimum amount of TESPT for interfacial bonding and the highest damping performance occurred at 6 wt% TESPT relative to iron sand content. Treated iron sand was found to be more evenly dispersed in the

rubber with much less particle pullout on fracture surface supporting improved interfacial adhesion with natural rubber. Tan δ was found higher for isotropic and anisotropic MREs with modified iron sand compared to MREs with unmodified iron sand, with 20-40% improvement over the whole frequency range explored and 11-20% improvement over the strain amplitude range explored. Tan δ for anisotropic MREs with silane modified iron sand increased with increased in magnetic field up to a saturation point at 600 mT. The higher energy absorption for isotropic MREs that occurred with modified iron sand was thought to be due to more energy absorbed at low strain amplitudes for the viscous flow of rubber better bonded to iron sand and at high strain amplitudes, to bring about bond failure and viscous flow of rubber chains that are more bulky due to the presence of coupling agent; for anisotropic MREs, similar mechanisms would be involved as well as further energy absorbed due to the breakdown of joint rubber shells with more trapped rubber released and magnetic interactions. Improvement in hysteresis loss of 20-41% was obtained for isotropic and anisotropic MREs with modified iron sand, however, hysteresis loss demonstrated no obvious trend with magnetic field which is in contrast to the results for the effect of magnetic field on tan δ over a range of frequency and strain amplitude; this was thought to be due to the different mode of loading used when studying hysteresis loss. The presence of TESPT and formation of different lengths of aligned particle chains did not strongly affect the value of T_g and maximum tan δ at T_g; this is explained by the segmental motion of rubber chains being by far the most significant influence on energy absorption at this temperature as supported by the literature. It was evident that surface modification of iron sand using TESPT generally resulted in increases in

MRE damping performance due to improvement in iron sand-rubber interfacial bonding.

Energy absorption of isotropic and anisotropic MREs with silane treated iron sand were compared with existing antivibration rubbers contained different contents of carbon black filler (30, 50 and 70 phr) in a natural rubber matrix. Energy absorption for existing antivibration rubbers was generally higher than isotropic and anisotropic MREs and this was believed to be largely due the presence of carbon black in the formulation. For samples containing carbon black, it was assumed that increased energy could be absorbed due to breakdown and reformation of carbon black filler networks. Further assessment was carried out on materials that were the same as anisotropic MREs, except they had additions of carbon black. The energy absorption was found higher than existing antivibration rubber samples of the same carbon black contents, supporting the use of iron sand to improve damping. However, trends for energy absorption at around T_g were found to reverse which is considered to be due to the segmental motion of rubber chains being by far the most significant influence on energy absorption in the glass transition zone and so care should be taken when using the materials at such temperature although this is unlikely to be the service temperature for these materials.

A model was developed to include viscous flow of the rubber matrix, interfacial damping and magnetism-induced damping to give the total predicted damping capacity of MREs (ψ_{MRE}). ψ_{MRE} was found to be dependent on frequency, iron sand content, strain amplitude and magnetic field up to magnetic saturation. It was found that ψ_{MRE} matched the experimental trends with average percentage difference of 8.1% for MREs with modified iron sand and 21.8% for MREs with

unmodified iron sand. Although the model was not completely accurate, it can serve as a foundation model that covers all damping mechanisms to which improvements can be made in the future.

It is believed that the research objectives stated in the introduction have been met with the completion of this thesis. Isotropic and anisotropic MREs based on iron sand and natural rubber were successfully produced and a greater understanding of the MRE damping mechanisms have been attained.

Chapter 10

Recommendations and Future Work

The results obtained from this study have laid down an important platform from which to further improve the processing methods and properties of MREs based on natural rubber and iron sand. Some recommendations for future work are proposed as follows:

- Applying a magnetic field at elevated temperature during processing allowed iron sand particles to organise into chain like columnar structures vertically arranged through the material which provided much larger damping. It was not possible with available equipment to bring about horizontal alignment of iron sand particles, but this would be recommended for future work as it could provide further improvement in the MRE damping performance.
- In this research, damping of MREs was tested in a passive mode through dynamic mechanical analysis and hysteresis testing. Further testing in a semi active or active mode could be carried out to study the damping performance of MREs under an applied responsive magnetic field during testing or in service to give improved in-service performance.
- Development of prototypes and products for practical applications including seismic bearings and engine bushings.

References

1. Girish, B.M., B.M. Satish, and K. Mahesh, *Vibration damping of high-chromium ferromagnetic steel and its dependence on magnetic domain structure.* Journal of Alloys and Compounds, 2009. **484**(1-2): p. 296-299.
2. Lu, H., X. Wang, T. Zhang, Z. Cheng, and Q. Fang, *Design, Fabrication, and Properties of High Damping Metal Matrix Composites-A Review.* Materials, 2009. **2**(3): p. 958-977.
3. Thomson, P., G.J. Balas, and P.H. Leo, *The use of shape memory alloys for passive structural damping.* Smart Mater. Struct, 1995. **4**(36): p. 36-42.
4. Gillich, G.R., D. Amariei, N. Gillich, C.P. Chioncel, V. Bizau, and E.D. Birdeanu. *About the use of shape memory alloys in vibration damping*. in *Annals of DAAAM for 2008 & Proceedings of the 19th International DAAAM Symposium*. 2008. Vienna, Austria
5. Mielczarek, A., N. Kopp, and W. Riehemann, *Ageing effects after heat treatment in Cu Al Mn shape memory alloys.* Materials Science and Engineering: A, 2009. **521-522**(0): p. 182-185.
6. Hu, X.S., K. Wu, and M.Y. Zheng, *Effect of heat treatment on the stability of damping capacity in hypoeutectic Mg Si alloy.* Scripta Materialia, 2006. **54**(9): p. 1639-1643.
7. Xiuqing, Z., L. Lihua, M. Naiheng, and W. Haowei, *The effect of heat treatment on damping characterization of TiC/AZ91 composites.* Materials Letters, 2006. **60**(5): p. 600-604.
8. Dooris, A., Lakes, R. S., Myers, B. and Stephens, N., *High damping indium-tin alloys.* Mechanics of Time Dependent Materials, 1999. **3**(4): p. 305-318.
9. Chung, D.D.L., *Review: Improving cement-based materials by using silica fume.* Journal of Materials Science, 2002. **37**(4): p. 673-682.
10. Ciesielski, A., *An Introduction to Rubber Technology*. Vol. 1. 1999, Shawbury, Shrewsbury, Shropshire, SY4 4NR, UK: Rapra Technology Limited. 174.
11. Kothandaraman, B., *Rubber materials*. 1 ed, ed. K. B. Vol. 1. 2008, Florida, USA: CRC Press. 158.
12. James, A.J. and F.K. Thomas, *Engineering Materials Technology*. 5 ed, ed. H. Stephen. 2005, Ohio: Pearson Education Ltd. 886.
13. Lakes, R.S., *High Damping Composite Materials: Effect of Structural Hierarchy.* Journal of Composite Materials, 2001. **36**(3): p. 287-297.
14. Farshad, M. and A. Benine, *Magnetoactive elastomer composites.* Polymer Testing, 2004. **23**(3): p. 347-353.
15. Qilei, W., Y. Fengyu, Y. Qian, G. Hongyan, C. Junhui, and Z. Bin, *Study on Magnetic and Physical Mechanical Properties of NBR Composites Filled with Nano-Sro.6Fe2O3.* Journal of Elastomers and Plastics, 2011. **43**(3): p. 275-284.
16. Makled, M.H., T. Matsui, H. Tsuda, H. Mabuchi, M.K. El-Mansy, and K. Morii, *Magnetic and dynamic mechanical properties of barium ferrite natural rubber composites.* Journal of Materials Processing Technology, 2005. **160**(2): p. 229-233.

17. Stepanov, G.V., S.S. Abramchuk, D.A. Grishin, L.V. Nikitin, E.Y. Kramarenko, and A.R. Khokhlov, *Effect of a homogeneous magnetic field on the viscoelastic behavior of magnetic elastomers.* Polymer, 2007. **48**(2): p. 488-495.
18. Jerzy, K., K. Michal, and L. Daniel, *Magnetomechanical properties of anisotropic and isotropic magnetorheological composites with thermoplastic elastomer matrices.* Smart Mater. Struct, 2011. **20**(8): p. 12.
19. Chokkalingam, R., P. Rajasabai Senthur, and M. Mahendran, *Magnetomechanical behavior of Fe/PU magnetorheological elastomers.* Journal of Composite Materials, 2010. **45**(15): p. 1545-1552.
20. Chen, L., X.L. Gong, and W.H. Li, *Effect of carbon black on the mechanical performances of magnetorheological elastomers.* Polymer Testing, 2008. **27**(3): p. 340-345.
21. Fuchs, A., Q. Zhang, J. Elkins, F. Gordaninejad, and C. Evrensel, *Development and characterization of magnetorheological elastomers.* Journal of Applied Polymer Science, 2007. **105**(5): p. 2497-2508.
22. Ginder, J., *Magnetorheological elastomers: properties and applications.* Proc. SPIE, 1999. **3675**(1): p. 131.
23. Lerner, A.A. and K.A. Cunefare, *Performance of MRE-based Vibration Absorbers.* Journal of Intelligent Material Systems and Structures, 2008. **19**(5): p. 551-563.
24. Sun, T.L., X.L. Gong, W.Q. Jiang, J.F. Li, Z.B. Xu, and W.H. Li, *Study on the damping properties of magnetorheological elastomers based on cis-polybutadiene rubber.* Polymer Testing, 2008. **27**(4): p. 520-526.
25. Wang, Y., Y. Hu, H. Deng, X. Gong, P. Zhang, W. Jiang, and Z. Chen, *Magnetorheological elastomers based on isobutylene–isoprene rubber.* Polymer Engineering & Science, 2006. **46**(3): p. 264-268.
26. Lokander, M. and B. Stenberg, *Improving the magnetorheological effect in isotropic magnetorheological rubber materials.* Polymer Testing, 2003. **22**(6): p. 677-680.
27. Lokander, M. and B. Stenberg, *Performance of isotropic magnetorheological rubber materials.* Polymer Testing, 2003. **22**(3): p. 245-251.
28. Carlson, J.D. and M.R. Jolly, *MR fluid, foam and elastomer devices.* Mechatronics, 2000. **10**(4-5): p. 555-569.
29. Blom, P. and L. Kari, *Amplitude and frequency dependence of magneto-sensitive rubber in a wide frequency range.* Polymer Testing, 2005. **24**(5): p. 656-662.
30. Chen, L., X.-l. Gong, W.-q. Jiang, J.-j. Yao, H.-x. Deng, and W.-h. Li, *Investigation on magnetorheological elastomers based on natural rubber.* Journal of Materials Science, 2007. **42**(14): p. 5483-5489.
31. Alberdi-Muniain, A., N. Gil-Negrete, and L. Kari, *Influence of carbon black and plasticisers on dynamic properties of isotropic magnetosensitive natural rubber.* Plastics, Rubber and Composites, 2012. **41**(7): p. 310-317.
32. Sun, Y., X. Zhou, Y. Liu, G. Zhao, and Y. Jiang, *Effect of magnetic nanoparticles on the properties of magnetic rubber.* Materials Research Bulletin, 2009. **45**(7): p. 878-881.
33. Dobrzanski, L.A., A. Tomiczek, B. Tomiczek, A. Slawska, and O. Iesenchuk, *Polymer matrix composite materials reinforced by Tb0.3Dy0.7Fe1.9*

magnetostrictive particles. Journal of Achievements in Materials and Manufacturing Engineering, 2009. **37**(1): p. 16-23.
34. Bryan, K.R., A. Robinson, and R.M. Briggs, *Spatial and temporal variability of titanomagnetite placer deposits on a predominantly black sand beach.* Marine Geology, 2007. **236**(1-2): p. 45-59.
35. Briggs, R.M., J.C. Laurent, T.M. Hume, and A. Swales, *Provenance of black sands on the west coast, North Island, New Zealand*, in *AusIMM New Zealand Branch Annual Conference*. 2009, AusIMM: Queenstown, New Zealand. p. 41-50.
36. Jerzy, K., L. Daniel, M. Rafal, and Z. Piotr, *Smart Magnetic Composites (SMC); Metal, Ceramic and Polymeric Composites for Various Uses*, ed. J. Cuppoletti. 2011, Rijeka, Croatia: InTech. 684.
37. Davis, L.C., *Model of magnetorheological elastomers.* Journal of Applied Physics, 1999. **85**(6): p. 3348-3351.
38. Park, J.O., K.Y. Rhee, and S.J. Park, *Silane treatment of Fe3O4 and its effect on the magnetic and wear properties of Fe3O4/epoxy nanocomposites.* Applied Surface Science, 2010. **256**(23): p. 6945-6950.
39. Taghvaei, A.H., H. Shokrollahi, A. Ebrahimi, and K. Janghorban, *Soft magnetic composites of iron-phenolic and the influence of silane coupling agent on the magnetic properties.* Materials Chemistry and Physics, 2009. **116**(1): p. 247-253.
40. Tian, Y., Y. Liu, M. He, G. Zhao, and Y. Sun, *High damping properties of magnetic particles doped rubber composites at wide frequency.* Materials Research Bulletin. **48**(5): p. 2002-2005.
41. Popp, K.M., M. Kroger, W.h. Li, X.Z. Zhang, and P.B. Kosasih, *MRE Properties under Shear and Squeeze Modes and Applications.* Journal of Intelligent Material Systems and Structures, 2010. **21**(15): p. 1471-1477.
42. Zhou, X., Y. Sun, Y. Jiang, Y. Liu, and G. Zhao, *Effect of magnetic nanoparticles on damping property of nature rubber.* Polymer Bulletin, 2011. **66**(9): p. 1281-1288.
43. Collette, C., G. Kroll, G. Saive, V. Guillemier, M. Avraam, and A. Preumont, *Isolation and damping properties of magnetorheologic elastomers.* Journal of physics. Conference series, 2009. **149**(1): p. 012091.
44. Nayak, B., S.K. Dwivedy, and K.S.R.K. Murthy, *Dynamic analysis of magnetorheological elastomer-based sandwich beam with conductive skins under various boundary conditions.* Journal of Sound and Vibration, 2010. **330**(9): p. 1837-1859.
45. Gong, X.L., X.Z. Zhang, and P.Q. Zhang, *Fabrication and characterization of isotropic magnetorheological elastomers.* Polymer Testing, 2005. **24**(5): p. 669-676.
46. Jolly, M.R., J.D. Carlson, and C.M. Beth, *A model of the behaviour of magnetorheological materials.* Smart Materials and Structures, 1996. **5**(5): p. 607.
47. Li, R. and L.Z. Sun, *Dynamic viscoelastic modeling of magnetorheological elastomers.* Acta Mechanica, 2014. **225**(4-5): p. 1347-1359.
48. Jie, Y., G. Xinglong, D. Huaxia, Q. Lijun, and X. Shouhu, *Investigation on the mechanism of damping behavior of magnetorheological elastomers.* Smart Materials and Structures, 2012. **21**(12): p. 125015.

49. Chen, L. and S. Jerrams, *A rheological model of the dynamic behavior of magnetorheological elastomers.* Journal of Applied Physics, 2011. **110**(1): p. 013513.
50. Kwak, G.H., K. Inoue, Y. Tominaga, S. Asai, and M. Sumita, *Characterization of the vibrational damping loss factor and viscoelastic properties of ethylene-propylene rubbers reinforced with micro-scale fillers.* Journal of Applied Polymer Science, 2001. **82**(12): p. 3058-3066.
51. Monika, B., K. Jaroslaw, K. Janusz, and S. Bogdan, *Vibration Control of Mechanical Systems - introduction to the problem.* Acta Montanistica Slovaca, 1998. **3**(4): p. 504-509.
52. Barry, C., ed. *Elastomers*. 1 ed. Vol. 1. 2012, Technical reference: Hopkinton, Ma. 19-31.
53. Chung, D.D.L., *Materials for Vibration Damping.* J. Mater. Sci., 2001. **36**(24): p. 5733-5737.
54. Wu, J.H., C.H. Li, H.T. Chiu, Z.J. Shong, and P.A. Tsai, *Reinforcement of Dynamically Vulcanized EPDM/PP Elastomers Using Organoclay Fillers: Dynamic Properties of Rubber Vibration Isolators and Antivibration Performance.* Journal of Thermoplastic Composite Materials, 2009. **22**(5): p. 503-517.
55. Zhang, J., R.J. Perez, and E.J. Lavernia, *Documentation of damping capacity of metallic, ceramic and metal-matrix composite materials.* Journal of Materials Science 1993. **28**(9): p. 2395-2404.
56. Schaller, R., *Metal matrix composites, a smart choice for high damping materials.* Journal of Alloys and Compounds, 2003. **355**(1-2): p. 131-135.
57. Seo, Y.I., B.-H. Lee, Y.D. Kim, and K.H. Lee, *Grain size effects on magnetomechanical damping properties of ferromagnetic Fe-5 wt.% Al alloy.* Materials Science and Engineering: A, 2006. **431**(1-2): p. 80-85.
58. Ortin, J. and L. Delaey, *Hysteresis in shape-memory alloys.* International Journal of Non-Linear Mechanics, 2002. **37**(8): p. 1275-1281.
59. Manoj, N.R., L. Chandrasekhar, M. Patri, B.C. Chakraborty, and P.C. Deb, *Vibration damping materials based on interpenetrating polymer networks of carboxylated nitrile rubber and poly(methyl methacrylate).* Polymers for Advanced Technologies, 2002. **13**(9): p. 644-648.
60. Liu, Z.Y., Y.Y. Wang, G.S. Huang, and J.R. Wu, *Damping characteristics of chlorobutyl rubber/poly(ethyl acrylate)/piezoelectric ceramic/carbon black composites.* Journal of Applied Polymer Science, 2008. **108**(6): p. 3670-3676.
61. Huang, G.S., L.X. Jiang, and Q. Li, *Molecular design of damping rubber based on polyacrylate-containing silicone.* Journal of Applied Polymer Science, 2002. **85**(4): p. 746-751.
62. Wu, C.Y., C.Y. Wei, W.H. Guo, and C.F. Wu, *Dynamic mechanical properties of acrylic rubber blended with phenolic resin.* Journal of Applied Polymer Science, 2008. **109**(4): p. 2065-2070.
63. Oprea, S., *Effects of Fillers on Polyurethane Resin-based Polyurethane Elastomeric Bearing Materials for Passive Isolation.* Journal of Composite Materials, 2008. **42**(25): p. 2673-2685.
64. Yamada, N., S. Shoji, H. Sasaki, A. Nagatani, K. Yamaguchi, S. Kohjiya, and A.S. Hashim, *Developments of high performance vibration absorber from*

poly(vinyl chloride) chlorinated polyethylene epoxidized natural rubber blend. Journal of Applied Polymer Science, 1999. **71**(6): p. 855-863.
65. Chung, D.D.L., *Structural composite materials tailored for damping.* Journal of Alloys and Compounds, 2003. **355**(1-2): p. 216-223.
66. Finegan, I.C. and R.F. Gibson, *Recent research on enhancement of damping in polymer composites.* Composite Structures, 1999. **44**(2-3): p. 89-98.
67. Sumita, M., H. Gohda, S. Asai, K. Miyasaka, A. Furuta, Y. Suzuki, and K. Uchino, *New damping materials composed of piezoelectric and electro-conductive, particle-filled polymer composites: effect of the electromechanical coupling factor.* Die Makromolekulare Chemie, Rapid Communications, 1991. **12**(12): p. 657-661.
68. Zhang, C., J.F. Sheng, and C.A. Ma, *Dynamic mechanical behavior of a novel polymeric composite damping material.* Chinese Chemical Letters, 2005. **16**(11): p. 1527-1530.
69. Hillberry, B.M., E. Society of Automotive, T. American Society for, and Materials, *The measurement of the dynamic properties of elastomers and elastomeric mounts*. Vol. STP535-EB. 1973: Society of Automotive Engineers. 132.
70. Graesser, E.J. and C.R. Wong. *The relationship of traditional damping measures for materials with high damping capacity: a review*. in *Symposium on M3D: Mechanics and Mechanisms of Material Damping, VK Kinra, and A. Wolfenden, eds., American Society for Testing Materials, Philadelphia*. 1992.
71. Rabinow, J., *The Magnetic Fluid Clutch.* American Institute of Electrical Engineers, 1948. **67**(2): p. 1308 - 1315
72. Klingenberg, D.J., *Magnetorheology: Applications and challenges.* AIChE Journal, 2001. **47**(2): p. 246-249.
73. Watson, J.R., *Method and apparatus for varying the stiffness of a suspension bushing*, in *U.S. Patent 5609353*. 1997., Ford Motor Co: USA. p. 1-3.
74. Deng, H.X. and X.L. Gong, *Application of magnetorheological elastomer to vibration absorber.* Communications in Nonlinear Science and Numerical Simulation, 2008. **13**(9): p. 1938-1947.
75. Dyke, S.J., J.R. Spencer, M.K. Sain, and J.D. Carlson, *Modeling and control of magnetorheological dampers for seismic response reduction.* Smart Materials and Structures, 1996. **5**(5): p. 565-575.
76. Olabi, A.G. and A. Grunwald, *Design and application of magnetostrictive materials.* Materials & Design, 2008. **29**(2): p. 469-483.
77. Jin, S., T.H. Tiefel, R. Wolfe, R.C. Sherwood, and J.J. Mottine, *Optically Transparent, Electrically Conductive Composite Medium.* Science, 1992. **255**(5043): p. 446-448.
78. Dong, X.M., M. Yu, C.R. Liao, and W.M. Chen, *A new variable stiffness absorber based on magneto-rheological elastomer.* Transactions of Nonferrous Metals Society of China, 2009. **19**(13): p. S611-S615.
79. Jiang, W.Q., J.J. Yao, X.L. Gong, and L. Chen, *Enhancement in Magnetorheological Effect of Magnetorheological Elastomers by Surface Modification of Iron Particles.* Chinese Journal of Chemical Physics, 2008. **21**(1): p. 87-92.

80. Chen, L., X.L. Gong, and W.H. Li, *Microstructures and viscoelastic properties of anisotropic magnetorheological elastomers.* Smart Materials and Structures, 2007. **16**(6): p. 2645.
81. Gong, X.L., L. Chen, and J.F. Li, *Study of utilizable magnetorheological elastomers.* International Journal of Modern Physics B, 2007. **21**(28n29): p. 4875-4882.
82. Lokander, M., T.r. Reitberger, and B. Stenberg, *Oxidation of natural rubber-based magnetorheological elastomers.* Polymer Degradation and Stability, 2004. **86**(3): p. 467-471.
83. Alberdi-Muniain, A., N. Gil-Negrete, F.J. Nieto, L. Kari, and J. Vinolas. *An experimental study of magneto-sensitive natural rubber components applied in a vibration isolation system*. in *6th European Conference on Constitute Models for Rubber*. 2009. Dresden, Germany: Taylor & Francis.
84. Lejon, J. and L. Kari, *Preload, frequency, vibrational amplitude and magnetic field strength dependence of magnetosensitive rubber.* Plastics, Rubber and Composites, 2009. **38**(8): p. 321-326.
85. Yoon, J.H., I.H. Yang, U.C. Jeong, K.H. Chung, J.Y. Lee, and J.E. Oh, *Investigation on variable shear modulus of magnetorheological elastomer based on natural rubber due to change of fabrication design.* Polymer Engineering & Science, 2013. **53**(5): p. 992-1000.
86. Li, R. and L.Z. Sun, *Viscoelastic responses of silicone-rubber-based magnetorheological elastomers under compressive and shear loadings.* Journal of Engineering Materials and Technology, 2013. **135**(2): p. 021008.
87. Wang, Y.L., Y.A. Hu, L. Chen, X.L. Gong, W.Q. Jiang, P.Q. Zhang, and Z.Y. Chen, *Effects of rubber/magnetic particle interactions on the performance of magnetorheological elastomers.* Polymer Testing, 2006. **25**(2): p. 262-267.
88. Guan, X., X. Dong, and J. Ou, *Magnetostrictive effect of magnetorheological elastomer.* Journal of Magnetism and Magnetic Materials, 2008. **320**(3-4): p. 158-163.
89. Possinger, T., C. Bolzmacher, L. Bodelot, and N. Triantafyllidis. *Interfacial adhesion between the iron fillers and the silicone matrix in magneto-rheological elastomers at high deformations*. in *Smart Sensors, Actuators, and MEMS VI*. 2013. Grenoble, France: SPIE.
90. Fuchs, A., J. Sutrisno, F. Gordaninejad, M.B. Caglar, and L. Yanming, *Surface polymerization of iron particles for magnetorheological elastomers.* Journal of Applied Polymer Science, 2010. **117**(2): p. 934-942.
91. Mysore, P., X. Wang, and F. Gordaninejad. *Thick magnetorheological elastomers*. in *Active and Passive Smart Structures and Integrated Systems 2011*. 2011. San Diego, California, USA: SPIE.
92. Bednarek, S., *The giant linear magnetostriction in elastic ferromagnetic composites within a porous matrix.* Journal of Magnetism and Magnetic Materials, 2006. **301**(1): p. 200-207.
93. Nayak, B., S.K. Dwivedy, and K.S.R.K. Murthy, *Fabrication and characterization of magnetorheological elastomer with carbon black.* Journal of Intelligent Material Systems and Structures, 2014. **1045389**(X14535011): p. 1-10.

94. Liao, G., X. Gong, and S. Xuan, *Influence of shear deformation on the normal force of magnetorheological elastomer.* Materials Letters, 2013. **106**(0): p. 270-272.
95. Yu, M., B. Ju, J. Fu, X. Liu, and Q. Yang, *Influence of composition of carbonyl iron particles on dynamic mechanical properties of magnetorheological elastomers.* Journal of Magnetism and Magnetic Materials, 2012. **324**(13): p. 2147-2152.
96. Bica, I., *The influence of the magnetic field on the elastic properties of anisotropic magnetorheological elastomers.* Journal of Industrial and Engineering Chemistry, 2012. **18**(5): p. 1666-1669.
97. Yanceng, F., G. Xinglong, X. Shouhu, Z. Wei, Z. Jian, and J. Wanquan, *Interfacial friction damping properties in magnetorheological elastomers* Smart Mater. Struct., 2011. **20**(3): p. 1-8.
98. Fan, Y., X. Gong, S. Xuan, L. Qin, and X. Li, *Effect of Cross-Link Density of the Matrix on the Damping Properties of Magnetorheological Elastomers.* Industrial & Engineering Chemistry Research, 2012. **52**(2): p. 771-778.
99. Boczkowska, A., S.F. Awietjan, S.A. Pietrzko, and K.O.K. J., *Mechanical properties of magnetorheological elastomers under shear deformation.* Composites Part B: Engineering, 2012. **43**(2): p. 636-640.
100. Barlow, F.W., *Rubber compounding : principles, materials, and techniques*. 2 ed. 1993, Marcel Dekker: CRC Press. 312.
101. Rodgers, B., *Rubber Compounding: Chemistry And Applications*. 1 ed. 2004, New York: CRC Press. 645.
102. Hoffman, W., *Rubber Technology Handbook*. 1989, Cincinatti: Hanser/Gardner Publications. 475.
103. Lewis, W.K., L. Squires, and R.D. Nutting, *Mechanism of Rubber Vulcanization with Sulfur.* Industrial & Engineering Chemistry, 1937. **29**(10): p. 1135-1144.
104. Kantiyong, L., *Magnetic and Mechanical Prperties of Barium Ferrite Natural Rubber Composites*, in *Chemistry*. 2009, Kasetsart University: Kasetsart. p. 118.
105. Ginder, J.M., Clark, S. M , Schlotter, W. F , Nichols, M. E., *Magnetostrictive Phenomena in Magnetorheological Elastomers.* International Journal of Modern Physics B, 2002. **16**(17-18): p. 2412-2418.
106. Hu, Y., Y.L. Wang, X.L. Gong, X.Q. Gong, X.Z. Zhang, W.Q. Jiang, P.Q. Zhang, and Z.Y. Chen, *New magnetorheological elastomers based on polyurethane/Si-rubber hybrid.* Polymer Testing, 2005. **24**(3): p. 324-329.
107. Xiuying, Q., L. Xiushou, L. Weihua, C. Jun, G. Xinglong, Y. Tao, L. Wei, S. Kang, and C. Xiaodong, *Microstructure and magnetorheological properties of the thermoplastic magnetorheological elastomer composites containing modified carbonyl iron particles and poly(styrene- b -ethylene-ethylenepropylene- b -styrene) matrix.* Smart Materials and Structures, 2012. **21**(11): p. 115028.
108. Wu, J., X. Gong, L. Chen, H. Xia, and Z. Hu, *Preparation and characterization of isotropic polyurethane magnetorheological elastomer through in situ polymerization.* Journal of Applied Polymer Science, 2009. **114**(2): p. 901-910.

109. Wang, Y., Y. Hu, X. Gong, W. Jiang, P. Zhang, and Z. Chen, *Preparation and properties of magnetorheological elastomers based on silicon rubber/polystyrene blend matrix.* Journal of Applied Polymer Science, 2007. **103**(5): p. 3143-3149.
110. Kari, L. and P. Blom, *Magneto-sensitive rubber in a noise reduction context - exploring the potential.* Plastics, Rubber and Composites, 2005. **34**(8): p. 365-371.
111. Geoffrey, P.M. and P.C. Gregory. *Energy absorption in axial and shear loading of particulate magnetostrictive composites*. in *Smart Structures and Materials 2000: Active Materials: Behavior and Mechanics*. 2000. Newport Beach, CA: SPIE.
112. Mcknight, G.P. and G.P. Carman. *Energy Absorption and Damping in Magnetostrictive Composites*. in *Materials Research Symposium, Smart Materials*. 1999. Boston, USA.: Cambridge University Press.
113. Kear, D., *Geology of Ironsand Resources of New Zealand*. 1979, New Zealand Department of Scientific and Industrial Research: Wellington. p. 1-152.
114. United Nations, E.a.D.D.E., *Atlas of Mineral Resources of the ESCAP Region V 4: New Zealand : Explanatory Brochure*. 1988, United Nations: Bangkok, Thailand. p. 28.
115. Lawton, D.C., *Geophysical Exploration of Quaternary Ironsand deposits at Taharoa, Waikato north head and Raglan, West Coast North Island, New Zealand*. 1979, University of Auckland: Auckland. p. 336.
116. Kear, D., *Mineral Deposits of New Zealand*. 1 ed, ed. D. Kear. Vol. 13. 1988, Australia: The Australasian institute of Mining and Metallurgy. p 99-117.
117. Christie, T. and B. Brathwaite, *Mineral Commodity Report 15 - Iron*. 1998: Institute of Geological and Nuclear Science Ltd,New Zealand. p. 1-16.
118. Stokes, S., C.S. Nelson, T.R. Healy, and N.A. Arthur, *The Taharoa Iron Sand Deposit*, in *Mineral Deposits of New Zealand*, D. Kear, Editor. 1988, The Australasian institute of Mining and Metallurgy: Australia. p. 105-109.
119. Ross, D.I., *Surface magnetic permeability measurements on some Taranaki ironsand deposits.* New Zealand Journal of Geology and Geophysics, 1963. **6**(2): p. 197-208.
120. Callister W. D and R.D. G., *Materials Science and Engineering: An Introduction*, ed. 8th. 2010, USA: John Wiley and Sons. 922.
121. Jakubovics, J.P., *Magnetism and magnetic materials*. 2nd ed. ed. 1994, London: Maney Publishing. 144.
122. Jiles, D., *Introduction to magnetism and magnetic materials*. 2nd ed. 1998, Florida, USA: CRC Press. 568.
123. Telford, W.M., L.P. Geldart, R.E. Sheriff, and D.A. Keys, *Applied Geophysics*. 1 ed. Vol. 1. 1976, Cambridge: Cambridge University Press. 860.
124. White, M.A., *Properties of Materials*. 1 ed. 1999, New York: Oxford University Press. 334.
125. Paranis, D.S., *Principles of Applied Geophysics*. 3 ed. Vol. 1. 1979, U.S.A: Chapman and Hall. 275.
126. Cullity, B.D. and C.D. Graham, *Antiferromagnetism*, in *Introduction to Magnetic Materials*. 2008, John Wiley & Sons, Inc. p. 151-173.

127. Cullity, B.D. and C.D. Graham, *Ferrimagnetism*, in *Introduction to Magnetic Materials*. 2008, John Wiley & Sons, Inc. p. 175-195.
128. John, F.S., *The role of magnetic susceptibility in magnetic resonance imaging: MRI magnetic compatibility of the first and second kinds.* Medical Physics, 1996. **23**(6): p. 815-850.
129. Wright, J.B., *Iron-titanium oxides in Some New Zealand ironsands.* New Zealand Journal of Geology and Geophysics, 1964. **7**(3): p. 424-444.
130. Boczkowska, A. and S. Awietjan, *Microstructure and properties of magnetorheological elastomers*, in *Advanced Elastomer -Technology, Properties and Applications*. 2012, InTech: Rijeka, Croatia. p. 147-180.
131. Li, J., X. Gong, H. Zhu, and W. Jiang, *Influence of particle coating on dynamic mechanical behaviors of magnetorheological elastomers.* Polymer Testing, 2009. **28**(3): p. 331-337.
132. Fan, Y.C., X.L. Gong, W.Q. Jiang, W. Zhang, B. Wei, and W.H. Li, *Effect of maleic anhydride on the damping property of magnetorheological elastomers.* Smart Materials and Structures, 2010. **19**(5): p. 055015.
133. Ansarifar, A., A. Azhar, N. Ibrahim, S.F. Shiah, and J.M.D. Lawton, *The use of a silanised silica filler to reinforce and crosslink natural rubber.* International Journal of Adhesion and Adhesives, 2005. **25**(1): p. 77-86.
134. Choi, S.S., I.S. Kim, and C.S. Woo, *Influence of TESPT content on crosslink types and rheological behaviors of natural rubber compounds reinforced with silica.* Journal of Applied Polymer Science, 2007. **106**(4): p. 2753-2758.
135. Vinod, V.S., S. Varghese, and B. Kuriakose, *Degradation behaviour of natural rubber-aluminium powder composites: effect of heat, ozone and high energy radiation.* Polymer Degradation and Stability, 2002. **75**(3): p. 405-412.
136. Rooj, S., A. Das, V. Thakur, R.N. Mahaling, A.K. Bhowmick, and G. Heinrich, *Preparation and properties of natural nanocomposites based on natural rubber and naturally occurring halloysite nanotubes.* Materials & Design, 2010. **31**(4): p. 2151-2156.
137. Ismail, H. and H.P.S. Abdul Khalil, *The effects of partial replacement of oil palm wood flour by silica and silane coupling agent on properties of natural rubber compounds.* Polymer Testing, 2000. **20**(1): p. 33-41.
138. Zeng, Z., W. Ren, C. Xu, W. Lu, Y. Zhang, and Y. Zhang, *Effect of bis(3-triethoxysilylpropyl) tetrasulfide on the crosslink structure, interfacial adhesion, and mechanical properties of natural rubber/cotton fiber composites.* Journal of Applied Polymer Science, 2009. **111**(1): p. 437-443.
139. Pickering, K.L., A. Abdalla, C. Ji, A.G. McDonald, and R.A. Franich, *The effect of silane coupling agents on radiata pine fibre for use in thermoplastic matrix composites.* Composites Part A: Applied Science and Manufacturing, 2003. **34**(10): p. 915-926.
140. Wang, M.J., *Effect of Polymer-Filler and Filler-Filler Interactions on Dynamic Properties of Filled Vulcanizates.* Rubber Chemistry and Technology, 1998. **71**(3): p. 520-589.
141. Choi, S.S., *Influence of storage time and temperature and silane coupling agent on bound rubber formation in filled styrene butadiene rubber compounds.* Polymer Testing, 2002. **21**(2): p. 201-208.
142. Wu, J., X. Gong, Y. Fan, and H. Xia, *Improving the magnetorheological properties of polyurethane magnetorheological elastomer through*

plasticization. Journal of Applied Polymer Science, 2012. **123**(4): p. 2476-2484.
143. Fan, J. and H. Chen. *Influence of curing time on the anisotropic microstructure of magnetorheological elastomer*. in *Advances in Heterogeneous Material Mechanics 2008: Proceedings of the Second International Conference on Heterogeneous Materials Mechanics*. 2008. Huangshan, China: DEStech Publications, Incorporated.
144. Deniz, V., B. Karaagac, and M. Inal, *Predicting optimum cure time of rubber compounds by means of ANFIS.* Materials & Design, 2008. **35**(0): p. 833-838.
145. Deniz, V., B. Karaagac, and M. Inal, *Artificial neural network approach for predicting optimum cure time of rubber compounds.* Materials & Design, 2009. **30**(5): p. 1685-1690.
146. Simpson, R.B., *Rubber Basics*. 2002, Shawbury, UK: Rapra Technology. 212.
147. ASTM-D2084, *Standard Test Method for Rubber Property—Vulcanization Using Oscillating Disk Cure Meter*. 2011, ASTM International: West Conshohocken. p. 11.
148. Stefan, B., Alois, D , Konrad, B, *Mechanical Aspects of High Damping Rubber*, in *2nd Int. PhD Symposium in Civil Engineering*. 1998: Budapest. p. 1-7.
149. Jones, D.I.G., *Handbook of viscoelastic vibration damping*. 1 ed. 2001, New York, USA.: John Wiley & Sons. 410.
150. Macioce, P., *Viscoelastic Damping 101 - Insight*. 2010, Roush Industries, Inc. p. 1-3.
151. James, A., S., *Integrated system damping and isolation of a three dimensional structure*, in *Mechanical engineering*. 1996, Naval Postgraduate School: Carlifornia. p. 175.
152. Arcanjo, L., *The use of damping material in industrial machines*, in *Faculty of Engineering and Applied Science*. 1985, University of Southamton: Southamton. p. 159.
153. Lin, C., G. Xing-long, and L. Wei-hua, *Damping of Magnetorheological Elastomers.* Chinese Journal of Chemical Physics, 2008. **21**(6): p. 581.
154. Chandra, R., S.P. Singh, and K. Gupta, *Damping studies in fiber-reinforced composites - a review.* Composite Structures, 1999. **46**(1): p. 41-51.
155. Lavernia, E.J., J. Zhang, and R.J. Perez, *Damping Behavior and Mechanisms in Particulate Reinforced Metal Matrix Composites Processed Using Spray Atomization and Deposition.* Key Engineering Materials, 1995. **104**(0): p. 691-728.
156. Shokrollahi, H. and K. Janghorban, *Soft magnetic composite materials (SMCs).* Journal of Materials Processing Tech, 2007. **189**(1): p. 1-12.
157. Jeong, W.H., Y.H. Han, and B.M. Song, *Effects of grain size on the residual loss of Mn-Zn ferrites.* Journal of Applied Physics, 2002. **91**(10): p. 7619-7621.
158. Choudhury, P.K. and O.N. Singh, *Electromagnetic Materials*, in *Encyclopedia of RF and Microwave Engineering*. 2005, John Wiley & Sons, Inc. p. 1227-1228.
159. Kallio, M., *The elastic and damping properties of magnetorheological elastomers*. 1 ed. 2005, Finland: VTT Technical Research Centre of Finland. 146.

160. Kelly, A. and a.W.R. Tyson, *Tensile properties of fibre-reinforced metals: copper/tungsten and copper/molybdenum.* Journal of the Mechanics and Physics of Solids, 1965. **13**(6): p. 329-350.
161. Eshelby, J.D., *The continuum theory of lattice defects.* Solid state physics, 1956. **3**(0): p. 79-144.
162. Popov, V.L., *Coulomb's Law of Friction*, in *Contact Mechanics and Friction*. 2010, Springer: Berlin. p. 133-154.
163. De Silva, C.W., *Vibration damping, control, and design*. 1 ed. 2007, Florida: CRC Press. 634.
164. Schoeck, G., *Internal Friction Due to Precipitation.* physica status solidi (b), 1969. **32**(2): p. 651-658.
165. Lavernia, E.J., R.J. Perez, and J. Zhang, *Damping behavior of discontinuously reinforced ai alloy metal-matrix composites.* Metallurgical and Materials Transactions A, 1995. **26**(11): p. 2803-2818.
166. Gatos, K.G. and J. Karger-Kocsis, *Estimation of the vulcanization time for rubber by considering their linear viscoelastic response assessed by a plate-plate rheometer.* Kautschuk Gummi Kunststoffe, 2004. **57**(7-8): p. 350-354.
167. Menard K, P., *Time and Temperature Scans Part II*, in *Dynamic Mechanical Analysis*. 2008, CRC Press. p. 123-143.
168. Mezger, T.G., *The Rheology Handbook.* 2 ed. 2006, Hannover, Germany: Curt R. Vincentz. 299.
169. Roy, R.K., *Design of Experiments Using The Taguchi Approach: 16 Steps to Product and Process Improvement*. 1 ed. 2001, New York: John Wiley & Sons. 537.
170. Mitra, A., *The Taguchi method.* Wiley Interdisciplinary Reviews: Computational Statistics, 2011. **3**(5): p. 472-480.
171. Derakhshandeh, B., A. Shojaei, and M. Faghihi, *Effects of rubber curing ingredients and phenolic-resin on mechanical, thermal, and morphological characteristics of rubber/phenolic-resin blends.* Journal of Applied Polymer Science, 2008. **108**(6): p. 3808-3821.
172. Shirazi, M., A.G. Talma, and J.W.M. Noordermeer, *Viscoelastic properties of short aramid fibers-reinforced rubbers.* Journal of Applied Polymer Science, 2012. **128**(4): p. 2255-2261.
173. Han, J., N. Shi, L. Xie, Y. Ma, and C. Wu, *Effect of Filler Networking on Viscoelastic Properties and Reinforcement of Natural Rubber Vulcanizates.* Journal of Macromolecular Science, Part B, 2010. **49**(3): p. 429-439.
174. Liu, Q.X., X.B. Ding, H.P. Zhang, and X. Yan, *Preparation of High-Performance Damping Materials Based on Carboxylated Nitrile Rubber: Combination of Organic Hybridization and Fiber Reinforcement.* Journal of Applied Polymer Science, 2009. **114**(5): p. 2655-2661.
175. Kar, K.K. and A.K. Bhowmick, *Effect of holding time on high strain hysteresis loss of carbon black filled rubber vulcanizates.* Polymer Engineering & Science, 1998. **38**(12): p. 1927-1945.
176. Kucherskii, A.M., *Hysteresis losses in carbon-black-filled rubbers under small and large elongations.* Polymer Testing, 2005. **24**(6): p. 733-738.
177. Arrighi, V., I.J. McEwen, H. Qian, and M.B. Serrano Prieto, *The glass transition and interfacial layer in styrene-butadiene rubber containing silica nanofiller.* Polymer, 2003. **44**(20): p. 6259-6266.

178. Hathaway, K., A. Clark, and J. Teter, *Magnetomechanical damping in giant magnetostriction alloys.* Metallurgical and Materials Transactions A, 1995. **26**(11): p. 2797-2801.
179. Rendek, M. and A. Lion, *Amplitude dependence of filler-reinforced rubber: Experiments, constitutive modelling and FEM Implementation.* International Journal of Solids and Structures, 2010. **47**(21): p. 2918-2936.
180. Ahankari, S.S. and K.K. Kar, *Hysteresis measurements and dynamic mechanical characterization of functionally graded natural rubber–carbon black composites.* Polymer Engineering & Science, 2010. **50**(5): p. 871-877.
181. Guo, Z.X. and J. Yu, *Grafting of dendritic polyethers onto nanometre silica surface.* Journal of Materials Chemistry, 2002. **12**(3): p. 468-472.
182. Zhao, J., M. Milanova, M.M.C.G. Warmoeskerken, and V. Dutschk, *Surface modification of TiO2 nanoparticles with silane coupling agents.* Colloids and Surfaces A: Physicochemical and Engineering Aspects, 2012. **413**(0): p. 273-279.
183. Flory, P.J. and J. Rehner, *Statistical Mechanics of Cross-Linked Polymer Networks II. Swelling.* The Journal of Chemical Physics, 1943. **11**(11): p. 521-526.
184. Hunsche, A., U. Gorl, A. Muller, M. Knaack, and T. Gobel, *Investigations concerning the reaction silica/organosilane and organosilane/polymer. Part 1: Reaction mechanism and reaction model for silica/organosilane.* Kautschuk und Gummi, Kunststoffe, 1997. **50**(12): p. 881-889.
185. Hunsche, A., U. Gorl, H.G. Koban, and T. Lehmann, *Investigations on the reaction silica/organosilane and organosilane/polymer. Part 2: Kinetic aspects of the silica-organosilane reaction.* Kautschuk und Gummi, Kunststoffe, 1998. **51**(7-8): p. 525-533.
186. Shebanova, O.N. and P. Lazor, *Raman study of magnetite (Fe3O4): laser-induced thermal effects and oxidation.* Journal of Raman Spectroscopy, 2003. **34**(11): p. 845-852.
187. Shih, P.T.K. and J.L. Koenig, *Raman studies of the hydrolysis of silane coupling agents.* Materials Science and Engineering, 1975. **20**(0): p. 137-143.
188. Amanda, A., B.A. Julio, L.D. Gemma, K.G. Yurii, V. Nuria, M.B. Xavier, M. Jorge, M. Jordi, M. Maria, and N.M. Dmitri, *Ecologically Friendly Polymer-Metal and Polymer-Metal Oxide Nanocomposites for Complex Water Treatment*. 1 ed. Nanocomposites - New Trends and Developments, ed. E. Farzad. 2012, Rijeka, Croatia: InTech. Chapter 8: 187-213.
189. Hou, Y., J. Yu, and S. Gao, *Solvothermal reduction synthesis and characterization of superparamagnetic magnetite nanoparticles.* Journal of Materials Chemistry, 2003. **13**(8): p. 1983-1987.
190. Zhang, H., C. Li, J. Guo, L. Zang, and J. Luo, *In Situ Synthesis of Poly(methyl methacrylate)/SiO2 Hybrid Nanocomposites via "Grafting Onto" Strategy Based on UV Irradiation in the Presence of Iron Aqueous Solution.* Journal of Nanomaterials, 2012. **2012**(0): p. 1-9.
191. Sideridou, I.D. and M.M. Karabela, *Effect of the amount of 3-methacyloxypropyltrimethoxysilane coupling agent on physical properties of dental resin nanocomposites.* Dental Materials, 2009. **25**(11): p. 1315-1324.
192. Gorl, U., J. Munzenberg, D. Luginsland, and A. Muller, *Investigations on the reaction silica/organosilane and organosilane/polymer-Part 4: Studies on the*

chemistry of the silane sulfur chain. Kautschuk Gummi Kunststoffe, 1999. **52**(9): p. 588-597.
193. Luginsland, H.D., *Reactivity of the sulfur chains of the tetrasulfane silane Si 69 and the disulfane silane TESPD.* Kautschuk Gummi Kunststoffe, 2000. **53**(1): p. 10-19.
194. Sun, L., R.F. Gibson, F. Gordaninejad, and J. Suhr, *Energy absorption capability of nanocomposites: A review*. Composites Science and Technology, 2009. **69**(14): p. 2392-2409.
195. Gu, H., Y. Guo, S.Y. Wong, C. He, X. Li, and V.P.W. Shim, *Effect of interphase and strain-rate on the tensile properties of polyamide 6 reinforced with functionalized silica nanoparticles.* Composites Science and Technology, 2013. **75**(0): p. 62-69.
196. Li, Y., B. Han, L. Liu, F. Zhang, L. Zhang, S. Wen, Y. Lu, H. Yang, and J. Shen, *Surface modification of silica by two-step method and properties of solution styrene butadiene rubber (SSBR) nanocomposites filled with modified silica.* Composites Science and Technology, 2013. **88**(0): p. 69-75.
197. Mele, P., S. Marceau, D. Brown, D.Y. Puydt, and N.D. Alberola, *Reinforcement effects in fractal-structure-filled rubber.* Polymer, 2002. **43**(20): p. 5577-5586.
198. Jiles, D.C., *Theory of the magnetomechanical effect.* Journal of Physics D: Applied Physics, 1995. **28**(8): p. 1537.
199. Fujii, N. and T. Tohyama, *Antivibration rubber composition*, in U.S. Patent, Editor. 2011, Tokai Rubber Industries, Ltd.: USA. p. 1-6.
200. Katsumi, T. and F. Sekido, *Rubber composition for laminated vibrationproofing structure*, E. Patent, Editor. 1997, Sumitomo Rubber Industries, Ltd.: Germany. p. 1-24.
201. Shimada, J., H. Oishi, and T. Shirokawa, *Rubber Composition for Seismic Isolation Laminates*, U.S. Patent, Editor. 2001, The Yokohama Rubber Co., Ltd.,: USA. p. 1-12.
202. Kraus, G., *Reinforcement of elastomers by carbon black*, in *Fortschritte der Hochpolymeren-Forschung*. 1971, Springer Berlin Heidelberg: Berlin. p. 155-237.
203. Radiguet, M., D.S. Kammer, and J.F. Molinari, *The role of viscoelasticity on heterogeneous stress fields at frictional interfaces.* Mechanics of Materials, 2014. **80**(0): p. 276-287.
204. Buyukozturk, O., A.H. Nilson, and F.O. Slate, *Deformation and fracture of particulate composite.* Journal of the Engineering Mechanics Division, 1972. **98**(3): p. 581-593.
205. Chikazumi, S. and C.D. Graham, *Physics of Ferromagnetism*. 2 ed. 1997, New York: Oxford University Press. 668.

Appendices

Appendix I

Results of cure time of rubber compounds for formulations stated in Table 4.3

Sample type	Cure time (min)
1	5.3
2	5.3
3	5.3
4	5.3
5	5.3
6	4.7
7	5.1
8	4.8
9	5.4
10	4.5
11	4.3
12	4.7
13	4.5
14	4.6
15	4.8
16	4.5
17	4.2
18	4.5
19	4.2
20	4.5
21	4.6
22	4.9
23	4.6
24	4.6
25	4.4

Appendix II

Results of cure time of rubber compounds for formulations stated in Table 5.1

Materials	**Function**	**loading (phr)**					
Natural rubber	raw material/matrix	100	100	100	100	100	100
ZnO	accelerator/activator	5	5	5	5	5	5
Stearic acid	accelerator/activator	1	1	1	1	1	1
Paraffin oil	plasticiser	2	2	2	2	2	2
Naphthenic oil	plasticiser	3	3	3	3	3	3
Iron sand	filler	70	70	70	70	70	70
CBS	accelerator	2	2	2	2	2	2
TMTD	accelerator	1	1	1	1	1	1
Sulphur	crosslinking agent	1.5	1.5	1.5	1.5	1.5	1.5
Silane coupling agent level (wt %)							
TESPT	coupling agent	0	2	4	6	8	10
Curing characteristics (minutes)							
Cure time	(t_{90})	4.57	4.53	4.33	4.23	4.4	4.46

* phr = per hundred rubber

Appendix III

Results of cure time of rubber compounds for formulations stated in Table 7.2

Materials	**MRE/ISO**	**MRE/AN**	**MRE/AN/30CB**	**MRE/AN/50CB**	**Comparative sample 1 (CS/30CB)**	**Comparative sample 2 (CS/50CB)**	**Comparative sample 3 (CS/70CB)**
Natural Rubber	100	100	100	100	100	100	100
ZnO	5	5	5	5	5	5	5
Stearic Acid	1	1	1	1	1	1	1
Paraffin Oil	2	2	2	2	2	-	-
Naphthenic Oil	3	3	3	3	3	10	5
Iron sand	70	70	70	70	-	-	-
Carbon black	-	-	30	50	30	50	70
CBS	2	2	2	2	2	1.9	1
TMTD	1	1	1	1	1	0.8	-
Sulphur	1.5	1.5	1.5	1.5	1	0.8	1.5
Curing condition							
Temperature (ºC)	150	150	150	150	150	150	150
Pressure (MPa)	12	12	12	12	12	12	12
Magnetic field during curing (mT)	0	600	600	600	-	-	-
Curing characteristics (minutes)							
Cure time (t_{90})	4.23	4.23	4.19	4.07	4.46	3.90	5.1

Appendix IV

Experimental procedure to determine coefficient of friction between iron sand and rubber

For the measurement of coefficient of friction between iron sand and rubber, test specimens were prepared using two iron sand coated plates with dimensions 35 mm x 150 mm x 3mm and rubber sheet with dimension 35 mm x 150 mm x 3mm. A schematic arrangement of test specimens during testing is shown as follows:

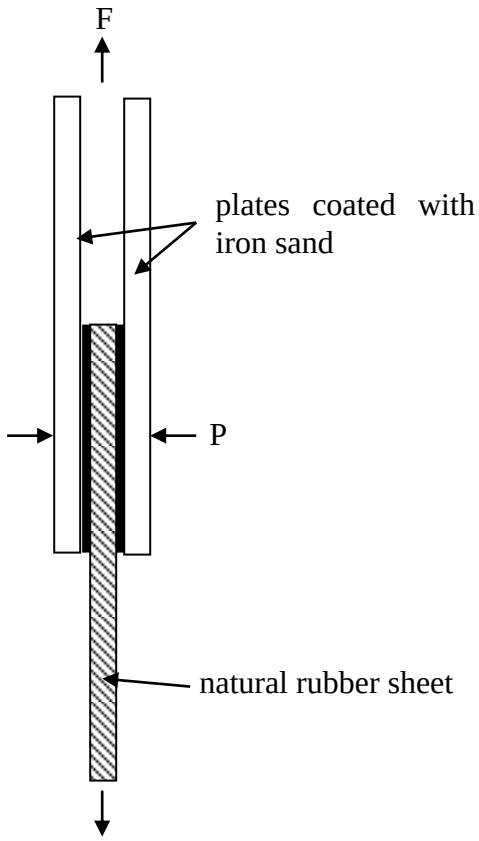

Schematic of friction experiments with the centre specimen being rubber sheet and the outer specimens being iron sand coated plates

The central specimen was rubber sheet and the two outer specimens were iron sand coated plates. The overlapping length of the specimens was approximately 40 mm. The normal force P was first applied manually by clamping the outer plates, which compressed the rubber sheet and was measured with the load cell at approximately 100N.The specimens were inserted in Instron tensile tester and the relative sliding motion between the specimens was applied with the actuator of the testing machine. The friction force, F, was measured with the load cell of the testing machine. The coefficient of friction was calculated as follows:

$$\mu = \frac{F}{2P} \tag{A.1}$$

where factor 2 comes from the fact that there are two contact surfaces on each specimen. Five specimens were prepared and average coefficient of friction of the five specimens was measured.

Results

Sample	Frictional force (N)	Coefficient of friction (μ)
1	31.57	0.16
2	50.26	0.25
3	39.02	0.20
4	46.31	0.23
5	40.28	0.20
Average	**41.49**	**0.21**

Appendix V

Results of cure time of rubber compounds for formulations stated in Table 8.1

Materials	**Function**	**loading (phr)**				
Natural Rubber	matrix	100	100	100	100	100
ZnO	accelerator/activator	5	5	5	5	5
Stearic Acid	accelerator/activator	1	1	1	1	1
Paraffin Oil	plasticiser	2	2	2	2	2
Naphthenic Oil	plasticiser	3	3	3	3	3
Iron sand	filler	0	10	30	50	70
CBS	accelerator	2	2	2	2	2
TMTD	accelerator	1	1	1	1	1
Sulphur	crosslinking agent	1.5	1.5	1.5	1.5	1.5
Curing characteristics (minutes)						
Cure time	(t_{90})	5.3	4.5	4.36	4.2	4.23

* phr = per hundred rubber

Published Papers

Copyright Information for Published Papers

1. A new method to predict optimum cure time of rubber compound using dynamic mechanical analysis, Previously Published in Journal of Applied Polymer Science. © 2013 Wiley Periodicals, Inc. Used with permission. Copyright license number: 3546270045096.
2. Dynamic properties of magnetorheological elastomers based on iron sand and natural rubber, Previously Published in Journal of Applied Polymer Science. © 2014 Wiley Periodicals, Inc. Used with permission. Copyright license number: 3546270339784.
3. The effect of silane coupling agent on iron sand for use in magnetorheological elastomers, Part 1: Surface chemical modification and characterization, Previously Published in Composites Part A: Applied Science and Manufacturing. © 2015 Elsevier, Ltd. Used with permission. Copyright license number: 3546270452117.
4. Comparison of dynamic properties of magnetorheological elastomers with existing antivibration rubbers, Previously Published in Composites Part B: Engineering. © 2015 Elsevier, Ltd. Used with permission. Copyright license number: 3702891478116.

Journal of Applied Polymer Science

A New Method to Predict Optimum Cure Time of Rubber Compound Using Dynamic Mechanical Analysis

S. Raa Khimi, K. L. Pickering
School of Engineering, The University of Waikato, Hamilton 3216, New Zealand
Correspondence to: K.L. Pickering (E-mail: klp@waikato.ac.nz)

ABSTRACT: The degree of vulcanization of a rubber compound has a big influence on the properties of the final product. Therefore, precisely defining the curing process including optimum cure time is important to ensure the production of final products having high performance. Typically, vulcanization is represented using vulcanization curves. The main types of equipment used for producing vulcanization curves are the oscillating disc rheometer (ODR) and the moving die rheometer (MDR). These can be used to plot graphs of torque versus time at a constant temperature to show how cure is proceeding. Based on the results obtained, optimum cure time (t_{90}) is calculated as the time required for the torque to reach 90% of the maximum achievable torque. In this study, the use of Dynamic Mechanical Analysis (DMA) for assessment of t_{90} was assessed. DMA was carried out using shear mode isothermal tests to measure the changes in material properties caused by vulcanization. The results revealed that the shear storage modulus (G′), shear loss modulus (G″), and tan δ all reflect the vulcanization process, however, tan δ gave the best representation of level of vulcanization. Indeed, the curve of tan δ was able to be used to derive the t_{90} for rubber compounds and showed good agreement with the results from an MDR. © 2013 Wiley Periodicals, Inc. J. Appl. Polym. Sci. **2014**, *131*, 40008.

KEYWORDS: rubber; curing; dynamic mechanical analysis

Received 12 May 2013; accepted 24 September 2013
DOI: 10.1002/app.40008

INTRODUCTION

Rubbers are one of the most widely used groups of materials in engineering products. The advantages of rubbers such as elasticity and high damping make them dominant in various applications including tires, dampers, gaskets, seals, and conveyor belts. However, in order to produce its unique material properties, the rubber compound, which is generally a mixture of rubber, vulcanization agent, accelerator, fillers, and several additional ingredients, needs to be vulcanized to form a cohesive rubber based solid. During the vulcanization process, the rubber compound is heated up to a temperature at which irreversible reaction between the rubber molecular chains and the vulcanization agent starts to form crosslinks leading to an elastic, three-dimensional structure.[1]

Typically, vulcanization is represented using vulcanization curves such as that shown in Figure 1. The main types of equipment used for producing vulcanization curves are the oscillating disk rheometer (ODR) and the moving die rheometer (MDR), both of which are technically classified as curemeters.[2–4] In a curemeter, a piece of rubber compound is contained in a sealed test cavity with a rotor that oscillated at a constant angular displacement. As vulcanization proceeds at a specific temperature, the torque required to shear the compound is monitored and a curve of torque versus time can be generated.[4,5] The working principal of the curemeter is based on the fact that the stiffness of the rubber compound increases with the formation of the crosslinks during vulcanization. The use of a curemeter to determine the vulcanization characteristics is specified in ASTM D 2084.[6]

Generally, three stages are clearly represented by a vulcanization curve. The first stage is the induction period which is characterized by slow chemical reaction between rubber and the additives. It enables safe processing and good flow of the rubber compound inside a mould cavity. The second stage is where curing of rubber molecular chains occur to form network structures. Vulcanization rate can be considered as the rate of this stage. Optimum cure time (t_{90}), which as stated earlier, is the time required for the torque to reach 90% of the maximum achievable torque (T_{90}) and relates to the time necessary for the cured rubber to achieve optimal properties.[7] The last stage can involve overcuring reactions depending on the rubber type, vulcanization agent and temperature. In an ideal case, an equilibrium degree of vulcanization is obtained and the torque versus time graph plateaus. However, some compounds show reversion due to overheating during the test that corresponds to break down of rubber networks. Conversely, additional crosslinks may

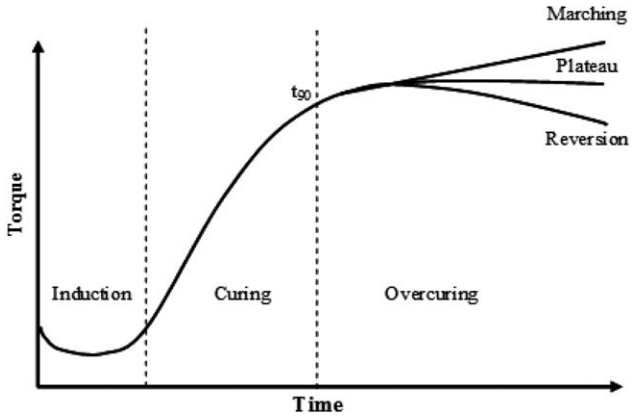

Figure 1. Vulcanization curve of rubber.

occur (induced by reaction of very reactive vulcanization agent such as hyperoxides) to produce a marching curve. It is well known that overcure of rubber compound usually has an undesirable effect on product quality. Therefore, a precise determination of cure time is necessary to ensure the production of final products having optimum performance with competitive cost.[4,5,8]

In addition, a good understanding of factors that affect vulcanization is crucial to predict the optimum cure time. Rubber compounds that have different formulations may not produce the same network density. Some of the most important factors that affect the cure time are addition of fillers, formation of sulphur linkages, and thermal instability of sulphur linkages.[2,3] The effect of cure time is more evident in the compound with filler due to rubber–filler interactions.[9] For filled elastomers, the cure time is usually shorter than unfilled elastomers and the maximum torque value increases as filler content increases.

Considering the fact that the fundamentals of curemeter application involve monitoring the shear modulus to assess the vulcanization, suggest that the shear mode of Dynamic Mechanical Analysis (DMA) could also be used for evaluating the optimum cure time of a rubber compound. DMA can be simply described as applying a sinusoidal deformation to a sample whilst analyzing the material's response to that deformation. From this, a variety of fundamental material parameters can be determined such as storage and loss modulus, tan δ, viscosity, and glass transition temperature. Lately, DMA has been used for monitoring cure of thermosetting resins, by which the viscosity of the initial stage of curing and the latter stage of curing (after gelation) are generally studied. Based on the changes in viscosity, DMA can detect cure development and important transitions in cure process such as gelation and vitrification point.[10–13] However, according to the author's knowledge, no comprehensive work was dedicated to monitor and predict optimum cure time

Table I. Formulations of Rubber Compound

Material	Natural rubber	ZnO	Stearic Acid	CBS	TMTD	Paraffin oil	Naphthenic oil	Sulphur	Titanomagnetite loading	Titanomagnetite particle size
Sample/Unit	phr	phr	phr	phr	phr	phr	phr	phr	phr	μm
1	100	5	1	2	1	2	3	1.5	0	0
2	100	5	1	2	1	2	3	1.5	30	0-32
3	100	5	1	2	1	2	3	1.5	30	32-45
4	100	5	1	2	1	2	3	1.5	30	45-56
5	100	5	1	2	1	2	3	1.5	30	56-75
6	100	5	1	2	1	2	3	1.5	30	75-106
7	100	5	1	2	1	2	3	1.5	50	0-32
8	100	5	1	2	1	2	3	1.5	50	32-45
9	100	5	1	2	1	2	3	1.5	50	45-56
10	100	5	1	2	1	2	3	1.5	50	56-75
11	100	5	1	2	1	2	3	1.5	50	75-106
12	100	5	1	2	1	2	3	1.5	70	0-32
13	100	5	1	2	1	2	3	1.5	70	32-45
14	100	5	1	2	1	2	3	1.5	70	45-56
15	100	5	1	2	1	2	3	1.5	70	56-75
16	100	5	1	2	1	2	3	1.5	70	75-106
17	100	5	1	2	1	2	3	1.5	100	0-32
18	100	5	1	2	1	2	3	1.5	100	32-45
19	100	5	1	2	1	2	3	1.5	100	45-56
20	100	5	1	2	1	2	3	1.5	100	56-75
21	100	5	1	2	1	2	3	1.5	100	75-106

phr, per hundred rubber

Table II. Optimum Cure Time (t_{90}) of the Formulations as Evaluated by MDR

Sample	t_{90} MDR (min)
1	5.10
2	4.65
3	5.19
4	4.85
5	5.25
6	4.71
7	4.41
8	4.82
9	4.64
10	4.51
11	4.92
12	4.46
13	4.42
14	4.58
15	4.31
16	4.47
17	4.47
18	4.70
19	4.55
20	4.54
21	4.20

of rubber compounds. In this study, the DMA is tested for suitability for monitoring cure of rubber compounds.

EXPERIMENTAL

Material and Specimen Preparation

In order to check the applicability of DMA to predict the optimum cure time and to evaluate the consistency of the measurements, 21 formulations of rubber compound were investigated. The formulations used in this study are shown in Table I. Natural rubber (SMR L) and other chemicals such as zinc oxide, stearic acid, *n*-cyclohexyl-2-benzothiazole sulfenamide (CBS), tetra methyl thiuramdisulphide (TMTD), paraffin oil, and naphthenic oil were all purchased from Field Rubber Limited, Auckland. Both unfilled and filled rubbers were involved in this study. Titanomagnetite was used as filler, which was milling to various sizes using planetary mono mill (Pulverisette 6) produced by Fristech GmbH.

The mixing and compounding was carried out using a conventional laboratory two roll mill (model XK150) according to ASTM designation D3184-80. Nip gap (distance between front and back roller), time of compounding and sequence of addition of the ingredients (the ingredients were added in the following sequence: rubber, activator, plasticizer, filler, accelerator, and crosslinking agent) were kept constant for all the compounds. Samples were punched from the uncured compound in the form of circular discs with 10 mm diameter and thickness of 3 mm for DMA shear mode testing.

Equipment and Procedure

Moving Die Rheometer (MDR). The MDR 2000 is a rotor less curemeter designed to measure vulcanization of rubber compounds under isothermal test conditions with constant strain and frequency. It has gained much acceptance by the rubber industry and offers several substantial advantages over previous ODR techniques as described in ASTM D 2084. The design of the MDR 2000 allows the lower half of the die to perform an oscillating rotation of 0.5° with torque measured at the upper die by a torque transducer. The curing characteristics of the compound were determined at 150°C under a constant frequency of 1.66 Hz and the t_{90} values were derived from the vulcanization curve. The results of the cure time measurements with the MDR are listed in Table II.

Dynamic Mechanical Analysis (DMA). The DMA instrument used to perform these experiments was a Perkin Elmer DMA 8000. It is made up of six major components (Figure 2): a force motor, a drive shaft, a high sensitivity displacement detector (LVDT), a sample fixture, a furnace, and a temperature controller. DMA measurements were conducted on circular disc specimens in shear mode. The specimen loading is shown in Figure 3. The driveshaft motion was kept in a horizontal direction during the test and the temperature controller was placed at a minimum distance from the sample. The furnace was first preheated to 150°C and then an isothermal test was carried out

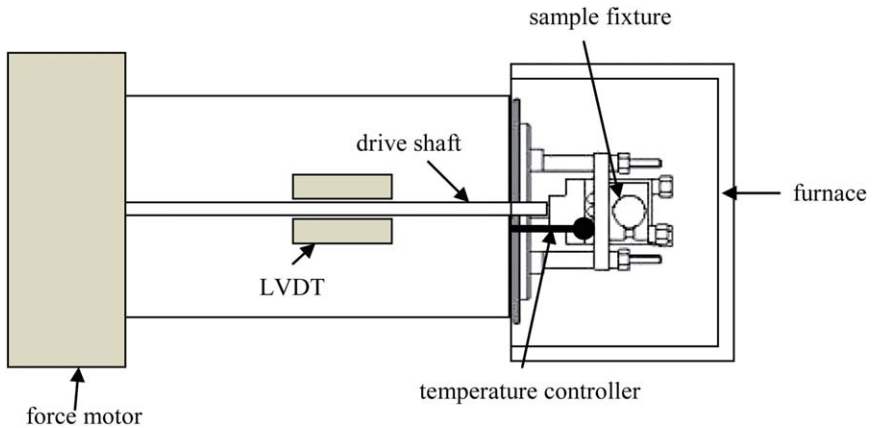

Figure 2. Scheme of the DMA 8000. [Color figure can be viewed in the online issue, which is available at wileyonlinelibrary.com.]

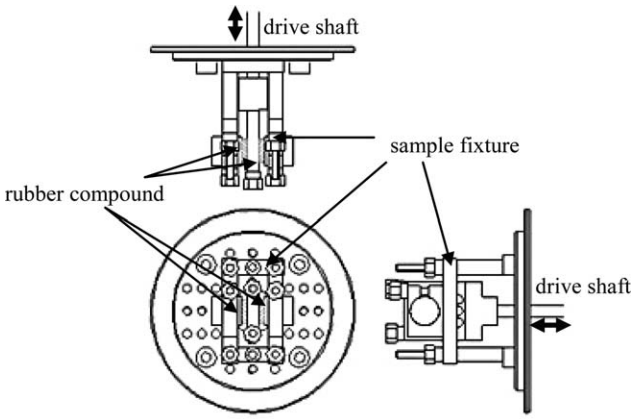

Figure 3. Scheme of the shear mode specimen loading in DMA.

under a fixed frequency of 1.66 Hz and constant displacement amplitude of 0.1 mm. The temperature was held at 150°C for 15 min to allow full vulcanization to occur. Data were collected approximately every 5 s in the isotherm period. Shear storage modulus (G'), shear loss modulus (G'') and tan δ were recorded as a function of time in order to deduce a direct connection between the dynamic time sweep test and optimum curing time.

RESULTS AND DISCUSSION

A typical time sweep plot of the unfilled natural rubber compound (NR) measured by DMA is shown in Figure 4, including G' and G''. As can be seen, G'' increases representing when the curing process started and reaches a peak after 5 min. This is thought to be due to softening of the material as the material is exposed to the oven temperature. After the maximum point, G'' was found to decrease rapidly for 3 min, followed by a gradual decrease for approximately 15 min. This is believed to occur due to the reduction of viscous flow in the material and therefore low energy being absorbed. In contrast, it is apparent that G' does not change at the beginning of the curing stage. This indicates that the stiffness of the rubber remains low at the early stage of vulcanization. After 5 min, a rapid increase of G' was observed, followed by a continuous increment up to 15 min. This represents the increase of stiffness as a result of crosslink formation. The results obtained agreed with previous work carried out by Gatos et al.[14] using a plate–plate rheometer.

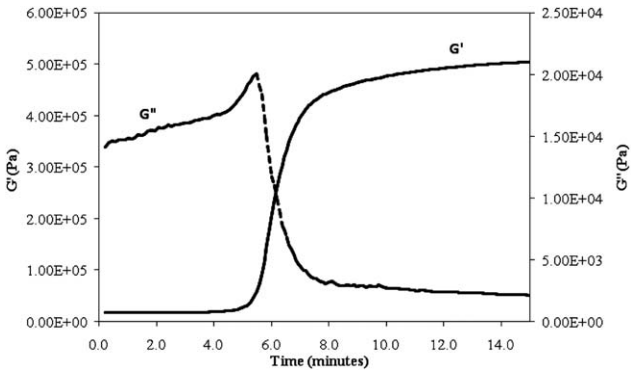

Figure 4. Time sweep plot, including G″ and G′ for NR compound.

Table III. Differences of t_{90} Value Measured by MDR and Calculated from the Gelation Point of G″ or G′ Graphs for Unfilled Natural Rubber Compound (NR)

		Time
Method	t_{90} MDR	5.1 min
	t_{90} Gelation Point	6.1 min
Error (%)		20%

Altogether, it can be seen that neither parameter shows a plateau value that indicates an equilibrium degree of vulcanization. A gelation point can be detected at 6.1 min; the gelation point is taken to be the crossover of G'' and G' where tan δ equals 1. In monitoring cure of thermosetting resins by DMA, the gelation point can be defined as a point where the crosslinks have progressed to form a network across the specimen and the material changes from a viscous liquid to a viscoelastic solid.[15] However, the values obtained show a significant difference with the value from a conventional curemeter with an average percentage error of 20% (Table III). It can be concluded that there is not a direct correlation between t_{90} and G'' or G' graphs.

Another important parameter obtained in dynamic time sweep test is tan δ. Tan δ is calculated as the quotient of the loss and the storage moduli. Therefore, it reveals the ratio of the viscous and the elastic portion of the materials.[16] The results for tan δ as a function of time for NR are depicted in Figure 5. As can be seen, three stages of curing process can be observed for the tan δ curve suggests that, this parameter and its changes with time apparently reflect the development of crosslinking reaction inside the rubber. In induction period, tan δ increased to a maximum which indicates the softening of the material and slow chemical reaction between vulcanizing agent, rubber and other compound constituents. The peak could relate to where optimum flow of the rubber compound through the mould cavity can occur giving the compound its final shape for curing. In the curing stage, tan δ was found to decrease rapidly which can again be explained by development of crosslinks between the rubber molecular chains that increase the elasticity of the

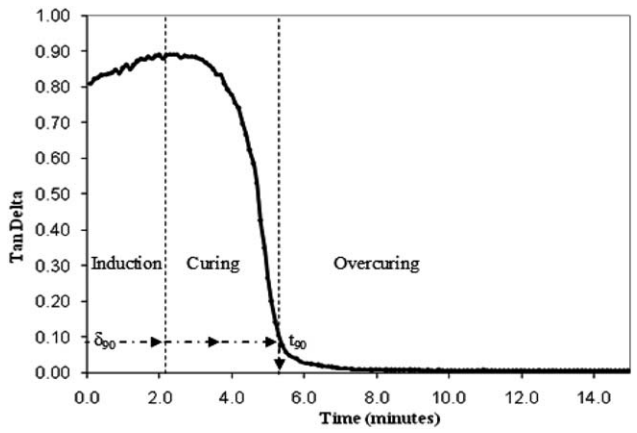

Figure 5. Tan δ curve as a function of time for NR compound.

Table IV. Percentage Error of Optimum Cure Time (t_{90}) Measured by DMA

Sample	t_{90} MDR (min)	t_{90} DMA (min)	DMA error (%)
1	5.10	5.30	3.92
2	4.65	4.70	1.08
3	5.19	5.10	−1.73
4	4.85	4.80	−1.03
5	5.25	5.40	2.86
6	4.71	4.50	−4.46
7	4.41	4.30	−2.49
8	4.82	4.70	−2.49
9	4.64	4.50	−3.02
10	4.51	4.60	2.00
11	4.92	4.80	−2.44
12	4.46	4.50	0.90
13	4.42	4.20	−4.98
14	4.58	4.50	−1.75
15	4.31	4.20	−2.55
16	4.47	4.50	0.67
17	4.47	4.60	2.91
18	4.70	4.90	4.26
19	4.55	4.60	1.10
20	4.54	4.60	1.32
21	4.20	4.40	4.76
Average error (%)			0.58

material. As previously discussed, the end of this stage corresponds to the optimum vulcanization time (t_{90}). In most cases of torque versus time graphs (vulcanization curves) generated by the MDR, the final stage of vulcanization is characterized by a plateau at a maximum value.[14] A potentially equivalent plateau is well resolvable in the tan δ curve, but tan δ stabilizes at a minimum value as a function of time.

In a typical MDR vulcanization curve, the time to achieve the optimum network density, at a given temperature is the time required for the torque to reach 90% of the maximum achievable torque.[6] The T_{90} can be calculated as follows:

$$T_{90} = T_{\min} + 0.9\ (T_{\max} - T_{\min}) \quad (1)$$

where $T_{\max}$ and $T_{\min}$ are the maximum and minimum torque values. The value of t_{90} can now be found from the graph of torque versus time. Considering the capability of the DMA to monitor the formation of the crosslinking network by the tan δ curve, an equivalent t_{90} could be obtained similiarly from δ_{90} according to Eq. (2):

$$\delta_{90} = \delta_{\max} - 0.9(\delta_{\max} - \delta_{\min}) \quad (2)$$

where now $\delta_{\max}$ and $\delta_{\min}$ are the maximum and minimum tan δ values. It is assumed that t_{90} could now be obtained from tan δ versus time graphs at δ_{90}. From the tan δ curve of NR in Figure 5, the t_{90} value obtained using Eq. (2) is 5.3 min. There was little difference between MDR and DMA values with percentage error of 3.9%. It should be mentioned at this point that even different types of conventional curemeters present variation of optimum curing time for the same sample.[14] Therefore, as both techniques use a shear excitation and measure a quantity that is related to the shear modulus, the similarity is reasonable.

In addition, it is possible that cure rate could also be determined from the tan δ versus time curve, as a decrease in tan δ value with time such that it could be obtained by the slope in the curing stage. However, further work would be needed to assess that. The sensitivity of the DMA is also sufficient to record the overcuring of rubber (after t_{90}).

In order to assess that DMA is reliable for assessment of t_{90}, further rubber compounds were analysed. In this step, t_{90} of 20 further rubber compounds with various filler loading and particle size as mentioned in Table I were measured using MDR and DMA. A percentage error criteria was used for comparison of these two techniques. The percentage errors for t_{90} measurements using DMA are given in Table IV. In view of the results obtained, the percentage errors for all compounds were lower than +/− 5% with average percentage error of 0.58%. The results for all compounds at different particle sizes and loading were satisfactory and reliable with acceptable proximity. This indicates that the DMA is capable to measure different types of curing behaviours which is more apparent in the compounds with fillers as discussed ealier.

CONCLUSIONS

This study was devoted to assess the capability of DMA to predict the optimum curing time (t_{90}) of rubber compounds. This was performed by investigating natural rubber compounds with a conventional sulphur crosslinking system. It is known that the oscillating disk rheometer (ODR) and moving die rheometer (MDR) are by far the most commonly used equipment to characterize the curing behavior of rubbers. The results of isothermal curing test of the DMA indicate that several parameters such as shear storage modulus (G'), shear loss modulus (G'') and tan δ reflect the vulcanization process. However, only the tan δ curve shows a strong correlation with crosslink development. This means that the three stages of curing can be clearly observed, with the final stage of vulcanization characterized by a plateau. Contradictory to the typical MDR vulcanization curve where the torque reaches maximum, tan δ value stabilizes at a minimum value and the t_{90} can be calculated as the time when tan δ reduces to 90% of its maximum value. The measured values were generally in agreement with results obtained by a MDR with range of errors lower than +/− 5% and average percentage error of 0.58%. Overall, the presented results show that DMA can be use as a new equipment to predict the optimum curing time of rubber.

ACKNOWLEDGMENTS

The authors would like to thank for the support from the Polymer and Composite Research Group of the University of Waikato.

REFERENCES

1. Jaunich, M.; Stark, W.; Hoster, B. *Polym. Test.* **2009**, *28*, 84.
2. Deniz, V.; Karaagac, B.; Inal, M. *Mater. Design* **2008**, *35*, 833.
3. Deniz, V.; Karaagac, B.; Inal, M. *Mater. Design* **2009**, *30*, 1685.
4. Ciesielski, A. *An Introduction to Rubber Technology, Vol. 1*; Rapra Technology Limited: Shawbury, Shrewsbury, Shropshire, SY4 4NR, UK, **1999**. p 1.
5. Hoffman, W. *Rubber Technology Handbook*; Hanser/Gardner Publications: Cincinnati, **1989**. p 475.
6. ASTM-D2084, Standard Test Method for Rubber Property—Vulcanization Using Oscillating Disk Cure Meter. ASTM International: West Conshohocken, **2011**. p 11.
7. Simpson, R. B. *Rubber Basics*. Rapra Technology: Shawbury, UK, **2002**. p 212.
8. Aggarwal, S. L. *J. Polym. Sci. Part C: Polym. Lett.* **1990**, *28*, 210.
9. Leblanc, J. L. *Prog. Polym. Sci.* **2002**, *27*, 627.
10. Stark, W. *Polym. Test.* **2013**, *32*, 231.
11. Tsang, C. F.; Hui, H. K. *Thermochim. Acta* **2001**, 367–368, 169.
12. Wang, J.; Laborie, M.-P. G.; Wolcott, M. P. *Thermochim. Acta* **2007**, *465*, 18.
13. Xie, M.; Zhang, Z.; Gu, Y.; Li, M.; Su, Y. *Thermochim. Acta* **2009**, *487*, 8.
14. Gatos, K. G.; Karger-Kocsis, J. *Kautschuk Gummi Kunststoffe* **2004**, *57*, 350.
15. Menard K. P. Time and Temperature Scans Part II, in Dynamic Mechanical Analysis; CRC Press: Boca Raton, **2008**. pp 123–143.
16. Mezger, T.G. The Rheology Handbook, 2 ed.; Curt R. Vincentz: Hannover, Germany, **2006**. p 299.

Journal of Applied Polymer Science

Dynamic Properties of Magnetorheological Elastomers Based on Iron Sand and Natural Rubber

S. Raa Khimi,[1] K. L. Pickering,[1] B. R. Mace[2]
[1]School of Engineering, University of Waikato, Hamilton 3216, New Zealand
[2]Department of Mechanical Engineering, University of Auckland, Auckland 1142, New Zealand
Correspondence to: S. Raa Khimi (E-mail: klp@waikato.ac.nz)

ABSTRACT: In this study, magnetorheological elastomers (MREs) based on iron sand and natural rubber were prepared. The Taguchi method was employed to investigate the effect of a number of factors, namely, the iron sand content, iron sand particle size, and applied magnetic field during curing on the loss tangent (tan δ) and energy dissipated during cyclic loading. Tan δ was measured through dynamic mechanical analysis over a range of frequency (0.01–130 Hz), strain amplitude (0.1–4.5%), and temperature (−100 to 50°C). The energy dissipated was measured with a universal tester under cyclic tensile loading. The data were then statistically analyzed to predict the optimal combination of factors, and finally, experiments were conducted for verification. It was found that the iron sand content had the greatest influence on tan δ when measured over a range of frequency, and the energy dissipated during hysteresis tests. However, none of the factors showed a significant influence on tan δ when measured over a range of strain amplitude. Furthermore, the iron sand content and magnetic field were also found to influence the width of the peak in tan δ as a function of the temperature. The morphological characteristics of the MREs were also examined with scanning electron microscopy. © 2014 Wiley Periodicals, Inc. J. Appl. Polym. Sci. **2015**, *132*, 41506.

KEYWORDS: dynamic properties; magnetorheological elastomers; statistical methods

Received 28 April 2014; accepted 5 September 2014
DOI: 10.1002/app.41506

INTRODUCTION

A material with a high damping capability is desired from the viewpoint of vibration suppression in structures. Rubber is by far the most commonly used material for damping; here, damping relies on the energy absorbed due to viscous flow that occurs during deformation in this viscoelastic material. However, the enhancement of damping through rubber modification or rubber selection to increase the viscous flow, not surprisingly, generally results in a reduction in stiffness and strength.[1] More recently, magnetorheological elastomers (MREs) have been developed such that the inclusion of magnetic particles in rubber enables additional damping through magnetic interactions between neighbouring magnetic particles and interfacial damping between the particles and the rubber matrix. Furthermore, the damping and stiffness can be varied by the application of an applied magnetic field during fabrication or in service. MREs are often referred to as solid analogs of the previously developed magnetorheological fluids (MRFs) used in the damping of automotive suspensions. In MRFs, magnetic particles are contained within an oil. The main advantage of MREs over MRFs is that particle sedimentation is overcome. Moreover, MREs do not need containers or seals to hold the fluid or prevent leakage.[2] MREs can be used for damping, either alone or within a composite structures, such as those including steel plates.

MREs can be fabricated to contain a uniform suspension of magnetic particles (isotropic MREs). However, it has been found that when a magnetic field is applied during curing, chainlike structures of magnetic particles are formed within the rubber (which become anisotropic MREs); this provides much larger damping and stiffness values.[3] Figure 1 shows the structure of isotropic and anisotropic MREs. The formation of such chainlike structures relies on a mechanism such that when individual particles are exposed to an applied magnetic field, magnetic dipole moments pointing along the field direction are induced within them. A magnetic force will cause the north pole of one particle to attract the south pole of its neighbour; this results in the formation of chains and columnar structures inside the matrix. When the matrix is cured, the particle structure is set in place.[4]

The magnetic particles of choice for MREs are iron particles, and suitable matrix materials include natural rubber, silicone rubber, polybutadiene, polyisobutylene, polyisoprene, and polyurethene rubber.[3,5–10] These materials are nonmagnetic

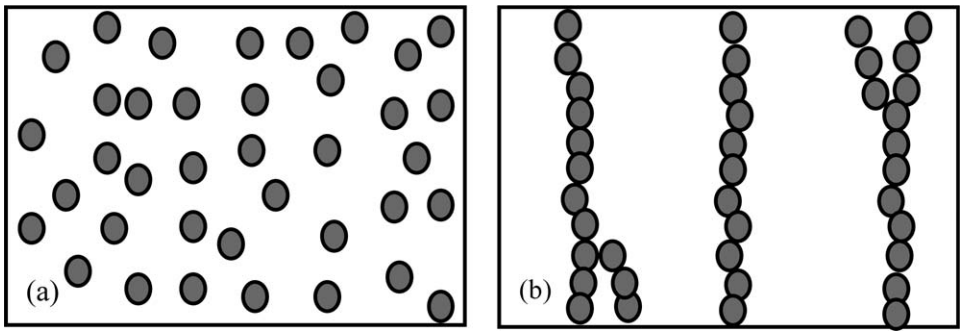

Figure 1. MRE structure: (a) isotropic and (b) anisotropic MRE.

viscoelastic materials into which the magnetic particles can be added and subsequently processed into a final solid form through conventional rubber or plastic processing.[11–13] Recent work has focused on carbonyl iron and natural rubber MRE because of their associated ease of processing and good damping performance.[14–16] However, one of the biggest challenges in the development of MREs is cost. Carbonyl iron particles, the most commonly used particles, are expensive at $13–15/kg in bulk. The more cheaply produced iron particles iron oxide (Fe_3O_4) and barium ferrite ($BaFe_{12}O_{19}$) tend to be irregular in shape, tend to have wider size distributions, and simply do not perform as well.[17,18] Some iron alloy particles actually perform better than carbonyl iron, but they are significantly more expensive.[19] It is apparent that more applications would quickly become commercially viable if the material cost could be reduced.

This work aims to fabricate iron sand and natural rubber MREs. Iron sand was chosen because it has a high permeability and saturation magnetization, has a low cost, and is readily available in New Zealand. It is derived from the erosion of andesitic and rhyolitic volcanic rocks, which are the main types of iron ore deposits in New Zealand. Iron sand is a dark, high-density sand that occurs along the west coast of the North Island from Wanganui to Kaipara Harbour near Auckland over a distance of 480 km. It contains titanomagnetite, a mineral itself containing iron and titanium, which is highly magnetic.[20,21]

The conventional approach of experimental design is that one factor is varied and the remaining factors are kept constant; it is expensive and time-consuming. Hence, several design-of-experiment methods have been developed that can reduce the number of experiments, time, and cost required to model the response functions.[22] Among them, the Taguchi method has had great success in the design and optimization of the controllable factors to achieve a high-quality product or process.[23,24] This method has been used successfully, for example, to optimize the processing conditions and chemical formulation in rubber.[25,26] As far we are aware, there has been no published analysis of the factors effecting the dynamic properties of MREs with the Taguchi method. In this study, the loss tangent (tan δ) was considered as the fundamental parameter to assess damping. Tan δ gives a comparison of the energy lost to that stored; it is obtained by dividing the loss modulus (G'') by the storage modulus (G').[1] However, another estimate of damping used in the literature is the amount of energy dissipated during cyclic deformation; this can be calculated from the area of the hysteresis loop. In the next section, the Taguchi method is briefly reviewed. Then, the experimental methods used to fabricate the MREs, the factors investigated, and the characterization methods are described. This is followed by a presentation of the results and discussion. Finally, the conclusions are summarized, and some finding remarks are made.

TAGUCHI METHOD

The Taguchi method, pioneered by Genichi Taguchi, provides a simple, efficient, and systematic approach to study the effects of multiple variables by identifying the performance trend for each factor and determining the combination that yields the optimum conditions.

The Taguchi method generally includes the following steps:

1. Identification of the factors and their levels.
2. Selection of an appropriate orthogonal array (OA) and assignment of the factors and levels to the OA.
3. The conducting of the experiment.
4. Analysis of the experimental data and determination of the optimal levels.
5. Verification of the optimum design factors through experimentation.

The key component in the design of the experiment is the identification of factors and their levels. With the finalized factors and levels, the Taguchi method makes use of an OA for experimental design. The Taguchi method allows for 18 different standards of OAs, and the details of OA selection are published in refs.[24,27] After OA selection, the experiments are carried out, and the results can then be analyzed with the signal-to-noise (S/N) ratio to determine the effect of each factor and the level that maximizes the performance. The S/N can be divided into three categories depending on the desired output performance: nominal (used where a target value is desired), the smaller the better, and the larger the better, for which eqs. (1), (2), and (3) are used, respectively, to determine S/N:

$$\frac{S}{N} = -10\log\frac{\sum_{i=0}^{n}(Y_i - \mathrm{D})^2}{n} \quad (1)$$

$$\frac{S}{N} = -10\log\frac{\sum_{i=0}^{n}Y_i^2}{n} \quad (2)$$

$$\frac{S}{N} = -10\log\frac{\sum_{i=0}^{n}\left(\frac{1}{Y_i^2}\right)}{n} \quad (3)$$

where D is the average of the observed data, n is the number of observations, i is the level, and Y_i is the observed data at level i. Another function of S/N is that it is able to determine the ranking of factors through the calculation of the average effect of a factor at a level. This is given by simple statistical calculation as follows:[25]

$$Aj = \frac{\sum_{i=0}^{n}\left(\frac{S}{N}\right)i}{n} \quad (4)$$

where A_j is the average for factor j, $(S/N)_i$ represents the S/N observation of a factor at level i, and n represents the total number of observations for that factor. By plotting the average factor effect against the corresponding factor level, a main effect plot is obtained, and the trend of the influence of each factor on the results is extracted. The relative effects of factors affecting the response can be calculated by an analysis of variance (ANOVA). ANOVA is a powerful statistical analysis tool that can be used in the Taguchi method to determine statistically significant factors and to explore the relative contribution of each factor and level to the total variation. ANOVA provides information on the sum of squares (SS), degrees of freedom, percentage confidence level, and percentage contribution. SS is a measure of the total variability of the observed data. The SS is defined as follows:

$$\mathrm{SS} = \frac{\sum_{i=0}^{n} X_a^2}{n} - \frac{T^2}{N} \quad (5)$$

where a is the factor, X_a is the sum of the observed data at factor a, $T = \Sigma X_a$ is the sum of all of the data, and N is the total number of data points. The degrees of freedom represent the number of levels for each factor, which may vary independently and is equal to the number of levels of each factor minus one. The percentage confidence level represents the probability of the occurrence and the reliability of the data. The percentage contribution is calculated as follows:

$$\text{Percentage contribution} = \frac{SS_a}{SS_T} \times 100\% \quad (6)$$

where SS_a is the sum of squares of factor a and SS_T is the total sum of squares. With S/N and ANOVA analyzed, the optimal combination of the factors can be predicted, and finally, an experiment can be conducted to verify the optimal factors.

EXPERIMENTAL

Materials

A fixed masterbatch formulation for rubber was used in this study (Table I). Natural rubber (Standard Malaysian Rubber (SMR) L grade) and other chemicals, including zinc oxide, stearic acid, *n*-cyclohexyl-2-benzothiazole sulfenamide (CBS), tetramethylthiuram disulfide (TMTD), paraffin oil, and naphthenic oil, were all purchased from Field Rubber, Ltd. (Auckland). Iron sand was collected from Ngarunui Beach, Raglan. The iron sand was then milled with a planetary monomill (Pulverisette 6) produced by Fristech GmbH and subsequently sieved to obtain a wide range of particle size fractions.

Table I. Masterbatch Formulation

Material	Function	phr
Natural rubber	Raw material and matrix	100
ZnO	Activator/peptiser	5
Stearic acid	Activator/peptiser	1
CBS	Accelerator	2
TMTD	Accelerator	1
Paraffin oil	Plasticizer	2
Naphthenic oil	Plasticizer	3
Sulfur	Crosslinking agent	1.5

Experimental Design

Selection of Factors and Levels. In this study, three factors were considered: the iron sand content, particle size, and applied magnetic field during curing. These factors were varied at five levels, as shown in Table II, on the basis of the existing literature.[3,4,9,14,16]

Selection of OA and Analysis of Data. Given the three factors and five levels considered in this study, an L25 OA was selected for the Taguchi method. The L25 OA is shown in Table III and consisted of 25 experiments corresponding to 25 rows and three design factors assigned to the respective columns along with their levels. The analysis of the S/N was subsequently used to evaluate the experimental results. In this study, because the tan δ and amount of energy dissipated (hysteresis tests) were intended to be maximized, the larger-the-better target for S/N was chosen. ANOVA was used to statistically assess the percentage contribution and relationship between each factor. ANOVA was performed with STATISTICA software.

Preparation of the Iron Sand–Natural Rubber MREs. Formulations were determined according to the OA and were compounded with a conventional laboratory two-roll mill (model XK150) according to ASTM D 3184-80. The *nip gap* (the distance between the front and back rollers), time of compounding, and sequence of addition of the ingredients (rubber, activator, plasticizer, filler, accelerator, and crosslinking agent)

Table II. Experimental Control Factors and Their Respective Levels

Factor	Symbol	Unit	Level 1	Level 2	Level 3	Level 4	Level 5
Iron sand content	*I*	phr	0	30	50	70	100
Particle size	*P*	μm	0-32	32-45	45-56	56-75	75-106
Magnetic field	*M*	mT	0	300	500	700	1000

Table III. Experimental Layout of an L25 OA According to the Taguchi Method

	Factors and their levels		
Sample type	*I*	*P*	*M*
1	1	1	1
2	1	2	2
3	1	3	3
4	1	4	4
5	1	5	5
6	2	1	2
7	2	2	3
8	2	3	4
9	2	4	5
10	2	5	1
11	3	1	3
12	3	2	4
13	3	3	5
14	3	4	1
15	3	5	2
16	4	1	4
17	4	2	5
18	4	3	1
19	4	4	2
20	4	5	3
21	5	1	5
22	5	2	1
23	5	3	2
24	5	4	3
25	5	5	4

were kept constant for all of the compounds. The cure time at 150°C was then determined according to the procedure, as described in ref. 28. Compounded rubber samples weighing 13 g were placed in a 60 × 50 × 3 mm mold. The isotropic MREs were cured in a compression moulder at 150°C under a pressure of approximately 12 MPa. The anisotropic MREs were subjected to an external magnetic field in a specially developed electromagnetic thermally coupled device (as shown in Figure 2) at 80°C for 30 min and were subsequently cured in a compression moulder at 150°C under a pressure of approximately 12 MPa. Finally, postcure treatment was performed by the cooling of the anisotropic MREs at room temperature for 30 min under an external magnetic field of the same strength as that used during precuring. The postcure treatment was necessary to reorientate the magnetic dipoles after they were exposed to the compression stress during compression molding.

Characterization

Dynamic Mechanical Analysis (DMA). DMA was carried out with a PerkinElmer dynamic mechanical analyzer (DMA 8000). Tan δ was measured over a wide range of frequency, strain amplitude, and temperature. The influence of the frequency and strain amplitude on tan δ was assessed with two circular disc specimens with a diameter of 10 mm and a thickness of 3 mm in shear mode at room temperature. Tan δ was measured over the frequency range 0.01–130 Hz at a fixed strain amplitude of 0.5% and over the strain amplitude range 0.1–4.5% at a fixed frequency of 100 Hz. To determine the influence of the temperature on tan δ, the samples were analyzed in dual-cantilever mode at a frequency of 1 Hz with a strain amplitude of 0.5% and over the temperature range from −100 to 50°C. The samples were then heated at rate of 2°C/min. The samples were rectangular with dimensions of 30 ×6 ×3 mm^3.

Hysteresis. *Hysteresis loss* is defined as the amount of energy dissipated during cyclic deformation when the samples are stretched and then allowed to retract at the same rate to their unstretched state. In this study, the hysteresis loss was determined on tensile dumbbells with an Instron 4204 at a crosshead speed of 500 mm/min according to ASTM D 412-80. The stress–strain curve was recorded, and the hysteresis loss was calculated as follows:

Hysteresis loss = Area under the loading curve − Area under the recovery curve (7)

Morphology. The microstructures of the isotropic and anisotropic MREs were observed with scanning electron microscopy (SEM; Hitachi S-4700). The samples were cut into pieces with a surface area of 5 × 3 mm^2 and coated with a thin layer of platinum before observation at an accelerating voltage of 20 kV.

RESULTS AND DISCUSSION

The trends obtained in this study were similar to typical trends observed in previous works for the influence of frequency,[14,29,30] strain amplitude,[16,31] and temperature[32,33] on tan δ and the hysteresis loop obtained after a complete reversed stress cycle.[34,35] To calculate the optimum levels for the different factors with *S*/*N* and ANOVA, reference points for tan δ were selected. To optimize tan δ over a range of frequency from 0.01 to 130 Hz, the maximum value of tan δ was taken as the reference point; it was consistently observed at 130 Hz (the maximum frequency applied). To optimize tan δ over a range of strain amplitude (0.1–4.5%), the reference point was chosen to be within the plateau region at 3% strain amplitude. With respect to the choice of a reference point over a range of temperature, attention was given to the peak of the curve of tan δ versus temperature, which represented the glass-transition temperature (T_g), where the material undergoes drastic changes in the mechanical energy of the molecular vibrational motion. The addition of particulate

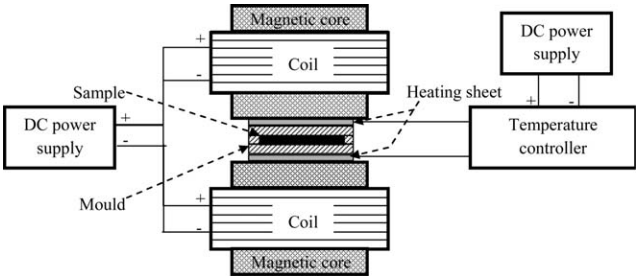

Figure 2. Sketch of the specially developed electromagnetic, heat-coupled device (DC = direct current).

Table IV. Tan δ and Hysteresis Loss Used to the Calculate *S*/*N*s and ANOVA

Sample type	Maximum tan δ over 0.01–130 Hz (130 Hz)[a]	Tan δ at a plateau over 0.1–4.5% strain amplitude (3%)[b]	Tan δ in the transition region of −47 to 0°C (−35°C)[c]	Hysteresis loss (kJ/m^3)
1	0.093	0.098	0.758	31.59
2	0.093	0.098	0.749	31.96
3	0.097	0.099	0.720	31.71
4	0.096	0.098	0.758	31.72
5	0.095	0.098	0.744	32.44
6	0.111	0.103	1.082	39.04
7	0.078	0.129	0.870	52.46
8	0.131	0.112	0.946	69.98
9	0.095	0.137	1.142	55.11
10	0.112	0.113	0.958	49.46
11	0.118	0.099	0.881	45.55
12	0.114	0.107	1.025	94.15
13	0.125	0.110	1.128	110.92
14	0.103	0.090	0.676	96.41
15	**0.171**	**0.155**	0.670	57.10
16	0.133	0.104	0.913	57.58
17	0.112	0.098	**1.216**	119.48
18	0.158	0.118	0.843	95.26
19	0.161	0.134	0.952	70.09
20	0.169	0.130	0.842	75.51
21	0.114	0.095	1.061	100.05
22	0.113	0.098	0.920	99.29
23	0.103	0.090	0.851	**154.61**
24	0.151	0.148	0.851	104.10
25	0.078	0.071	0.946	133.34

The highest values are shown in bold.
[a] Strain amplitude = 0.5%.
[b] Frequency = 100 Hz.
[c] Strain amplitude = 0.5% and frequency = 1 Hz.

fillers into rubber is generally not expected to change the temperature at which tan δ reaches a peak. What is commonly apparent, however, is a broadening of the transition region after T_g to the plateau region.[32,36] In this study, T_g of the natural rubber was −47°C, and the transition region after T_g to the plateau region was observed at −47 to 0°C. To reflect the broadening of the peak, a reference point for tan δ was selected at −35°C. In hysteresis testing, the amount of energy dissipated was calculated from the area of the hysteresis loop. Table IV shows the values of the tan δ and hysteresis loss obtained for these reference points, which were subsequently used to calculate the *S*/*N*s and ANOVA, with each value representing an average from the three samples. The highest values for each test type are shown in bold.

Morphology

Figure 3 shows SEM images of the isotopic and anisotropic MREs. From the SEM micrographs, it can be seen that the isotropic MREs had a homogeneous iron sand particle distribution in the rubber matrix without obvious aggregation [Figure 3(a)]. Figure 3(b–e) shows anisotropic MREs cured at different magnetic fields. Clearly, as expected, the application of a magnetic field at elevated temperature allowed the iron sand particles to organize into chainlike columnar structures. It can also be noted that the chains became longer and more aligned as the magnetic field strength increased. A higher magnification micrograph [Figure 3(f)] highlighted that there were obvious gaps between the iron sand particles and rubber; this suggested weak interaction between the iron sand and rubber.

Effect of the Frequency on Tan δ

The trends for the influence of the frequency on tan δ when the factors were varied over their different levels are shown on the main effect plots in Figure 4. As discussed earlier, the higher the value of *S*/*N* was, the better the signal was; this implied that the highest value in the main effect plots could be used as the conditions to attain the optimized tan δ. The *S*/*N* increased with increasing iron sand content until it reached a maximum value at 70 parts per hundred rubber (phr) and, thereafter, decreased at the highest iron sand content (100

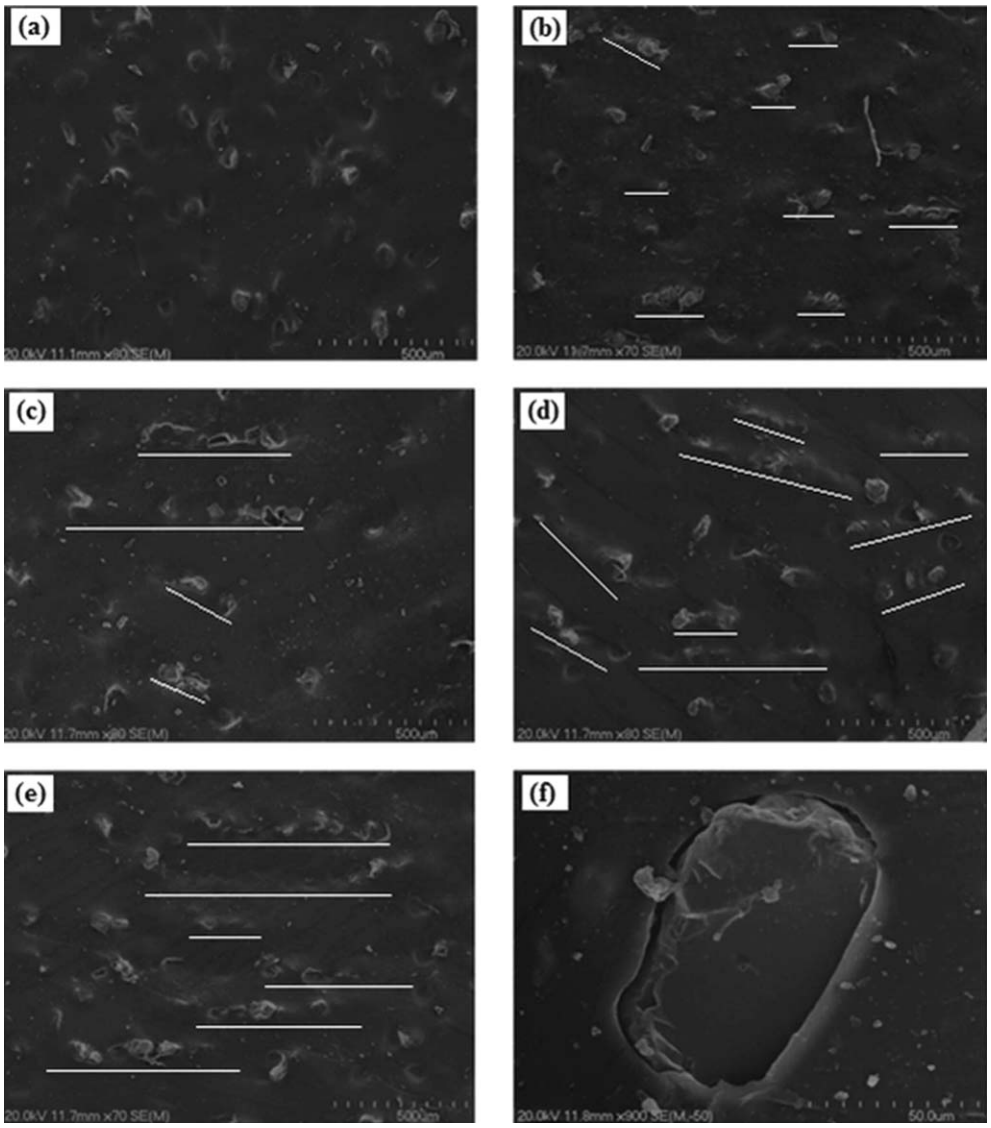

Figure 3. SEM images of the iron sand–natural rubber MREs: (a) isotropic MRE, 0 mT; (b) anisotropic MRE, 300 mT; (c) anisotropic MRE, 500 mT; (d) anisotropic MRE, 700 mT; (e) anisotropic MRE, 1000mT; and (f) interphase of the iron sand–natural rubber matrix.

phr). The increase of *S*/*N* with increasing iron sand content could be explained by the increase in energy absorbed due to interfacial friction caused by the increase in the interfacial area with the increase in iron sand content. The decrease in *S*/*N* at the highest iron sand content could be explained by the poor dispersion of iron sand particles, which was due to the insufficient amounts of rubber matrix to wet the iron sand thoroughly. Similar findings were observed in other studies.[15,37] As shown in Figures 4(b,c), the particle size and magnetic field had minimal influence on *S*/*N*, but the *S*/*N*s at 45–56 μm and 300 mT were the highest. The minimal influence of the magnetic field on the *S*/*N*s appeared to be due to the minimal increase of particle separation as the test was performed at a low fixed strain amplitude (0.5%) in shear mode such that particle chains generally rotated rather than extended. The results suggest that the highest value for tan δ might have been obtained with 70-phr iron sand, a 45–56-μm particle size, and a 300-mT magnetic field during curing.

Table V shows the ANOVA results for the effect of the frequency on tan δ. It can be seen from the level of contribution that the iron sand content had the greatest influence on tan δ, with a 99.9% confidence level. The particle size and magnetic field showed much less influence (lower percentage contribution), with confidence levels of 99 and 97%, respectively.

The final and essential step to complete the Taguchi analysis, namely, the conducting of an experiment to verify the suggested optimum conditions, was carried out with the optimized conditions (70-phr iron sand, 45–56-μm particle size, and 300-mT magnetic field), and the value of tan δ found (0.22) was indeed higher than the highest value achieved previously (0.171 for sample type 15). This supported the optimum conditions suggested by *S*/*N* and ANOVA. The variation of tan δ with frequency is shown in Figure 5(a). Tan δ was higher for the optimized sample over the whole frequency range explored. G' and G'' are also plotted in Figure 5(b,c) to help highlight the mechanisms involved. G' and G'', similar to tan δ, were

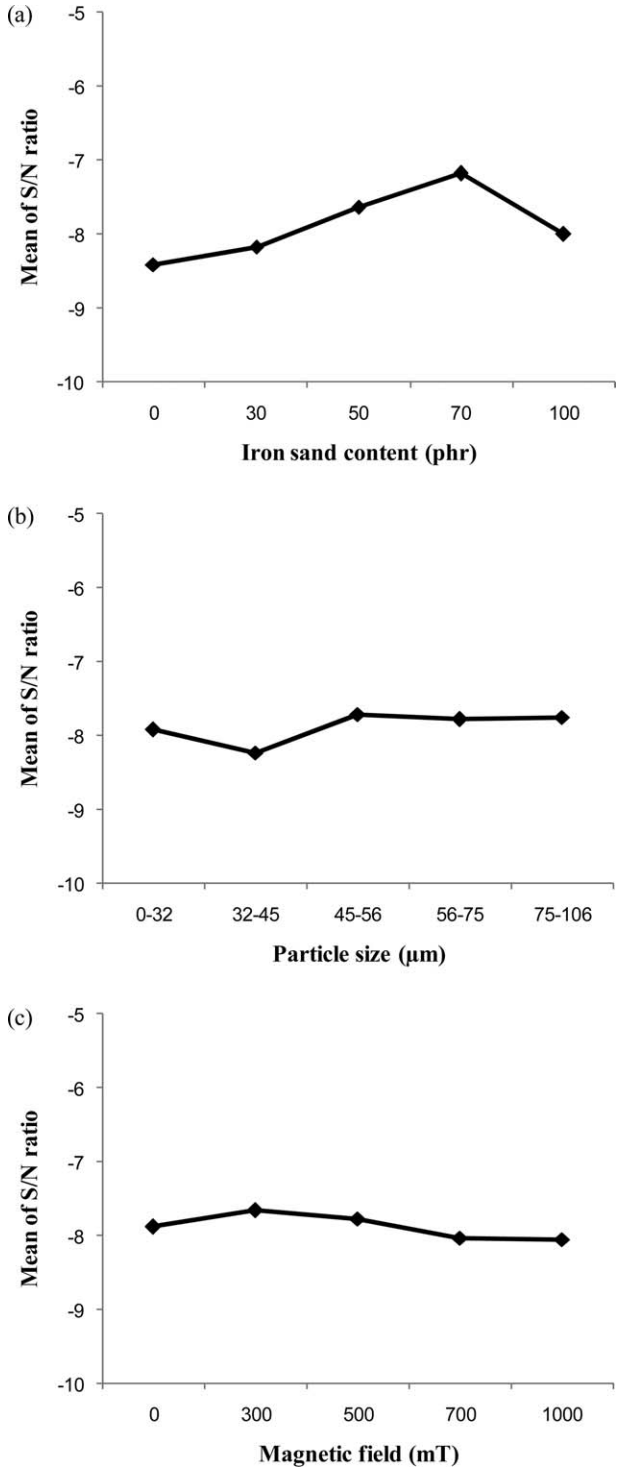

Figure 4. Main effect plots for the *S*/*N* of tan δ at 130 Hz: (a) effect of the iron sand content, (b) effect of the iron sand particle size, and (c) effect of the magnetic field during curing.

frequency-dependent, and the increase in tan δ as the frequency increased was mainly due to the increase in G'' as opposed to G'. The increase in G'' could again be explained by the increased energy loss due to the increase of interfacial friction between the iron sand and rubber with increasing frequency.

Effect of the Strain Amplitude on Tan δ

Figure 6 shows the main effect plots of the *S*/*N*s for the influence of strain amplitude on tan δ. The highest *S*/*N*s were observed at a 30-phr iron sand content, a 56–75-μm particle size, and a 500-mT magnetic field during curing. However, no obvious trend of the *S*/*N*s was observed for any factor as the level changed. This was attributed to the poor bonding between the iron sand and rubber, as supported by their morphology. This was in agreement with results reported by other researchers.[37] The weak interaction between the iron sand and natural rubber was fully disrupted at low strain amplitudes, and therefore, at high strain amplitudes, the damping was dominated by the viscous flow of the rubber matrix. As was the case for the selected reference point (3% strain amplitude) here, it should also be noted that the suggested optimum conditions were different compared with the optimum conditions for the effect of the frequency on tan δ (70 phr, 45–56 μm, and 300 mT). A lower optimum iron sand content (30 phr) supported that at the reference point for the experiment on the effect of the strain amplitude on tan δ, the energy absorbed was more dominated by the viscous flow in the rubber matrix. However, the suggested optimum magnetic field was higher; this indicated that the formation of longer particle chains opposed the higher shearing force with increasing strain amplitudes, such that the particle chain orientation changed and transformed elastic energy into magnetic energy, which then dissipated by magnetic hysteresis.[6,38]

Table VI shows the ANOVA results for the effect of the strain amplitude on tan δ. The variability for each factor was tested at a 99.9% confidence level. None of the factors had a significant influence on tan δ, and hence, the percentage contribution was approximately the same for each factor.

As expected, an experiment with optimized conditions (30-phr iron sand content, 56–75-μm particle size, and 500-mT magnetic field) resulted in a slightly higher value of tan δ (0.160) compared with the highest achieved previously (0.155 for sample type 15). Figure 7 shows the tan δ, G', and G'' of the optimized sample and sample type 15 over a range of strain amplitude (0.1–4.5%). It was found that tan δ and G' were amplitude-dependent at low strain amplitudes and reached a plateau at about 1% strain amplitude. The amplitude dependence at low strain is typically attributed to the Payne effect.[39] This effect is frequently explained by the breakdown of filler aggregates to release trapped rubber to allow more viscous flow, the separation of dipole–dipole interaction between neighbouring particles, and filler–rubber detachment and reformation that increases with increasing strain amplitude. Once the strain amplitude is high enough, all of the interactions are destroyed to such an extent that it cannot be reconstructed, and the Payne effect diminishes. Consequently, the energy loss is largely reliant on the rubber matrix.

Effect of the Temperature on Tan δ

The main effect plots of the *S*/*N*s for the influence of the temperature on tan δ are depicted in Figure 8. The Taguchi method suggested that an optimized value for tan δ could be obtained with a 30-phr iron sand content, a 32–45-μm particle size, and

Table V. ANOVA Results for the Effect of the Frequency on Tan δ

Factor	SS	Degrees of freedom	Confidence level (%)	Contribution (%)
Iron sand content (phr)	0.024	4	99.9	72.73
Particle size (μm)	0.005	4	99	15.15
Magnetic field (mT)	0.004	4	97	12.12

a 1000-mT magnetic field during curing. As shown in Figure 8(a), *S*/*N*s of the filled compounds were higher compared to those of the unfilled compound. The addition of iron sand constrained the rubber chains and, therefore, increased the temper-

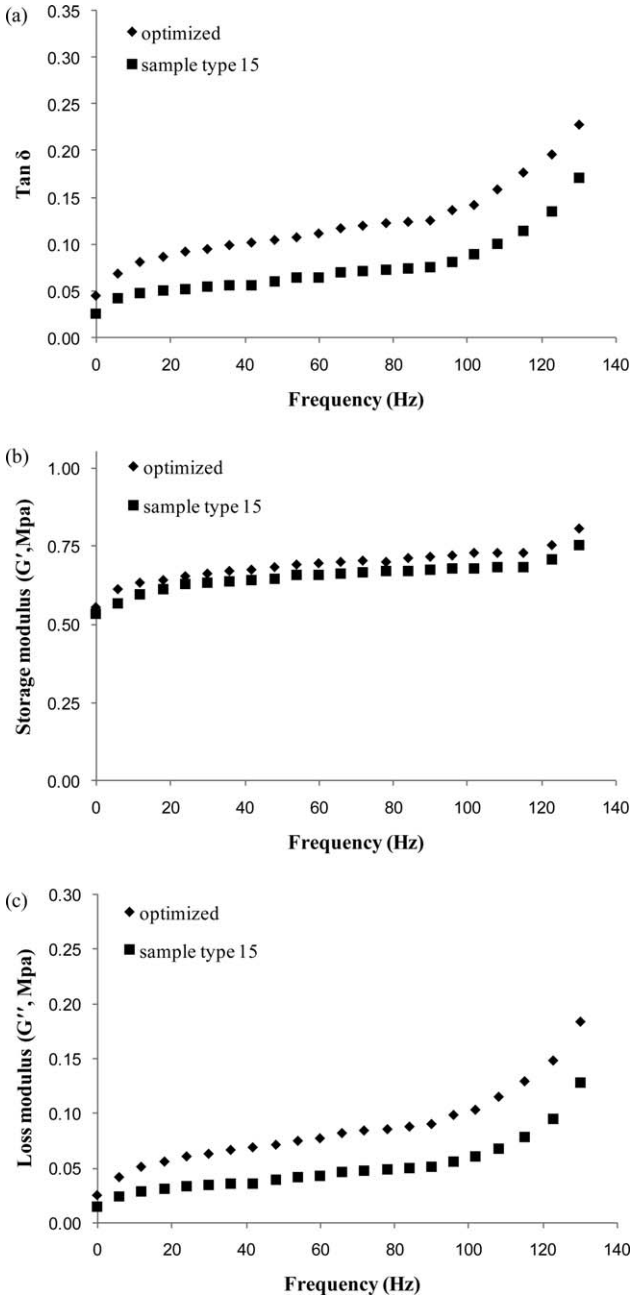

Figure 5. (a) Tan δ, (b) G', and (c) G'' versus the frequency for the optimized sample and sample type 15.

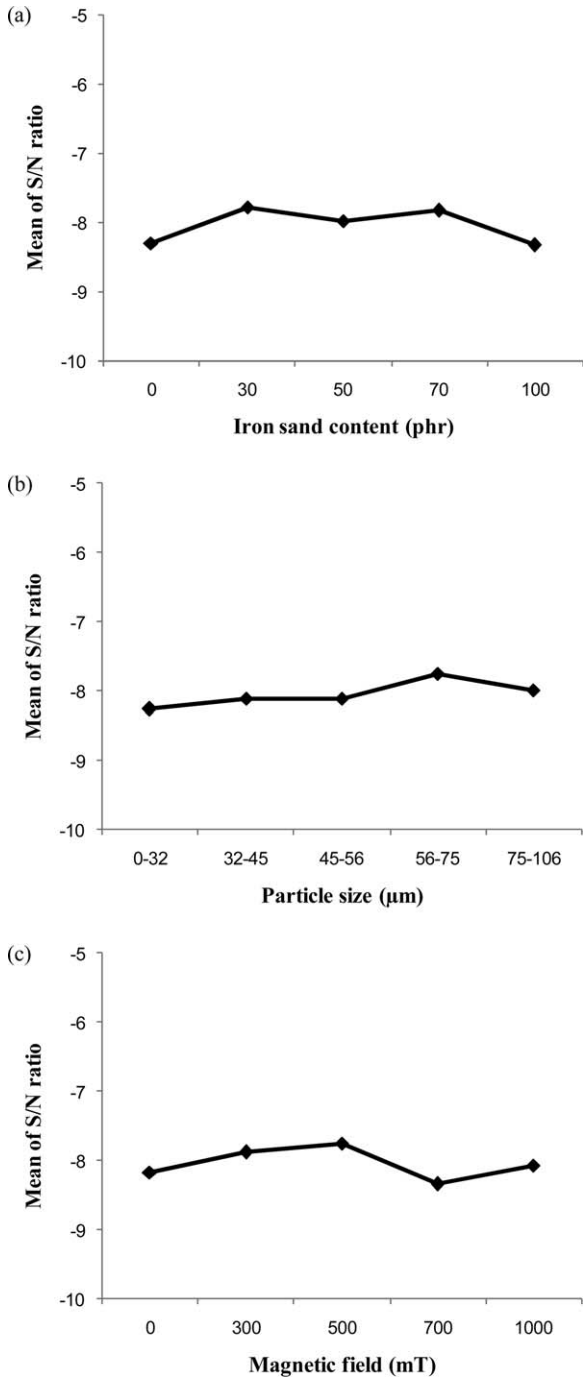

Figure 6. Main effect plots for *S*/*N* of tan δ at 3% strain amplitude: (a) effect of the iron sand content, (b) effect of the iron sand particle size, and (c) effect of the magnetic field during curing.

Table VI. ANOVA Results for the Effects of Tan δ on the Strain Amplitude

Factor	SS	Degrees of freedom	Confidence level (%)	Contribution (%)
Iron sand content (phr)	0.005	4	99.9	35.71
Particle size (μm)	0.004	4	99.9	28.57
Magnetic field (mT)	0.005	4	99.9	35.71

ature required for their mobility; this increased the relaxation at the reference temperature.[36] As shown in Figure 8(b), the *S*/*N*s decreased with increasing particle size; this was likely to be due to the decrease in the surface area of the iron sand adhered to the rubber. As shown in Figure 8(c), the *S*/*N* increased with increasing magnetic field until it reached a maximum at 1000 mT. This indicated that the formation of magnetic particle chains and columnar structures provided additional damping by further restriction of the intermolecular conformational changes during relaxation, as supported by the morphology. As also noted, the suggested optimum conditions were different compared with those observed previously for the effect of the frequency and strain amplitude on tan δ. As this test was performed in dual-cantilever mode at a fixed low frequency (1 Hz) and strain amplitude (0.5%) over the temperature range, the deformation of the material was much lower compared with that tested in shear loading. Therefore, at the selected reference point used for this experiment, the additional damping through interfacial friction and magnetic particle interaction was expected to be much lower. A lower optimum iron sand content (30 phr) supported that the damping was largely reliant on the intermolecular relaxation of the rubber matrix. However, the suggested optimum magnetic field at 1000 mT suggested that the energy absorbed by the formation of longer particle chains was not due to the separation of dipole–dipole interactions; perhaps the longer particle chains provided additional damping through further restriction of the intermolecular conformational changes during relaxation.

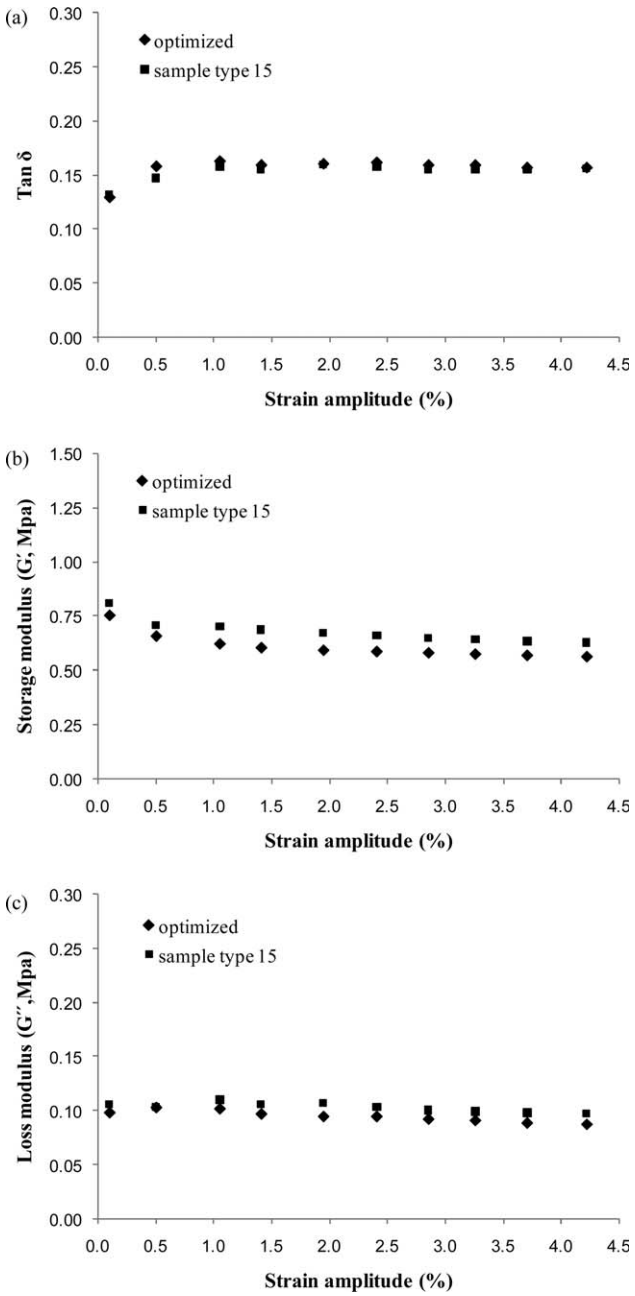

Figure 7. (a) Tan δ, (b) G', and (c) G'' versus strain amplitude for the optimized sample and sample type 15.

Table VII shows the ANOVA results for the effect of the temperature on tan δ. The iron sand content and magnetic field both showed a significant influence on tan δ with a confidence level of 99%. It was also apparent that the particle size had much less influence, with a less than 10% contribution.

Finally, an experiment was carried out to compare the value of tan δ for the optimized sample (30-phr iron sand content, 32–45-μm particle size, and 1000-mT magnetic field) with those achieved previously for the sample with the highest value of tan δ in the transition zone (sample type 17). In addition, the unfilled natural rubber was included for comparison (see Figure 9). The values of tan δ for the optimized sample, sample type 17, and unfilled natural rubber were 1.280, 1.216, and 0.803, respectively. As also shown, the tan δ peak of natural rubber was higher compared to those of the optimized sample and sample type 17. However, the widths of the tan δ peaks for the optimized sample and sample type 17 were wider, and tan δ for the optimized sample at $-35^{\circ}C$ was the highest. This could again be explained as being due to the confinement of molecular chain movement. Because rubber materials are always in practice used in the rubbery phase, the performance and behaviour of the materials in the temperature range after the transition region were more crucial. In the rubbery phase (occurring

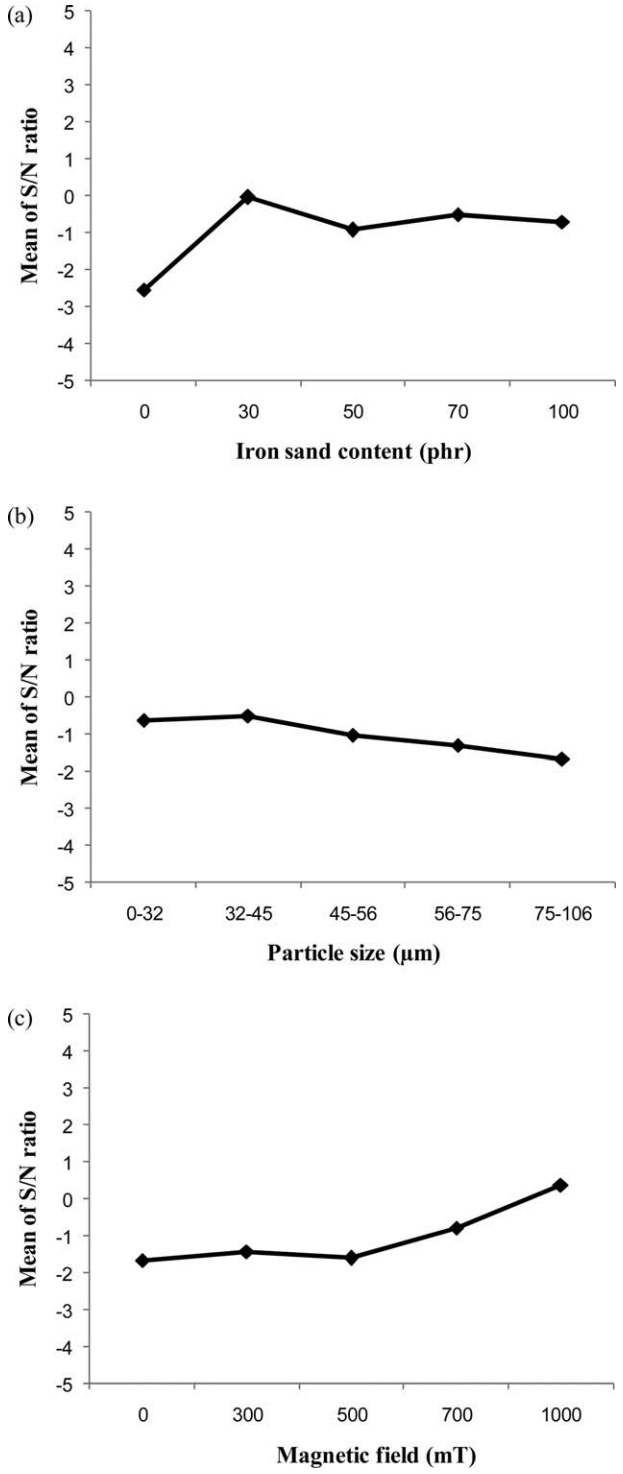

Figure 8. Main effect plots for *S*/*N* of tan δ at −35°C: (a) effect of the iron sand content, (b) effect of the iron sand particle size, and (c) effect of the magnetic field during curing.

in the plateau after the peak), it can also be seen that the optimized sample had the largest value of tan δ, followed by sample type 17 and the unfilled natural rubber. This was because, at higher temperatures, the thermal energy was comparable to the potential energy barriers for the viscous flow; therefore, the interfacial friction, breakdown, and reformation of the filler–filler interaction and filler–rubber detachment were the main causes of damping.

Hysteresis

The main effect plots of the *S*/*N*s for hysteresis loss are presented in Figure 10. The relationship between the iron sand content and *S*/*N* was approximately linear, with the amount of energy dissipated increasing with the iron sand content up to 100 phr. The increase in energy dissipated could be attributed to interfacial friction, the breakdown of filler aggregates to release trapped rubber to allow more viscous flow, and filler–rubber detachment and reformation. As shown in Figure 10(b,c), the particle size and magnetic field had minimal influence on the hysteresis loss, but the *S*/*N*s at 45–56 μm and 1000 mT were the highest. It is also noted that the suggested optimum conditions to obtain highest the hysteresis loss were similar to those for the optimum conditions when assessing the influence of the frequency on tan δ. The Taguchi method suggested that the highest hysteresis loss and tan δ could be obtained with high iron sand contents (100 and 70 phr, respectively), with particle size not being greatly influential (although a particle size of 45–56 μm gave the highest values for both hysteresis and tan δ). However, the suggested magnetic field during curing gave a contrary conclusion (1000 and 300 mT, respectively, for hysteresis and tan δ); this could have been due to the different mode of loading during testing (tensile vs shear). This suggested that the energy absorption due to interactions between magnetic particle alignment was less efficient in the tensile mode compared with those in the shear mode with DMA; this was not surprising, given that in tension, it is largely only the spacing increasing between chains, whereas in shear, the spacing within chain between the particles increases (see Figure 11).

Table VIII shows the ANOVA results for the hysteresis loss. The confidence levels for all factors were 98% and higher. From the levels of contribution, it can be seen that the most influential factor by far was the iron sand content; this was followed by the particle size (80.71 and 14.38%, respectively). The influence of the magnetic field was much less at 4.91%.

Figure 12 shows the stress–strain loops of the sample at the suggested optimum conditions (100-phr iron sand, 45–56-μm particle size, and 1000 mT), and those for the highest hysteresis loss achieved previously (sample type 23) after a complete reversed stress cycle. As shown, the area of the hysteresis loop for the optimized sample was larger than that in sample type 23. The amounts of energy lost for the optimized sample and sample type 23 were 160.96 and 154.61 kJ/m^3, respectively. This supported the optimum conditions suggested by the *S*/*N* and ANOVA. As the strain increased, the curvilinear part at the beginning of stretching was attributed to interfacial friction, the breakdown of filler aggregates, and filler–rubber detachment and reformation, and as the strain increased, the amount of energy dissipated increased. This was believed to be mainly dominated by the viscous flow in the rubber phase, as reported in the literature.[35] As the strain increased, the cross-sectional area of the tested samples decreased, and the rubber molecular chains came closer to each other. Under further strain, the

Table VII. ANOVA Results for the Effects of the Temperature on Tan δ

Factor	SS	Degrees of freedom	Confidence level (%)	Contribution (%)
Iron sand content (phr)	0.185	4	99	48.15
Particle size (μm)	0.035	4	70	9.22
Magnetic field (mT)	0.164	4	99	42.62

chains constrained each other; therefore, they slid with respect to each other, and this resulted in a further increase in dissipated energy. When the load was removed, the rubber molecular chains did not completely regain their original configuration, and the energy dissipated was expected to be converted into heat.[35,40]

CONCLUSIONS

In this study, iron sand and natural rubber MREs were manufactured, and experiments were designed with the Taguchi method to assess the effects of the iron sand content, iron sand particle size, and applied magnetic field during curing on the tan δ (over a wide range of frequency, strain amplitude, and temperature) and energy dissipated during cyclic loading. SEM micrographs revealed that the isotropic MREs had homogeneous iron sand particle distribution, and curing the materials under an applied magnetic field at an elevated temperature resulted in the iron sand particles organizing into chainlike columnar structures. For the effect of the frequency on tan δ, the Taguchi method suggested that the optimum conditions were obtained with 70-phr iron sand, a 45–56-μm particle size, and a 300-mT magnetic field; this was supported by the experiment. It was found that the iron sand had the greatest influence on tan δ followed by the particle size and magnetic field. The suggested optimum conditions to obtain the highest hysteresis loss were similar to the optimum conditions suggested when assessing the influence of the frequency on tan δ. The Taguchi method suggested that the highest hysteresis loss could be obtained with a 100-phr iron sand content (slightly different than the 70-phr iron sand content suggested for frequency), with the particle size not being greatly influential (although a particle size of 45–56 μm gave the highest values for both

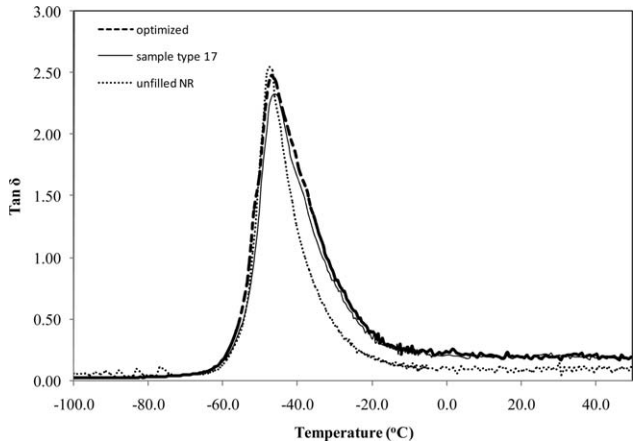

Figure 9. Tan δ versus the temperature for natural rubber (NR), the optimized sample, and sample 17.

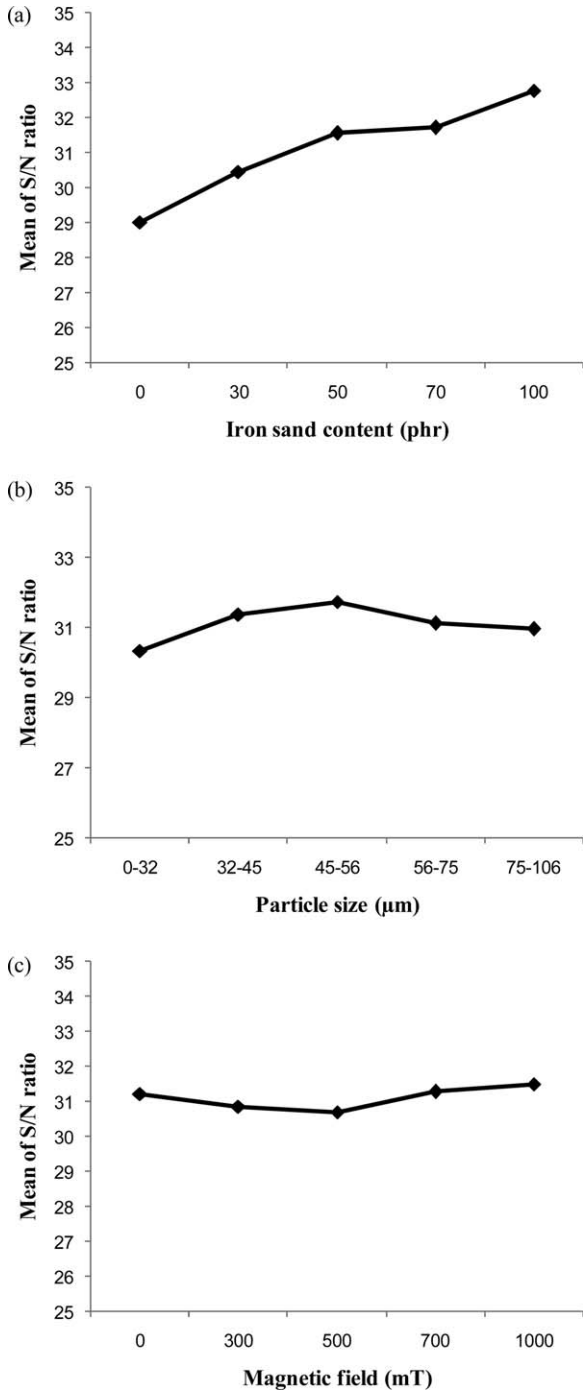

Figure 10. Main effect plots for *S/N* of hysteresis loss: (a) effect of the iron sand content, (b) effect of the iron sand particle size, and (c) effect of the magnetic field during curing.

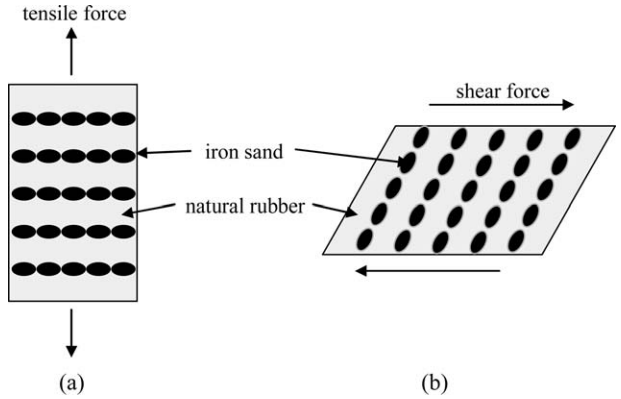

Figure 11. Comparison of the influence of the loading types on the particle separation, (a) tensile and (b) shear modes.

Table VIII. ANOVA Results for the Hysteresis Loss

Factor	SS	Degrees of freedom	Confidence level (%)	Contribution (%)
Iron sand content (phr)	43,038.6	4	99.9	80.71
Particle size (μm)	7669.1	4	99.9	14.38
Magnetic field (mT)	2616.7	4	98	4.91

hysteresis and tan δ). However, the optimum magnetic field during curing was different for the maximization of tan δ and hysteresis loss (300 and 1000 mT, respectively); this could have been due to the different modes of loading during testing (tensile vs shear). For the effect of the strain amplitude on tan δ, none of the factors showed a significant influence on tan δ over a range of strain amplitude; this was attributed to the poor bonding between the iron sand and rubber such that the weak interactions between the iron sand and natural rubber were fully disrupted at low strain amplitudes. Therefore, at high strain amplitudes, the damping was dominated by the viscous flow of the rubber matrix. For

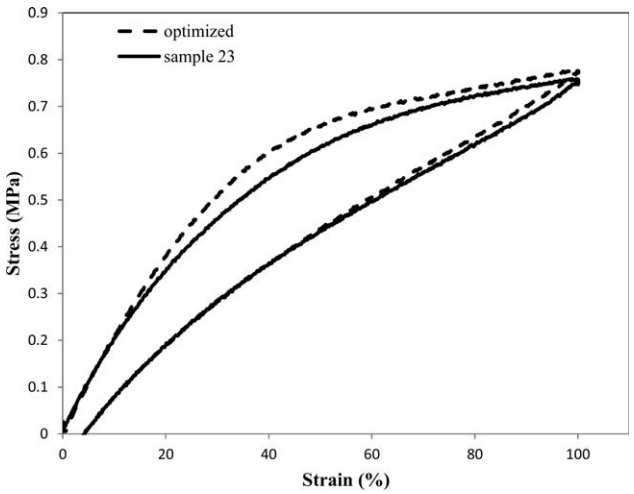

Figure 12. Hysteresis loops of the optimized sample and sample 23.

the effect of the temperature on tan δ, the optimum conditions suggested by the Taguchi method were 30-phr iron sand, a 32–45-μm particle size, and a 1000-mT magnetic field. It was found that addition of iron sand and the formation of magnetic particle chains constrained the conformational changes of the rubber molecular chains from taking part in the relaxation process and, therefore, increased the temperature at which the molecular chains started to mobilize, such that the width of the peak of tan δ increased. The different optimum conditions for different tests carried out herein would appear to have been due to the relatively different amounts of energy absorbed by different degrees that different mechanisms were involved with different loading conditions and at different frequencies and strain amplitudes.

ACKNOWLEDGMENTS

The authors are grateful for the support from the Polymer and Composite Research Group of the University of Waikato.

REFERENCES

1. Lakes, R. S. *J. Compos. Mater.* **2001**, *36*, 287.
2. Jerzy, K.; Daniel, L.; Rafal, M.; Piotr, Z. Smart Magnetic Composites (SMC); Metal, Ceramic and Polymeric Composites for Various Uses; InTech: Rijeka, Croatia, **2011**.
3. Chokkalingam, R.; Rajasabai Senthur, P.; Mahendran, M. *J. Compos. Mater.* **2010**, *45*, 1545.
4. Jerzy, K.; Michal, K.; Daniel, L. *Smart Mater. Struct.* **2011**, *20*, 12.
5. Chen, L.; Gong, X. L.; Li, W. H. *Polym. Test.* **2008**, *27*, 340.
6. Fuchs, A.; Zhang, Q.; Elkins, J.; Gordaninejad, F.; Evrensel, C. *J. Appl. Polym. Sci.* **2007**, *105*, 2497.
7. Ginder, J. *Proc. SPIE* **1999**, *3675*, 131.
8. Lerner, A. A.; Cunefare, K. A. *J. Intell. Mater. Syst. Struct.* **2008**, *19*, 551.
9. Sun, T. L.; Gong, X. L.; Jiang, W. Q.; Li, J. F.; Xu, Z. B.; Li, W. H. *Polym. Test.* **2008**, *27*, 520.
10. Wang, Y.; Hu, Y.; Deng, H.; Gong, X.; Zhang, P.; Jiang, W.; Chen, Z. *Polym. Eng. Sci.* **2006**, *46*, 264.
11. Lokander, M.; Stenberg, B. *Polym. Test.* **2003**, *22*, 677.
12. Lokander, M.; Stenberg, B. *Polym. Test.* **2003**, *22*, 245.
13. Carlson, J. D.; Jolly, M. R. *Mechatronics* **2000**, *10*, 555.
14. Blom, P.; Kari, L. *Polym. Test.* **2005**, *24*, 656.
15. Chen, L.; Gong, X.-L.; Jiang, W.-Q.; Yao, J.-J.; Deng, H.-X.; Li, W.-H. *J. Mater. Sci.* **2007**, *42*, 5483.
16. Alberdi-Muniain, A.; Gil-Negrete, N.; Kari, L. *Plast. Rubber Compos.* **2012**, *41*, 310.
17. Sun, Y.; Zhou, X.; Liu, Y.; Zhao, G.; Jiang, Y. *Mater. Res. Bull.* **2009**, *45*, 878.
18. Makled, M. H.; Matsui, T.; Tsuda, H.; Mabuchi, H.; El-Mansy, M. K.; Morii, K. *J. Mater. Process. Technol.* **2005**, *160*, 229.
19. Dobrzanski, L. A.; Tomiczek, A.; Tomiczek, B.; Slawska, A.; Iesenchuk, O. *J. Achievements Mater. Manufacturing Eng.* **2009**, *37*, 16.

20. Bryan, K. R.; Robinson, A.; Briggs, R. M. *Marine Geol.* **2007**, *236*, 45.
21. Briggs, R. M.; Laurent, J. C.; Hume, T. M.; Swales, A. In AusIMM New Zealand Branch Annual Conference, New Zealand; AusIMM: Carlton South Vic., Australia, **2009**, p 41.
22. Montgomery, D. C. Design and Analysis of Experiments; Wiley: Hoboken, NJ, **1997**.
23. Arvidsson, M.; Gremyr, I. In Robust Design Methodology for Reliability; Wiley: Hoboken, NJ, **2009**.
24. Mitra, A. Wiley Interdiscip. *Rev. Comput. Stat.* **2011**, *3*, 472.
25. Derakhshandeh, B.; Shojaei, A.; Faghihi, M. *J. Appl. Polym. Sci.* **2008**, *108*, 3808.
26. Bhattacharya, M.; Bhowmick, A. K. *Wear* **2010**, *269*, 152.
27. Roy, R. K. Design of Experiments Using the Taguchi Approach: 16 Steps to Product and Process Improvement; Wiley: New York, **2001**.
28. Khimi, S. R.; Pickering, K. L. *J. Appl. Polym. Sci.* **2013**, *131*, 40008.
29. Boczkowska, A.; Awietjan, S. F.; Pietrzko, S. A.; KurzydÅowski, K. *J. Compos. B* **2012**, *43*, 636.
30. Kari, L.; Blom, P. *Plast. Rubber Compos.* **2005**, *34*, 365.
31. Shirazi, M.; Talma, A. G.; Noordermeer, J. W. M. *J. Appl. Polym. Sci.* **2013**, *128*, 2255.
32. Han, J.; Shi, N.; Xie, L.; Ma, Y.; Wu, C. *J. Macromol. Sci. B Phys.* **2010**, *49*, 429.
33. Liu, Q. X.; Ding, X. B.; Zhang, H. P.; Yan, X. *J. Appl. Polym. Sci.* **2009**, *114*, 2655.
34. Kar, K. K.; Bhowmick, A. K. *Polym. Eng. Sci.* **1998**, *38*, 1927.
35. Kucherskii, A. M. *Polym. Test.* **2005**, *24*, 733.
36. Arrighi, V.; McEwen, I. J.; Qian, H.; Serrano Prieto, M. B. *Polymer* **2003**, *44*, 6259.
37. Yanceng, F.; Xinglong, G.; Shouhu, X.; Wei, Z.; Jian, Z.; Wanquan, J. *Smart Mater. Struct.* **2011**, *20*, 1.
38. Hathaway, K.; Clark, A.; Teter, J. *Metall. Mater. Trans. A* **1995**, *26*, 2797.
39. Rendek, M.; Lion, A. *Int. J. Solids Struct.* **2010**, *47*, 2918.
40. Ahankari, S. S.; Kar, K. K. *Polym. Eng. Sci.* **2010**, *50*, 871.

Composites: Part A 68 (2015) 377–386

Contents lists available at ScienceDirect

Composites: Part A

journal homepage: www.elsevier.com/locate/compositesa

The effect of silane coupling agent on iron sand for use in magnetorheological elastomers Part 1: Surface chemical modification and characterization

K.L. Pickering *, S. Raa Khimi, S. Ilanko

School of Engineering, The University of Waikato, Hamilton 3216, New Zealand

ARTICLE INFO

Article history:
Received 4 May 2014
Received in revised form 18 September 2014
Accepted 5 October 2014
Available online 12 October 2014

Keywords:
A. Particle-reinforcement
B. Interface/interphase
D. Surface analysis
E. Surface treatments

ABSTRACT

Bis-(3-triethoxysilylpropyl) tetrasulphane (TESPT) was employed for surface modification of iron sand for use in magnetorheological elastomers (MREs). The amount of TESPT was varied at five levels (2, 4, 6, 8 and 10 wt%) relative to iron sand content to assess the optimum amount of coupling agent for interfacial bonding and damping performance. Evidence that coupling had occurred between iron sand and TESPT was identified by Raman Spectroscopy and the grafting percentage was determined by thermogravimetric analysis. Subsequently, isotropic MREs containing unmodified and modified iron sand particles and natural rubber were prepared. Crosslink density assessment by swelling testing provided evidence that the tetrasulphane group of TESPT formed crosslinks with the rubber chains. The results exhibited the advantages of TESPT as a coupling agent between iron sand particles and rubber and also revealed that 6% TESPT content produced the highest crosslink density. The effects of the amount of TESPT on dynamic mechanical properties the morphological characteristics of the MREs were also investigated.

1. Introduction

Magnetorheological elastomers (MREs) are a new group of damping materials which consist of a non-magnetic matrix (normally an elastomer) containing a suspension of magnetically permeable particles. The most commonly used magnetic particles for MREs are carbonyl iron particles and suitable matrix materials include natural rubber, silicone rubber, polybutadiene, polyisobutylene, polyisoprene, and polyurethene rubber [1–7]. The main advantage of MREs is that the damping and stiffness can be varied by application of an applied magnetic field during fabrication or in service. Damping occurs by the viscous flow of the rubber matrix and inclusion of magnetic particles in rubber enables additional damping through magnetic particle interaction and interfacial damping. MREs can be classified into two kinds: isotropic MREs and anisotropic MREs. Isotropic MREs can be characterized by having a uniform magnetic particle distribution in the matrix. Anisotropic MREs have a special chain-like structure of magnetic particles in a matrix resulting from curing the matrix under an applied magnetic field. Over the past few years, MREs have attracted increasing attention and have been considered for applications such as adaptive tuned vibration absorbers [8], automotive engine mounts [4] and semi active seismic dampers [9].

New Zealand iron sand possesses physical and magnetic properties that make it suitable for use in MREs. Compared to commonly use magnetic particles, such as pure iron and carbonyl iron, iron sand has a number of advantages, including high permeability and saturation magnetisation, low cost and it is readily available in New Zealand. It is derived from erosion of andesitic and rhyolitic volcanic rocks which are the main types of iron ore deposits in New Zealand. Iron sand is a dark, high-density sand that occurs along the west coast of the North Island from Wanganui to Kaipara Harbour near Auckland, over a distance of 480 km. It contains titanomagnetite, a mineral containing iron and titanium, which is highly magnetic [19,20].

Similarly for all MREs, the damping of MREs depends not only on the types of rubber matrix and magnetic particles, but also on the level of adhesion between the particles and the rubber matrix such that the strength of interaction between the particles and matrix has to be sufficiently strong to obtain efficient interfacial damping. For MREs this sets a challenge. Here, as for other MRE components, the incompatibility of the inorganic magnetic fillers and the matrix can actually lead to poor wettability and adhesion between the filler and matrix as well as non-uniformity of filler dispersion leading to low energy absorption [10–12]. Therefore,

* Corresponding author. Tel.: +64 078384672.
E-mail address: klp@waikato.ac.nz (K.L. Pickering).

http://dx.doi.org/10.1016/j.compositesa.2014.10.005
1359-835X/

it is sensible to modify the surface of the iron sand in order to improve ease of adhesion with and dispersion within the rubber matrix in order to realise the full potential of MREs.

Surface modification of inorganic particles can be achieved using a number of approaches [13]; most commonly, the filler surface is chemically modified to become more compatible with the matrix using methods such as polymer coating [14], surfactant absorption [15] and bifunctional coupling agent treatments [16,17]. Among various modification approaches, the bifunctional coupling agent treatment using silane based coupling agents is the most successful and cost effective treatment for improving the adhesion between inorganic particle and rubber matrix. These chemicals are silicon-based chemicals that contain hydrolysable groups (such as methoxy, ethoxy or acetoxy) at one end that will interact with inorganic materials and organofunctional groups (such as amino, vinyl or sulphide) at the other end that can react with the rubber matrix. Therefore, inorganic and organic materials can be coupled together with the silane coupling agent acting as a bridge between them. Although this type of surface modification is well established for enabling different types of fillers such as silica [18,19], aluminium powder [20], halloysite nanotubes [21], wood flour [22] and natural fibre [23,24] to be used as reinforcement fillers in rubber compounds, its effect on inorganic magnetic particles for used in MREs has not been extensively studied. Some research has been reported on modification of carbonyl iron particles using silane coupling agents used as a filler in silicon rubber [25,26] and polyurathene rubber [16] based MREs; the results showed that the mechanical and damping performance of MREs increased due to increased dispersion and interaction between particles and the matrix. Although it is accepted that the effectiveness of silane to interact with the substrate is dependent on a number of factors including hydrolysis time, presence of solvent, temperature and pH [27], none have assessed the optimum silane content coupled to the particles to allow for improved subsequent bonding. Furthermore, as far as the authors are aware, there is no work carried out on surface modification of inorganic magnetic particles for use in natural rubber based MREs.

In this study, isotropic MREs based on iron sand and natural rubber were prepared. Bis-(3-triethoxysilylpropyl) tetrasulphane (known as TESPT or Si 69) which is the most popular and effective silane coupling agent for hydrocarbon rubber (see Fig. 1) was used for surface modification of iron sand particles [13]. TESPT contains ethoxy hydrolysable groups at both ends that enable the silicon groups to bond with iron sand particles and the tetrasulphane group of its centre which is capable of bonding with the rubber matrix. Iron sand contains stable oxides that potentially have reactive sites including Fe–O bonds and OH groups on their surface [28,29]. Therefore, there is potential for improvement of iron sand and natural rubber interaction by using TESPT as a coupling agent. The effects of TESPT content on dynamic mechanical properties were investigated using two methods. The loss tangent, commonly called tan δ, is considered as the fundamental parameter to assess damping. Tan δ gives a comparison of the energy lost to that stored; it is obtained by dividing the loss modulus (G″ or E″) by the storage modulus (G′ or E′) [30]. The other estimate of damping used was the amount of energy dissipated during cyclic deformation, which can be calculated from the area of the hysteresis loop (hysteresis loss).

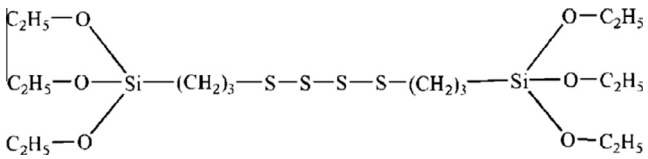

Fig. 1. Molecular structure of TESPT.

2. Experimental

2.1. Materials

Natural rubber (SMR L grade) and other chemicals including zinc oxide, stearic acid, n-cyclohexyl-2-benzothiazole sulfenamide (CBS), tetramethylthiuram disulphide (TMTD), paraffin oil, and naphthenic oil were all purchased from Field Rubber Limited, Auckland. Bis-(3-triethoxysilylpropyl) tetrasulphane (TESPT) was purchased from Leap LabChem Co., Limited, China. Iron sand was collected from Ngarunui Beach, Raglan. The iron sand was milled using a planetary mono mill (Pulverisette 6) produced by Fristech GmbH and subsequently sieved to obtain a 45–56 μm particle size.

2.2. Surface modification of iron sand particles

The surface modification of iron sand particles was carried out by an aqueous alcohol solution method. The particles were subjected to surface treatment with TESPT at 2%, 4%, 6%, 8%, 10% by weight (wt%) of the particles. An aqueous alcohol solution of 95% ethanol was used and the pH of the solution was adjusted with acetic acid to 4.0–4.5. The TESPT of predetermined quantity was dispersed in the ethanol solution at a ratio of 1:100 and the mixed solution was stirred for 5 min to assure the hydrolization of the silane coupling agent. The iron sand particles were then added and stirred for an additional 30 min at room temperature to ensure a uniform distribution of the coupling agent on the surface of iron sand particles. The mixture was filtered and washed three times with ethanol to remove unreacted coupling agent. The treated iron sand particles were then dried at 80 °C in an oven until a constant weight was achieved.

2.3. Preparation of iron sand-natural rubber isotropic MREs

The compound formulation used in this study is given in Table 1. Formulations were compounded using a conventional laboratory two roll mill (model XK150) according to ASTM designation D3184-80. The front roller speed was 23.86 rpm and the rear roller speed was 32.81 rpm, diameter of rolls was 150 mm, friction ratio of two rolls was 1:1.4 and the roller temperature was set at 80 °C. The nip gap (distance between front and back roller) was maintained at 2 mm during compounding. The compounding began with softening the rubber on its own in the two roll mill (mastication). Mastication reduces the viscosity and increase the plasticity of natural rubber which is brought about by heat generated in two roll mill through conduction from the heated roller and shearing of rubber during milling. After mastication, during which the rubber had become invested on the hot roll (2–3 min), additives (other than accelerators and sulphur) were then added followed by iron sand; addition of accelerators and sulphur were delayed to the last part of the process to prevent premature vulcanization during compounding. The mixing time was approximately 40 min. The cure time at 150 °C was then determined according to the procedure as described in reference [31] and the results are shown in Table 1. Compounded rubber samples weighing 13 g were placed in a mould 60 × 50 × 3 mm and were cured in a compression moulder at 150 °C under a pressure of approximately 12 MPa.

2.4. Raman Spectroscopy

Raman spectra were acquired with a Ramanstation 400R (PerkinElmer) spectrometer equipped with an air cooled charged

Table 1
Formulation of rubber compound.

Materials	Function	Loading (phr*)					
Natural rubber	Raw material/matrix	100	100	100	100	100	100
ZnO	Activator/peptiser	5	5	5	5	5	5
Stearic acid	Activator/peptiser	1	1	1	1	1	1
Paraffin oil	Plasticiser	2	2	2	2	2	2
Naphthenic oil	Plasticiser	3	3	3	3	3	3
Iron sand	Filler	70	70	70	70	70	70
CBS	Accelerator	2	2	2	2	2	2
TMTD	Accelerator	1	1	1	1	1	1
Sulphur	Crosslinking agent	1.5	1.5	1.5	1.5	1.5	1.5
Silane coupling agent level (wt%)							
TESPT	Coupling agent	0	2	4	6	8	10
Curing characteristics (minutes)							
Cure time	(t_{90})	4.57	4.53	4.33	4.23	4.40	4.46

* phr = per hundred rubber.

coupled device (CCD) detector and data points were recorded at 1 cm^{-1} intervals. The excitation source was a 785 nm near infrared laser focused on surface of samples with a spot approximately 200 μm in diameter. Calibration was validated against a polystyrene standard disk (PerkinElmer) prior to measurement. Samples were analysed while placed on aluminium foil. The Raman instrument was visually focused onto the surface of each location to be analysed on the modified iron sand samples. Laser power was set to approximately 40 mW (40% of maximum, estimated to be 6×105 W/m^2 on the 200 μm diameter spot) to acquire spectra from all samples (after initial trials) for consistency across the range of materials analysed. Spectra were collected over the range 3200–200 cm^{-1} and each spectrum was acquired as the sum of five repeats of 60s exposures on the sample. Five separate spectra were acquired at different locations on each sample analysed.

2.5. Thermogravimetric analysis

The grafting percentage of silane coupling agent with iron sand particles was determined by thermogravimetric analysis (TGA) using an TA Instrument SDT 2910 thermal analyser operated in dynamic mode, heating from ambient temperature to 300 °C at 5 °C/min in air purged at 150 ml/min with an empty pan used as a reference. Thermal gravimetric curves were obtained. The grafting percentage was calculated as the fraction of the mass of grafted silane coupling agent divided by the mass of iron sand particles at 280 °C [32,33] as follows:

$$\textit{Silane grafting}\ (\%) = \frac{\textit{Grafted silane coupling agent}/g}{\textit{iron sand particles}/g} \quad (1)$$

The amount of grafted silane coupling agent was calculated from the weight loss of treated iron sand at 280 °C minus weight loss of iron sand particles at 280 °C.

2.6. Crosslink density

Determination of crosslink density in MREs was obtained using a swelling test. MREs samples with dimensions of 30 mm × 5 mm × 3 mm were weighed, and then immersed in toluene for 72 h at room temperature in a dark environment. The toluene was replaced at 24 h intervals over this time to minimise interference from toluene soluble fractions remaining in the samples. After 72 h, samples were drained and dried and the swollen mass was recorded. Samples were then dried at 80 °C in an oven until a constant weight was achieved. For each experimental point, 3 samples were produced and the average values were calculated. The crosslink density was calculated by applying the Flory–Rehner equations as follows [34]

$$V_r = \frac{V_p}{V_p + V_s} = \frac{\frac{m_{dry}}{\rho_r}}{\left(\frac{m_{dry}}{\rho_r} + \frac{m_{wet} - m_{dry}}{\rho_s}\right)} \quad (2)$$

$$[X] = \frac{-\left[\ln(1 - V_r) + V_r + \chi V_r^2\right]}{V_o\left(V_r^{\frac{1}{3}} - \frac{V_r}{2}\right)} \quad (3)$$

where V_r is the volume fraction of MREs, m_{wet} is the swollen equilibrium mass, m_{dry} is the dry MREs mass, ρ_r is the density of natural rubber (910 kg/m^3), ρ_s is the density of toluene (866 kg/m^3), $[X]$ represents the crosslink concentration in mol/cm^3, χ is the interaction parameter between the rubber and toluene (0.393) and V_o is the molar volume of toluene (106.4 cm^3/mol).

2.7. Morphology

The microstructures of isotropic MREs were observed using a Hitachi S-4700 scanning electron microscope (SEM). The samples were frozen and snapped into pieces to expose their interior and coated with a thin layer of platinum prior to observation at an accelerating voltage of 20 kV.

2.8. Dynamic mechanical analysis

Dynamic mechanical analysis was carried out using a Perkin Elmer dynamic mechanical analyser (DMA 8000). Tan δ was measured over a wide range of frequency, strain amplitude and temperature. The influence of frequency and strain amplitude on tan δ was assessed using two circular disc specimens with a diameter of 10 mm and a thickness of 3 mm in shear mode at room temperature. Tan δ was measured over the frequency range of 0.01–130 Hz at a fixed strain amplitude of 0.5% and over a strain amplitude range of 0.1–4.5% at a fixed frequency of 100 Hz. For the influence of temperature on tan δ, the samples were analysed in dual cantilever mode at a frequency of 1 Hz, with a strain amplitude of 0.5% over a temperature range of −100 to 50 °C. The samples were rectangular with dimensions 30 mm × 6 mm × 3 mm.

2.9. Hysteresis

Hysteresis loss is defined as the amount of energy dissipated during cyclic deformation when the samples are stretched and then allowed to retract at the same rate to the unstretched state. In this study, the hysteresis loss was determined for tensile

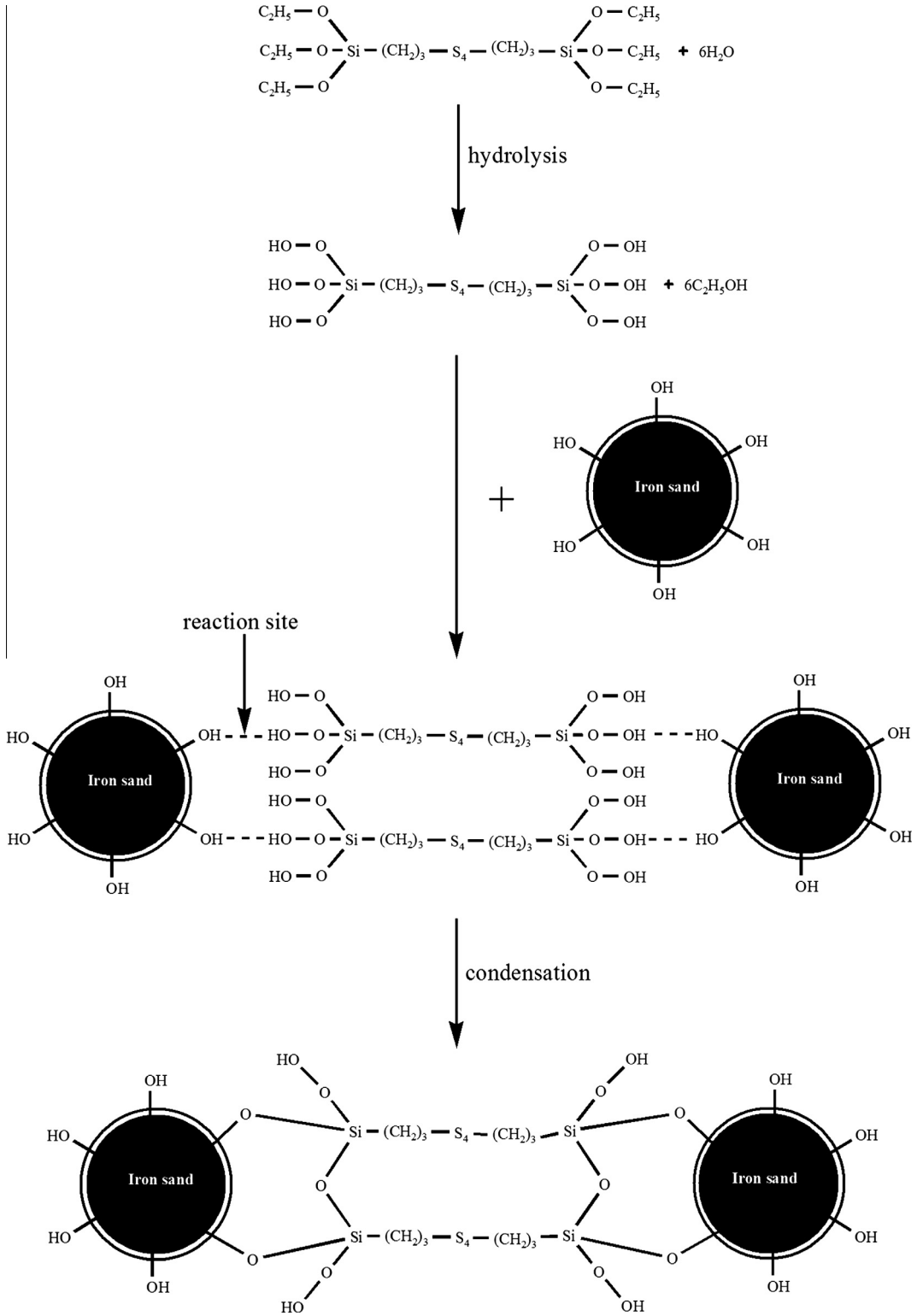

Fig. 2. Illustration of the reactions of TESPT with iron sand particle surface.

dumbbells using an Instron 4204 at a crosshead speed of 500 mm/min according to ASTM D412-80. The stress–strain curve was recorded and hysteresis loss was calculated as

$$\text{Hysteresis loss} = \text{Area under the loading curve} - \text{Area under the recovery curve} \quad (4)$$

3. Results and discussion

3.1. Characterization of surface modified iron sand particles

Fig. 2 shows a schematic of the potential reaction mechanisms of TESPT with iron sand particles. In the presence of water in an

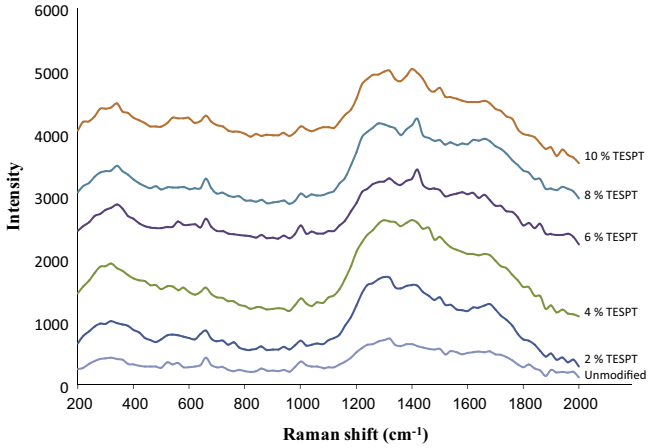

Fig. 3. Raman spectra of iron sand particles at different TESPT contents. (For interpretation of the references to colour in this figure legend, the reader is referred to the web version of this article.)

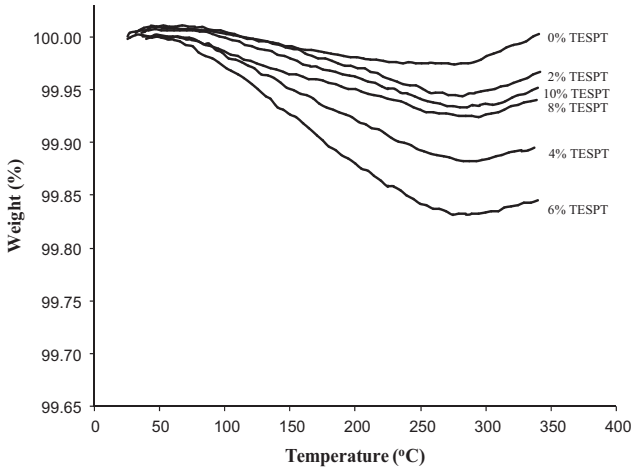

Fig. 4. TGA curves for iron sand particles at different TESPT contents.

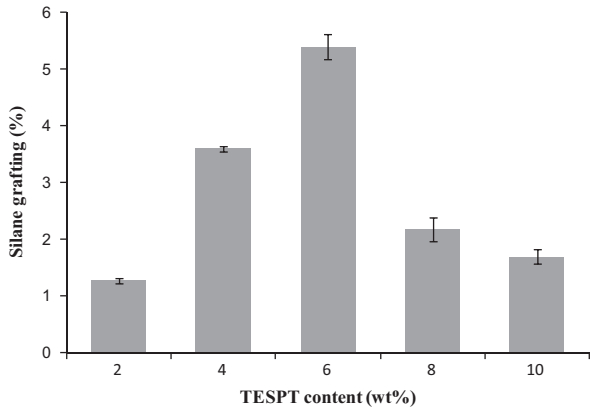

Fig. 5. Silane grafting percentage for iron sand particles at different TESPT contents.

ethanol solution and under acid catalysed conditions the ethoxy reactive groups of the silane are hydrolysed thereby forming silanol groups (–Si–O–OH) and liberating ethanol [35,36]. The silanol groups are highly reactive intermediates which are presumed responsible for bond formation with the iron sand. When iron sand was added into the solution, the hydroxyl groups on the surface of the iron sand is believed to react with the silanol groups and subsequent drying condenses silanol groups to form siloxane linkages. Evidence for this was provided by Raman Spectroscopy analysis of unmodified and modified iron sand particles as shown in Fig. 3. For iron sand, a number of peaks can be seen including a broad peak between 1100 and 1900 cm^{-1}, similar to observation elsewhere [37]. The growth of peaks at around 300 cm^{-1} for all modified iron sand particles is indicative of the formation of Si–O–iron sand and/or Si–O–Si bonds that would occur during reaction of iron sand with TESPT, although, the latter could also occur due to polymerisation of TESPT to produce siloxane; however, production of siloxane would not be expected to improve interfacial bonding. The increased height of the peaks around 1400 cm^{-1} (representing CH_2 bending in TESPT) from 0 to 6 wt% TESPT followed by no further increase from 6 wt% onwards suggests that coverage of iron sand particles by TESPT increases to 6 wt% when it reaches a saturation coverage [38].

Fig. 4 shows TGA curves for unmodified and modified iron sand particles at different TESPT contents. All samples showed weight loss over the temperature range of 50–280 °C with weight increase above 280 °C which is believed to have resulted from the oxidation of iron sand particles [39]. Similar trends have been observed in TGA curves for other magnetite particles [40]. As can also be seen, the unmodified iron sand particles were relatively stable in the air and only slightly weight loss between 100 °C and 280 °C which was probably due to vaporization of physically absorbed water at the surface of iron sand particles. The weight losses for modified particles increased with increasing TESPT content until 6% and then reduced for 8% and 10% TESPT. The weight loss for modified particles could be attributed to the decomposition and evaporation of silane coupling agent on the surface of iron sand particles such that suggests the silane coupling agent is strongly bound to particle surfaces by what is expected to be covalent bonds [41]. The amount of TESPT attached to the surfaces of iron sand particles was quantitatively determined by TGA (taking the loss due to physically absorbed water into account) over the temperature range of 50–280 °C (each value representing an average from 3 samples) and is presented in Fig. 5. It was not possible to conduct TGA analysis of TESPT on its own, however, a separate experiment was conducted where TESPT was heated at 280 °C in a furnace for which a residual weight of only 0.6% was obtained. Thus, residual TESPT is not considered to have a significant effect on the obtained data. It can be seen that the percentage of grafted silane appears to increase with increasing TESPT content until it reached a maximum value at 6% TESPT and thereafter decreased for higher TESPT contents (8% and 10%). At high TESPT content, the potential for hydrolysed TESPT to react with itself to produce polymeric siloxane increases as an alternative to reacting with iron sand. This polymeric siloxane could act as a barrier between TESPT and iron sand preventing reaction, particularly given that the siloxane polymer can react with multiple OH groups on the iron sand particles and screen other OH groups between those bonded with polymeric siloxane as described in the literature [42]. Polymeric siloxane that has not reacted with OH groups on iron sand would easily have been removed by washing the modified iron sand with ethanol and evaporation by drying during the preparation of the modified particles. This was checked by an extra wash with dichloromethane (DCM) following three times washing with ethanol for which the TGA weight loss and silane grafting percentage was found to be no significant different with those washed using just ethanol. Any remaining unreacted polymeric siloxane may also form e.g. oligomers by hydrogen bonding to the grafted TESPT such that may weaken the composites properties since the silane molecules may not link the filler to the matrix [42].

Fig. 6 shows a schematic of possible reaction mechanisms for the tetrasulphane group of TESPT with natural rubber. The

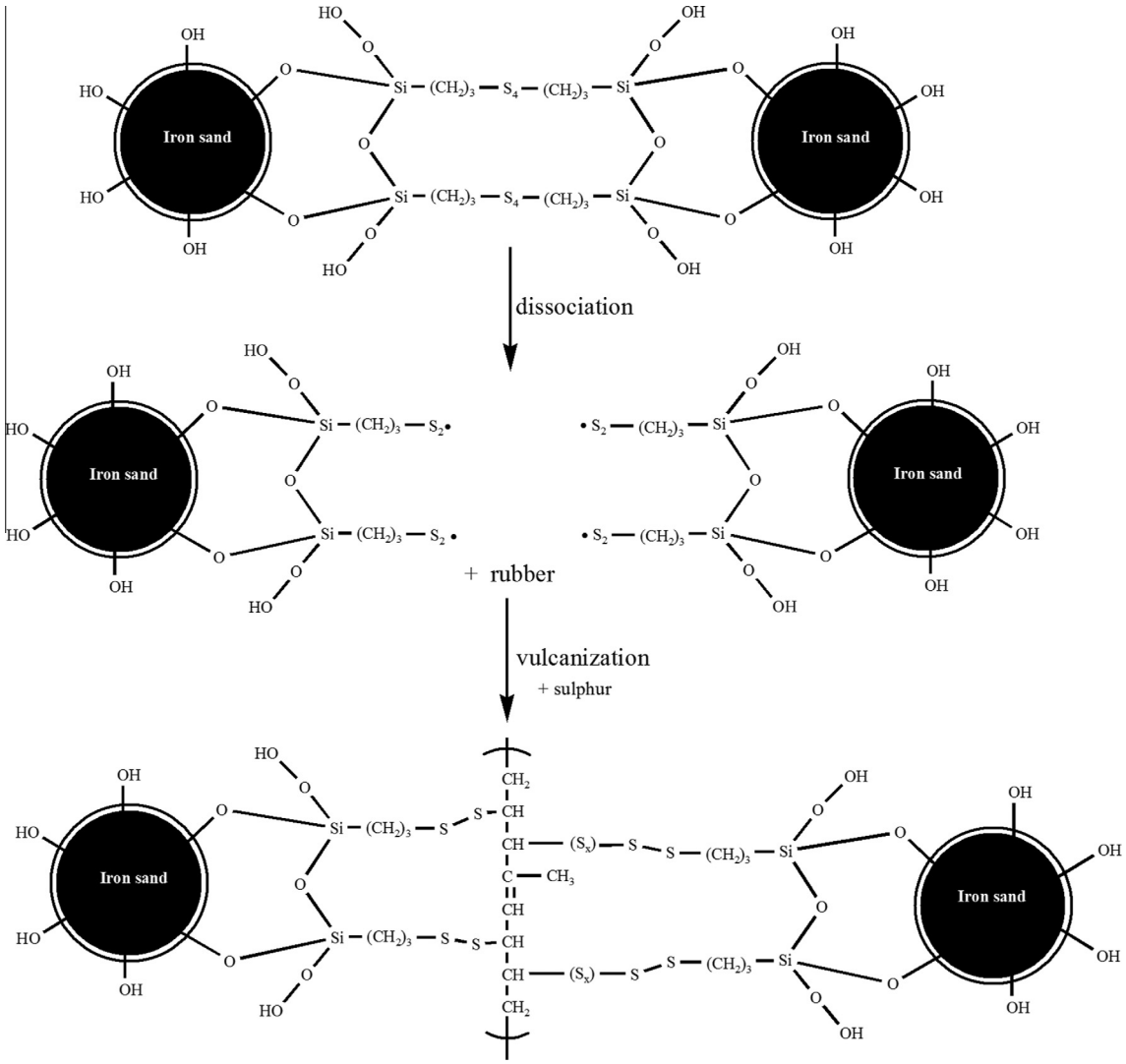

Fig. 6. Schematic illustration of the reaction mechanisms of tetrasulphane group of TESPT with the natural rubber (S_2 represents sulfidic radicals of tetrasulphane group of TESPT).

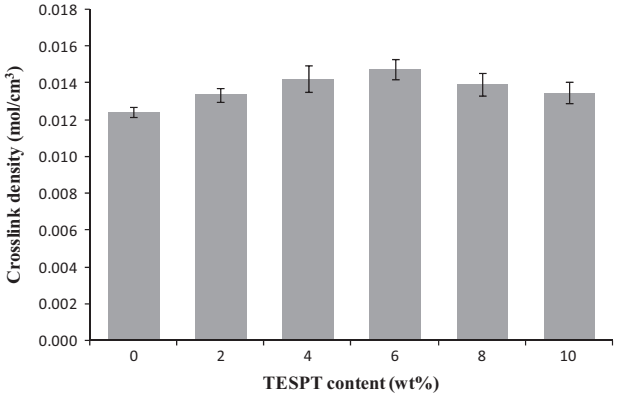

Fig. 7. Crosslink density of MREs with different TESPT contents.

tetrasulphane group of the TESPT could have been first dissociated during the compounding process to produce sulfidic radicals that subsequently react either directly or through sulphur crosslinking agent (S_x) with the rubber molecules in the presence of accelerators at elevated temperature during vulcanization to form crosslinks with the rubber molecules [43–45]. Evidence for this would be provided by crosslink density measurements of MREs filled with unmodified and modified iron sand particles at different TESPT contents as shown in Fig. 7. It can be seen that the crosslink density gradually increased as the TESPT content increased from 2% to 6%; this highlights the potential formation of new crosslinks in the rubber network due to interaction between tetrasulphane group of TESPT with the rubber molecules. In order to assess the time required for the tetrasulphane group of TESPT to react with rubber and form crosslinks, another compound was prepared, the same as that containing 6 wt% silane coupling agent except that the sulphur crosslinking agent was excluded. It was found that the compound cured in 5.63 min which is not too different from time used here supporting substantial TESPT rubber crosslinking could have occurred. At higher TESPT contents (8% and 10%) the crosslink density decreased which is not surprising given the evidence from TGA results that at such TESPT contents less silane is coupled to the iron sand, which would be expected to lead to less crosslinking between iron sand and rubber. The obtained results support the use of TESPT as a coupling agent for iron sand particles and natural rubber and also a content of 6% TESPT is more suitable than 8% and 10% TESPT.

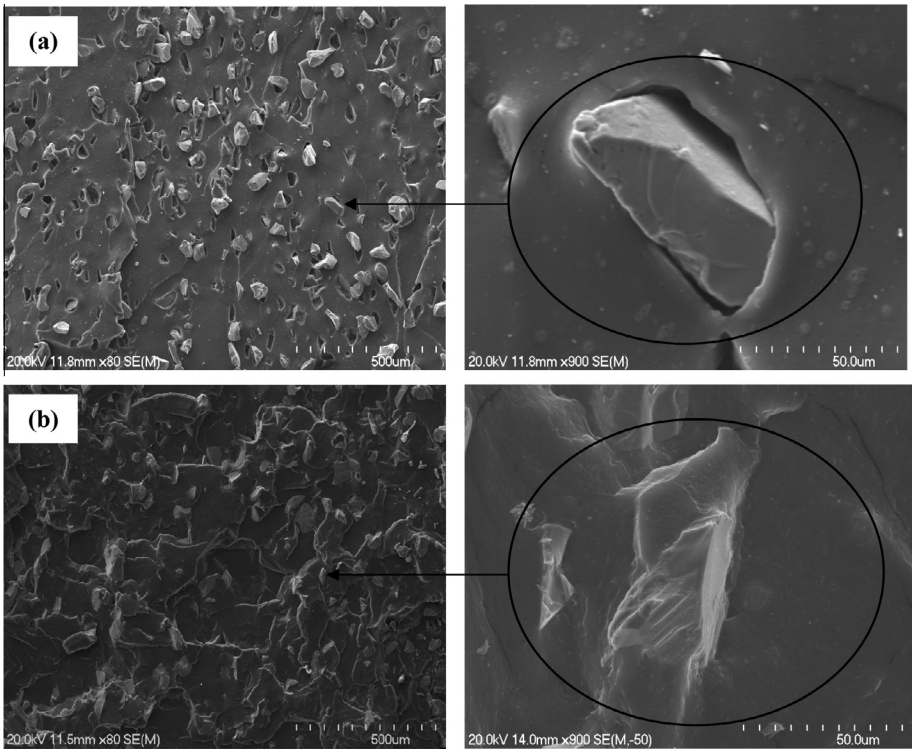

Fig. 8. SEM images of fracture surface of isotropic MREs with; (a) unmodified and (b) modified iron sand particles (treated with 6% TESPT).

3.2. Morphology

Fig. 8 shows SEM images of fracture surface of isotropic MREs with unmodified and modified iron sand particles. It can be seen for unmodified particle MREs, the surface is smooth with less matrix tearing and uneven distribution of iron sand particles in the rubber matrix. Clearly, there are a lot of cavities remaining due to the particle pull out from the rubber matrix and obvious gaps between iron sand particle and rubber, suggesting weak interaction between iron sand and rubber (Fig. 8a). In Fig. 8b, the surface of isotropic MREs with modified iron sand particles is rougher due to matrix tearing than for MREs with unmodified particles. It is also evident that iron sand particles are more evenly dispersed in the rubber with much less aggregates in the matrix. Clearly, much less particle pullout can be seen supporting improved interfacial adhesion between iron sand and natural rubber suggesting stronger interaction between iron sand and rubber was obtained by using modified iron sand particles supporting Si-O-iron sand bonding.

3.3. Dynamic mechanical properties

The variation of tan δ with frequency for MREs with different TESPT contents is shown in Fig. 9a. Tan δ is the highest for the MREs with modified iron sand treated with 6% TESPT and the increases in tan δ compared to MREs with unmodified iron sand is on average 40% over the whole frequency range explored. G′ and G″ are also plotted in Fig. 9(b and c) to help highlight the mechanisms involved. G′ and G″, similar to tan δ are frequency dependent. It can be seen that the increase of tan δ as the frequency increased, is mainly due to increasing G″ as opposed to changes in G′. The increased energy loss is assumed to be due to covalent bonding bringing about more intimate contact between the particles and rubber such that during deformation, increasing energy is expended overcoming friction, physical bonding as well as covalent bonding. At high TESPT content (8% and 10%), the lower tan δ values could again be explained by less silane grafting due to the formation of siloxane oligomer attached to the first layer of reacted TESPT on particle surfaces which could further reduce the energy absorption capability of the MREs. Energy loss in the materials could also be attributed to interfacial friction of weakly or partially bonded iron sand particles and rubber with increasing frequency. It is also apparent that the G′ for MREs with modified iron sand are higher compared to MREs with unmodified iron sand. Explanation for general increment of G′ for MREs with modified iron sand could be related to efficient stress transfer between particles and matrix which can improve stiffness, strength and failure strain of the materials [46]. Furthermore, improved interfacial bonding and degree of iron sand particle dispersion in the matrix might increase the effective particle–matrix interfacial area such that increased constraint of polymer chains occurs during deformation and improved the ability of the material to store elastic energy associated with recoverable elastic deformation [47].

The variation of tan δ with strain amplitude for MREs with different TESPT contents is shown in Fig. 10a; G′ and G″ are also plotted in Fig. 10(b and c). As expected, MREs with modified iron sand treated with 6% TESPT had the highest tan δ over the whole strain amplitude range explored with a 20% increase in tan δ compared to MREs with unmodified iron sand. As can be observed in Fig. 10(a and b), the tan δ and G′ were amplitude dependent at low strain amplitudes before reaching a plateau, with the tan δ for MREs with modified iron sand reaching a plateau at around 2.5% strain amplitude, whereas the tan δ of the MREs with unmodified iron sand reached a plateau at 2% strain amplitude. It was evident that strong interfacial bonding between the iron sand and rubber as well as better dispersion increased the dependency of tan δ on the amplitude of the applied strain and the change of tan δ values over the strain amplitude range for all tested samples is mainly due to a decrease in G′ as the strain amplitude increased. The decrease in G′ as the strain amplitude increased for MREs with modified iron sand could be explained by the increase of particle detachment from the matrix with increasing strain amplitude. As can also be

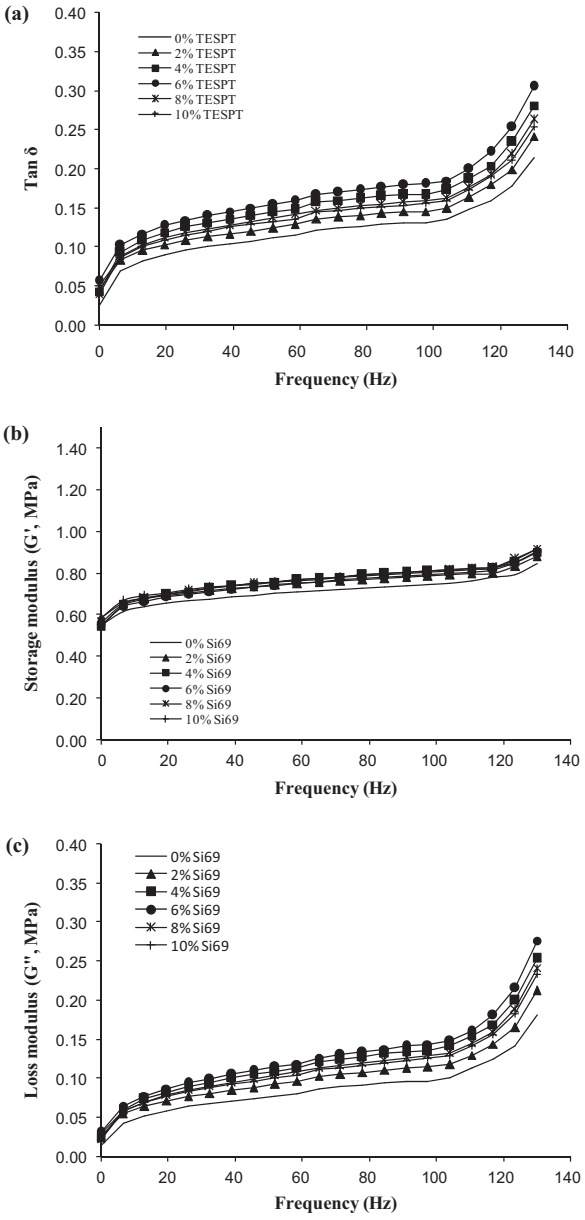

Fig. 9. (a) Tan δ, (b) storage modulus (G′) and (c) loss modulus (G″) vs. frequency for MREs with different TESPT contents.

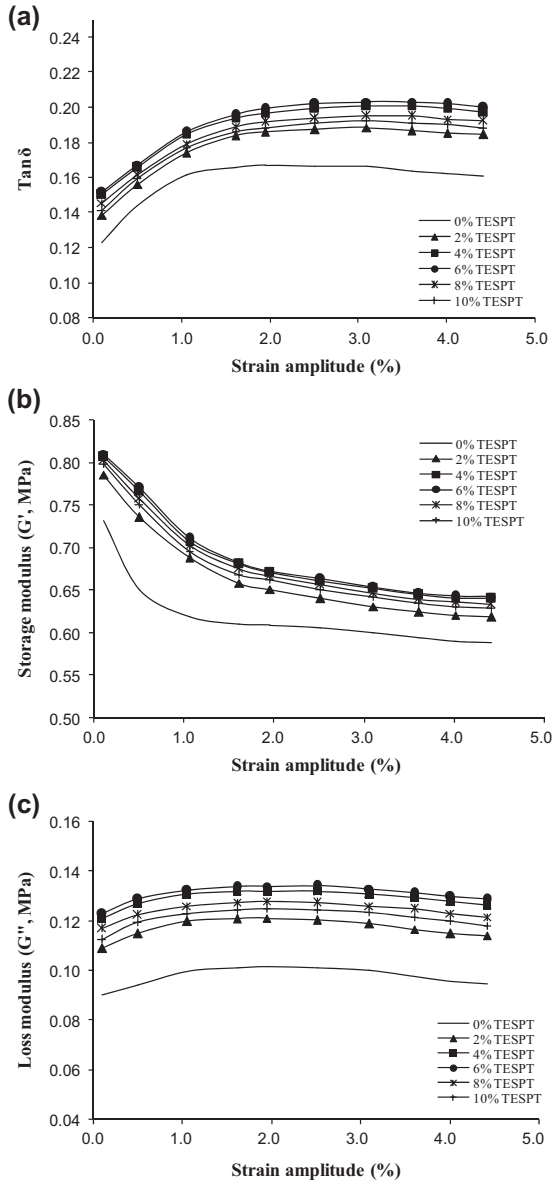

Fig. 10. (a) Tan δ, (b) storage modulus (G′) and (c) loss modulus (G″) vs. strain amplitude for MREs with different TESPT contents.

seen, G″ for MREs with modified iron sand are higher compared to MREs with unmodified iron sand. The higher loss modulus could be attributed to the energy loss due to stress released after debonding and increase of energy absorbed during viscous flow which is more constrained due to formation of chemical linkages between iron sand and rubber. Once the strain amplitude is high enough, all the interactions are destroyed to such an extent it cannot be reconstructed and consequently, the energy loss is largely reliant on the viscous flow of the rubber matrix.

Fig. 11 presents the tan δ versus temperature curves for MREs with different TESPT contents. The tan δ peak is associated with glass transition temperature (Tg) of the materials. In the glass transition zone, the energy dissipation is mainly from the segmental motion of macromolecular chain of rubber matrix in spite of breakdown of filler-filler or filler rubber interaction [48]. It can be seen that the presence of coupling agent does not strongly affect the peak height and width of the curves. This is in agreement with similar finding reported by other researchers [23,49,50]. However, an enlarged graph of the tan δ versus temperature around the peaks

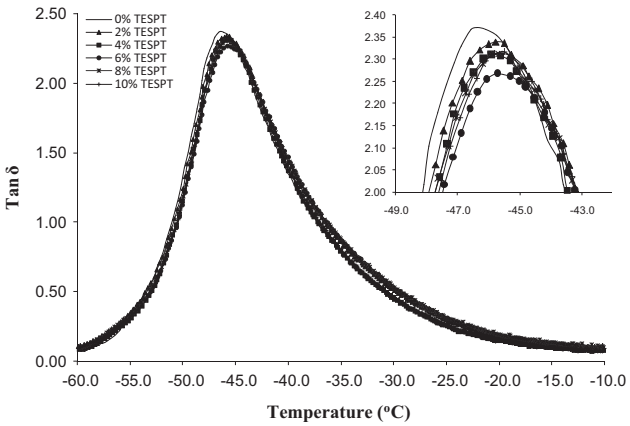

Fig. 11. Tan δ versus temperature curves for MREs with different TESPT contents.

showed a slight decrease of the height of the tan δ peak and the Tg values shifted to a slightly higher temperature for MREs with

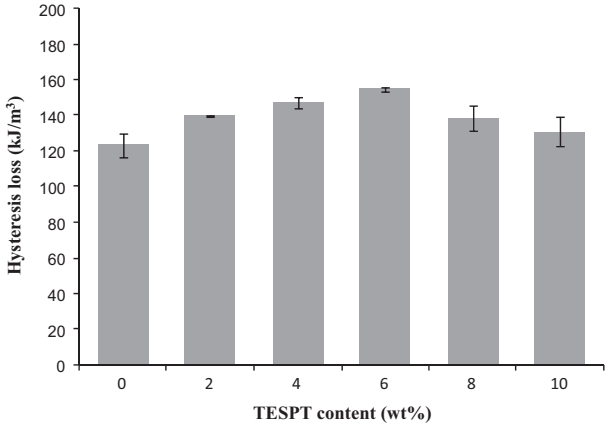

Fig. 12. Hysteresis loss for MREs with different TESPT contents.

modified iron sand compared with MREs with unmodified iron sand. In addition, the decreased height of the tan δ peak was in an order similar to the silane grafting percentage as previously discussed. The decrease height of the damping peak and a shift of Tg to higher temperature could be attributed to strong filler rubber interaction which resulted in restriction in mobility and flexibility of rubber chains in the materials.

Fig. 12 shows hysteresis loss for MREs with different TESPT contents. As can be seen, hysteresis loss increased with increasing TESPT content until it reached a maximum value at 6% TESPT and thereafter decreased at higher TESPT content (8% and 10%). The results are in agreement with the silane grafting percentage as previously discussed. The effect of coupling agent on the hysteresis loss of MREs could again be explained by the energy loss due to stress released after debonding and increase of energy absorbed during viscous flow which is more constrained due to formation of chemical linkages between iron sand and rubber. Some authors have considered constraint in liaise of a rubber shell mechanisms [13]. The molecular chain mobility would be reduced by the formation of silane linkages between iron sand and rubber, resulting in a rubber shell on the filler surface in which the polymer viscosity and Young modulus would be increased. The higher Young's modulus of rubber near the surface of iron sand in the rubber shell would gradually decrease with increased distance from the filler surface and finally reach the same level as that of the rubber matrix at a certain distance. When the MREs were subjected to dynamic strain, the rubber shell around the particles would begin to break down and increase the amount of energy loss. In addition, hysteresis loss could also be attributed to interfacial friction at the filler matrix interface and breakdown of filler aggregates. The decrease of hysteresis loss at higher TESPT content could again be explained by the lower silane grafting and formation of weak siloxane oligomer that may begin to break down at a relatively lower level of strain.

4. Conclusions

In this work, iron sand particles were modified at five different TESPT contents (2, 4, 6, 8 and 10 wt%) relative to the iron sand content to assess the optimum amount of for use in MREs. TESPT contains ethoxy hydrolysable groups that enable bonding with iron sand particles and a tetrasulphane group capable of bonding with the rubber matrix. Raman Spectroscopy showed evidence that siloxane linkages were formed between TESPT and iron sand. Weight loss measured using TGA supports that silane coupling agent is strongly bound to particle surfaces and the silane grafting percentage was found to be the highest at 6% TESPT. Crosslink density measurement of MREs made using TESPT treated iron sand highlight that the tetrasulphane group of TESPT formed crosslinks with the rubber molecular chains. Treated iron sand was found to be more evenly dispersed in the rubber with much less particle pullout on fracture surface supporting improved interfacial adhesion with natural rubber. Tan δ was found to be highest for the MREs with modified iron sand treated with 6% TESPT and 40% larger than that unmodified iron sand over the whole frequency range explored and 20% higher over the whole strain amplitude explored. However, the presence of coupling agent did not strongly affect the peak temperature of tan δ versus temperature curves. An increase in hysteresis loss was also obtained for MREs with modified iron sand treated with 6% TESTPT content compared with MREs with unmodified iron sand.

Acknowledgement

The authors would like to thank for the support from the Polymer and Composite Research Group of the University of Waikato.

References

[1] Chen L, Gong XL, Li WH. Effect of carbon black on the mechanical performances of magnetorheological elastomers. Polym Testing 2008;27(3):340–5.
[2] Chokkalingam R, Rajasabai Senthur P, Mahendran M. Magnetomechanical behavior of Fe/PU magnetorheological elastomers. J Compos Mater 2010;45(15):1545–52.
[3] Fuchs A, Zhang Q, Elkins J, Gordaninejad F, Evrensel C. Development and characterization of magnetorheological elastomers. J Appl Polym Sci 2007;105(5):2497–508.
[4] Ginder J. Magnetorheological elastomers: properties and applications. Proc SPIE. 1999;3675(1):131.
[5] Lerner AA, Cunefare KA. Performance of MRE-based vibration absorbers. J Intell Mater Syst Struct 2008;19(5):551–63.
[6] Sun TL, Gong XL, Jiang WQ, Li JF, Xu ZB, Li WH. Study on the damping properties of magnetorheological elastomers based on cis-polybutadiene rubber. Polym Testing 2008;27(4):520–6.
[7] Wang Y, Hu Y, Deng H, Gong X, Zhang P, Jiang W, et al. Magnetorheological elastomers based on isobutylene–isoprene rubber. Polym Eng Sci 2006;46(3):264–8.
[8] Deng HX, Gong XL. Application of magnetorheological elastomer to vibration absorber. Commun Nonlinear Sci Numer Simul 2008;13(9):1938–47.
[9] Dyke SJ, Spencer JR, Sain MK, Carlson JD. Modeling and control of magnetorheological dampers for seismic response reduction. Smart Mater Struct 1996;5(5):565–75.
[10] Park JO, Rhee KY, Park SJ. Silane treatment of Fe3O4 and its effect on the magnetic and wear properties of Fe3O4/epoxy nanocomposites. Appl Surface Sci 2010;256(23):6945–50.
[11] Taghvaei AH, Shokrollahi H, Ebrahimi A, Janghorban K. Soft magnetic composites of iron-phenolic and the influence of silane coupling agent on the magnetic properties. Mater Chem Phys 2009;116(1):247–53.
[12] Tian Y, Liu Y, He M, Zhao G, Sun Y. High damping properties of magnetic particles doped rubber composites at wide frequency. Mater Res Bull 2013;48(5):2002–5.
[13] Wang MJ. Effect of polymer-filler and filler-filler interactions on dynamic properties of filled vulcanizates. Rubber Chem Technol 1998;71(3):520–89.
[14] Sun Y, Zhou X, Liu Y, Zhao G, Jiang Y. Effect of magnetic nanoparticles on the properties of magnetic rubber. Mater Res Bull 2009;45(7):878–81.
[15] Jiang WQ, Yao JJ, Gong XL, Chen L. Enhancement in magnetorheological effect of magnetorheological elastomers by surface modification of iron particles. Chin J Chem Phys 2008;21(1):87–92.
[16] Wu J, Gong X, Chen L, Xia H, Hu Z. Preparation and characterization of isotropic polyurethane magnetorheological elastomer through in situ polymerization. J Appl Polym Sci 2009;114(2):901–10.
[17] Xiuying Q, Xiushou L, Weihua L, Jun C, Xinglong G, Tao Y, et al. Microstructure and magnetorheological properties of the thermoplastic magnetorheological elastomer composites containing modified carbonyl iron particles and poly(styrene- b -ethylene-ethylenepropylene- b -styrene) matrix. Smart Mater Struct 2012;21(11):115028.
[18] Ansarifar A, Azhar A, Ibrahim N, Shiah SF, Lawton JMD. The use of a silanised silica filler to reinforce and crosslink natural rubber. Int J Adhes Adhes 2005;25(1):77–86.
[19] Choi SS, Kim IS, Woo CS. Influence of TESPT content on crosslink types and rheological behaviors of natural rubber compounds reinforced with silica. J Appl Polym Sci 2007;106(4):2753–8.
[20] Vinod VS, Varghese S, Kuriakose B. Degradation behaviour of natural rubber-aluminium powder composites: effect of heat, ozone and high energy radiation. Polym Degrad Stab 2002;75(3):405–12.

[21] Rooj S, Das A, Thakur V, Mahaling RN, Bhowmick AK, Heinrich G. Preparation and properties of natural nanocomposites based on natural rubber and naturally occurring halloysite nanotubes. Mater Des 2010;31(4):2151–6.
[22] Ismail H, Abdul Khalil HPS. The effects of partial replacement of oil palm wood flour by silica and silane coupling agent on properties of natural rubber compounds. Polym Testing 2000;20(1):33–41.
[23] Zeng Z, Ren W, Xu C, Lu W, Zhang Y, Zhang Y. Effect of bis(3-triethoxysilylpropyl) tetrasulfide on the crosslink structure, interfacial adhesion, and mechanical properties of natural rubber/cotton fiber composites. J Appl Polym Sci 2009;111(1):437–43.
[24] Pickering KL, Abdalla A, Ji C, McDonald AG, Franich RA. The effect of silane coupling agents on radiata pine fibre for use in thermoplastic matrix composites. Compos A Appl Sci Manuf 2003;34(10):915–26.
[25] Wang YL, Hu YA, Chen L, Gong XL, Jiang WQ, Zhang PQ, et al. Effects of rubber/magnetic particle interactions on the performance of magnetorheological elastomers. Polym Testing 2006;25(2):262–7.
[26] Possinger T, Bolzmacher C, Bodelot L, Triantafyllidis N. Interfacial adhesion between the iron fillers and the silicone matrix in magneto-rheological elastomers at high deformations, p. 87631Y-Y-11.
[27] Monticelli F, Toledano M, Osorio R, Ferrari M. Effect of temperature on the silane coupling agents when bonding core resin to quartz fiber posts. Dent Mater 2006;22(11):1024–8.
[28] Yakobi HJD, Ladino LA, Abbatt JPD. Feldspar minerals as efficient deposition ice nuclei. Atmos Chem Phys Discuss 2013;13(6):17299–326.
[29] Puvanakrishnan R, Bose SM, Reddi BR. Immobilization of trypsin on sand: mode of binding. J Biosci 1982;4(1):51–9.
[30] Lakes RS. High damping composite materials: effect of structural hierarchy. J Compos Mater 2001;36(3):287–97.
[31] Khimi SR, Pickering KL. A new method to predict optimum cure time of rubber compound using dynamic mechanical analysis. J Appl Polym Sci 2013;131(6). 40008(1-6).
[32] Guo ZX, Yu J. Grafting of dendritic polyethers onto nanometre silica surface. J Mater Chem 2002;12(3):468–72.
[33] Zhao J, Milanova M, Warmoeskerken MMCG, Dutschk V. Surface modification of TiO2 nanoparticles with silane coupling agents. Colloids Surfaces A: Physicochem Eng Aspects 2012;413(0):273–9.
[34] Flory PJ, Rehner J. Statistical mechanics of cross-linked polymer networks II. Swelling. J Chem Phys 1943;11(11):521–6.
[35] Hunsche A, Gorl U, Muller A, Knaack M, Gobel T. Investigations concerning the reaction silica/organosilane and organosilane/polymer. Part 1: Reaction mechanism and reaction model for silica/organosilane. Kautschuk und Gummi, Kunststoffe. 1997;50(12):881–9.
[36] Hunsche A, Gorl U, Koban HG, Lehmann T. Investigations on the reaction silica/organosilane and organosilane/polymer. Part 2: Kinetic aspects of the silica-organosilane reaction. Kautschuk und Gummi, Kunststoffe. 1998;51(7–8):525–33.
[37] Shebanova ON, Lazor P. Raman study of magnetite (Fe3O4): laser-induced thermal effects and oxidation. J Raman Spectrosc 2003;34(11):845–52.
[38] Shih PTK, Koenig JL. Raman studies of the hydrolysis of silane coupling agents. Mater Sci Eng 1975;20:137–43.
[39] Amanda A, Julio BA, Gemma LD, Yurii KG, Nuria V, Xavier MB, et al. Ecologically friendly polymer–metal and polymer–metal oxide nanocomposites for complex water treatment. In: Farzad Ebrahimi, editor. Nanocomposites - New Trends and Developments. InTech, vol. 1. Croatia: Rijeka; 2012, ISBN 978-953-51-0762-0. p. 187–213. http://dx.doi.org/10.5772/50412.
[40] Hou Y, Yu J, Gao S. Solvothermal reduction synthesis and characterization of superparamagnetic magnetite nanoparticles. J Mater Chem 2003;13(8):1983–7.
[41] Zhang H, Li C, Guo J, Zang L, Luo J. In situ synthesis of poly(methyl methacrylate)/SiO2 Hybrid Nanocomposites via "Grafting Onto" Strategy Based on UV irradiation in the presence of iron aqueous solution. J Nanomater 2011;2012:1–9.
[42] Sideridou ID, Karabela MM. Effect of the amount of 3-methacyloxypropyltrimethoxysilane coupling agent on physical properties of dental resin nanocomposites. Dent Mater 2009;25(11):1315–24.
[43] Choi SS. Influence of storage time and temperature and silane coupling agent on bound rubber formation in filled styrene butadiene rubber compounds. Polym Testing 2002;21(2):201–8.
[44] Gorl U, Munzenberg J, Luginsland D, Muller A. Investigations on the reaction silica/organosilane and organosilane/polymer-Part 4: studies on the chemistry of the silane sulfur chain. Kautsch Gummi Kunstst 1999;52(9):588–97.
[45] Luginsland HD. Reactivity of the sulfur chains of the tetrasulfane silane Si 69 and the disulfane silane TESPD. Kautsch Gummi Kunstst 2000;53(1):10–9.
[46] Sun L, Gibson RF, Gordaninejad F, Suhr J. Energy absorption capability of nanocomposites: a review. Compos Sci Technol 2009;69(14):2392–409.
[47] Gu H, Guo Y, Wong SY, He C, Li X, Shim VPW. Effect of interphase and strain-rate on the tensile properties of polyamide 6 reinforced with functionalized silica nanoparticles. Compos Sci Technol 2013;75(0):62–9.
[48] Li Y, Han B, Liu L, Zhang F, Zhang L, Wen S, et al. Surface modification of silica by two-step method and properties of solution styrene butadiene rubber (SSBR) nanocomposites filled with modified silica. Compos Sci Technol 2013;88(1):69–75.
[49] Mele P, Marceau S, Brown D, Puydt DY, Alberola ND. Reinforcement effects in fractal-structure-filled rubber. Polymer 2002;43(20):5577–86.
[50] Li Y, Han B, Liu L, Zhang F, Zhang L, Wen S, et al. Surface modification of silica by two-step method and properties of solution styrene butadiene rubber (SSBR) nanocomposites filled with modified silica. Compos Sci Technol 2013;88(0):69–75.

Composites Part B 83 (2015) 175–183

Contents lists available at ScienceDirect

Composites Part B

journal homepage: www.elsevier.com/locate/compositesb

Comparison of dynamic properties of magnetorheological elastomers with existing antivibration rubbers

S. Raa Khimi [a, b, *], K.L. Pickering [a]

[a] School of Engineering, The University of Waikato, Hamilton, 3216, New Zealand
[b] School of Materials and Mineral Resources Engineering, USM Engineering Campus, Universiti Sains Malaysia, 14300, Nibong Tebal, Penang, Malaysia

ARTICLE INFO

Article history:
Received 16 March 2015
Received in revised form
12 June 2015
Accepted 6 August 2015
Available online 24 August 2015

Keywords:
A. Particle-reinforcement
B. Vibration
D. Mechanical testing

ABSTRACT

Tan δ and energy dissipated during hysteresis testing of isotropic and anisotropic MREs containing silane modified iron sand particles in a natural rubber matrix were compared with existing antivibration rubbers. Tan δ was measured using dynamic mechanical analysis (DMA) over a range of frequency (0.01–130 Hz), strain amplitude (0.1–4.5%), and temperature (−100–50 °C). Energy dissipated was measured using a universal tester under cyclic tensile loading. The chosen antivibration rubbers for comparison contained different contents of carbon black filler (30, 50 and 70 phr) in a natural rubber matrix. It was found that energy absorption for comparative samples was generally higher than isotropic and anisotropic MREs over the range of frequency and strain amplitude explored, as well as in hysteresis testing and this was believed to be largely due the presence of carbon black in the formulation. Further assessment was carried out on materials that were the same as anisotropic MREs except they had additions of carbon black. The energy absorption was found higher than comparative samples with the same carbon black contents, supporting the use of iron sand to improve damping. However, trends for energy absorption at around T_g were found to reverse which is considered to be due to the segmental motion of rubber chains being by far the most significant influence on energy absorption in the glass transition zone.

1. Introduction

Magnetorheological elastomers (MREs) are a new group of damping materials which consist of a non-magnetic matrix (normally an elastomer) containing a suspension of magnetically permeable particles. Damping occurs by the viscous flow of the rubber matrix and inclusion of magnetic particles in rubber enables additional damping through magnetic particle interaction and interfacial damping. The magnetic particles of choice are carbonyl iron, magnetite, iron oxides, barium ferrite or Terfenol-D [1–3] and suitable matrix materials include natural rubber, silicone rubber, polybutadiene, polyisobutylene, polyisoprene and polyurethene rubber [4–11]. The main advantage of MREs is that the damping and stiffness can be varied by application of an applied magnetic field during fabrication or in service. MREs can be classified into two kinds: isotropic MREs and anisotropic MREs [12]. Fig. 1 shows structure of isotropic and anisotropic MREs. Isotropic MREs can be characterized by having a uniform magnetic particle distribution in the matrix. Anisotropic MREs have a special chain-like structure of magnetic particles in a matrix resulting from curing the matrix under an applied magnetic field. Over the past few years, MREs have attracted increasing attention and have been considered for applications such as adaptive tuned vibration absorbers [13], automotive engine mounts [8] and semi active seismic dampers [14].

In this study, isotropic and anisotropic MREs based on natural rubber and silane modified iron sand particles were prepared. The natural rubber was used as a matrix because of its associated ease of processing and good damping performance [14–16] and iron sand was chosen as magnetic particles because it has high permeability and saturation magnetisation, low cost and is readily available in New Zealand. Surface modification of iron sand using silane coupling agent was found to provide coupling between iron sand and natural rubber [15]. It has also been reported that the silane modified particles decrease the interfacial tension around the particles and results in improved dispersion of magnetic particles in isotropic MREs and an improved degree of magnetic particle alignment in anisotropic MREs [16,17].

* Corresponding author. School of Engineering, The University of Waikato, Hamilton, 3216, New Zealand. Tel.: +64 078384672.
E-mail address: raa_khimi@hotmail.com (S.R. Khimi).

http://dx.doi.org/10.1016/j.compositesb.2015.08.033
1359-8368/

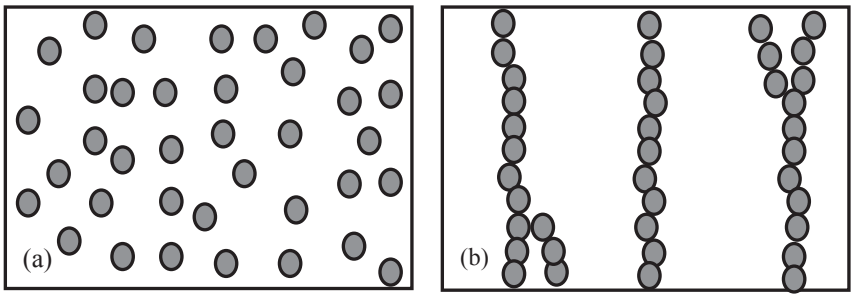

Fig. 1. MRE structure: (a) isotropic MRE; and (b) anisotropic MRE.

This work aims to assess the potential of developed MREs for potential use in vibration damping. The dynamic properties of isotropic and anisotropic MREs were compared with existing antivibration rubbers. The dynamic properties were investigated using two different methods. The loss tangent, commonly called tan δ, is considered as the fundamental parameter to assess damping. Tan δ gives a comparison of the energy lost to that stored; it is obtained by dividing the loss modulus (G″ or E″) by the storage modulus (G′ or E′) [12,18]. The other estimate of damping used was the amount of energy dissipated during cyclic deformation, which can be calculated from the area of the hysteresis loop. The antivibration rubbers for comparison were prepared according to existing formulations from published patents (see details in Table 1). Those chosen, contained different contents of carbon black filler (30, 50 and 70 phr) in a natural rubber matrix. In addition, anisotropic MREs containing silane modified iron sand and a predetermined amount of carbon black were also prepared in order to investigate the influence of carbon black on the damping performance of the MREs.

2. Experimental

2.1. Materials

Natural rubber (SMR L grade) and other chemicals including zinc oxide, stearic acid, n-cyclohexyl-2-benzothiazole sulfenamide (CBS), tetramethylthiuram disulphide (TMTD), paraffin oil, and naphthenic oil were all purchased from Field Rubber Limited, Auckland. Bis-(3-triethoxysilylpropyl) tetrasulphane (TESPT) was purchased from Leap Lab Chem Co. Ltd. Carbon black was purchased from Shijiazhuang Changhang Co. Ltd. Iron sand was collected from Ngarunui Beach, Raglan. The iron sand was then milled using a planetary mono mill (Pulverisette 6) produced by Fristech GmbH and subsequently sieved to obtain a 45–56 μm particle size range.

2.2. Surface modification of iron sand

The surface modification of iron sand was carried out using an aqueous alcohol solution method. Iron sand particles were subjected to surface treatment with TESPT at 6 wt% relative to the weight of the particles. An aqueous alcohol solution of 95 vol% ethanol was used and the pH of the solution was adjusted with acetic acid to 4.0–4.5. TESPT of predetermined quantity was dispersed in the ethanol solution at a ratio of 1:100 and the mixed solution was stirred for 5 min to ensure hydrolization of the silane coupling agent. The iron sand particles were then added and stirred for an additional 30 min at room temperature to ensure a uniform distribution of the coupling agent on the surface of iron sand particles. The mixture was filtered and washed three times with ethanol to remove unreacted coupling agent. The treated iron sand particles were then dried at 80 °C in an oven until a constant weight was achieved.

2.3. Preparation of MREs and comparative samples

The compound formulation used in this study is given in Table 2. The formulations of comparative samples based on published patents comprised of natural rubber and carbon black as the major components with processing aids and crosslinking agent. Additives such as anti antioxidant, anti-thermal aging agent and petroleum resin were excluded from the formulations. Formulations were compounded using a conventional laboratory two roll mill (model XK150) according to ASTM designation D3184-80. The front roller speed was 24 rpm and the rear roller speed was 33 rpm, the roller diameters were 150 mm, friction ratio of two rollers was 1:1.4 and the roller temperature was set to 80 °C. The nip gap (distance between front and back roller) was maintained at 2 mm during compounding. The compounding began with softening the rubber on its own in the two roll mill (mastication). Mastication reduces the viscosity and increases the plasticity of natural rubber by mean of heat generated in the two roll mill through conduction from the

Table 1
Comparative samples' patent specifications.

Comparative sample	Patent number	Applicant	Title	Description
1	US 2011/0166276 A1 [18]	Tokai Rubber Industries Ltd	Antivibration rubber composition	The invention relates to a vibration damping rubber composition to be used for an engine mount or the like adapted to support an engine in an automobile or the like and suppress transmission of vibrations.
2	EP 0 481 810 B1 [19]	Sumitomo Rubber Industries Ltd	Rubber composition for laminated vibration proofing structure	The present invention relates to a rubber composition for use in the seismic isolation of a bridge, a building or a house.
3	US6180711 B1 [20]	Yokohama Rubber Co. Ltd	Rubber composition for seismic isolation laminates	This invention relates to a rubber composition for seismic isolation laminate for buildings.

Table 2
Formulation of rubber compounds.

Materials	MRE/ISO	MRE/AN	MRE/AN/30CB	MRE/AN/50CB	Comparative sample 1 (CS/30CB)	Comparative sample 2 (CS/50CB)	Comparative sample 3 (CS/70CB)
Natural Rubber	100	100	100	100	100	100	100
ZnO	5	5	5	5	5	5	5
Stearic Acid	1	1	1	1	1	1	1
Paraffin Oil	2	2	2	2	2	–	–
Naphthenic Oil	3	3	3	3	3	10	5
Iron sand	70	70	70	70	–	–	–
Carbon black	–	–	30	50	30	50	70
CBS	2	2	2	2	2	1.9	1
TMTD	1	1	1	1	1	0.8	–
Sulphur	1.5	1.5	1.5	1.5	1	0.8	1.5
Curing condition							
Temperature (°C)	150	150	150	150	150	150	150
Pressure (MPa)	12	12	12	12	12	12	12
Magnetic field during curing (mT)	0	600	600	600	–	–	–

*MRE = Magnetorheological elastomers.
*ISO = Isotropic.
*AN = Anisotropic.
*CB = Carbon black.
*CS = Comparative sample.

heated roller and shearing of rubber during milling. After 2–3 min the rubber became invested on the hot roll and additives (other than accelerators and sulphur) were then added followed by filler (iron sand or carbon black); addition of accelerators and sulphur were delayed to the last part of the process to prevent premature vulcanization during compounding. The mixing time was approximately 40 min. The cure time at 150 °C was then determined according to the procedure as described elsewhere [19]. Compounded rubber samples weighing 13 g were placed in a mould 60 × 50 × 3 mm. The isotropic MREs and comparative samples were cured in a compression moulder at 150 °C under a pressure of approximately 12 MPa. The anisotropic MREs were subjected to an external magnetic field in a specially developed electromagnetic-thermal coupled device (as shown in Fig. 2) at 80 °C for 30 min and subsequently were cured in a compression moulder at 150 °C under a pressure of approximately 12 MPa. Finally, post-cure treatment was performed by cooling the anisotropic MREs at room temperature for 30 min under an external magnetic field of the same strength as that used during pre-curing. The post-cure treatment was considered necessary to reorientate the magnetic dipoles after compression moulding.

2.4. Dynamic mechanical analysis

Dynamic mechanical analysis (DMA) is a technique used to measure damping of materials as they are deformed under periodic force. In DMA, a sinusoidal force at different frequencies, strain amplitudes and temperatures is applied and displacement of the materials is measured, allowing one to determine the storage modulus (G′ or E′), loss modulus (G″ or E″) and tan δ. DMA was carried out using a Perkin Elmer dynamic mechanical analyser (DMA 8000). It is made up of six major components (Fig. 3): a force motor, a drive shaft, a high sensitivity displacement detector (LVDT), a sample fixture, a furnace and a temperature controller. The driveshaft motion was kept in a horizontal direction during the test and the temperature controller was placed at a minimum distance from the sample. Tan δ was measured over a wide range of frequency, strain amplitude and temperature. The influence of frequency and strain amplitude on tan δ was assessed using two circular disc specimens with a diameter of 10 mm and a thickness of 3 mm in shear mode at room temperature. Tan δ was measured over the frequency range of 0.01–130 Hz at a fixed strain amplitude of 0.5% and over a strain amplitude range of 0.1–4.5% at a fixed frequency of 100 Hz. For the influence of temperature on tan δ, the samples were analysed in dual cantilever mode at a frequency of 1 Hz with a strain amplitude of 0.5% and over a temperature range from −100–50 °C. The samples were rectangular with dimensions 30 mm × 6 mm × 3 mm.

2.5. Hysteresis

Hysteresis loss is defined as the amount of energy dissipated during cyclic deformation when the samples are stretched and then allowed to retract at the same rate to the unstretched state. In this study, the hysteresis loss was determined for tensile dumbbells using an Instron 4204 at a crosshead speed of 500 mm/min

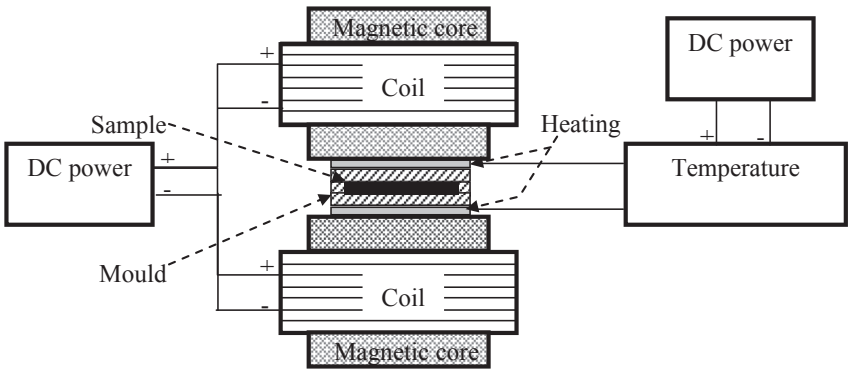

Fig. 2. Sketch of specially developed electromagnetic-heat coupled device.

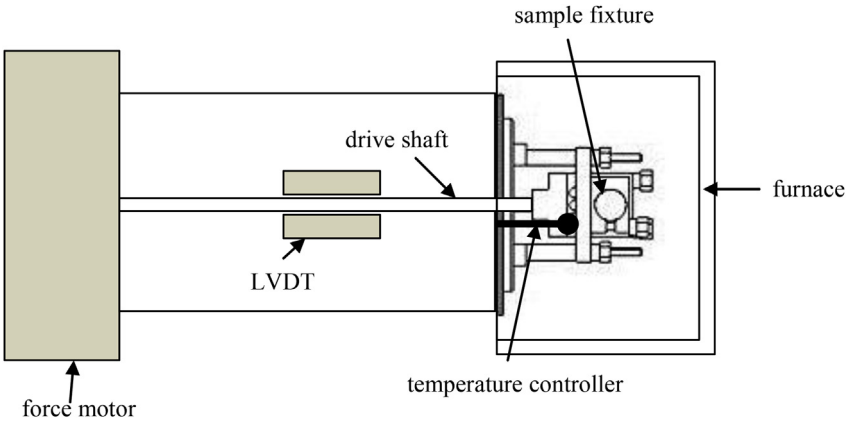

Fig. 3. Scheme of the DMA 8000.

according to ASTM D412-80. The stress–strain curve was recorded and hysteresis loss was calculated as:

$$\text{Hysteresis loss} = \text{Area under the loading curve} - \text{Area under the recovery curve} \quad (1)$$

2.6. Morphology

The microstructures of isotropic and anisotropic MREs were observed using a Hitachi S-4700 scanning electron microscope (SEM). The samples were cut into pieces with a surface area of 5 mm × 3 mm and coated with a thin layer of platinum prior to observation at an accelerating voltage of 20 kV.

3. Results and discussion

3.1. Morphology

Fig. 4 shows SEM images of MREs and comparative samples. It can be seen that MRE/ISO had uniform iron sand particle distribution in the rubber matrix without obvious aggregation (Fig. 4a). Fig. 4b shows an MRE/AN sample cured under an applied magnetic field of 600 mT at elevated temperature; as expected, the iron sand organized into chain-like columnar structures. For comparative samples, the carbon black particles were generally evenly distributed in the rubber matrix but with some aggregates ranged probably from below the resolution of the SEM up to 20 μm as seen in Fig. 4c. It can be seen that the distribution of carbon black in the rubber matrix has occurred similarly to that obtained elsewhere [20]. For MRE/AN/50CB sample (Fig. 4d), it can be seen that the presence of carbon black has constrained the movement of iron sand particles and the chain-like columnar structures are shorter and less aligned than MRE/AN sample.

3.2. Dynamic mechanical analysis

3.2.1. Frequency sweep measurements

The variation of tan δ with frequency for MREs and comparative samples is depicted in Fig. 5a. Generally, tan δ increased with increasing frequency, with tan δ values for both MRE/ISO and MRE/AN found to be lower than for the others at most frequencies, although relatively larger increases in tan δ above 100 Hz compared to other samples occurred, such that at the highest frequencies explored, tan δ values for MRE/ISO and MRE/AN were at the upper end of those obtained. The increase of tan δ as the frequency increased for isotropic MREs and comparative samples could be due to increased energy absorbed through viscous flow of the rubber matrix and interfacial damping between the particle and the rubber matrix [15]; for anisotropic MREs similar mechanisms would be involved as well as potentially, energy absorbed through magnetic interactions [21]; for samples containing carbon black, increased energy could be absorbed due to overcoming inter-particle interactions (Van der Waals) [22]. The difference in trends observed for MREs and comparative samples are likely to be due to the relatively different amounts of energy absorbed by different mechanisms involved with different reinforcement particles at different frequencies.

It can also be seen that tan δ of MRE/AN is about 8% higher than MRE/ISO over the whole frequency range explored; the higher tan δ of MRE/AN can be attributed to multiple mechanisms such that include constraint of joint rubber shells between neighbouring iron sand particles, less trapped rubber due to formation of aligned structures and damping through inter-particle magnetic interactions as well as magnetomechanical effect (change of magnetic domain structure induced by application of stress) [21,22]. For the comparative samples, tan δ increased in the following order: CS/30CB < CS/50CB < CS70/CB, correlating with the increased content of carbon black. A significant improvement of tan δ was observed for comparative samples when compared to MRE/ISO and MRE/AN; it was suspected that this could be due to the presence of carbon black in the formulation. In order to assess the influence of carbon black on damping performance of MREs, two compounds were prepared that were the same as MRE/AN except they had additions of 30 and 50 phr carbon black (MRE/AN/30CB and MRE/AN/50CB). It was found that such additions of carbon black gave good improvement of tan δ. The tan δ values for MRE/AN/30CB and MRE/AN/50CB were 21% and 43% higher than MRE/AN, indeed, the tan δ were 10% and 7% higher compared to CS/30CB and CS/50CB over the whole frequency range explored; supporting the use of iron sand to improve damping through interfacial damping between the particle and the rubber matrix and magnetic interactions (magnetomechanical and inter-particle interaction).

The effect of carbon black on tan δ can be analysed further using storage modulus (G′) and loss modulus (G″) plots as shown in Fig. 5 (b and c). It is apparent that G′ and G″ for samples containing carbon black are much higher than those for MRE/ISO and MRE/AN. The G′ increases with increasing carbon black content up to the highest values at 70 phr carbon black. The increase in G′ can be explained by increased carbon black particle-rubber interactions and carbon black particle–particle interactions as reported by

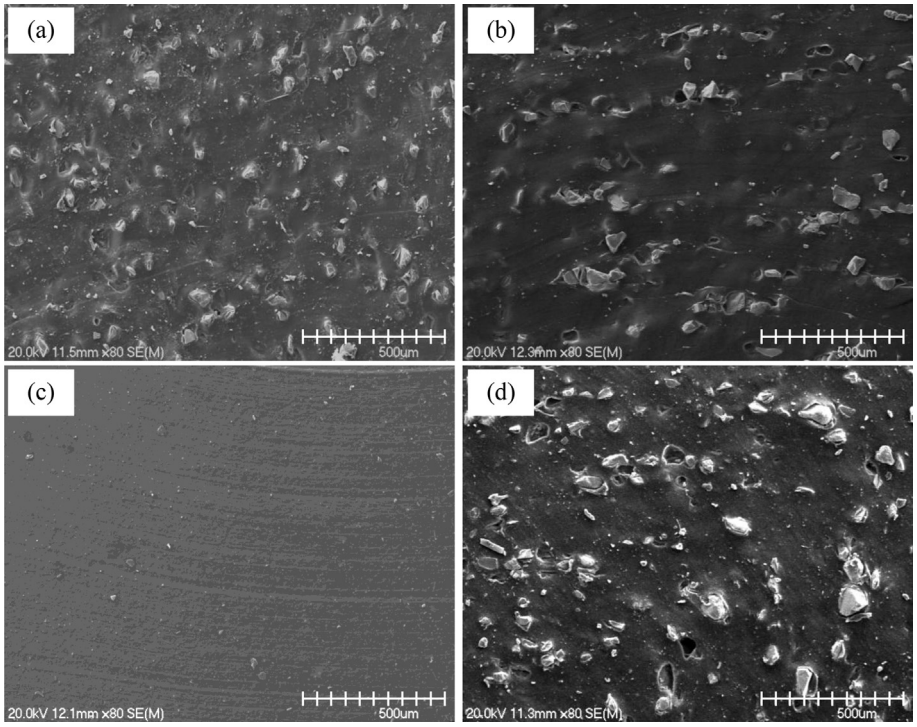

Fig. 4. SEM images of surface of; (a) MRE/ISO (ISO), (b) MRE/AN, (c) CS/50CB and (d) MRE/AN/50CB at ×80 magnitude of enlargement.

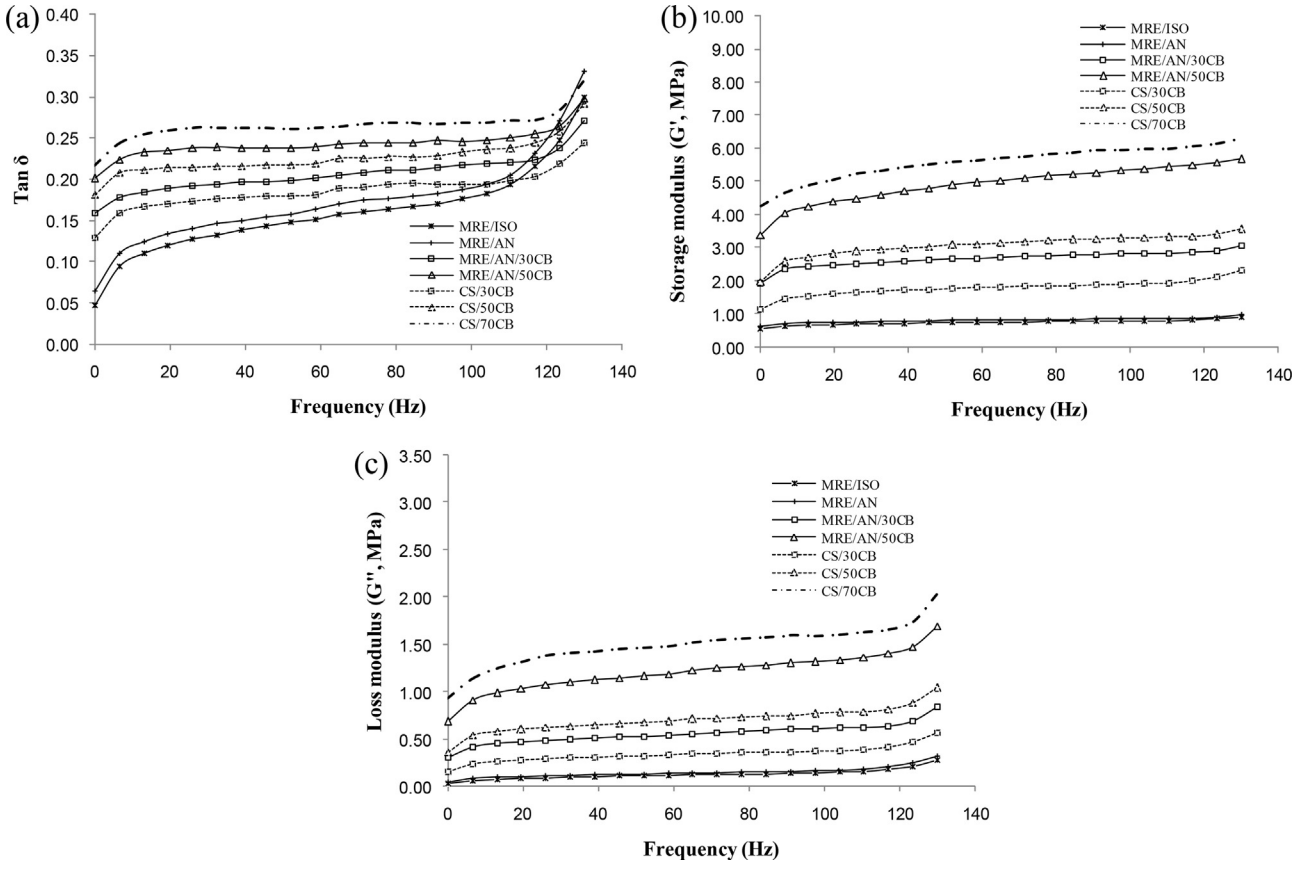

Fig. 5. (a) Tan δ, (b) storage modulus (G′) and, (c) loss modulus (G″) versus frequency for MREs and comparative samples.

number of researchers [22,23]. The particle-rubber interactions include physical adsorption of rubber chains on carbon black filler surfaces and chemical bonding between functional groups on the surface of carbon black (mostly quinonic groups) with rubber molecular chains which will restrain the mobility of rubber on the filler surface [24]. The particle–particle interactions relate to the tendency of carbon black particles to form aggregates at different levels [24]. Carbon black aggregates agglomerate together to form what are known as primary aggregates, held together by Van der Waals bonds. Further agglomeration occurs between primary aggregates to produce secondary aggregates, again held together by Van der Waals bonds, although the secondary aggregates are less rigidly held together. The particle-rubber interactions and particle–particle interactions lead to the formation of a carbon black filler networks in the rubber matrix as shown in Fig. 6. These contain rubber with different degrees of constraint (bound rubber, occluded rubber and trapped rubber), higher than that for rubber away from carbon black particles [25]. These constrained rubber regions improve the ability to store elastic energy, resulting in increased G′. The increase of G″ with increasing carbon black content during deformation can be explained by the increased energy loss that occurs due to the breakdown and reformation of the carbon black filler networks.

3.2.2. Strain amplitude sweep measurements

The variation of tan δ with strain amplitude for MREs and comparative samples is depicted in Fig. 7a. Tan δ was amplitude dependent at low strain amplitude before reaching a plateau, with tan δ for MRE/AN and MRE/ISO reaching a plateau at around 2.5% strain amplitude, whereas for the other samples containing carbon black the tan δ reached a plateau at around 1.5% strain amplitude. The increased amplitude dependence for MRE/AN and MRE/ISO compared to comparative samples indicates that the amplitude of applied strain required to break stronger interfacial bonding between iron sand and rubber was relatively larger compared to easier that required for breaking down carbon black filler networks. At the plateau region, it would appear that most of the filler-rubber interactions diminish (Van der Waals for carbon black and Van der Waals and covalent for iron sand) and tan δ is largely reliant on the rubber matrix which is at its largest due to greatest amount of rubber free to flow and friction between rubber chains and iron sand [15,26].

Tan δ of MRE/AN was found to be 8.5% higher than that of MRE/ISO over the whole strain amplitude range explored; the higher tan δ for MRE/AN can again be explained due to additional damping through breakdown of joint rubber shells, more trapped rubber released and magnetic interactions (magnetomechanical and interparticle interaction). Indeed, it can also be seen that although the tan δ for MRE/AN is lower at low strain amplitudes, it is slightly higher than for CS/30CB above a strain amplitude of 2%. For the comparative samples, tan δ increased in the following order: CS/30CB < CS/50CB < CS70/CB, along with the increased content of carbon black. Similarly, tan δ values for MRE/AN/30CB and MRE/AN/50CB were higher than MRE/AN (6% and 15%, respectively) and the tan δ approximately 4% and 5% higher compared to CS/30CB and CS/50CB over the strain amplitude range explored as was seen for range of frequency discussed in the previous section.

Again, the effect of carbon black on improved tan δ can be analysed further using G′ and G″ plots as shown in Fig. 7 (b and c). It is apparent that G′ and G″ for samples containing carbon black are much higher than MRE/ISO and MRE/AN, which is not surprising given similar trends with influence of frequency on G′ and G''. As previously discussed, the increase of G′ with increase in carbon black content can be explained by increased amount of constrained rubber in filler networks and the increased energy loss is likely due to breakdown and reformation of filler networks during cyclic deformation along with more constrained rubber flow.

3.2.3. Temperature sweep measurements

Fig. 8 presents the tan δ versus temperature curves for MREs and comparative samples. The tan δ peak is associated with the glass transition temperature (T_g) of the materials. In general, the trend for the height of the tan δ peak is different compared to trends observed previously for the effect of frequency and strain amplitude on tan δ; the tan δ peaks for MRE/ISO and MRE/AN are higher than for the others and the height of the tan δ peak decreased with increasing carbon black content in the following order: CS/30CB > CS/50CB > CS70/CB. To explain the trend seen here, it is necessary to consider the relative change of contributions by different energy dissipation mechanisms in the glass transition zone. It is known for materials containing non-magnetic particles, that in the glass transition zone, contribution from segmental motion of rubber chains generally far outweighs that through breakdown of filler–filler and filler-rubber interactions [27]; furthermore for anisotropic MREs, the damping through magnetic interactions around T_g is thought to be insignificant compared with that due to segmental motion of rubber chains with the height of the tan δ peak for anisotropic MREs having been observed to be lower than unfilled natural rubber [28]. Based on such importance of rubber chain motion, the higher tan δ peak for MRE/ISO and MRE/AN can be explained due to a greater volume of free rubber chains participating in large scale motions at T_g which is likely to be due to less constrained rubber with iron sand particles in the MRE/ISO and MRE/AN than with carbon black particles in the MREs containing carbon black and comparatives samples due to the difference in interfacial area, being much smaller in the case of the much larger iron sand particles. For samples containing carbon black, further regions of constrained rubber would also form within carbon black filler networks; this constrained rubber is shielded from deformation and loses its ability to participate in the energy dissipation process. There also appears to be a slightly higher tan δ peak for MRE/AN compared with MRE/ISO which is likely to be due to formation of aligned structures in anisotropic MREs reducing the amount of trapped rubber. The decrease in height of the tan δ peak with increased carbon black content could be explained by the increased amount of constrained rubber on carbon black surfaces and within filler networks. The height of the tan δ peaks for MRE/AN/30CB and MRE/AN/50CB were found to be lower than the tan δ peaks for CS/30CB and CS/50CB, supporting iron sand contributing to rubber constraint. It is also apparent that T_g values

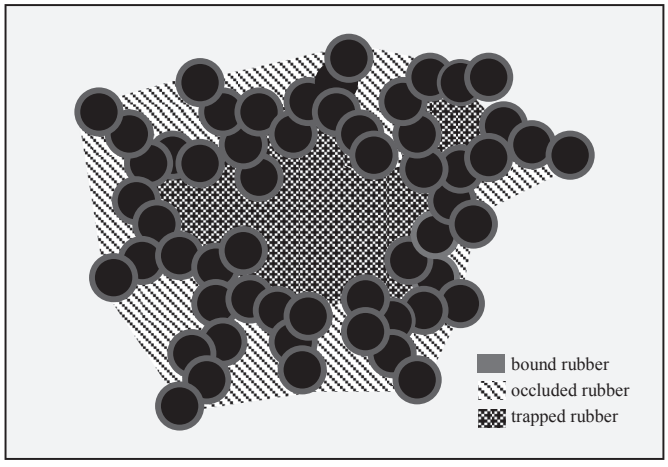

Fig. 6. Schematic presentation of carbon black filler network.

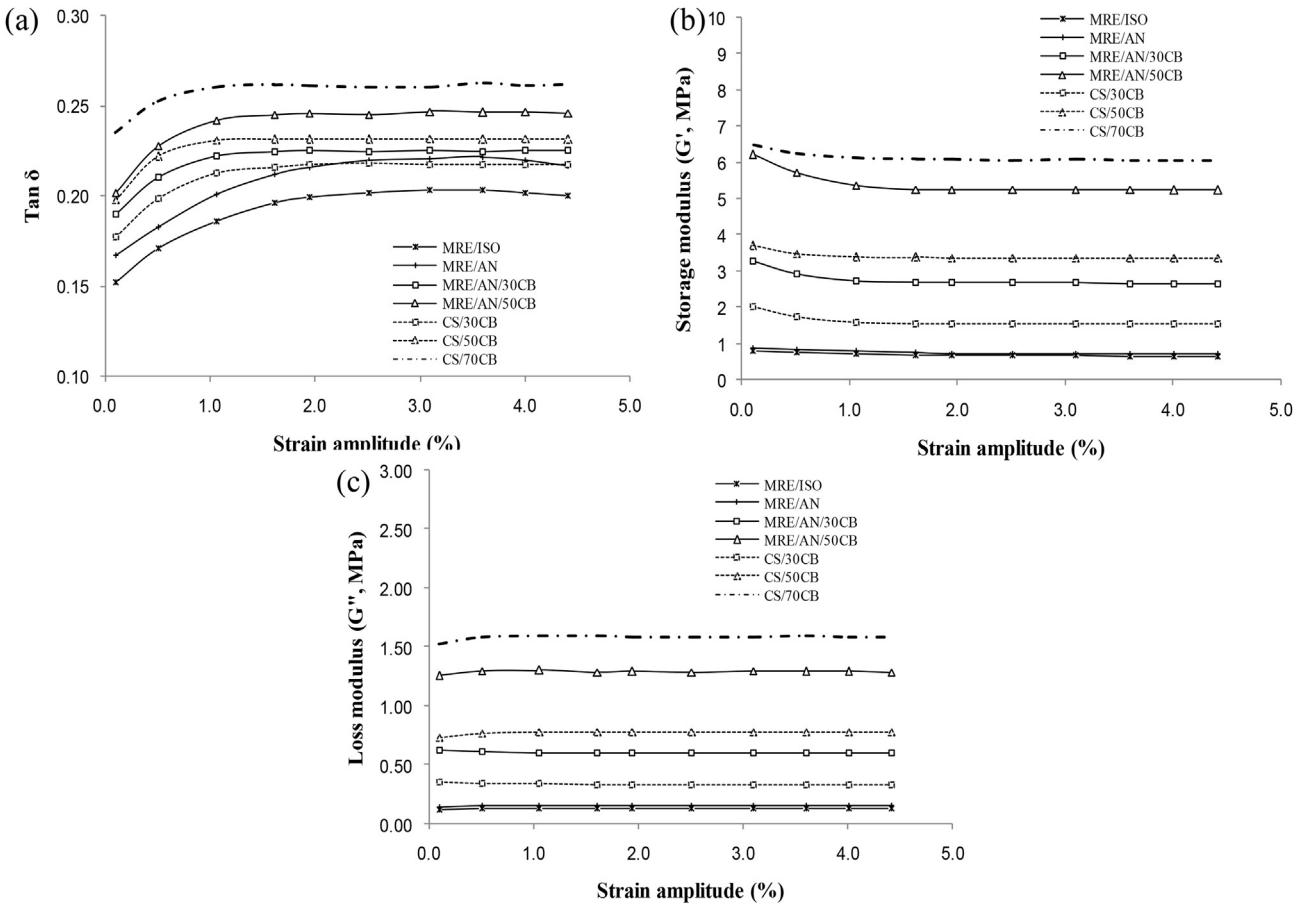

Fig. 7. (a) Tan δ, (b) storage modulus (G′) and, (c) loss modulus (G″) versus strain amplitude for MREs and comparative samples.

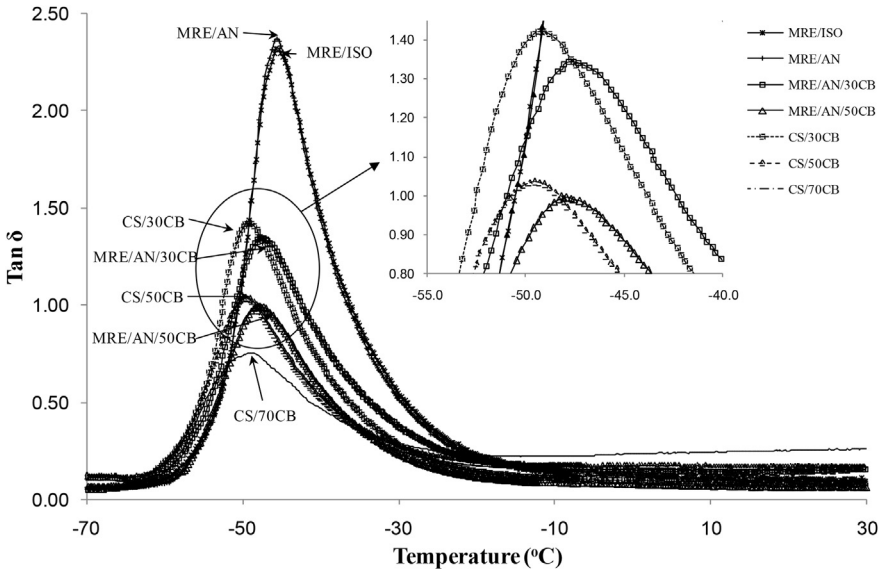

Fig. 8. Tan δ versus temperature curves for MREs and comparative samples.

for MRE/ISO and MRE/AN are the highest followed by MRE/AN/30CB and MRE/AN/50CB and comparative samples. This observation suggests that strong interfacial bonding between iron sand and rubber increased the temperature required for the rubber molecular chains to attain maximum segmental motion compared to weak Van der Wall bonds in samples containing carbon black.

3.3. Hysteresis

Fig. 9 shows hysteresis loss for MREs and comparative samples. Hysteresis loss for both MRE/ISO and MRE/AN was found to be lower than for the other samples. Hysteresis loss in isotropic MREs could be associated with the energy absorbed during viscous flow

which is constrained due to strong interfacial bonding between iron sand and rubber and energy loss due to stress released in breaking the interfacial bonding [15] and given higher hysteresis loss than for unfilled rubber (31 kJ/m^3, as obtained elsewhere [28]); for anisotropic MREs similar mechanisms would be involved as well as energy loss due to breakdown of joint rubber shells with more trapped rubber released, however, the damping through magnetic interactions would appear to be insignificant given that the hysteresis loss for MRE/AN was lower than MRE/ISO. This seems to contradict the results for the effect of frequency and strain amplitude on tan δ, which could be explained as being due to a different mode of loading as shown in Fig. 10 (tensile versus shear). In tension as in the case here, it is largely the spacing increasing between chains that are changing, whereas in shear loading, the spacing within chains and so between the particle increases [28]. It is possible that in the direction of tensile loading, the particles are separated to such an extent in anisotropic MREs that inter-particle attraction is less effective than for the isotropic MREs.

For the comparative samples, hysteresis loss increased in the following order: CS/30CB < CS/50CB < CS70/CB, along with the increased content of carbon black. This could be explained due to increased energy absorbed caused by breakdown and reformation of carbon black filler networks with increase in carbon black content which becomes more significant than the reduction of segmental motion of rubber chains (away from T_g). Furthermore, when the applied strain increases to such an extent the filler network can be broken down, the constrained rubber would be released and therefore allow more viscous flow during deformation, resulting in an increase of dissipated energy [29,30]. As can also be seen, hysteresis loss for MRE/AN/30CB and MRE/AN/50CB significantly increased compared to MRE/AN (21% and 71%, respectively), supporting the data obtained for assessment of the effect of frequency and strain amplitude on tan δ, that addition of carbon black results in higher energy dissipation in the materials (other than around T_g). Also hysteresis losses for MRE/AN/30CB and MRE/AN/50CB were approximately 5% and 8% higher compared to CS/30CB and CS/50CB, supporting the use of iron sand to improve hysteresis loss through interfacial damping between the particle and the rubber matrix (constraint of viscous flow due to strong interfacial bonding between iron sand and rubber, energy loss due to breakdown of the interfacial bonding and breakdown of joint rubber shells with more trapped rubber released).

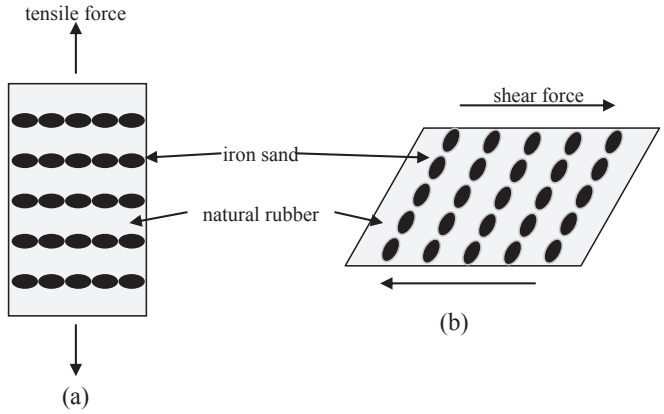

Fig. 10. Comparison of influence of loading types on particle separation, (a) tensile mode, (b) shear mode.

4. Conclusion

It was found that isotropic MREs had uniform iron sand particle distribution without obvious aggregation and alignment of magnetic particles occurred for anisotropic MREs as a consequence of curing the materials under an applied magnetic field at elevated temperature. For comparative samples, carbon black particles were generally evenly distributed in the rubber matrix with some aggregates, but none larger than 20 μm. SEM also revealed that addition of carbon black into anisotropic MREs constrained the movement of iron sand particles; chain-like columnar structures became shorter and less aligned. Energy absorption for comparative samples (CS/30CB, CS/50CB and CS/70CB) was generally found higher than MRE/ISO and MRE/AN over the range of frequency and strain amplitude explored, as well as in hysteresis testing and this

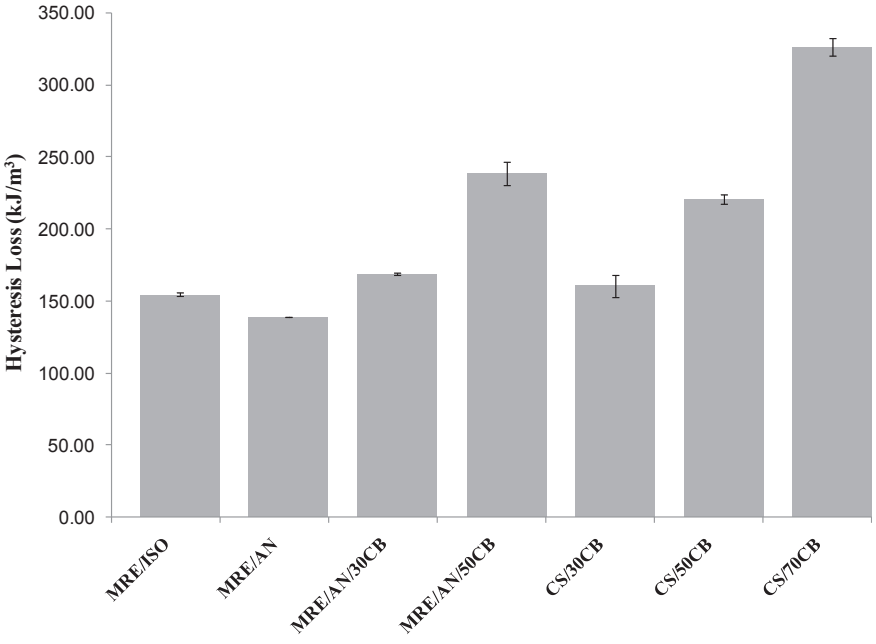

Fig. 9. Hysteresis loss for MREs and comparative samples.

was believed to be largely due the presence of carbon black in the formulation. Further assessment carried out on materials that were the same as MRE/AN except they had additions of 30 and 50 phr carbon black (MRE/AN/30CB and MRE/AN/50CB) gave generally higher energy absorption than comparative samples of the same carbon black contents (CS/30CB and CS/50CB), supporting the use of iron sand to improve damping through interfacial damping between the particle and the rubber matrix and magnetic interactions (magnetomechanical and inter-particle interaction). However, trends for energy absorption at around T_g were found to reverse which can be explained by the segmental motion of rubber chains being by far the most significant influence on energy absorption at this temperature as supported by literature and so care should be taken when using the materials at such temperature although this is likely to be away from the service temperature for these materials.

Acknowledgements

The authors would like to thank for the support from the Polymer and Composite Research Group of the University of Waikato.

References

[1] Sun Y, Zhou X, Liu Y, Zhao G, Jiang Y. Effect of magnetic nanoparticles on the properties of magnetic rubber. Mater Res Bull 2009;45(7):878–81.
[2] Makled MH, Matsui T, Tsuda H, Mabuchi H, El-Mansy MK, Morii K. Magnetic and dynamic mechanical properties of barium ferrite natural rubber composites. J Mater Process Technol 2005;160(2):229–33.
[3] Dobrzanski LA, Tomiczek A, Tomiczek B, Slawska A, Iesenchuk O. Polymer matrix composite materials reinforced by Tb0.3Dy0.7Fe1.9 magnetostrictive particles. J Achiev Mater Manuf Eng 2009;37(1):16–23.
[4] Chen L, Gong XL, Li WH. Effect of carbon black on the mechanical performances of magnetorheological elastomers. Polym Test 2008;27(3):340–5.
[5] Jerzy K, Michal K, Daniel L. Magnetomechanical properties of anisotropic and isotropic magnetorheological composites with thermoplastic elastomer matrices. Smart Mater Struct 2011;20(8):12.
[6] Chokkalingam R, Rajasabai Senthur P, Mahendran M. Magnetomechanical behavior of Fe/PU magnetorheological elastomers. J Compos Mater 2010;45(15):1545–52.
[7] Fuchs A, Zhang Q, Elkins J, Gordaninejad F, Evrensel C. Development and characterization of magnetorheological elastomers. J Appl Polym Sci 2007;105(5):2497–508.
[8] Ginder J. Magnetorheological elastomers: properties and applications. Proc SPIE 1999;3675(1):131.
[9] Lerner AA, Cunefare KA. Performance of MRE-based vibration absorbers. J Intelligent Material Syst Struct 2008;19(5):551–63.
[10] Sun TL, Gong XL, Jiang WQ, Li JF, Xu ZB, Li WH. Study on the damping properties of magnetorheological elastomers based on cis-polybutadiene rubber. Polym Test 2008;27(4):520–6.
[11] Wang Y, Hu Y, Deng H, Gong X, Zhang P, Jiang W, et al. Magnetorheological elastomers based on isobutylene–isoprene rubber. Polym Eng Sci 2006;46(3):264–8.
[12] Boczkowska A, Awietjan SF, Pietrzko SA, KOK J. Mechanical properties of magnetorheological elastomers under shear deformation. Compos Part B Eng 2012;43(2):636–40.
[13] Deng HX, Gong XL. Application of magnetorheological elastomer to vibration absorber. Commun Nonlinear Sci Numer Simul 2008;13(9):1938–47.
[14] Dyke SJ, Spencer JR, Sain MK, Carlson JD. Modeling and control of magnetorheological dampers for seismic response reduction. Smart Mater Struct 1996;5(5):565–75.
[15] Pickering KL, Raa Khimi S, Ilanko S. The effect of silane coupling agent on iron sand for use in magnetorheological elastomers part 1: surface chemical modification and characterization. Compos Part A Appl Sci Manuf.
[16] Xiuying Q, Xiushou L, Weihua L, Jun C, Xinglong G, Tao Y, et al. Microstructure and magnetorheological properties of the thermoplastic magnetorheological elastomer composites containing modified carbonyl iron particles and poly(styrene- b -ethylene-ethylenepropylene- b -styrene) matrix. Smart Mater Struct 2012;21(11):115028.
[17] Wang YL, Hu YA, Chen L, Gong XL, Jiang WQ, Zhang PQ, et al. Effects of rubber/magnetic particle interactions on the performance of magnetorheological elastomers. Polym Test 2006;25(2):262–7.
[18] Lakes RS. High damping composite materials: effect of structural hierarchy. J Compos Mater 2001;36(3):287–97.
[19] Raa Khimi S, Pickering KL. A new method to predict optimum cure time of rubber compound using dynamic mechanical analysis. J Appl Polym Sci 2013;131(6) [n/a-n/a].
[20] Kasgoz A, Akin D, Durmus A. Rheological and electrical properties of carbon black and carbon fiber filled cyclic olefin copolymer composites. Compos Part B Eng 2014;62(0):113–20.
[21] Kallio M. The elastic and damping properties of magnetorheological elastomers. 1st ed. Finland: VTT Technical Research Centre of Finland; 2005.
[22] Wang MJ. Effect of polymer-filler and filler-filler interactions on dynamic properties of filled vulcanizates. Rubber Chem Technol 1998;71(3):520–89.
[23] Kraus G. Reinforcement of elastomers by carbon black. Fortschritte der Hochpolymeren-Forschung. Berlin: Springer Berlin Heidelberg; 1971. p. 155–237.
[24] Jovanovic V, Samarzija-Jovanovic S, Budinski-Simendic J, Markovic G, Marinovic-Cincovic M. Composites based on carbon black reinforced NBR/EPDM rubber blends. Compos Part B Eng 2013;45(1):333–40.
[25] Wang M-J. The role of filler networking in dynamic properties of filled rubber. Rubber Chem Technol 1999;72(2):430–48.
[26] Rendek M, Lion A. Amplitude dependence of filler-reinforced rubber: experiments, constitutive modelling and FEM Implementation. Int J Solids Struct 2010;47(21):2918–36.
[27] Li Y, Han B, Liu L, Zhang F, Zhang L, Wen S, et al. Surface modification of silica by two-step method and properties of solution styrene butadiene rubber (SSBR) nanocomposites filled with modified silica. Compos Sci Technol 2013;88(0):69–75.
[28] Raa Khimi S, Pickering KL, Mace BR. Dynamic properties of magnetorheological elastomers based on iron sand and natural rubber. J Appl Polym Sci.
[29] Kucherskii AM. Hysteresis losses in carbon-black-filled rubbers under small and large elongations. Polym Test 2005;24(6):733–8.
[30] Meier JG, Kluppel M. Carbon black networking in elastomers monitored by dynamic mechanical and dielectric spectroscopy. Macromol Mater Eng 2008;293(1):12–38.